ADVANCING PHOTOACOUSTIC IMAGING AS A TOOL FOR DISEASE DIAGNOSIS

A Dissertation
Presented to
The Academic Faculty

by

Timothy Wayne Sowers

In Partial Fulfillment
of the Requirements for the Degree
Doctor of Philosophy in
Bioengineering

Georgia Institute of Technology
December 2020

ADVANCING PHOTOACOUSTIC IMAGING AS A TOOL FOR DISEASE DIAGNOSIS

Approved by:

Dr. Stanislav Emelianov, Advisor
Department of Biomedical Engineering and School of Electrical and Computer Engineering
Georgia Institute of Technology and Emory University

Dr. Levent Degertekin
Department of Mechanical Engineering
Georgia Institute of Technology

Dr. Brooks Lindsey
Department of Biomedical Engineering
Georgia Institute of Technology and Emory University

Dr. David Ku
Department of Mechanical Engineering
Georgia Institute of Technology

Dr. Muralidhar Padala
Department of Biomedical Engineering and Emory Department of Surgery
Georgia Institute of Technology and Emory University

Date Approved: October 24, 2020

For the love of my life, Liza George.

ACKNOWLEDGEMENTS

First and foremost, I would like to acknowledge and thank my wife, Liza George. You have been unfailingly supportive throughout this process. Whether my experiments were going well or not, our relationship has always a bright spot in my life. I'd also like to thank my parents. I would not have gotten here without their unfailing and loving support.

I would also like to thank my adviser, Stanislav Emelianov. He has created a diverse and interdisciplinary environment in the lab where individuals have great intellectual and personal freedom. His continual drive and enthusiasm for the next new research question is something I will take with me.

I would like to thank members of my committee. Their willingness to contribute to the quality of this dissertation with their expertise is greatly appreciated.

Among all the lab members who have helped me along the way, I would like to single out and thank Andrei Karpiouk and Don VanderLaan. All the practical skills associated with conducting intravascular photoacoustic experiments, I learned from them.

I would also like to thank all the individuals who contributed directly to my work. This includes Nich Dana for his early lessons on the Monte Carlo simulation software I use in this work, Eleanor Barber for her exceptionally good lessons in cell culture, and Heechul Yoon for his expertise with the Verasonics system. I'd also like to acknowledge Ethan Smith, who worked with me from his first year as an undergraduate doing a variety of tasks including biological assays, wet-lab procedures, aiding in imaging and animal experiments,

and doing data analysis. Finally, I'd like to acknowledge David Qin for working with me on the fluence compensation project on this report. I hope the knowledge I passed on proves as useful to you as the information Nich passed to me several year ago.

A variety of other individuals have contributed to my work here at Georgia Tech through ideation, training on equipment and protocols, and going over all the small details and refinements that can make or break an experiment. These people include Diego Dumani, Brandyn Orr, Steve Yarmoska, Kristina Hallam, Andrew Zhao, Lingyi Zhao, Jisha Somasekharan, In-Cheol Sun, Yiying Zhu.

No acknowledgement section would be complete without including the efforts of collaborators. I would like to thank Dr. Robert Taylor and Gigi Joseph for histological analysis at the early stages of the safety studies on intravascular photoacoustics. I would like to thank Dr. Teresa Snow for discussing the best way to handle the statistics in my last research aim. I would also like to thank Dr. Muralidhar Padala and his lab members, especially Susan Schmarkey and Daisuke Onohara, for their contributions to the *in vivo* intravascular photoacoustic safety studies.

TABLE OF CONTENTS

LIST OF TABLES

LIST OF FIGURES

LIST OF SYMBOLS AND ABBREVIATIONS

ANSI	American National Standards Institute
cm	centimeter
C_p	specific heat capacity
D	diameter
EC50	half maximal effective concentration (light dosage that will cause damage 50% of the time)
ECM	extracellular matrix
E_p	energy per pulse (of laser)
F	fluence
g	gram
g	anisotropy coefficient
GET	Gomori's Elastin Trichrome
gm	gram mole
HCAEC	human coronary artery endothelial cell
HCl	hydrochloric acid
H&E	Hematoxylin & Eosin
IACUC	Institutional Animal Care and Use Committee
ICG	Indocyanine Green
IVPA	intravascular photoacoustic
IVUS	intravascular ultrasound
J	joule
L	liter
LDL	low density lipoprotein

L_z	length in the axial direction (of an artery)
M	molar
MC	Monte Carlo
MCX	Monte Carlo Extreme
MCXLAB	Monte Carlo Extreme for MATLAB
MECCF	maximum expected cumulative fluence
mJ	millijoule
mL	milliliter
mM	millimolar
mm	millimeter
MPE	maximum permissible exposure
MTT	3-(4,5-dimethylthiazol-2-yl)-2,5-diphenyltetrazolium bromide
n	index of refraction
NA	numerical aperture
$N_{A\text{-lines}}$	number of A-lines per frame
Nd:YAG	Neodymium-doped yttrium aluminum garnet (a common laser type)
NIRF	near infrared fluorescence
nm	nanometer
OCT	optical coherence tomography
OPO	optical parametric oscillator
p	statistical measure of significance
PA	photoacoustic
P_r	pullback rate (of a catheter)
PRF	pulse repetition frequency
SDS	sodium dodecyl sulfate

SMC	smooth muscle cell
SNR	signal-to-noise ratio
SO_2	oxygen saturation
US	ultrasound
v_s	speed of sound (in tissue)
β	bulk modulus
Γ	Grueneisen parameter
μ_a	optical absorption coefficient
µg	microgram
µL	microliter
µm	micrometer
μ_s	optical scattering coefficient
°	degree(s)

SUMMARY

Photoacoustic imaging is a promising tool for disease diagnosis. The modality uses short pulses of laser light to generate ultrasonic waves from tissue. Photoacoustics can take advantage of the optical properties of tissue to differentiate between different tissue types. In addition, photoacoustic imaging is highly complementary with ultrasound imaging, which makes it possible to overlay photoacoustic signals with ultrasound signals displaying anatomic information. Applications for photoacoustic imaging include improved diagnosis and characterization of primary tumors, cancer metastasis, atherosclerosis, arthritis, and other diseases and pathologies. In this dissertation, photoacoustic imaging as a diagnostic tool is advanced in two ways.

First, the delivery and distribution of light in tissue is addressed. Monte Carlo simulations of light propagation are used to optimize light delivery (Chapter 3). A variety of tissue types, light wavelengths, species characteristics, and device geometries are considered. Optimal geometries are recommended for researchers depending on whether they are imaging mice or humans. It was found that several times less light will be delivered in humans, which has implications for clinical translation of imaging experiments conducted in mice. The simulations were validated using a set of matched simulations and experiments. Next, a new technique is introduced which could make it possible to compensate for the decrease in fluence with respect to tissue depth (Chapter 4). The viability of the technique is tested using simulations of a broad range of tissue. Also, a set of simulations mimicking contrast agents in breast tissue is used to estimate the potential benefit of the technique. The results indicate the technique could make it possible to make

relative quantitative comparisons of photoacoustic signal from different absorbers deep in tissue. This justifies further experiments *ex vivo*.

Next, the safety of intravascular photoacoustic imaging is evaluated. Intravascular photoacoustics is a catheter based imaging technique meant to identify lipid plaques formed from atherosclerosis. Intravascular photoacoustic imaging can result in the same region of tissue being irradiated hundreds of times because the artery must be irradiated repeatedly as the catheter is rotated and retracted to produce one 3D image. This makes safety a concern. In this dissertation, the safety of intravascular photoacoustic imaging is evaluated *in vitro* and *in vivo*. Several cell types found in healthy and diseased arteries were irradiated *in vitro* at different dosages (Chapter 5). The first finding is that cell death occurs only at the upper limit of expected light dosages required for intravascular photoacoustic imaging. The second finding is that any damage from photoacoustic imaging is likely to be from heat accumulation over many light pulses, rather than from optical breakdown caused by high fluences from any single pulse. Next, *in vivo* studies were conducted on swine (Chapter 6). Damage was observed at the highest light irradiation dosages. However, there was no vessel wall damage found at dosages that have been used to successfully image plaque *in vivo* in other recent studies. These results indicate that intravascular photoacoustic imaging can be used to identify lipid plaques without damaging the vessel wall.

CHAPTER 1: SUMMARY OF SPECIFIC AIMS

1.1 Aim 1: Optimizing light delivery for photoacoustic imaging systems

The central hypothesis of this aim is that fluence delivery, and thus image quality, can be optimized by varying the geometry of one's experimental setup in a manner dependent on the species and tissue type of the imaging target. In this aim, Monte Carlo modeling was conducted to investigate the effect of the light delivery angle, light delivery position, imaging target species, tissue type, and laser wavelength on the amount of light delivered to the imaging plane. For each species, tissue type, and light wavelength the fiber position and light emission angle that maximized peak fluence was reported. Matched modeling and experiments were conducted to validate the model. The work in this aim is meant to give researchers guidance on the optimal experimental geometry for a variety of applications of photoacoustic imaging. Researchers can choose the optimal optical fiber distance and angle for the tissue type and wavelength that most closely matches their application. In addition, the work is meant to give insight into the differences in fluence that may occur when transitioning from preclinical studies in mice to clinical use in humans.

1.2 Aim 2: Fluence Compensation in Deep Tissue for Quantitative Photoacoustic Imaging

The central hypothesis of this aim is that it is possible to compensate for fluence variations in deeper regions of tissue by using compression to track the change in photoacoustic signal

of native absorbers as a function of depth. In this aim, the viability of this method is investigated using Monte Carlo simulations. First, it is determined that the fluence decreases at a exponential rate for homogenous tissue for a wide range of optical properties. This establishes that the technique would be viable in most tissue types. Then, the expected improvement in photoacoustic signal from using the technique is evaluated using a simulation consisting of several regions of high intensity (contrast agents) in breast tissue at 789 nm. The work is meant to establish the viability and usefulness of this technique, which would serve to motivate future *ex vivo* and *in vivo* experiments. Once developed and implemented, the technique would make it possible to make quantitative comparisons of relative photoacoustic signals.

1.3 Aim 3: Safety of Intravascular Photoacoustic Imaging – In Vitro Studies

The central hypothesis of this aim is that a threshold of light dosage for cell death can be identified for cells *in vitro* and that damage at higher IVPA dosages are likely to be caused by heating of tissue. To investigate this, the viability of macrophages, smooth muscle cells, and endothelial cell after irradiation with light dosages relevant to IVPA imaging was evaluated. First, cells were irradiated with many pulses of light, similar to the exposure from 3D image acquisition during IVPA imaging and at IVPA relevant dosages. The cells were then evaluated for viability. Second, cells were irradiated with fewer pulses but at the highest optical fluence expected during IVPA imaging and again evaluated for viability. The first output of this aim is to indicate whether IVPA can be conducted at safe light dosages. Second, it will indicate if the damage mechanism is expected to be heat accumulation from many laser pulses or optical breakdown from high peak fluences of

single pulses. Third, it will guide the light dosage decisions chosen for the *in vivo* experiments conducted for aim 4.

1.4 Aim 4: Safety of Intravascular Photoacoustic Imaging – In Vivo Studies

The hypothesis of this aim is that IVPA imaging can be conducted at safe laser dosages, but there will be limitations on the amount of energy used for safety reasons. This is the first *in vivo* study on the safety of IVPA imaging the author is aware of that has been reported to date. The carotid arteries of two swine were irradiated using a real-time IVPA imaging system at multiple wavelengths and energy dosages. The tissues were evaluated for damage by a pathologist. The purpose of this aim is to indicate the dosages at which IVPA can be safely conducted without causing damage to vessel tissue, which will further IVPA imaging on its path toward clinical application.

CHAPTER 2: BACKGROUND

2.1 Photoacoustic Imaging

2.1.1 Physical Principals

Photoacoustic imaging is a relatively recent imaging modality in the field of biomedical research[1, 2], although the physical effect was first discovered by Alexander Graham Bell[3]. Photoacoustic signals are induced by the application of short pulses of electromagnetic radiation, which for biomedical applications is usually achieved using a short laser pulse at a near infrared wavelength. Chromophores in the tissue absorb the laser light, resulting in the sudden absorption of heat. The consequent thermal expansion and collapse induces an ultrasonic disturbance in the form of a photoacoustic wave. This photoacoustic wave can then be detected by an ultrasound transducer. Importantly, the location of that signal can also be inferred from the elapsed time between laser irradiation and photoacoustic signal acquisition based on the speed of sound in tissue.

Efficient conversion of the absorbed laser light into photoacoustic signal requires satisfaction of the thermal and stress confinement conditions. In practice, this means that for biological tissues, photoacoustic signal induction requires lasers with a pulse width on the order of several nanometers. A more detailed description of these conditions can be found in the literature[4].

The intensity of the photoacoustic signal at its source is defined by the photoacoustic pressure induced by the expansion and compression of the chromophore at the location of light absorption (Eq. 1.1)[5].

$$P_o = \mu_a F \Gamma \quad \text{(Eq 1.1)}$$

where

$$\Gamma = \frac{\beta {v_s}^2}{C_p} \quad \text{(Eq. 1.2)}$$

In this equation, the photoacoustic pressure is defined by the term P_o. The other terms include the optical absorption coefficient (μ_a), the fluence (F), and the Grueneisen parameter (Γ). The fluence is defined as the light energy per unit area at the site of photoacoustic signal generation. The Grueneisen parameter is a set of physical properties of the tissue that determines how efficiently the heat is converted into photoacoustic pressure (Eq. 1.2). It includes the bulk expansion modulus (β), the speed of sound in tissue (v_s), and the specific heat capacity (C_p).

Several observations can be made from the photoacoustic pressure equation (Eq. 1.1). First, all the terms on the right-hand side are linearly proportional to the photoacoustic pressure, which can have practical implications. First, improved light delivery into the target tissue will increase the photoacoustic signal. This will result in improved image quality. Second, the dependence of the absorption coefficient on light wavelength is a

mechanism of contrast in photoacoustic imaging. When irradiating at multiple wavelengths, the Grueneisen parameter will not change since it is a physical property of the tissue. For small wavelength changes (i.e., range of wavelengths), the fluence locally can also be assumed constant. As a result, changes in photoacoustic pressure from the same absorber in tissue using images taken using different but close laser wavelengths can be attributed to the difference in the optical absorption coefficient at these wavelengths. Since these values are widely available in the literature, this can be used identify certain tissue types, or even contrast agents, in tissue. Note that although fluence is not accounted for directly when comparing between wavelengths, increasing light delivery for each pulse is still desirable since a greater number of imaging targets will be detected above the noise floor.

A final benefit of photoacoustic imaging is that the hardware requirements make it a simple process to also acquire ultrasound (US) images. Since the photoacoustic signal is detected by an ultrasound transducer, this same transducer used for anatomical imaging can also be used for acquiring the photoacoustic signal. Thus, any photoacoustic signal can be overlaid with the anatomical images produced by ultrasound. In addition to traditional B-mode US which acquires the anatomical images, PA can also be combined with flow imaging and elasticity imaging[6].

Photoacoustic imaging has been developed for a wide variety of imaging applications in the biomedical field over the last several years. These applications have been widely reviewed and include detection of cancers and metastasis to lymph nodes, identifying circulating tumor cells, imaging of atherosclerotic plaques, evaluating blood oxygenation (SO_2) levels, contrast agent imaging, and even measurement of temperature[7-

[14]. At least one study using a photoacoustic imaging system for breast cancer diagnosis has gone through clinical trials[15].

2.2 Transdermal Photoacoustic Imaging Systems

Photoacoustic acquisition is most often achieved using a commercial ultrasound array with light delivered externally from a pulsed laser using an optical fiber[16, 17] (Figure 2.1). This allows researchers to take advantage of ultrasound transducers developed commercially for photoacoustic signal acquisition, rather than systems built custom in the lab. As stated previously, these systems can also easily be used to acquire anatomical information with B-mode ultrasound that can then be overlaid with the photoacoustic signal. A variety of studies serve as examples of this method[8, 9, 18, 19]. The system used in clinical studies for breast cancer imaging mentioned earlier also used this approach[15].

Besides hardware, several factors affect the measured intensity of the photoacoustic signal and thus image quality for this type of system. One is the amount of energy emitted from the optical fiber. This is controlled directly with the laser system. In fact, the pulse energy will vary linearly with fluence, so an increase in the energy irradiated will result in a proportional increase in photoacoustic signal (Eq. 1). However, there is a ceiling on the amount of light that can be used based on safety considerations, which limits the fluence that can be applied to skin. A second factor is the positioning and orientation of the optical fiber used to deliver light. Changing these design choices would affect the path light travels to the imaging target, and thus the amount of light that reaches the imaging target. The ideal geometry may be dependent on multiple factors, including the optical properties of

the tissue and the species of the imaging target. Determining the ideal geometry which maximizes the amount of light that reaches the target for a variety of imaging scenarios would be of value to the field.

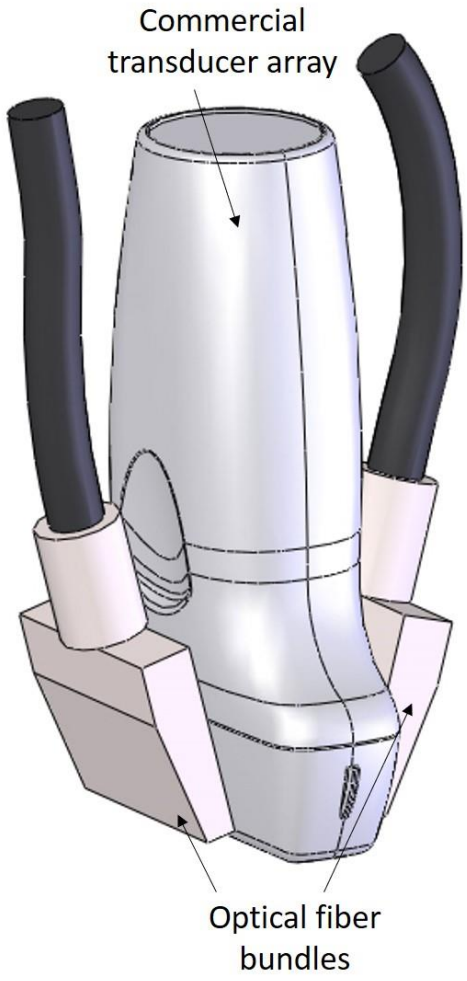

Figure 2.1 Representative image of the experimental setup commonly used for combined ultrasound and photoacoustic imaging. It consists of a linear ultrasound transducer array and light delivered from the side externally with bundles of optical fibers.

2.3 Intravascular Photoacoustics

2.3.1 Atherosclerosis

The leading cause of death worldwide is cardiovascular disease[20]. A primary driver of these deaths is coronary artery disease, in which lipid plaques grow in the vessel wall[21]. The biological progression is complex (Figure 2.2). Growth in the plaque can result in vessel occlusion, requiring an intervention to reinstate blood flow that is commonly achieved with deployment of a stent[22]. Alternatively, the plaques can suddenly rupture[23-25] or erode[25-27]. This exposes blood to coagulation inducing factors, resulting in blood clot formation. The clot can block blood flow at the site of the plaque. It can also block flow in downstream tissue if the clot breaks away from the site of the plaque and travels with blood in the vessel before eventually becoming lodged in a narrower vessel. Deaths from atherosclerosis commonly result from a heart attack after a clot blocks a coronary artery or a stroke if a clot travels downstream and blocks vessels in the brain.

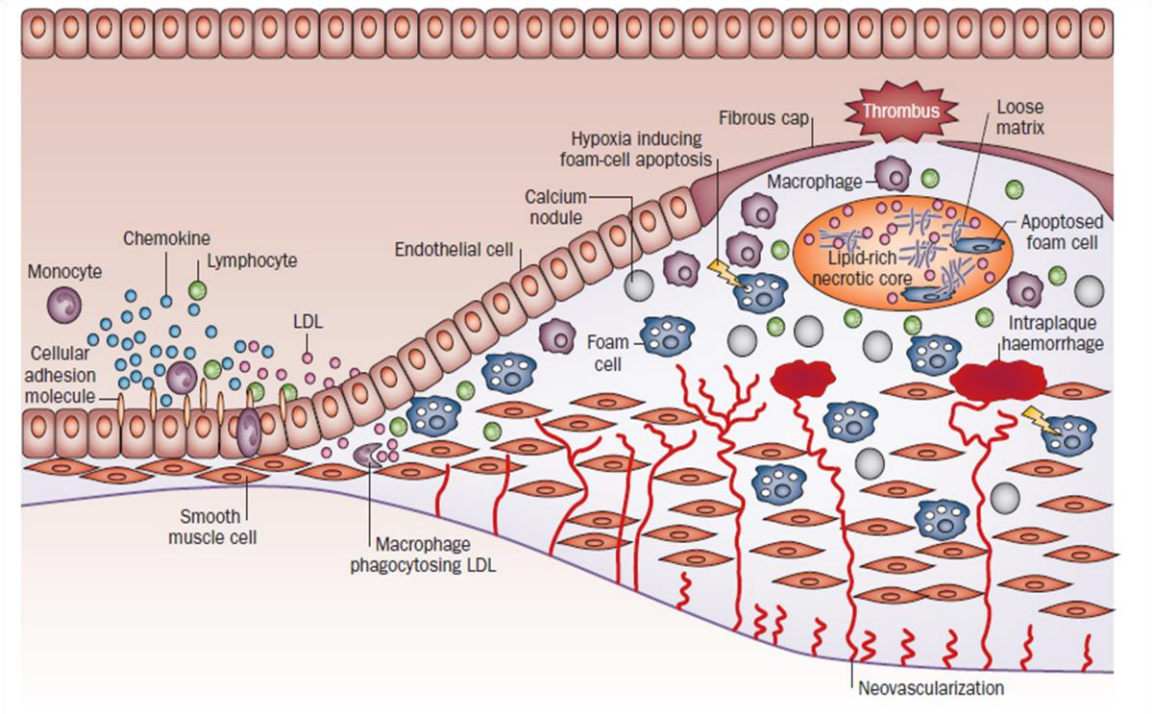

Figure 2.2 Development of an atherosclerotic plaque. Endothelial activation leads to chemokine production and expression of molecular markers on the surface of endothelial cells, which cause migration and adhesion of immune cells, including monocytes, to the endothelium. Increased endothelial permeability enables cells and LDL to cross into the vessel wall. Monocytes differentiate into macrophages, which take up modified LDL to form foam cells. Proinflammatory cytokines promote cell recruitment, smooth muscle cell proliferation and neovascularization. Both foam-cell formation and smooth-muscle proliferation cause a localized thickening of the vessel wall, which becomes a plaque. The fragile neovessels can bleed, causing intraplaque haemorrhage that can accelerate growth. Hypoxia and oxidative stress lead to foam-cell apoptosis and the formation of a lipid-rich necrotic core. Calcium is deposited within the plaque and a fibrous cap forms over the top of the plaque, shielding the thrombogenic content of the plaque from the circulation. As the plaque enlarges, it not only causes narrowing of the lumen, but can also lead to outward vessel-wall remodeling, a feature of plaques at high risk of rupture. The fibrous cap thins and the plaque eventually ruptures, which can lead to acute thrombosis and clinical events. High levels of inflammatory cells are found in the plaque at the time of rupture. Reproduced from ref [28] with permission from Springer Nature.

The progression of atherosclerotic plaques from their earliest stages to those that are vulnerable to rupture is biologically complex and not completely understood[29-31]. It is an inflammation driven process that involves a number of biological factors[28]. It is initiated by endothelial activation, which results in the migration of immune cells, especially monocytes, into the vessel wall. These monocytes take up low density lipoprotein (LDL), developing into foam cells. Focal proliferation of these cells and smooth muscle cells cause plaque growth. Eventually, hypoxia in these regions leads to cell death and the growth of a necrotic core. A fibrous cap at the top of the plaque can be formed. Plaque rupture or erosion arises from multiple factors, with the primary cause(s) still being an active subject of research.[23-27, 32-35]

Pathohistological studies have been conducted to determine the characteristics that differentiate rupture-prone or "vulnerable" plaques for clinical intervention[36-38]. These studies identified lipid content, widespread inflammation, and a thin fibrous cap as common characteristics of ruptured plaques. For example, in one histopathologic study a fibrous cap thickness <54 μm and a necrotic core area of 3.45 mm^2 were specified[37] as thresholds that differentiate between rupture prone and non-rupture prone plaques. These specific thresholds suggest that imaging modalities capable of measuring these features *in vivo* could inform clinicians deciding on the best course of intervention.

However, the concept of the vulnerable plaque has recently become controversial[39, 40]. The main criticism is that while these characteristics of plaque are commonly found in post-mortem examinations of ruptured plaque, they may not predict if a given plaque will rupture in a patient. Evidence for this is given in the PROSPECT trial[41], in which patients underwent coronary angiography, gray-scale ultrasound, and radiofrequency ultrasound

imaging following percutaneous coronary intervention after an adverse cardiovascular event. Only 26 out of 595 plaques (< 5%) identified as thin cap fibroatheromas were sites of recurrent events at 3.4 year follow up. Even when plaque burden (70%) and minimal lumen area (4.0 mm^2) were included, the event rate was only 18.2%. The study indicated that the high incidence of plaques meeting the "vulnerable" standards that did not rupture may make these criteria ineffective at directing clinical interventions.

It should be noted that there are limitations to this study. For one, radio frequency intravascular ultrasound (virtual histology) has only moderate sensitivity and specificity for identifying vulnerable plaque characteristics *in vivo*[39]. Given the high base incidence of plaques that did not meet the criteria of a thin-cap fibroatheroma (only 596 thin cap fibroatheroma out of 3160 identified lesions), moderate specificity would have resulted in a large proportion of the plaques being misidentified as thin-cap fibroatheromas. This could have artificially lowered the predictive rate of vulnerable plaque features. In addition, the study authors note that about half of the lesions responsible for recurrent events were evaluated with angiography but not ultrasound due to the small size of the artery, which means they also could have been misidentified at the first time point.

Other studies have lent weight to the idea that more accurate characterization of plaques could be useful in guiding clinical decisions on intervention. For example in the more recent Lipid Rich Plaque study[42], near-infrared spectroscopy was combined with intravascular ultrasound in a prospective study involving over 1500 patients. Patients with suspected coronary artery disease underwent imaging in segments that included non-culprit plaques. Measures of lipid presence were able to improve prediction of future events in non-culprit plaques, with a hazard ratio of 2.18 for the endpoint of major adverse

cardiovascular events at 2 year follow up. The study authors suggest that near-infrared spectroscopy and ultrasound can be used to inform decisions on intervention, especially in larger arteries where side effects from catheterization are less likely. These studies illustrate that it is still possible for improved plaque characterization to be useful for guiding clinical intervention, although more work is needed to identify the best features for differentiation and develop the imaging modalities to detect them.

In addition to plaque characteristics, some have argued that plaque vulnerability may need to be combined with other factors related to patient vulnerability. These include characteristics of blood related to thrombosis and the vulnerability of the myocardium based on a patient's prior medical history[40]. Evaluation of widespread inflammation may also be needed, as many patients experiencing acute coronary syndrome have multiple legions besides the culprit lesion[43]. Overall, other clinical measures may need to be incorporated into the decision making process beyond information taken from intravascular imaging methods.

Identification of clear diagnostic criteria for informing clinical interventions is inhibited by the widespread use of retrospective studies of culprit lesions[40]. Diagnostic criteria could be determined if additional prospective studies based on plaque characterization are conducted. However, the lack of imaging modalities with high sensitivity and specificity for the characteristics of ruptured culprit lesions have made this difficult. The development of imaging modalities that could accurately measure fibrous cap thickness, lipid content and area, and the presence of inflammatory markers *in vivo* would make it possible to rectify this shortcoming.

2.3.2 Intravascular Photoacoustic Imaging

Intravascular photoacoustics (IVPA) is a catheter-based system that can detect lipid in plaques in vessel walls using photoacoustic imaging. The technique takes advantage of the unique optical properties of lipid, which has absorption peaks at 1210 and 1720 nm[44]. The enhanced photoacoustic signal from irradiation at this wavelength can be used to differentiate lipid from surrounding tissue. This imaging technique has the potential to more accurately characterize plaque features such as lipid area, depth, and angular extent. In addition, the development of contrast agents shows it may be possible to evaluate the intensity of expression of biological markers in plaque[45].

The catheter design consists of a side firing optical fiber and ultrasound transducer[46, 47] (Figure 2.3). Initial designs used an optical fiber polished at an angle to refract light outward through the catheter. Other more recent designs similarly use a reflective mirror at a 45 degree angle to reflect the light[48]. The photoacoustic signal induced by the laser irradiation is detected by an ultrasound transducer oriented sideways such that its field of view overlaps the light emission from the optical fiber. The ultrasound transducer is also used to acquire ultrasound images. These can be overlaid with the intravascular photoacoustic image to give anatomic information about the location of any acquired photoacoustic signal. In this way, the size and extent of lipid in a plaque can be imaged and mapped to its location in the artery. Catheter designs reported in the literature have steadily improved over time[48].

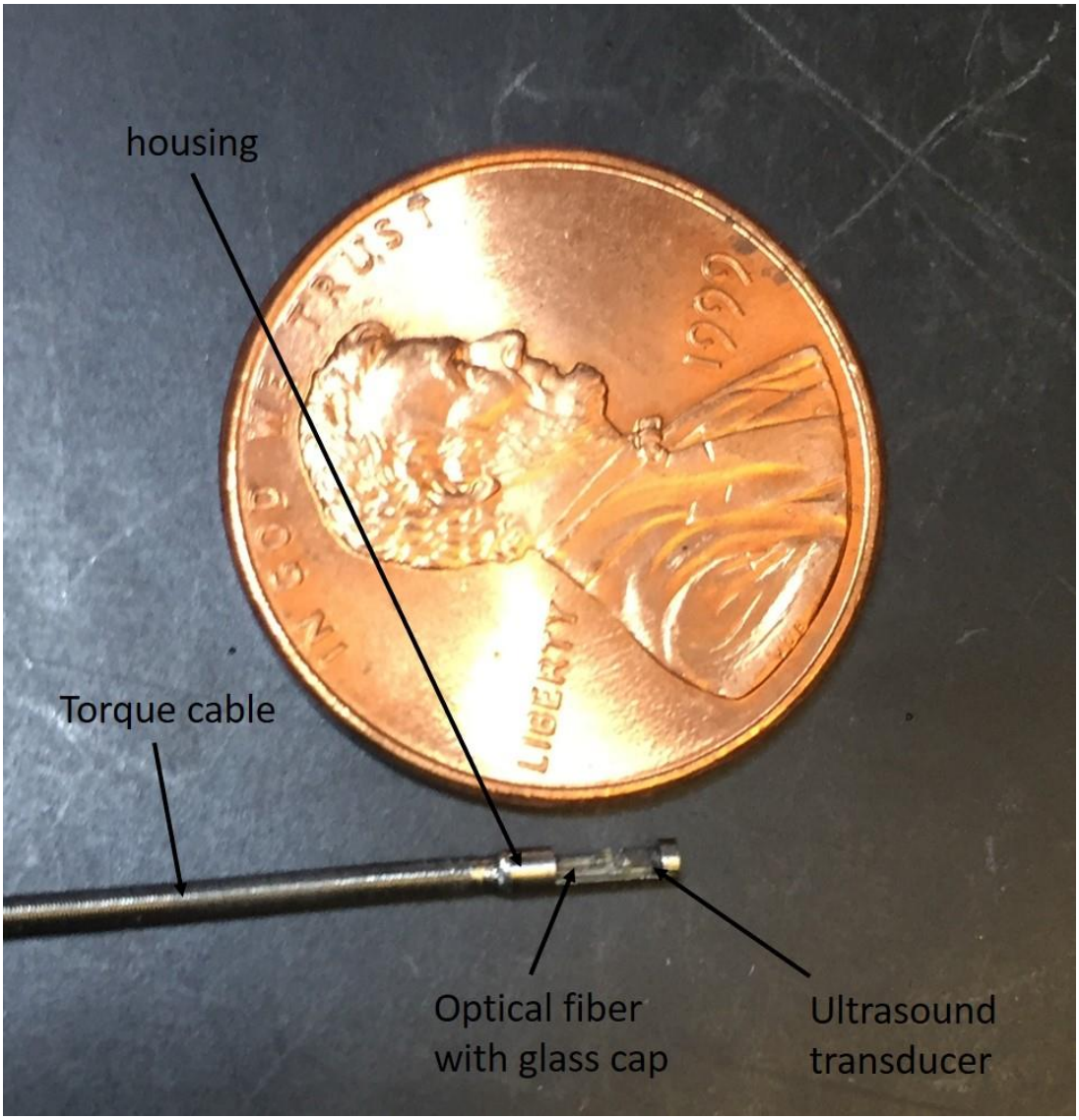

Figure 2.3 Image of a catheter used for real-time *in vivo* intravascular photoacoustic imaging. The outer shell consists of a hollow housing with the side partially cut away for delivery of light and propagation of ultrasonic signals. The housing is welded onto a torque cable to allow fast rotation of the catheter. The light is delivered through an optical fiber shown in the image, which is contained within a class cap that is set in place with epoxy, so it does not come into direct contact with liquid. The ultrasound transducer is located in front of the glass cap. Intravascular photoacoustic catheters also have an additional sheath (not shown), make of a common plastic such as polyethylene, to prevent damage to the tissue.

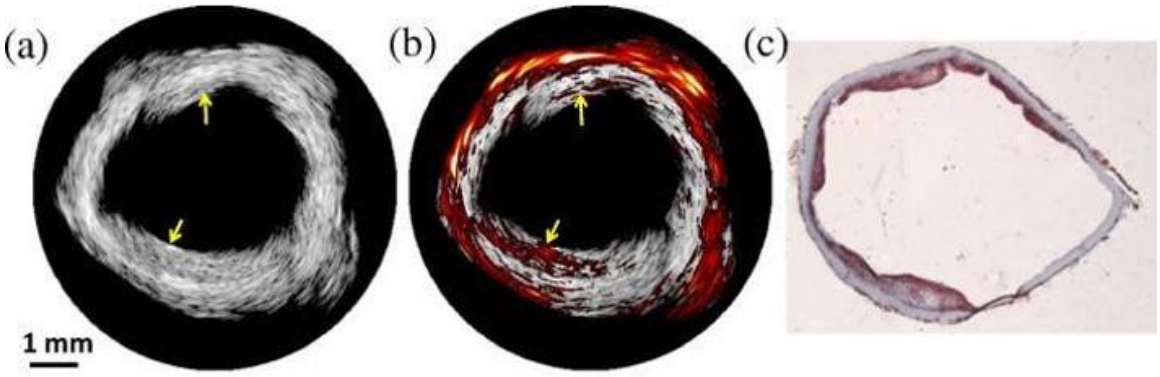

Figure 2.4 (a) IVUS and (b) combined IVUS/IVPA (1210 nm wavelength) images of the atherosclerotic vessel. The images were acquired at 25°C. Yellow arrows in these images indicate the location of atherosclerotic plaques. (c) Oil red O stain confirmed that the imaged aorta had lipid-rich plaques. The angular position of the histological slide was chosen based on the visual correlation of the shape of the vessel wall in histology and the IVUS image. Adapted from reference [49].

Intravascular photoacoustic imaging has seen rapid development over the last decade. It was first illustrated using imaging phantoms and rabbit arteries[46, 47]. Shortly afterward, successful imaging of lipid in human[50] arteries was achieved ex vivo. An example of an intravascular photoacoustic image of a human artery showing lipid plaque is shown in Figure 2.4. The ultrasound image does not clearly show plaque (Figure 2.4a), although it is detectable in the photoacoustic image (Figure 2.4b). The histology confirms the presence of lipid in the intima and media (Figure 2.4c). Other techniques were soon developed. For example, spectroscopic imaging of lipid plaque using multiple wavelengths of light was shown to enhanced plaque identification[51, 52]. Contrast agents have also been used to increase the sensitivity of plaque imaging and indicated the preference of macrophage infiltration[53]. Clinical use of IVPA first required the development of a real

time imaging system[54]. Finally, real time intravascular photoacoustic imaging of non-native lipid[55] and adventitial lipid has been achieved[56]. The use of IVPA to identify lipid in plaque in real-time in an *in vivo* swine model of atherosclerosis was only accomplished recently[57]. Preclinical development of intravascular photoacoustic imaging has demonstrated its potential value as a clinical imaging modality.

Table 2.1: Comparison of plaque imaging capabilities between IVPA and alternative modalities.

	Intravascular MRI	Angioscopy	Raman spectroscopy	NIR spectroscopy	OCT	IVUS	IVUS/IVPA
Penetration/ imaging depth	Excellent (10^{+} mm)	Poor (surface)	Poor (0.3 mm)	Good (1-2 mm)	Good (0.5-1 mm)	Excellent (8-10 mm)	Excellent (6-8 mm)
Depth resolved	Yes	No	No	No	Yes	Yes	Yes
Spatial resolution	Good (300 μm)	Very good	Poor/Poor	Poor/Good (depth/lateral)	Excellent (4-20 m)	Very good (150 μm)	Very good
Tissue composition	Good	Poor	Excellent	Very good	Good	Good	Excellent
Endogenous contrast	Good	Poor	Excellent	Excellent	Very good	Good	Excellent
Real-time	No	Yes	No	Yes	Yes	Yes	Feasible

Multiple imaging modalities[58] are currently used to assess atherosclerotic plaques besides IVPA. It's worth discussing the advantages and limitations (Table 2.1) of each to understand the unique advantages and limitations of IVPA. Angiography[59-62] is used to detect luminal stenosis and does not require the insertion of a catheter into the vessel. Although it is effective at detecting stenosis during acute cardiac events to inform

intervention, it gives no information about plaque extent and composition. Intravascular ultrasound (IVUS) is a catheter-based intervention[63, 64]. It has a penetration depth well beyond the thickness of the artery and by using radio frequency techniques can give some information about plaque composition. However, its spatial resolution is not sufficient to characterize thin cap fibroatheromas[63, 64] and its sensitivity and specificity for evaluating plaque composition is moderate[39]. Optical coherence tomography has limited penetration depth, but excellent spatial resolution capable of detecting thin fibrous caps[65-72]. It often requires the removal of blood through saline flushing or balloon occlusion, which can cause negative side effects.

Other modalities are currently in development that could contribute to plaque identification and characterization. Intravascular MRI[73, 74] is being developed to assess plaque, for example, using the diffusion coefficient of water as a surrogate for assessing plaque presence and composition[74]. However, it currently suffers from poor spatial resolution and is not conducted in real time. Raman spectroscopy[58] has poor penetration depth and spatial resolution, which would make it ineffective at assessing deep plaques. Near-infrared spectroscopy can be used to assess the presence of lipid along the imaging direction of the catheter[75-79]. However, the modality is not depth resolved and thus cannot assess plaque area or volume. It is also incapable of assessing fibrous cap thickness.

Intravascular photoacoustics has its own set of advantages and limitations. It has excellent penetration depth that can easily evaluate the deepest lesions. It achieves native contrast directly from the presence of lipid, which is a predictor of plaque severity. Since it is depth resolved, it can directly assess plaque area and volume. This makes it the only modality capable of producing a 3D representation of lipid in the artery wall.

Despite the clinical debate surrounding the potential predictors of vulnerable plaques, the development of intravascular photoacoustics into a clinical imaging modality would have multiple benefits. Intravascular photoacoustics could be used in prospective studies to more accurately assess if lipid area/volume can be used as predictors for adverse clinical events. Additionally, intravascular photoacoustics will be effective at identifying plaques that have not caused extreme luminal stenosis due to compensatory vessel expansion and remodeling. Thus, it would be valuable in assessing the "vulnerable patient" in addition to the presence of a vulnerable plaque. The use of contrast agents could make it possible to assess the level of inflammation in a plaque, as has been shown in studies in which contrast agents preferentially accumulated in activated macrophages[80]. Also, IVPA imaging would be able to assess the presence of adventitial lipid, which has been implicated in plaque development in multiple studies. For example, adventitial lipid has been connected to the development of atherosclerotic plaques through the release of inflammatory factors[81-83]. In humans, the thickness and volume of coronary epicardial adipose tissue correlates with coronary artery disease severity[81-83]. Also, the surgical removal of adventitial lipid in swine resulted in reduced percent stenosis 3 months later[82], indicating a possible causal relationship. The specificity of intravascular photoacoustic imaging to the detection of lipid and its ability to resolve the signal with depth gives IVPA a unique advantage in evaluating which plaques require clinical intervention.

Beyond its unique advantages, IPVA is compatible with other imaging methods used to characterize atherosclerotic plaques. Researchers have combined IVUS, IVPA, and near infrared fluorescence (NIRF) imaging[84]. Others have combined IVUS, IVPA,

and OCT[85, 86]. Combining IVPA with other modalities could give clinicians more types of actionable information about the characteristics of a specific plaque simultaneously.

So far, the discussion of IVPA in this chapter has revolved around the diagnosis of atherosclerotic plaque. However, it is important to consider what role IVPA could play in treatment. Currently, acute atherosclerotic plaques are treated by stent placement using percutaneous coronary intervention to relieve blockages or stabilize potentially vulnerable plaques[22]. To prevent the development of plaque in patients over longer time periods, medications such as statins are commonly prescribed[39]. However, other forms of treatment for atherosclerotic plaque are in development that would be complementary with IVPA imaging, including photodynamic and photothermal therapy[12]. In both techniques, the idea is to arrest the disease state in a targeted manner by subjecting an atherosclerotic plaque to fatal insult.

Photodynamic therapy is conducted with activation of a light sensitive drug that is delivered specifically to the plaque. The drug is referred to as a photosensitizer. Upon activation, the drug will damage surrounding biological tissue with the formation of reactive oxygen species[87, 88]. Photodynamic therapy is already an accepted form of cancer treatment[87-89], and research has naturally been conducted to determine if it can be used to treat atherosclerotic plaques. It has been applied successfully to larger animal models of atherosclerosis, including rabbits and swine. It has been shown to eradicate plaques[90] and reduce macrophage content[91, 92] in rabbits. In swine, photodynamic therapy reduced intimal thickness at long term time points of 3 and 6 months[93]. A phase I clinical trial in humans illustrated the safety of the photosensitizer motexafin lutetium at 6 months with no side effects[94] after the photosensitizer was shown to be effective at treating plaque in

rabbits[91]. A multi-center study has been funded to conduct studies in which photodynamic therapy is used to treat atherosclerotic plaque development in real time with follow up monitoring, although the results have yet to be reported[95]. Although not currently an accepted treatment method for atherosclerotic plaque, developments in photodynamic therapy and photosensitizers are ongoing[88].

Photothermal therapy is used to damage biological tissue in plaque from heating. Studies in mice using contrast agents to enhance the deposition of heat have been shown to result in macrophage death[96] and to reduce plaque formation and lipid storage[97]. It has also been shown that gold nanorods can be directly used as temperature sensors using photoacoustic imaging, making it possible to deliver the therapy in a targeted manner[98]. Clinical trials in the NANOM-FIM studies[99] used photothermal therapy which successfully reduced atheroma volume. However, the studies used contrast agents with unknown long-term toxicity, and the results have yet to be replicated.

Both these therapeutic treatments are highly complementary with intravascular photoacoustic imaging, as they are conducted using light. Intravascular photoacoustic imaging could be used to identify plaque using a lipid specific wavelength. Once plaques are identified and stratified based on risk, the intravascular photoacoustic catheter could be used to deliver an alternative wavelength of light used to activate a photosensitizer or heat the tissue for photothermal therapy. If photothermal therapy is used, it may even be possible to monitor the temperature of the tissue during application of the therapy in real time. Thus, intravascular photoacoustic imaging has a potential role in the treatment of atherosclerotic plaques in addition to diagnosis.

However, one area of intravascular photoacoustic imaging that has not been explored is safety. Since IVPA imaging must be acquired with many laser pulses while the catheter is rotated and retracted, each region of tissue can be irradiated up to hundreds of times. The effect of this on living artery tissue, and the consequent limitations in energy that can safely be used to achieve high image quality, are unknown. Determining if IVPA imaging can be conducted without laser irradiation damaging vessel tissue is one hurdle to clinical use of this technology. No prior work was found which investigated the safety of intravascular photoacoustics directly. Investigating the safety of IVPA imaging is the primary objective of the work described in chapters 3 and 4 of this dissertation.

CHAPTER 3: OPTIMIZING LIGHT DELIVERY FOR PHOTOACOUSTIC IMAGING SYSTEMS

3.1 Introduction

This chapter was adapted from: Sowers, T., Yoon, H., and Emelianov. S. Investigation of light delivery geometries for photoacoustic applications using Monte Carlo simulations with multiple wavelengths, tissue types, and species characteristics *J. Biomed. Opt.*, 2020. **25**(1), 016005, doi: 10.1117/1.JBO.25.1.016005.[100]

3.1.1 Abstract

Combined ultrasound and photoacoustic imaging systems are being developed for biomedical and clinical applications. One common probe configuration is to use a linear transducer array with external light delivery to produce coregistered ultrasound and photoacoustic images. The diagnostic capability of these systems is dependent on the effectiveness of light delivery to the imaging target. In this chapter, Monte Carlo modeling is used to investigate the optimal design geometry of an integrated probe. Simulations are conducted with multiple tissue compositions and wavelengths. The effect of a skin layer with the thickness of a mouse or a human is also considered. The model was validated using a tissue-mimicking gelatin phantom and corresponding Monte Carlo simulations. The optimal illumination angle is shallower with human skin thickness, whereas intermediate angles are ideal with mouse skin thickness. The effect of skin thickness

explains differences in the results of prior work. The simulations also indicate that even with identical hardware and imaging parameters, light delivery will be up to 3x smaller in humans than in mice due to the increased scattering from thicker skin. These findings have clear implications for the many researchers using mice to test and develop imaging methods for clinical translation.

3.1.2 Background

Photoacoustic imaging[1, 2, 14, 101-103] is an emergent area of research in biomedical imaging. The technique uses nanosecond pulses of light to induce ultrasonic waves from imaging targets in tissue, which can then be detected by an ultrasound transducer. The ultrasonic wave is induced by rapid expansion of the target as a result of heat generated from the absorbed laser light. The strength of the ultrasonic wave is dependent on the quantity of light delivered, a set of physical properties referred together as the Grueneisen parameter, and the optical absorption coefficient of the imaging target[2]. Since the optical absorption coefficient is wavelength dependent and has been characterized for a wide variety of tissue types, imaging targets can be identified by imaging a single region at multiple wavelengths and then comparing the changes in photoacoustic signal intensity with what would be predicted based on the known optical absorption coefficients.

As explained previously, photoacoustics (PA) is being widely developed for applications in the biomedical field, including, for example, the detection of various cancers and lymph node metastasis, detection of circulating tumor cells, identification of atherosclerotic plaques, evaluation of muscle oxygenation, identification of contrast

agents, and temperature sensing[7-14]. A significant benefit of PA is that it can be used synergistically with other imaging techniques, including conventional B-mode ultrasound, flow imaging, and elasticity imaging[6]. One common technique for PA image acquisition is to use a commercial linear ultrasound array with laser light delivered by an optical fiber[16, 17]. This method takes advantage of developments in commercial ultrasound transducer arrays to detect the ultrasonic PA waves, while making it possible to overlay the PA signal with anatomical information obtained from an ultrasound (US) B-mode image. Examples of studies that specifically use commercial ultrasound arrays with external light delivery can be found in the literature[8, 9, 18, 19, 104], including one application currently in clinical trials for breast cancer diagnosis[15].

Since the photoacoustic pressure generated at the imaging target is proportional to the laser fluence at that location, increased light delivery into the tissue will result in stronger photoacoustic signals from native absorbers. In addition, improved light delivery can enhance the use of photoacoustic contrast agents, which are being developed for contrast-enhanced imaging and super-resolution imaging[105, 106]. Various research groups have conducted studies to determine the optimal geometrical layout of the fiber bundle and transducer to increase light delivery. Haisch et al.[16] proposed the use of a fiber bundle and commercial transducer. They determined experimentally that a 40-50 degree angle between the fiber bundle and transducer is best for imaging depths from 10-25 mm, while smaller angles are better at greater depths using artificial tissue phantoms. The modeling of Wang et al.[107] indicates that decreasing the distance between the fiber bundle and the transducer imaging plane will increase light delivery. However, in contrast to the results of Haisch et al[16], they found that decreasing the angle between the fiber bundle and

transducer will monotonically increase fluence along the imaging plane at depths of 5-30 mm. Sivasubramanian et al.[108] modeled different combinations of the fiber bundle to transducer distance, fiber bundle to transducer angle, and the transducer to tissue distance to optimize the signal-to-noise ratio (SNR), and tested the results experimentally in chicken breast tissue without a skin layer. It was found that different combinations of these parameters can result in large differences in SNR. Finally, Sangha et al.[109] designed a motorized system in which the angle of the fiber bundle can be changed on demand during an experiment. This system was used to vary the light emission angle to separately optimize imaging of subcutaneous fat and periaortic fat in mice *in vivo*. They found differences between the optimal angle in their phantom, which had no skin mimicking layer, and experiments conducted in mice.

In this chapter, these studies are furthered by investigating the differences in the optimal design that arise from the presence of skin with the thickness of a human or mouse. The hypothesis is that the high scattering in this layer explains differences in the results of Haisch et al.[16], Wang et al[107], and Sangha et al[109]. The effect of changing the thickness of the skin layer at multiple wavelengths and with multiple soft tissue compositions below the skin using Monte Carlo simulations of photon propagation is evaluated. This is of particular interest to researchers, since the use of mice for *in vivo* validation of preclinical techniques is common. Experiments are conducted in a phantom at 1064 nm and the results are compared with simulations from the Monte Carlo software for validation. The results show that different light emission and transducer configurations maximize fluence delivery when using the skin thickness of a mouse versus the skin thickness of a human. Furthermore, differences in the optimal geometries between species can explain variability

in the results of prior work. Importantly, the results indicate that significant variations in fluence can be expected between mice and humans using an identical imaging setup and imaging parameters, which serves as a cautionary message to researchers expecting to directly translate results in mice to the clinic.

3.2 Materials and Methods

3.2.1 Monte Carlo Modeling Software

MCXLAB, a package within Monte Carlo eXtreme[110-112] that has been developed for use with MATLAB and GNU Octave, was used to simulate photon transport. The software simulates photon propagation from a defined source through a volume consisting of cubic voxels. The optical properties at each voxel are defined by the absorption coefficient, μ_a, scattering coefficient, μ_s, anisotropy, g, and index of refraction, n. In these simulations, all voxels were cubic with a length of 50 μm. The Monte Carlo software output makes it possible to attain the fluence in each voxel, normalized to the total energy from the light source. Thus, the output of the Monte Carlo simulation is the normalized fluence.

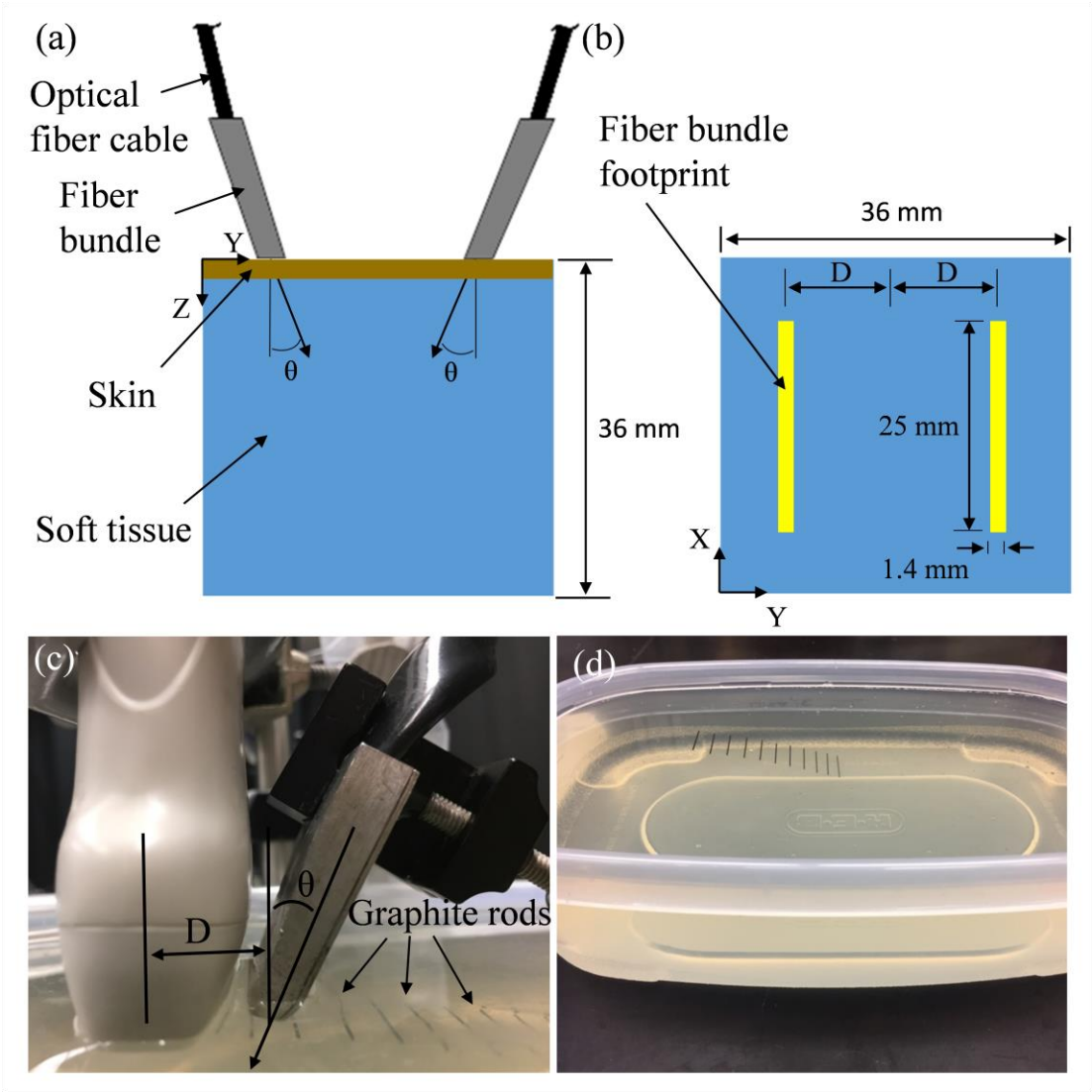

Figure 3.1 Diagram of the (a) (b) model and (c), (d) experimental setup. (a) A side view diagram of the tissue model geometry showing the location and orientation of the optical fibers used for light delivery. (b) A top view diagram of the tissue model geometry. The optical fibers have a rectangular footprint with dimensions of 25 mm × 1.4 mm. In general, two cables of optical fibers are used for light delivery during PA imaging experimentally, although only one was needed for our model and experiment due to the geometrical symmetry. (c) The experimental setup with the location of light emission from the optical fibers separated from the transducer array by a distance, D, and at an angle, θ. The distance D covers distance from the center of the transducer to the center of the rectangular optical fiber contained in the metal housing. If the angle is changed, the location of the metal housing is adjusted horizontally as needed to keep D constant. (d) Graphite rods at various depths in the gelatin phantom were used as PA absorbers. The rods all had a length of 2 cm and a diameter of 0.5 mm. Reproduced from Sowers et al.[100]

Combined US/PA systems that use a commercial ultrasound transducer with optical fibers for delivery of laser irradiation generally illuminate the imaging target with the distal end of the optical fibers positioned on each side of the transducer. In these simulations, the light emission from the distal end of the optical fibers was simulated as a light source of uniform fluence with an area of 25 x 1.4 mm^2. The center of the light emission area was offset from the center of the simulation space (in practice, the imaging plane of the transducer array) by a distance, D (Figure 3.1a,b). The light was emitted into the simulated volume at a uniform angle, θ. Since the optical fiber and transducer array setup is symmetrical across the imaging plane of the ultrasound transducer only one light source needed to be simulated. After the simulation, the average of the fluence output and its mirror across the imaging plane was used as the final fluence output. The boundary condition at the edge of the simulation volume was set such that any photons that crossed the boundary permanently escaped the simulation volume.

3.2.2 Modeling Parameters

The mouse and human modeling were simulated using multiple tissue types and wavelengths (Table 3.1). Simulations were conducted using both fibrous[113, 114] and fatty tissue[115]. Fibrous tissue is among the least scattering of the tissue types whereas fatty tissues are highly scattering. Thus, both extremes of light scattering, which often dominate absorption effects in tissue, are represented. Simulations were conducted at 700, 800, and 900 nm, which are commonly used for photoacoustic imaging. In addition, simulations were conducted at 1064 nm which is commonly used due to the ubiquity of the Nd:YAG

laser. To sample the space between tissue types, we also ran simulations at 800 nm in which the tissue composition was a linear combination of the fibrous and fatty tissue types in 20% increments. This combination of wavelengths and tissue compositions will allow other researchers to use our results as a general guide for their own photoacoustic applications. For example, a researcher evaluating plaque in the carotid artery would likely use results from more fibrous tissue, since the neck contains a large proportion of muscle. A researcher building a system to diagnose breast cancer, on the other hand, would use results from simulations using fatty tissue. As suggested in the literature, all tissues were simulated with an anisotropy coefficient of 0.9[116] and a refractive index of 1.4[115-119].

Species specific variations in the fluence distribution between mice and humans arising from differences in the thickness of their skin, which is highly scattering, was also investigated. The absorption and scattering properties of skin were taken from Bashkatov et al.[115], as the optical properties between the species have been shown to be similar[115, 120]. The thickness of epidermis and dermis in humans is 1 – 4 mm[115], while in mice it is only 0.3 – 0.5 mm[120, 121]. Each tissue type and wavelength combination were simulated with a 2 mm skin layer to mimic human skin and a 0.3 mm skin layer to mimic the skin of mice. It was assumed that the fiber bundle was pressed flush with the skin, so neither ultrasound gel nor another coupling medium was included in the simulation volume.

Table 3.1 List of optical properties for all tissue type and wavelength combinations that were simulated. Reproduced from Sowers et al.[100]

Human and Mouse Geometry Simulations						
Tissue Type	**Wavelengths (nm)**	**Absorption Coefficient (1/mm)**	**Scattering Coefficient (1/mm)**	**Anisotropy Coefficient ()**	**Index of Refraction ()**	**References**
Skin	700, 800, 900, 1064	0.042, 0.035, 0.031, 0.031	14.3, 15.9, 16.8, 16.8	0.9	1.4	[115-119]
Fatty Tissue	700, 800, 900, 1064	0.099, 0.095, 0.096, 0.097	12.2, 11.3, 10.2, 9.09	0.9	1.4	[115-119]
Fibrous Tissue	700, 800, 900, 1064	0.010, 0.016, 0.064, 0.076	2.31, 1.91, 1.63, 1.30	0.9	1.4	[113, 114, 116, 118, 119]
20% Fatty, 80% Fibrous Tissue	800	0.032	3.80	0.9	1.4	[113-119]
40% Fatty, 60% Fibrous Tissue	800	0.048	5.68	0.9	1.4	
60% Fatty, 40% Fibrous Tissue	800	0.063	7.56	0.9	1.4	
80% Fatty, 20% Fibrous Tissue	800	0.079	9.44	0.9	1.4	
Experimental Validation						
Tissue Type	**Wavelengths (nm)**	**Absorption Coefficient (1/mm)**	**Scattering Coefficient (1/mm)**	**Anisotropy Coefficient ()**	**Index of Refraction ()**	**References**
Milk	1064	0.02	7	0.7	1.338	[122-125]
Gelatin	1064	0.012	0.05	0.85	1.5	[126, 127]

For each species, tissue type, and wavelength combination, two sets of simulations were conducted. In the first set, the distance between the location of light emission and the center of the transducer, D, was held constant while the angle was varied. The distance, D, was set to 7 mm. This was chosen because it is close to the minimum possible given the size of the transducer used in our experiment and because many other transducers would be similarly sized. The angles were sampled from 20 to 70 degrees in 12.5 degree increments, which spans the range of angles likely to be used. In the second set of

simulations, the angle was held constant while the distance between the fiber bundle and the center of the transducer was varied. The angle was set to 45 degrees since it is intermediate in the angles used in the prior simulation and because we found from initial simulations that it commonly results in the highest fluence in the imaging plane. The distance, D, was varied from 5 to 13 mm. We used these distances because most transducers have a width greater than 10 mm and because we found that the fluence drops off significantly beyond 13 mm. The reported fluence for each simulation was the fluence averaged over a 0.5 mm x 20 mm rectangular region at the center of the imaging plane. A cubic volume with a length of 36 mm on each side and 10^9 photons were used to simulate each condition. Finally, we compared the fluence delivered to the imaging plane when the mouse skin thickness was used and when the human skin thickness was used. This was conducted to determine the extent to which the difference in skin thickness contributes to lower fluence when translating from mice to humans, even before other factors such as greater imaging depth are considered. The maximum fluence at all fiber angles for the simulations in which the distance was held constant was calculated for each tissue type, wavelength, and species combination. The ratio of the maximum fluences between each mouse and human skin thickness simulation pair is calculated for each tissue type and wavelength combination.

3.2.3 Experimental Validation

3.2.3.1 Experimental Setup and Analysis

The Verasonics system (Vantage 256™, Verasonics, Inc., Kirkland, WA) was used for ultrasound and photoacoustic signal acquisition. The previously developed acquisition sequence, which incorporates a laser, the Verasonics system, and motorized stages[128, 129] was used for acquisition of the US and PA data. The ultrasonic signals were acquired with a 128-element linear array transducer (Verasonics, Inc.; L11-4v) with a frequency bandwidth from 4-11 MHz. For ultrasound imaging, the center frequency was at 8 MHz and plane-wave compounding with 15 angles was utilized. Photoacoustic excitation was achieved with a Nd:YAG pumped optical parametric oscillator laser (Opotek Phocus). The laser operated at 10 Hz with 7 ns pulses. The laser irradiation was delivered to the phantom by optically coupling the laser output to a 9 mm diameter optical fiber bundle. The optical fiber bundle terminated in two rectangular bundles with dimensions of 25 mm x 1.4 mm.

The phantom used for the experimental validation consisted of multiple 0.5 mm diameter graphite rods embedded in a 6% gelatin (Sigma-Aldrich, G2500-1KG) phantom. Eleven rods were spaced 5-6 mm horizontally at depth increments of approximately 2 mm (Figure 3.1d). The phantom was irradiated at 1064 nm with 40 mJ per pulse measured out of the single optical fiber bundle used in the experiment (Figure 3.1c). The transducer and optical fiber bundle were scanned across the graphite rods using a 3D positioning system (Newport; Model ESP301) in 0.2 mm steps, with 1 US and 1 PA image taken at each location, which was repeated four times for statistical analysis. The translation distance for three-dimensional scanning was 50 mm, so a total of 251 steps were required. One

optical fiber bundle was sufficient to deliver laser irradiation to the rods (Figure 3.1c), due to the symmetry of the dual optical fiber bundle setup commonly found in the literature. This acquisition was repeated with the optical fiber bundle at each combination of three angles (20°, 40°, and 60°) and at three horizontal distances (7.5, 11.5, and 15.5 mm) from the transducer, resulting in a total of 9 acquisitions. If the angle was changed, the optical fiber was translated such that the distance, D, between the center of the transducer array and the center of the optical fiber remained constant._Both the ultrasound transducer and the optical fiber bundle output were located 2 mm above the gelatin phantom and coupled to the phantom using milk, which approximates the scattering and absorption coefficients of skin at 1064 nm[122-125].

Images were taken directly above each of the eleven graphite rods. These were used to determine the PA intensity from each rod by averaging the PA signal across the rod in each image. The standard deviation for each of those PA intensities was calculated using the four acquisitions taken at each location. Since the absorption coefficient and Grueneisen parameter would be the same for each of the graphite rods, the measured PA signal is directly proportional to the fluence at each rod. Thus, the PA intensity can be compared to the average fluence at the depth of each rod in the model.

However, in these experiments the effect of ultrasound attenuation, obliquity, and the depth dependent transducer focus would vary from rod to rod due to their placement at different depths in the phantom. To account for this, the US images of each rod were used to normalize the PA images in a manner similar to the work of Ranasinghesagara et al.[130, 131]. Given that the rods are nearly identical, the same magnitude of ultrasound should be measured at each rod once the ultrasound attenuation, obliquity, and depth dependent

transducer focus are taken into account. Thus, the PA intensities were normalized using the US data. The US intensity for each rod was calculated by averaging the ultrasound signal over the rod in each of the eleven images. The US intensities were then normalized so that the maximum US intensity had an intensity of one. Since the attenuation, obliquity, and depth dependent transducer focus would affect the ultrasonic signal twice during US acquisition (one for each direction of travel) the square root of the normalized ultrasound intensity for each rod was calculated. Finally, the PA intensity of each rod was normalized rod to rod by these values. These adjusted PA intensities, with their standard deviations, were plotted for each combination of angle and fiber distance.

3.2.3.2 Experiment Matched Modeling Parameters

To simulate the experiment, modeling was performed with parameters chosen to emulate the materials used in the experiment (Table 3.1). Thus, the volume for the Monte Carlo simulation consisted of a 2 mm layer with the optical properties of milk while the remainder of the volume was assigned the optical properties of water to approximate the optical properties of the gelatin phantom. At 1064 nm, milk has an absorption coefficient near 0.02 1/mm and a scattering coefficient of 7.0 1/mm[123, 124]. It has a lower anisotropy coefficient of 0.7[122, 123] and an index of refraction of 1.34[124, 125]. The absorption[127] and scattering coefficients[115, 117] of gelatin were approximated with that of water. At 1064 nm, gelatin has an anisotropy coefficient of 0.85 and a refractive index of 1.5[126]. A cubic volume with a length of 36 mm on each side and 10^9 photons were used to simulate each condition.

The model was evaluated to determine the fluence as a function of depth along the imaging plane of the transducer. The average fluence across voxels in a 0.5 mm x 20 mm area was used for comparison to the experiment since this is equivalent to the cross section of the rods. These values were plotted for each combination of fiber bundle angle and fiber distance.

3.2.4 Model Convergence

Across the imaging plane for each simulation, a 0.5 mm x 0.5 mm kernel was used to evaluate the SNR (average fluence divided by the standard deviation of fluence) at each voxel. The SNR values were averaged across the imaging plane for each experimental condition to determine the average SNR for each simulation.

3.3 Results

3.3.1 Modeling Parameters

The fluence versus depth along the center of the imaging plane for several simulations with the mouse skin and human skin thickness is displayed in Figure 3.2 and Figure 3.3. Only the plots for the 40% fat tissue at 800 nm (Figure 3.2a,b and Figure 3.3a,b), the purely fibrous tissue at 700 nm (Figure 3.2c,d and Figure 3.3c,d), and fat tissue at 1064 nm (Figure 3.2e,f and Figure 3.3e,f) are shown in the body of the text, although the results for all tissue types and wavelengths are included in Appendix A. The results with the mouse skin thickness are shown on the left (Figure 3.2a,c,e and Figure 3.3a,c,e) and results with the

human skin thickness are shown on the right (Figure 3.2b,d,f and Figure 3.3b,d,f). The y-axis is defined as the averaged normalized fluence. It is averaged because the fluence was calculated by averaging across the voxels in a 0.5 mm x 20 mm area at the center of the imaging plane. It is normalized because the MCXLAB software automatically normalizes the fluence output by the amount of energy irradiated into the simulation volume. Fluence drops significantly as a function of depth in all simulations. For the fibrous tissue, it drops to zero near 35 mm at the end of the simulation volume, whereas for the highly scattering fatty tissue it decreases to nearly zero at a depth of only 15 mm. As would be expected, the depth at which fluence reaches zero decreases monotonically as the fatty tissue component increases for the mixed tissue type simulations conducted at 800 nm. Fatty, and thus more highly scattering, bulk tissue results in lower fluences at the imaging plane. The peak of maximum fluence occurs between 2 and 6 mm for the majority of conditions that were simulated, no matter the angle of the fiber bundle.

For nearly all simulations, the fluence as a function of depth decreases by over an order of magnitude as the distance of the fiber bundle from the imaging plane increases (Figure 3.2). The decrease was smaller in a few simulations (fibrous tissue at 700 and 800 nm) although the fluence still decreased by at least a factor of 5. The likely cause is that in these simulations, the scattering coefficient of the soft tissue is still low relative to other simulated tissue types and the absorption coefficient in fibrous tissue is smaller than at 900 or 1064 nm.

Varying the light emission angle (Figure 3.3) while holding the distance constant had a more complex effect on the peak fluence. For simulations with the fatty tissue, 45 degrees was optimal for both humans and mice, with 32.5 degrees giving a fluence within

several percent of the maximum for all wavelengths. In fibrous tissue, 45 degrees was optimal with the mouse skin thickness while 20 degrees was optimal when the skin had the thickness of a human. For skin with the human thickness, 20 degrees was also the optimal angle for most mixed tissue types at 800 nm. The exception was for 80% fatty tissue, in which the optimal angle transitioned to 32.5 degrees. The variation between 20 degrees and 32.5 degrees was only a few percent at these conditions. For simulations with skin the thickness of a mouse, 45 degrees and 32.5 degrees were optimal and gave almost identical peak fluences. Across all the simulations in which angle was changed, the peak fluence varied by 10-50% between the angle with the optimal fluence and the angle with the least light delivery. The variation was greatest when the scattering coefficient of the soft tissue was small.

Perhaps most importantly, there is significant variation in the fluence at the imaging plane between simulations with different skin thicknesses when all other conditions are held constant. Using the simulations in which angle was varied, the ratio of maximum fluence delivered when the mouse skin thickness was used versus the human skin thickness varied from 0.68 to 3.53 (Table 3.2). The ratio is greatest for the most fibrous tissue and increased with greater fibrous tissue content in the simulations with the mixed tissue composition. For the fatty tissue, the ratio dropped below 1 at wavelengths from 700-900 nm. Given the optical properties of tissue types commonly used for photoacoustic applications, ratios between 1.5 and 2 can be expected. This has clear implications for the translatability of photoacoustic studies conducted in mice, even before other factors, such as the greater imaging depth required in humans, are taken into consideration.

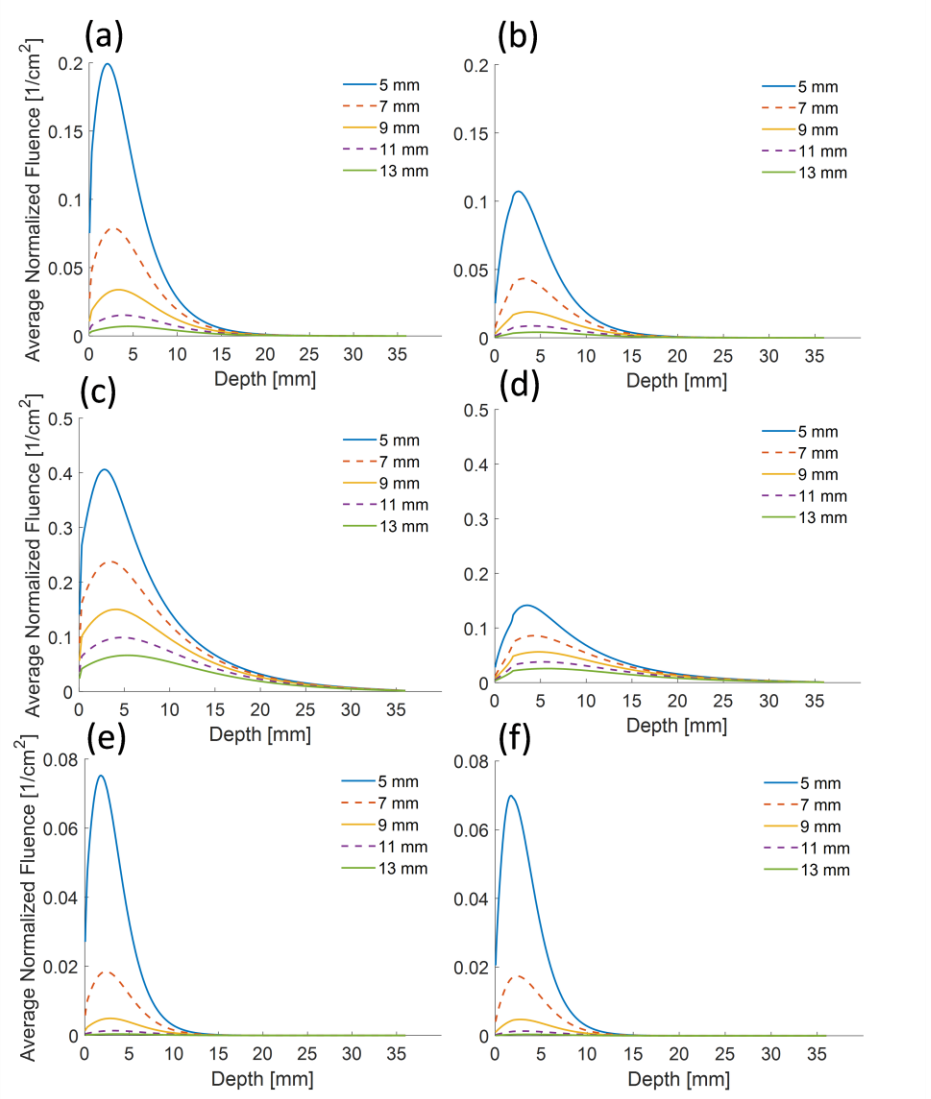

Figure 3.2 Plots of average normalized fluence versus depth. Simulations with a mouse skin thickness are on the left [(a), (c), and (e)], while simulations with the human skin thickness are on the right [(b), (d), and (f)]. Results for (a), (b) the 40% fat tissue at 800 nm; (c), (d) the purely fibrous tissue at 700 nm; and (e), (f) the purely fat tissue at 1064 nm are shown for the mouse and human skin thickness. Simulations were run with a constant angle of 45 deg and a variety of distances between the location of light emission from the optical fibers and the center of the transducer array. As expected, smaller distances between the location of light emission and the transducer result in higher fluences. Fluences are noticeably larger when the mouse skin thickness is used for the simulation, rather than the human skin thickness. Reproduced from Sowers et al.[100]

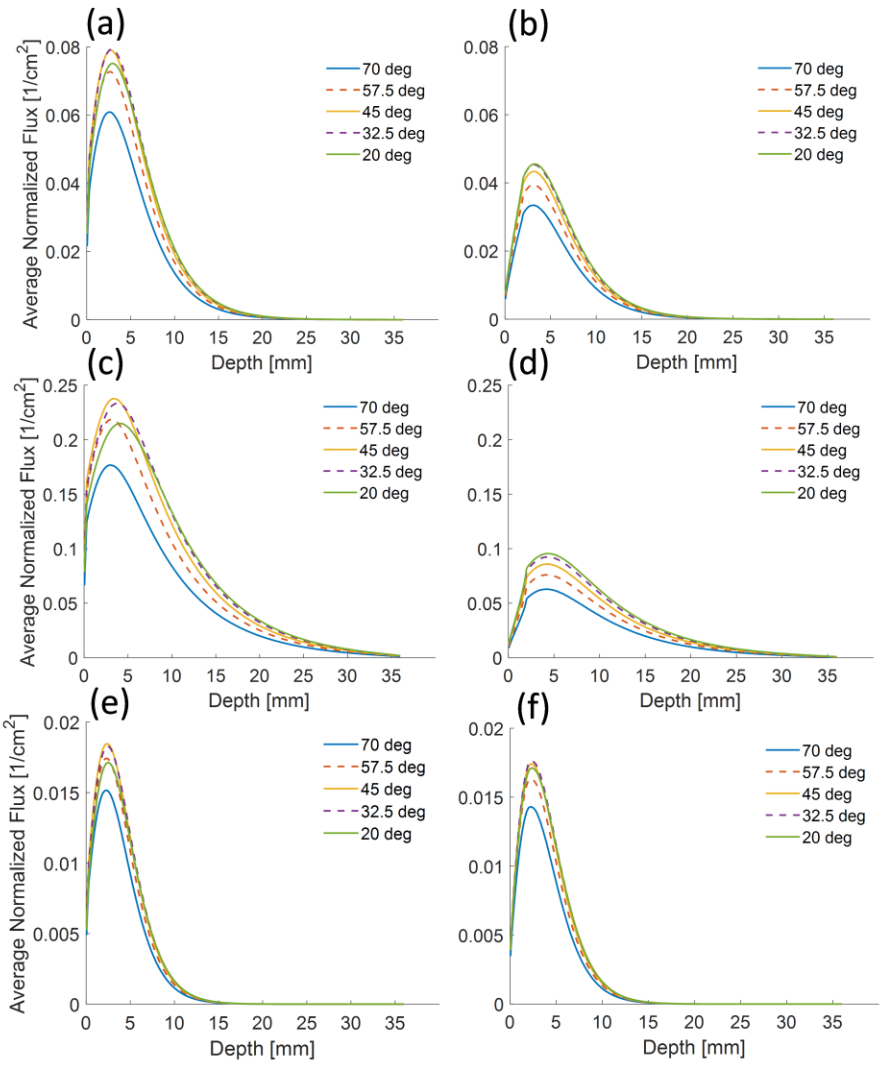

Figure 3.3 Plots of average normalized fluence versus depth. Simulations with a mouse skin thickness are on the left [(a), (c), and (e)], while simulations with the human skin thickness are on the right [(b), (d), and (f)]. Results for (a), (b) the 40% fat tissue at 800 nm; (c), (d) the purely fibrous tissue at 700 nm; and (e), (f) the purely fat tissue at 1064 nm are shown for the mouse and human skin thickness. Simulations were run with a constant distance of 7 mm between the location of light emission and the center of the US transducer, while varying the angle of light emission. In addition, shallower angles appear to deliver higher fluence across all depths for the human skin, while the optimal light emission angle is usually 45 deg when the simulations are run with the mouse skin thickness. Fluences are significantly higher when the mouse thickness is used instead of the human skin thickness. It is also highest for the least fatty tissues. Reproduced from Sowers et al.[100]

Table 3.2 Ratios of maximum fluence between the simulations with mouse and human skin thicknesses, for simulations in which the distance was held constant at 7 mm. Reproduced from Sowers et al.[100]

Fluence Ratios of Fatty and Fibrous Tissues by Wavelength				
	700	**800**	**900**	**1064**
Fatty tissue	0.68	0.81	0.92	1.05
Fibrous tissue	2.49	2.74	3.18	3.53
Fluence Ratios of Mixed Fatty and Fibrous Tissues by Fat Content				
	20% fat	**40% fat**	**60% fat**	**80% fat**
Mixed Tissue, 800 nm	2.09	1.74	1.41	1.10

3.3.2 Experimental Validation

Results of the experimental validation and matching simulation are shown in Figure 3.4. In both the experiment and the model, fluence varies significantly across all depths as the distance between the location of light emission and transducer center is increased. However, the change in the fluence is generally greater for the model than for the experiments. For the model, peak fluences between 20 and 60 degrees varied by only about 25%, with the maximum peak fluence arising at the shallower angle of 20 degrees. A similar difference for peak fluence with respect to light emission angle occurred when the location of light emission was farther from the transducer.

However, for the experiment the maximum fluence occurred at 40 degrees. In addition, variations in fluence were more significant. There was a 25% decrease in fluence when changing the light emission angle from 40 degrees to 20 degrees in the experiment with a 7.5 mm distance between the light emission and transducer center. At larger

distances, the change generally ranged from 10-20%. A light emission angle of 60 degrees resulted in fluences two times smaller than at a 40 degree angle when the distance was 7.5 mm, although this dropped closer to being two thirds lower at 11.5 and 15.5 mm.

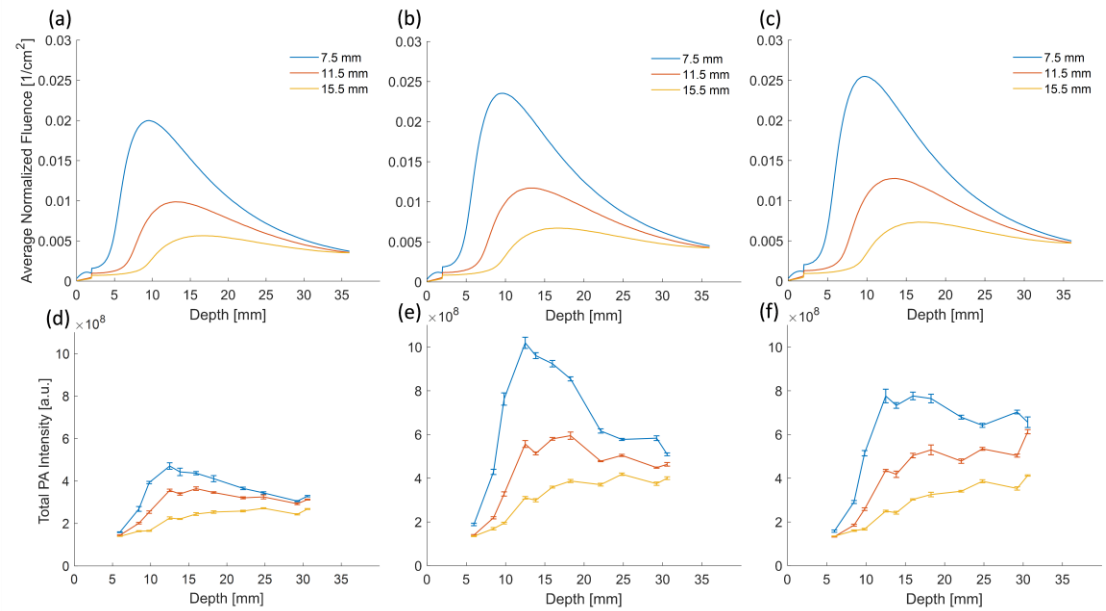

Figure 3.4 Comparison between (a)–(c) the experiment matched model and (d)–(f) the experimental results using the gelatin and graphite rod phantom. Simulations were conducted at 60 deg [(a) and (d)], 40 deg [(b) and (e)], and 20 deg [(c) and (f)]. In general, a smaller distance between the location of light emission and the transducer center results in higher fluences in both the experiment and simulations. Meanwhile, an angle of 20 deg or 40 deg is optimal for the model and experiment, respectively. Reproduced from Sowers et al.[100]

3.3.3 Model Convergence

The average SNR across the imaging plane was evaluated for each simulation. For the position and angle dependence studies in mice and humans, the average SNR across the imaging plane was 14.7. The minimum SNR for all conditions was 4.3. For the experimental phantom simulations, the average SNR was 28.8, with a minimum SNR of 15.0 for any single condition. The SNR values indicate that the photon count used for these simulations was sufficient. The smoothness of the processed data is evident in Fig. 2-3.

3.4 Discussion

In this chapter, a series of simulations have been conducted with different system geometries, tissue types, wavelengths, and species characteristics to optimize fluence delivery for a photoacoustic imaging system. The difference in fluence distributions when either a mouse or human skin thickness is used indicate that there are differences in optimal design as well as the quantity of fluence that can be expected at a given depth depending on the skin thickness. First, in both models the distance between the location of light emission from the optical fibers and the center of the ultrasound transducer has the most significant effect on the fluence delivered to the imaging plane. Minimizing this distance increases light delivery to the imaging plane. Variations of only several millimeters can result in changes in fluence of nearly two-fold.

Variations in the optimal angle were found to be dependent on the skin thickness and tissue composition. Angle had the greatest effect on fluence when the bulk tissue was more fibrous, and thus had a scattering coefficient several times smaller than the skin layer.

For simulations with the mouse skin thickness, a 45 degree angle was optimal for most conditions with 32.5 degrees often giving almost identical fluence. However, when the human skin thickness was used in the simulations, the optimal angle was instead 20 degrees, with 32.5 degrees sometimes giving similar results. The difference is due to the more complete scattering of light as it passes through the thicker 2 mm skin layer. For the human skin thickness, light is completely scattered such that the light propagation is diffusive rather than ballistic. This is illustrated in Figure 3.5, which depicts a cross section perpendicular to the imaging plane. Light propagating through the 2 mm thick skin layer has lost its directionality despite having an angle of illumination of 60 degrees (Figure 3.5a). However, when the skin scattering coefficient is decreased by a factor of 10, the angle of illumination is still evident, resulting in more light delivery to the imaging plane (Figure 3.5b). The mouse skin thickness is about 10 times smaller than the human skin thickness, so in the simulations the light maintains some of the directionality associated with the original illumination angle. As a result, the 45 degree angle, which directs the light closer to the imaging plane, is optimal.

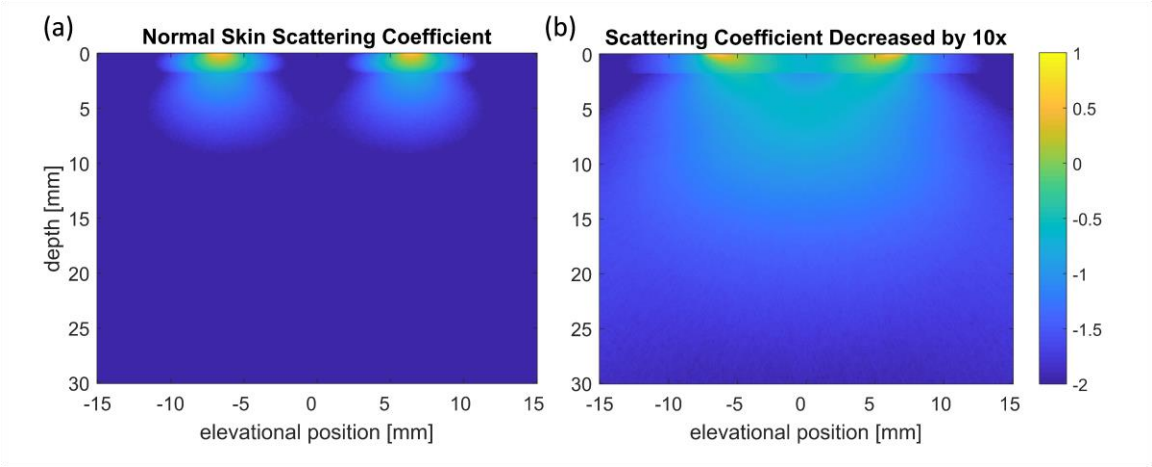

Figure 3.5 Color map of the fluence in a cross section of the simulation volume perpendicular to the center of the imaging plane. (a) A simulation with light emitted at a 60-deg angle through skin with a human skin thickness. (b) An identical simulation geometry with the human skin scattering coefficient decreased by a factor of 10. The difference in the fluence map clearly indicates the scattering effect of normal human skin thickness, which causes the photons to lose much of their ballistic directionality and instead have a more diffusive transport behavior. Reproduced from Sowers et al.[100]

Importantly, the extreme scattering in the thicker human skin layer results in lower fluences when the human skin thickness is used, even when using the optimal distance and angle configurations (Figure 3.2 and Figure 3.3). The modeling results indicate that the fluence will commonly be 50 to 100% higher in mice than in humans, and over 200% as high in fibrous tissue at 900 or 1064 nm. While this does not matter for imaging techniques developed for valuable preclinical applications, this should be strongly considered by researchers conducting techniques that are meant to be translated to humans, as most preclinical work is done in mouse models. While alternative methods for light delivery, such as using catheters or endoscopes, have been suggested that could circumvent this

issue, they are not common[132]. The simulations were conducted using a variety of bulk tissue compositions and wavelengths, so that researchers can approximate the extent to which this will affect their specific applications. Researchers should expect that when translating their results to the clinic, fluences in human tissue may be several times smaller using the same equipment and pulse energies, simply because of the increased scattering in human skin.

The experimental validation was used to validate the trends found in the model. This was done by producing a gelatin phantom containing discrete absorbers at different depths and covered by a thin layer of milk which approximates the optical properties of human skin. Then, the results of the experiment were compared to simulations of the experiments conducted on this phantom. In the model, there was a 2-4x difference in fluence when the distance between light emission from the optical fiber and the center of the ultrasound transducer was changed from 7.5 to 15.5. In the experiment, changing this distance also had the largest effect, with fluence decreasing by a factor of 2-3x. When changing the light emission angle, the model indicated that the fluence would vary by no more than 25% across the angles tested. In the experiment, the difference between 40 and 20 degrees was 25%. For the 40- and 60-degree tests, the change in angle had a larger effect on fluence at two fold. One potential source of error in these experiments is that some light, especially at extreme angles, could have been scattered upwards and been absorbed after hitting the transducer. This possibility was not incorporated into our modeling, as the transducer was not present. In addition, the optical properties of the gelatin were approximated with those of water. Lastly, our simulations did not consider light reflecting off the boundaries of the simulation, which could have been possible at the

gelatin-plastic and plastic-air interfaces. Finally, the light emitted from the optical fiber in the experiment would have been emitted at a distribution of angles, depending on the acceptance angle of the optical fiber in the milk medium. The result would have been light emitted at more extreme angles than the defined value. Given the NA of the optical fiber (0.22) and the index of refraction in milk (1.34), the maximum angle would have been about 10 degrees. At the 20-degree condition, some light would have been emitted at a smaller angle, or even in a direction perpendicular to the imaging plane. The result would be less light reaching the graphite underneath the ultrasound transducer, which could explain the lower PA intensity at that condition compared to the model. At the 70-degree condition, some light emitted at larger angles or light emitted perpendicular to the imaging plane would have been directed away from the graphite underneath the imaging plane of the transducer. Light emitted at more extreme angles would have also partially reflected off the milk/gelatin interface, based off calculations using the Fresnel equations, which could explain the low PA signal at that condition. For example, the percentage of light that would reflect off the milk/gelatin interface would be only 6% at 70 degrees but rise to 22% at 80 degrees (70-degree emission + 10-degree emission angle). The Monte Carlo simulation software only allowed light to be emitted at a constant angle, so these effects could not be replicated in the modeling results.

These issues could be addressed in future work. The optical properties of gelatin could be measured so the material could be accurately represented in the model. The shortcomings of the model would be more complex to address. A different skin layer using a solid material could be used instead of milk, so there is no mismatch in the index of refraction at the interface. One solution may be to use a second gelatin layer containing

intralipid. The issue with the unique distribution of light emitted from the optical fiber could be addressed with an alternative simulation software, or by introducing a custom light source into the code for MCXLAB. Alternatively, multiple simulations could be run with light emitted at a variety of angles within the angle of acceptance from the optical fiber. The fluence distribution of each simulation could be summed in a weighted average based on the likelihood of light being emitted at each of these angles. However, this would require a clear understanding of the probability distribution for the angle of light emission from the optical fiber, which is not known. Also, it would be expensive in terms of simulation time and memory.

Multiple researchers have investigated the optimal experimental geometry of similar imaging hardware in previous work. However, findings on the optimal angle for light delivery have varied. For example, Haisch et al.[16] found that angles from 40-50 degrees are optimal for depths from 10-25 mm, but that shallower angles are better for deeper targets. Sivasubramanian et al.[108] found that a combination of the fiber-transducer distance, transducer-tissue distance, and light emission angle affect SNR in tissue. Sangha et al.[109] found experimentally in a phantom that deeper focal depths resulted in higher depth penetration but at the cost of SNR in regions closer to the phantom surface, but this result did not carry over to *in vivo* experiments using a mouse. Conversely, Wang et al.[107] found that smaller angles will result in monotonically higher fluence in the imaging plane at depth ranging from 5 to 30 mm. The divergent results can be explained by the presence or lack of a high scattering layer that replicates skin. For example, Haisch et al.[16] did not include a skin layer in their phantom studies, while Sangha et al.[109] used both a phantom without a skin mimicking layer and validated the experimental work in a mouse.

Sivasbramanian et al.[108] also did not use a skin mimicking layer. Thus, their finding that angle can be actuated to improve fluence in the imaging plane is consistent with the simulations using mouse skin thickness in this work. In contrast, Wang et al.[107] and other researchers[133, 134] included a 2 mm thick skin layer in their simulations and the results of those studies therefore correspond with the results in the human model used here. Thus, the differences in the effect of angle found between these researchers are explainable by the presence, or lack, of a scattering skin layer. Our modeling also indicated that reducing the fiber to transducer distance will increase the fluence delivered at the imaging plane. This finding was consistent with prior work in the literature[16, 107, 135].

In this study, we evaluated the optimal design of an imaging system consisting of light emission and a commercial ultrasound transducer using the maximum fluence as the criterion for the optimal design. However, it has been found in the literature that in some instances, the increased background signal from other optical absorbers in the tissue can result in the optimal distance being farther away from the transducer[133, 136]. This effect is complex. The optimal distance can change, for example, when the transducer offset is increased. Also, studies on bright field designs[137-140] indicate that the increased clutter will not always offset the gain in fluence from moving the location of light emission closer to the imaging plane. In addition, the development of clutter removal techniques promises to reduce this effect[141-146]. In general, the clutter will be a function of the chromophores in the tissue being imaged and the wavelength used for imaging, among other variables, which will vary from application to application. Researchers should carefully consider these factors or conduct direct testing when determining if a greater distance is appropriate for their application. Studies in which the fluence is compensated to adjust for the decrease

at greater depths were not considered, although techniques exploring this are in development[147].

Within the scope of this study, only the distance between the location of light emission and the center of the ultrasound transducer and the light emission angle were examined to optimize light delivery. However, other parameters are worth mentioning that have already been studied. One method used light reflectors on the transducer face or around the end of the optical fibers and transducer to reflect upwardly scattered light back into the tissue[135, 148-150]. However, experimental testing of the phenomena showed mixed results. When imaging arteries in mice *in vivo*, the reflector did not show the improvements found from modeling[151], although curved reflectors have given better experimental results[148, 150]. Periyasami et al.[135] also considered different arrangements of the fiber bundles around the ultrasound transducer. The variation in fluence along the imaging plane was also not considered, as this has been found previously to vary little with the length of the optical fiber bundle[107]. Also, the effect of offsetting the fiber bundle from the tissue surface was not modeled, as this has already been investigated[135]. Finally, the width of the optical fiber bundle was not considered. This is because a larger width (with the same pulse energy) would effectively increase the average distance between the light source and the transducer bundle, which the results in this chapter and the results of others[16, 107, 135] have consistently shown result in a decrease in fluence. The other case, where the width of the optical fiber bundle is changed but the fluence is held constant rather than the pulse energy, results in an increase in depth penetration as has been shown previously[152].

Patient to patient or animal to animal variability was not considered in this work, since capturing all possible combinations is not possible. These could include differences

in size and anatomy, as well as hair, fur (in mice), and skin pigmentation. Instead, bulk tissue at a variety of tissue compositions and wavelengths were used as optical media to achieve generalizable results. The goal is to give practical guidance to researchers, who can use the simulation results that best match the optical properties for their specific application as a starting point for designing their own imaging system.

In this work, simulations and experimental validation were used to determine the optimal design geometry for the optical fiber and ultrasound transducer array combination that has become common for combined US and PA imaging. This work evaluated differences in the optimal device designs that would arise from different bulk tissue types, wavelengths, and system geometries. These results can be used by researchers as practical guidance for a variety of applications, because of the variety of tissue types and wavelengths that were simulated. Using the depth dependent fluence delivered to the imaging plane as the criterion for evaluating the optimal design, it was found that a smaller distance between the location of light emission from the optical fiber and the center of the transducer array results in the best light delivery for both species. However, the optimal light emission angle is dependent on the thickness of the skin layer and the tissue composition, with the former having the largest effect. The results are compared to the literature and it was found that the differences in skin layer thickness can explain variable findings for the optimal angles found in prior work. Perhaps most importantly, this work indicates that the same imaging system may deliver fluences several times smaller in humans than mice, which serves as a cautionary message for researchers currently developing new imaging techniques in mice models with the expectation that they will translate to humans.

3.5 Conclusions

In this chapter, experimental work and light transport modeling were completed to determine the optimal parameters for the design of a combined US/PA system consisting of an ultrasound linear array with external light delivery. The simulations included a variety of tissue compositions, wavelengths, and equipment geometries. The effect of incorporating either a skin layer with the thickness expected in a mouse or with the thickness expected in a human was also investigated. With both skin thickness and all tissue type and wavelength combinations, reducing the distance between the light source and imaging plane has the largest effect on the light delivery to the imaging plane. However, the optimal light emission angle varied depending skin thickness, tissue composition, and wavelength. In humans, shallower angles were found to increase fluence in the imaging plane across all depths. However, in mice an intermediate angle of 45 degrees was most often optimal. The difference is shown to be mainly a result of the increased scattering of thicker human skin. The difference in the optimal fiber bundle angle between simulations with different skin thicknesses also explains variations in the results of studies by other researchers. Perhaps most importantly, these results indicate that an identical imaging system will deliver significantly less light to the imaging plane in humans than in mice because of the scattering effect of the thicker skin layer.

CHAPTER 4: FLUENCE COMPENSATION FOR QUANTITATIVE PHOTOACOUSTIC IMAGING

4.1 Introduction

4.1.1 Abstract

In this chapter, a new technique is introduced that could be used to compensate for fluence variations deep in tissue, such that relative quantitative comparisons of photoacoustic signal intensity could be made. The technique is investigated using modeling methods. It requires slightly compressing tissue while simultaneously recording the photoacoustic intensity of native absorbers. Once acquired, the photoacoustic intensity as a function of depth during compression can be fitted exponentially to approximate the attenuation coefficient of light in that tissue. Once determined, the attenuation coefficient can be used to compensate the acquired photoacoustic image in the uncompressed state. The simulations run here establish that a constant exponential attenuation coefficient for fluence versus depth is expected in most soft tissues at depths near or greater than 1 cm, illustrating the viability of the technique. The expected improvement in measuring the relative photoacoustic intensity between five high absorbing regions in a simulation using the optical properties of breast tissue at 789 nm is estimated. The error in relative intensity is improved from 51-97% before using the technique to less than 5% afterwards. The studies illustrate the potential usefulness of the technique in clinical applications and justify further experimental study.

4.1.2 Background

As explained previously (Eq. 1.1) the magnitude of a photoacoustic signal is linearly dependent on the fluence at the target tissue. However, the true fluence distribution in tissue is not known. Thus, variations in the photoacoustic signal in an image are not solely attributable to the absorption coefficient and Grueneisen parameter of tissue which impedes identification of the target tissue. Indeed, fluence in tissue across an imaging depth of multiple centimeters can easily vary by more than an order or magnitude (for an example, see fluence distributions in Figure 3.2, Figure 3.3, or Appendix A). It would be desirable to compensate for this fluence distribution since it would make target identification more accurate and make it possible to quantitatively compare the concentration of absorbers in different regions of tissue.

Many researchers have developed a diverse set of methods for approaching this problem. Indeed, the subject of fluence compensation is well represented in the literature, with multiple reviews covering the prior art in depth[153, 154]. Some common approaches will now be discussed, although the reader is referred to the review papers for a more complete accounting.

Perhaps the most straight forward method for estimating the fluence distribution in tissue is to approximate it directly using modeling methods. Monte Carlo modeling is considered the gold standard for approximating light propagation in tissue with known optical properties[153, 155]. Multiple researchers have published work in which Monte Carlo simulations are used to estimate the fluence distribution in tissue[156-159]. The problem with these and other simulation methods is that they require the optical properties of the tissue

to be assumed, which is a constant source of inaccuracy. Often, these are approximated using the optical properties of the same tissue type measured and then reported in the literature by another researcher. However, the optical properties of soft tissues can vary widely between different specimens even for the same tissue type. For example, in one study that measured the optical properties in chicken breast tissue[114], the absorption coefficient of one sample was 2x higher than another while the scattering coefficient was 1.5x lower across all wavelengths in the range 400-800 nm.

Another method of approximation is the use of analytical approximations, such as modified forms of the Beer-Lambert law[153, 160]. In unmodified form, this law is valid for low scattering media and defines the decrease with an exponential equation where the exponential constant is defined as the product of the absorption coefficient and the depth in tissue. However, deep in highly scattering media this approximation breaks down[160] because the path highly scattered photons travel to a tissue target is significantly longer than the geometrical distance between the light source and the target. Modified forms of Beers law have been formulated and experimentally tested to account for the longer path length[160-166]. However, the adjustment terms are dependent on the tissue type and experimental geometry, making the results non-generalizable and thus of limited practical usefulness. They also suffer from the fact that the optical properties must be assumed, which is a constant source of error.

Methods which attempt to explicitly pair photoacoustic acquisition with a method for measuring optical properties have also been investigated[167-170]. These methods require additional system components, cost, and complexity. Another set of studies have been conducted which use a contrast agent of known optical properties as a detector for fluence

in tissue[171]. Other methods use multiple light sources, or a light source focused to different regions of the tissue, to extract bulk tissue optical properties[172-178].

In this chapter, we introduce a new concept that would make it possible to compensate for fluence deep in tissue and investigate its usefulness and potential effectiveness using Monte Carlo simulations. The concept requires that the fluence in tissue follows a uniform exponential decay in the regions over which the fluence compensation method in applied. The first simulations that are conducted model light propagation through a range of tissue compositions and wavelengths to confirm if the uniform exponential decay in fluence exists. These simulations are used to estimate the depths at which the technique could be applied, and how the appropriate depth may vary depending on tissue type. Finally, the effectiveness of the fluence compensation technique is evaluated using several high absorbing regions of indocyanine green (ICG)-like contrast agent, embedded in bulk tissue with the optical properties of breast tissue, to emulate potential applications in breast cancer diagnosis.

4.2 Description of Fluence Compensation Technique

The technique for fluence compensation proposed in this dissertation takes advantage of the fact that fluence decreases in an exponential manner deep in tissue. The method is similar to the multiple illumination method mentioned in the prior section, except that it would not require additional hardware and the measurements would be less affected by the optical properties of tissue outside of the imaging plane of the transducer. In effect, the

technique would make it possible to make quantitative comparisons of photoacoustic absorbers that lie in the tissue at greater depths.

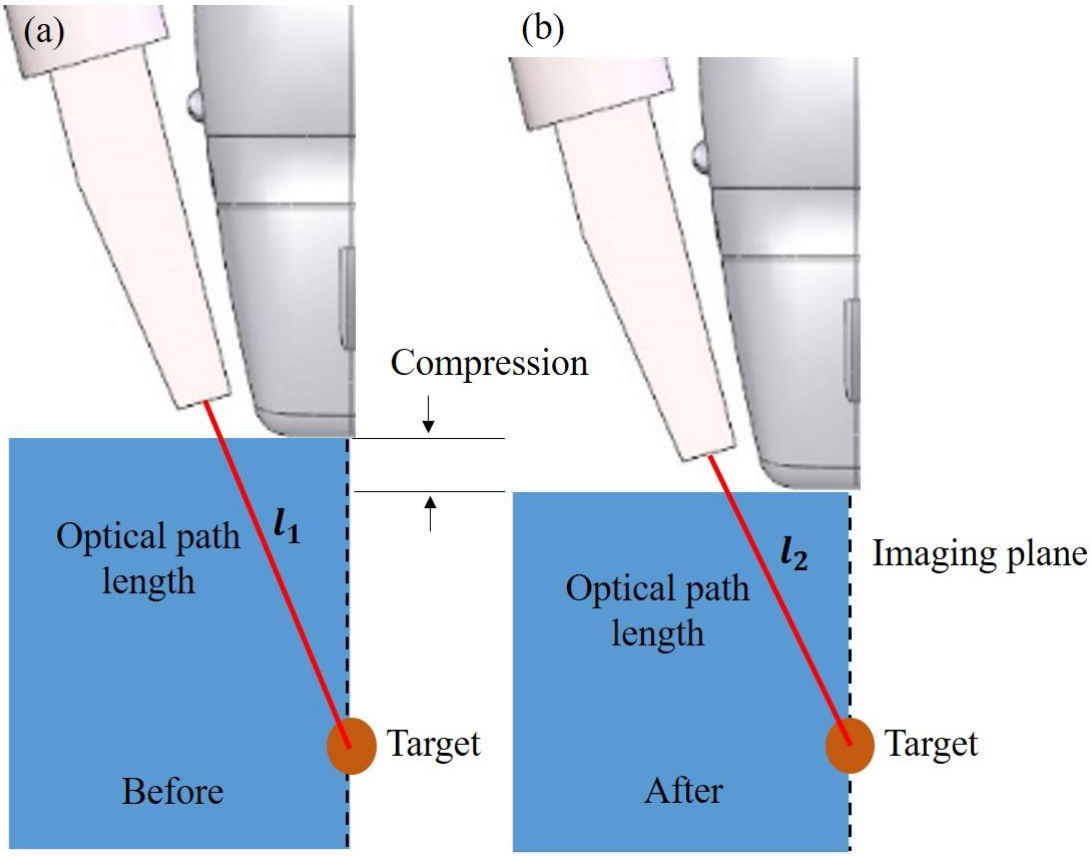

Figure 4.1 A schematic illustrating the use of the proposed fluence compensation technique. a) The optical fiber for laser delivery and one half of a linear ultrasound array are shown in the uncompressed state in the tissue over the bulk tissue (blue region). b) The same optical setup but after compression. Compression causes a change in the optical path length to the tissue target, and a consequent change in fluence that can be determined by comparing the photoacoustic intensity of the target at different compression depths. The attenuation coefficient of fluence can be determined by fitting the photoacoustic intensity of the target versus the optical path length the optical path length at multiple compression depths. Once the attenuation coefficient is known, it can be used to compensate for the decrease in fluence with depth in the photoacoustic image taken in the uncompressed state.

To determine the constant for exponential decay, fluence as a function of depth at several locations must be known. The proposed technique would take advantage of native absorbers in the tissue to reconstruct the exponential decay in fluence. By pressing gently on the tissue (Figure 4.1), and causing compression up to several millimeters, the photoacoustic intensity of native absorbers could be evaluated as a function of depth. The different photoacoustic signals would be derived from the same native absorber (displaced to different depths due to compression) so the Grueneisen parameter and optical absorption coefficient would be identical for each photoacoustic acquisition. Thus, changes in the photoacoustic intensity during compression would be attributable only to changes in fluence at the new depth. Fitting the fluence as a function of depth to an exponential curve would allow the rate of fluence attenuation to be calculated.

Once the exponential rate of attenuation is calculated, the intensity of the photoacoustic signal from each absorber in the tissue could be adjusted depending on its depth in the uncompressed state. The result would be a photoacoustic image in which quantitative comparisons between absorbers could be made, although only at greater depths where the exponential decay in fluence is present.

4.3 Materials and Methods

4.3.1 Monte Carlo Modeling Software

The same open source Monte Carlo simulation software, MCXLAB, used for simulations in the prior section was used for the fluence compensation experiments. Briefly, MCXLAB is a package within Monte Carlo Extreme[110-112] that can be set up through MATLAB to

simulate photon transport. The software simulates a volume which is separated into equally sized square voxels. The optical properties required for the simulations include the absorption coefficient, μ_a, scattering coefficient, μ_s, the anisotropy coefficient, g, and the index of refraction, n. For the simulations in this chapter a voxel length of 50 µm was used. The output of MCXLAB is the flux per voxel. The flux is automatically normalized to the energy input for the simulation. Since photoacoustic imaging requires a sufficiently short pulse that the energy can be assumed to have been deposited in the tissue instantaneously[4], the fluence is used to report results in this work. The fluence can be calculated simply by multiplying the flux in a voxel by the time length of the Monte Carlo simulation (5 ns).

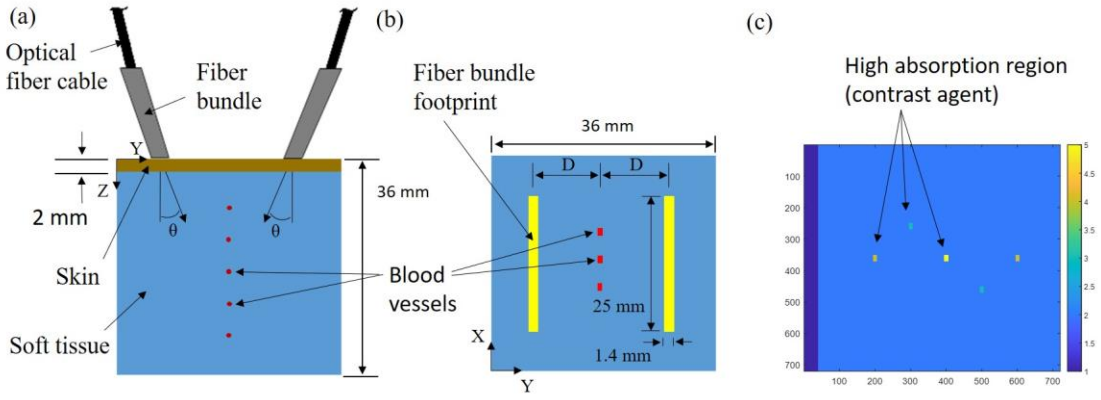

Figure 4.2 Schematic and diagrams that show the geometry of the simulations. A) the optical fiber bundles are shown at an angle, theta, with light propagating into the skin (2 mm) and bulk tissue (34 mm). The size of the optical fiber footprint is also shown by yellow rectangles in (b). The optical fibers are spaced a distance, D, from the imaging plane of the ultrasound transducer. Also shown (a,b) is the location of the high absorbing regions (red dots) used in the simulations using breast tissue at 789 nm. c) The location of the high absorbing regions in the imaging plane of the ultrasound transducer.

For these simulations, we used a common US/PA imaging setup with a linear transducer over the center of the simulation space with two optical fiber bundles placed on either of the long sides of the transducer to illuminate the tissue for photoacoustic excitation (Figure 4.2). Light was emitted from each of the two optical fibers, which were assumed to have a size of 25 x 1.4 mm^2. The center of the optical fibers (point of light emission) was offset from the transducer by a distance, D, of 7.5 mm. This is close to the minimum distance you could get the optical fiber to the imaging plane using a standard commercial ultrasound linear array. The light was emitted at a constant angle, θ, of 45 degrees. Due to the symmetry of the optical fiber geometry, light emission from only one optical fiber was needed which reduced the simulation time by a factor of 2. The results were then mirrored across the imaging plane and averaged to calculate the fluence distribution in the volume from both optical fibers. The boundary condition at the edge of the simulation was set such that any photons that crossed over the boundary permanently left the simulation volume. All simulations were conducted using 10^9 photons and in a cubic volume with 36 mm per side.

4.3.2 Modeling Parameters

Two sets of simulations were conducted to test the viability of the compression method. Each set used different optical properties (Table 4.1). The first set of simulations had two purposes. The first was to evaluate if the fluence follows a uniform exponential decrease in the far field from the transducer. This would be required for the technique to be usable in tissue that has sparse PA absorbers and a small ($\leq$ 5 mm) total compression depth. It

was also used to determine the depth the exponential decrease in fluence begins in different tissue type and wavelength combinations. To evaluate the behavior in a wide variety of tissue, multiple tissue types and wavelengths were used. The tissue consisted of various percentages of fibrous[113, 114] and fatty[115] tissue components. The tissue mixtures ranged from purely fibrous to purely fatty tissues, with mixtures of each in 20% increments. Fibrous tissue is one of the tissue types with the lowest scattering coefficients while fatty tissues have high scattering coefficients. Since scattering is the dominant optical property in soft tissue, this represents the extremes of expected optical behavior. Mixtures of each component represented tissue types between those extremes. The simulations were run at 700, 800, and 900 nm, which cover the near infrared region commonly used for photoacoustic imaging. In addition, simulations were run at 1064 nm which is often used due to the ubiquity of the Nd:YAG laser. Each tissue mixture was simulated at each of the 4 wavelengths, for a total of 24 simulations.

A 2 mm thick layer with the optical properties of human skin[115] was also placed at the surface of the simulation volume. Light was assumed to enter the tissue at the surface of the skin, with no light traveling through a coupling medium such as ultrasound gel. All tissues were simulated with an anisotropy coefficient of 0.9[116] and an index of refraction of 1.4[115-119].

Table 4.1 Optical properties used for simulations related to the fluence compensation technique.

Mixed Tissue Simulations						
Tissue Type	**Wavelengths [nm]**	**Absorption Coefficient [1/mm]**	**Scattering Coefficient [1/mm]**	**Anisotropy Coefficient []**	**Index of Refraction []**	**References**
Skin	700, 800, 900, 1064	0.042, 0.035, .031, 0.031	14.3, 15.9, 16.8, 16.8	0.9	1.4	(Jacques, 2013; Bashkatov, 2005; Tuchin, 2000; Schmitt, 1998; Wang, 2000)
Fatty Tissue	700, 800, 900, 1064	0.099, 0.095, 0.096, 0.097	12.2, 11.3, 10.2, 9.09	0.9	1.4	(Jacques, 2013; Bashkatov, 2005; Tuchin, 2000; Schmitt, 1998; Wang, 2000)
Fibrous Tissue	700, 800, 900, 1064	0.010, 0.016, 0.064, 0.076	2.31, 1.91, 1.63, 1.30	0.9	1.4	Marquez 1998; Filatova 2007; Tuchin, 2000; Schmitt, 1998; Wang, 2000)
20% Fatty, 80% Fibrous Tissue	700, 800, 900, 1064	0.028, 0.032, 0.070, 0.080	4.29, 3.80, 3.34, 2.86	0.9	1.4	(Marquez 1998; Filatova 2007; Jacques, 2013; Bashkatov, 2005; Tuchin, 2000; Schmitt, 1998; Wang, 2000)
40% Fatty, 60% Fibrous Tissue	700, 800, 900, 1064	0.046, 0.048, 0.077, 0.084	6.26, 5.68, 5.05, 4.42	0.9	1.4	
60% Fatty, 40% Fibrous Tissue	700, 800, 900, 1064	0.064, 0.063, 0.083, 0.088	8.23, 7.56, 6.75, 5.98	0.9	1.4	
80% Fatty, 20% Fibrous Tissue	700, 800, 900, 1064	0.082, 0.079, 0.090, 0.092	10.22, 9.44, 8.46, 7.53	0.9	1.4	
Simulation with Breast Tissue and High Absorbing Regions						
Tissue Type	**Wavelengths [nm]**	**Absorption Coefficient [1/mm]**	**Scattering Coefficient [1/mm]**	**Anisotropy Coefficient []**	**Index of Refraction []**	**References**
Breast Tissue	800	0.0082	7.67	0.9	1.4	(Troy 1996)

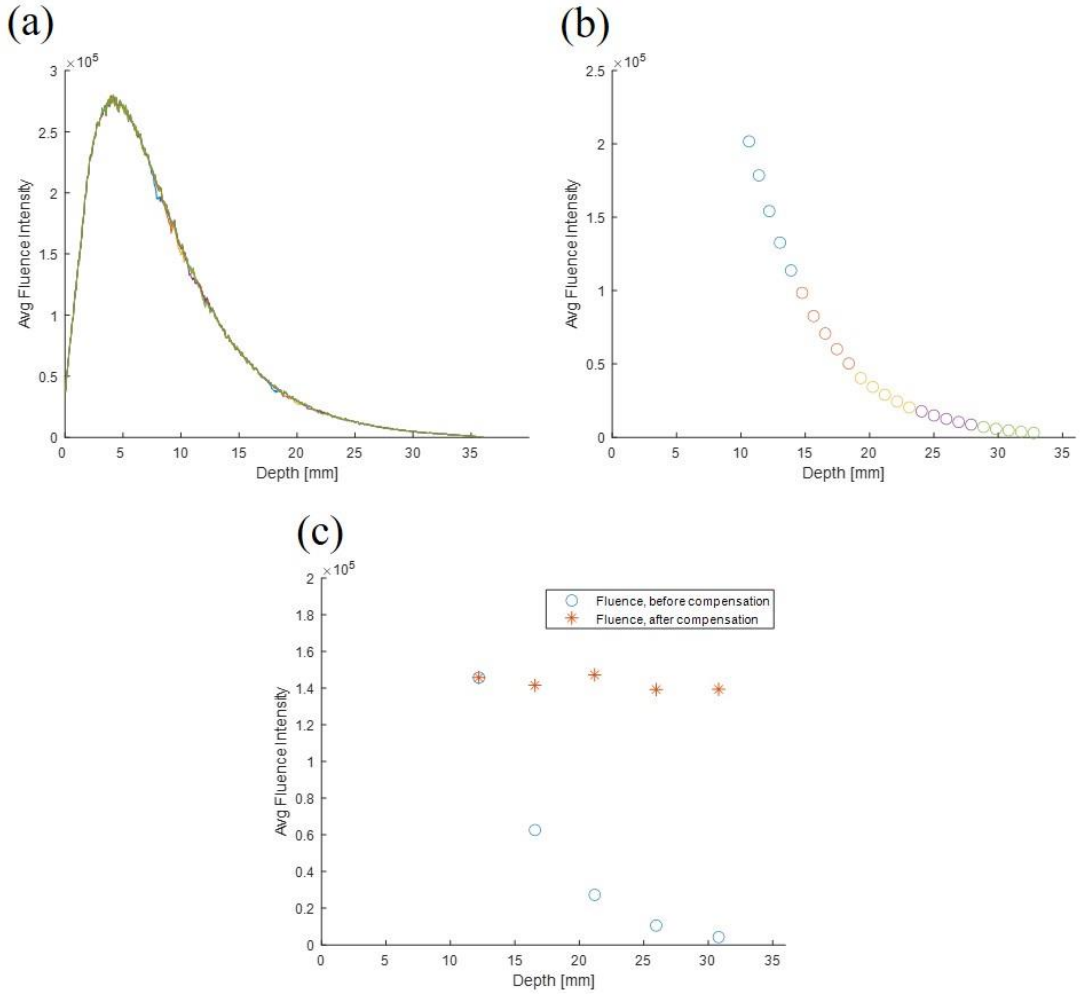

Figure 4.3 Three plots showing the method for fluence compensation. a) First, simulations are conducted with the high absorbing regions located at their original depths (12, 17, 22, 27, 32 mm). Four additional simulations are conducted with the high absorbing regions located 1 mm consecutively closer to the tissue surface. Here, the slight variations in the smoothness of the fluence curve illustrate the small effect of the high absorbing regions on the fluence distribution. b) The average fluence across each of the high absorbing regions are calculated. The average for each region is shown in a unique color, with the 5 points representing the average at each depth. An exponential fit is applied to each set of 5 points for a unique region to determine the attenuation coefficient. The attenuation coefficient for the 5 regions are averaged for these simulations, since the bulk tissue is homogenous. c) A plot of the fluence distribution before and after adjustment with the attenuation coefficient for fluence. The adjusted fluence is nearly uniform, which is ideal for comparison of photoacoustic intensity between the regions.

The fluence versus depth along the center voxel of the modeling volume (which would be equivalent to the fluence versus depth along the center of the imaging plane of the ultrasound array in a physical experimental setup) was extracted for each wavelength and tissue composition combination. The uniformity of the exponential decay was evaluated by applying an exponential fit across the data in short segments (4 mm) in small increments (1 mm) along the fluence versus optical path length curve. The optical path length of the target was calculated with the Pythagorean theorem using the target depth and the offset of the optical fiber bundle from the center of the imaging plane. The segments chosen ranged from 90% of the peak fluence to the maximum depth of 36 mm. The constant for the exponential decay was calculated for each segment, and the segments were evaluated for uniformity. The depth of maximum fit was evaluated by manually identifying the depth the exponential decay coefficient became constant.

The purpose of the second set of simulations was to evaluate and illustrate the potential effectiveness of the fluence adjustment technique. For these simulations, the bulk tissue was given the optical properties of fibrous breast tissue (found in older women, who would thus be more prone to the development of breast cancer) at 789 nm[179]. Inserted into the bulk tissue (Figure 4.2c) were 5 regions of high absorption that would emulate a contrast agent with a high absorption near 800 nm, such as indocyanine green. These regions of high absorption were used as the photoacoustic markers to calculate the rate of exponential decrease in fluence. The regions were located at 12, 17, 22, 27, and 32 mm. The first, third, and fifth regions were placed in the center of the imaging plane. The second and fourth remained in the imaging plane, but were offset at opposite sides of the center by 5 mm. Each region was assigned different relative concentrations by assigning them

different absorption coefficients. The first and fifth region has an absorption coefficient of 0.1 mm^{-1}, the third region had an absorption coefficient of 0.2 mm^{-1}, while the second and fourth region had absorption coefficients 0.05 mm^{-1}. These are representative of the same absorber at relative concentrations of 1, 2, and 0.5, respectively. A 2 mm skin layer was also located at the top of the simulation space, with the light entering directly at the skin surface as was done for the first set of simulations in this chapter. This simulation was then repeated with the high absorbing regions at different depths to mimic the effect of compression at the tissue surface. A total of five simulations were run. The first was with the regions at the depth specified above. Each of the four successive simulations was conducted with the regions progressively 1 mm closer to the skin surface (Figure 4.3a). Figure 4.3a illustrates this at the centerline, with the slight deviations in the fluence being caused by the presence of the high absorbing regions. The fluence was averaged across each of the high absorbing regions in each of the 5 "compressed" simulations. An exponential fit was applied to the average fluence versus optical path length for each of the five regions at different "compression" depths. An example of the average fluence in each high absorbing region at all five compression points is shown in Figure 4.3b. Each set of 5 points sharing a common color represent the same high absorbing region at the 5 different compression points. The exponential fit parameter was then used to compensate for the decay in fluence versus optical path length. An example of the fluence before and after this compensation is given in Figure 4.3c.

Evaluating the effectiveness of the compensation technique requires a comparison of the relative photoacoustic signals that would be found in this region before and after compensation. What is referred to here as a relative photoacoustic intensity (since the

Grueneisen parameter and absorption coefficient are constant because neither would change for the same target with "compression" depth) can be calculated by multiplying the relative concentration of each high absorbing region with the fluence distribution. This can be done separately with the unadjusted and adjusted fluence, to attain the unadjusted and adjusted photoacoustic intensity, respectively. Each of the unadjusted and adjusted relative photoacoustic intensities are then normalized to the intensity of the shallowest high absorbing region. The shallowest region is used because the true relative absorption coefficient assigned to the shallowest region in the simulation is 1.0. The normalized intensities before and after adjustment are then compared to the true relative concentrations assigned to the voxels in the simulation space.

4.4 Results

The effective attenuation coefficient for each of the wavelength and tissue type combinations was first calculated using a sliding window in 1 mm increments using segments lengths of 4 mm. The results for the all the tissue composition simulations at 700 nm are shown in Figure 4.4. For each simulation, the effective attenuation coefficient of each segment was plotted versus the midpoint of that 4 mm segment. The results show that the effective coefficient is low for segments at shallow depth but reaches a constant value with increasing depth. The variation in the effective attenuation coefficient also increases for some tissue types at extreme depths, but without any clear upward or downward trend. These behaviors are consistent for simulations at all wavelengths (Appendix B).

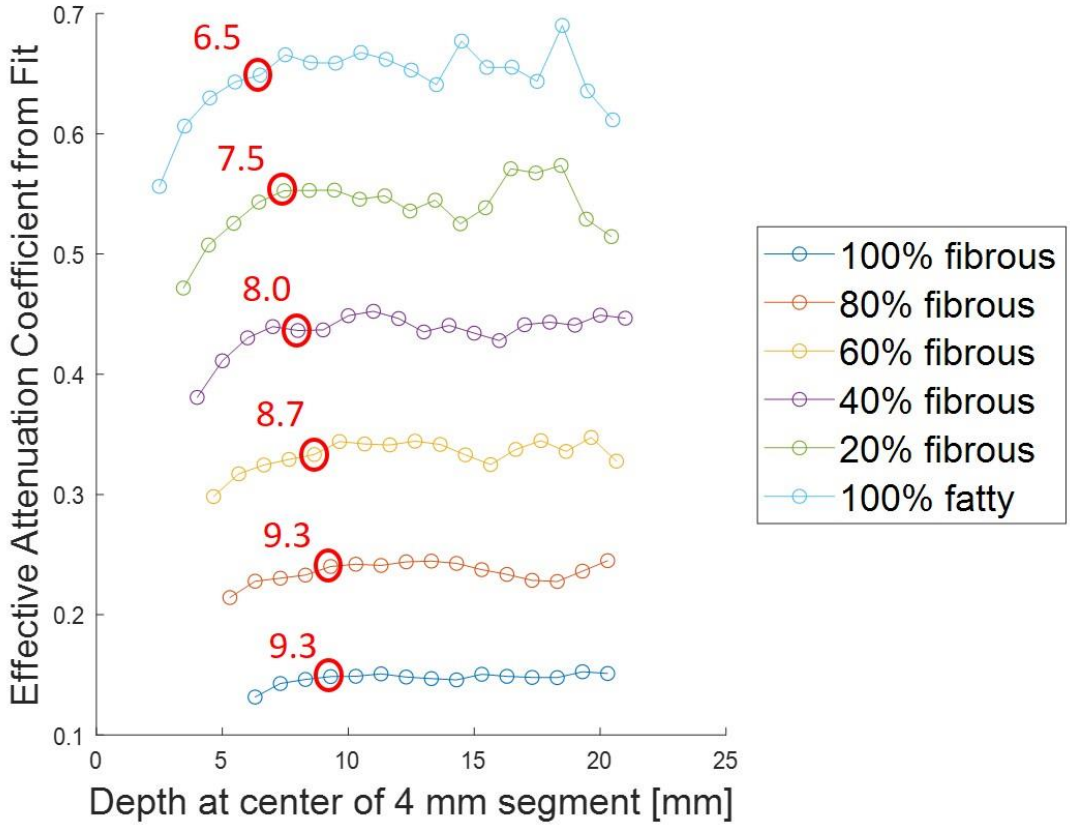

Figure 4.4 A plot of the effective attenuation coefficient of each 4 mm segment taken in 1 mm increments. The results indicate a uniform fluence distribution after a finite depth is reached, although there is some noise in the results at greater depths due to the low number of photons that reach deeper into fatty tissues. The depth of minimum fit is manually marked for each of the tissue components.

For all the effective attenuation curves, the point at which the effective attenuation reaches a constant was visually identified and marked (Figure 4.4). These points represent the minimum depth at which the fitting technique is valid. The results for all tissue type and wavelength combinations are shown in Figure 5.4. The depth of minimum constant fit was 8 mm or lower for all simulations. The depth of minimum fit also varied by tissue

composition, with the use of the technique at smaller depths being possible with fattier tissue. The average depth of minimum fit for the most fibrous tissue was near 7 mm, while for the fattiest tissue it was just below 5 mm. There was no clear pattern in the depth of minimum with respect to the wavelength of light used for the simulation.

The results of the simulations with 5 high absorbing regions in an optical medium that matched breast tissue at 789 nm are shown in Figure 4.6. The figure shows the true agent concentration, the normalized photoacoustic intensity calculated from the unadjusted fluence, and the normalized photoacoustic intensity calculated from the adjusted fluence. The photoacoustic intensity for all 3 data sets match for the high absorbing region at 12 mm because of the normalization. Afterwards, the photoacoustic intensity measured using the unadjusted fluence decreases relative to the true value as depth increases. The percent errors as a function of depth for all the high absorbing regions are 0%, 57%, 81%, 93%, and 97%. The percent error using the adjusted fluence were drastically improved. The percent error between the true relative concentrations and the photoacoustic intensities using the adjusted fluence were 0%, 2.9%, -1.0%, 4.5%, and 4.4%. This is a marked improvement over the adjusted values and illustrates the potential of the technique for making possible quantitative comparisons between photoacoustic absorbers deep in tissue.

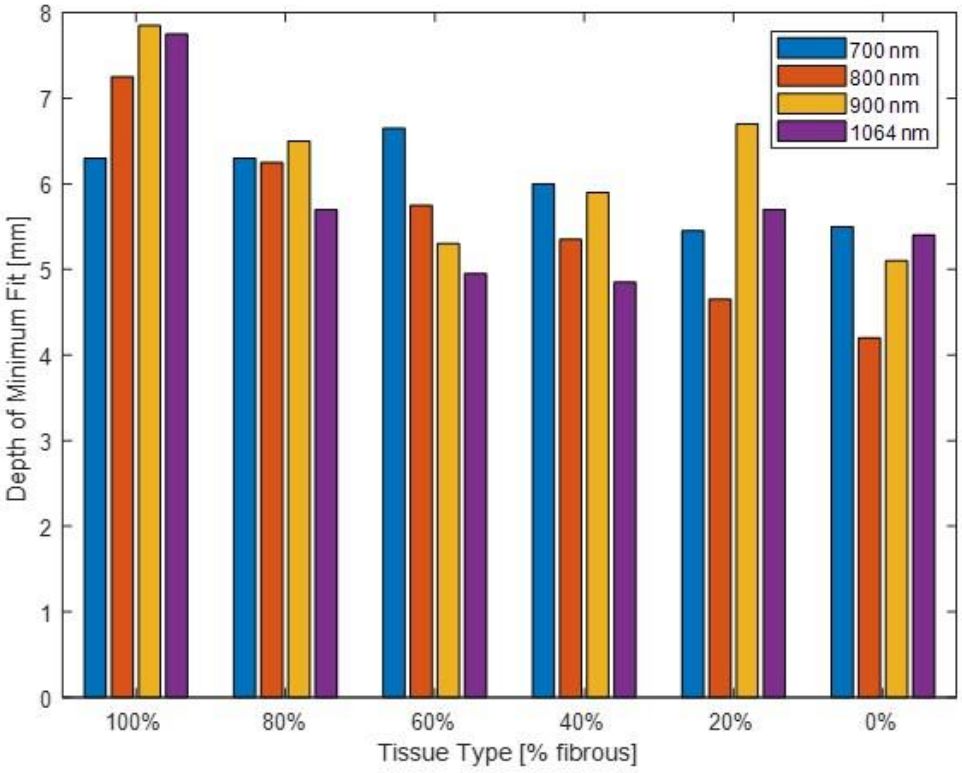

Figure 4.5 Plot of the depth of minimum fit for all tissue types and wavelengths. The depth of minimum fit ranges from 8 mm in fatty tissue to 5 mm in fibrous tissues. There is no clear trend for the depth of minimum fit with respect to the light wavelength.

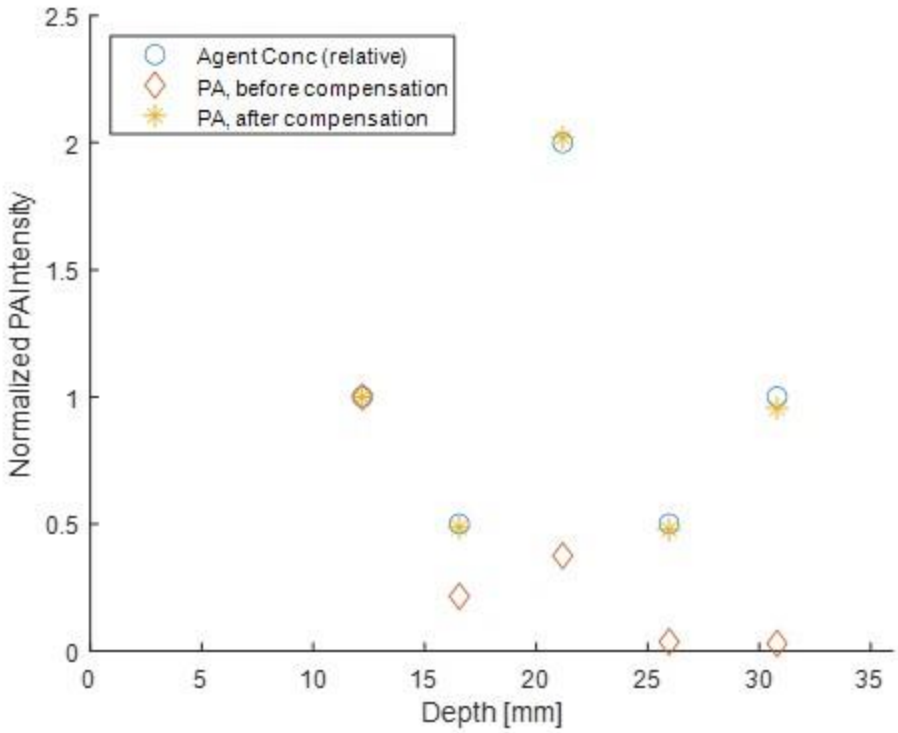

Figure 4.6 A plot of the normalized photoacoustic intensity versus depth for the high absorbing (contrast agent-like) regions. It includes for comparison the true relative concentrations, unadjusted relative concentrations, and relative concentrations after applying the technique for fluence compensation. The relative photoacoustic intensity using the unadjusted fluence clearly deviate from the true relative value with depth. This is a result of the decrease in fluence deeper in tissue. The relative photoacoustic intensities calculated after fluence adjustment are greatly improved, with errors of 5% or less.

4.5 Discussion

The simulations at all tissue composition and wavelength combinations showed a uniformity of fit at depths beyond 1 cm. This indicates the viability of the fluence compensation technique across most soft tissue types found in biomedical applications. The decrease in the effective attenuation coefficient at shallower depths is a consequence

of the sampled segment becoming closer to the peak of the fluence distribution. In this region, the fluence distribution is not uniformly exponential. At greater depths, the effective attenuation coefficient had greater variance, although there was no clear upward or downward trend across the tissue type and wavelength combinations. This can be explained by the fact that in the Monte Carlo simulations lower fluence, and thus fewer photons, were present deeper in tissue. Due to the random nature of photon propagation in Monte Carlo simulations, this would result in a noisy fluence distribution deeper in tissue.

The depth of minimum fit analysis indicated that this technique will be valid at smaller depths in fatty tissue. This is consistent with the fluence versus depth distribution in which the peak fluence occurs at smaller depths in fatty tissue. A uniform rate of fluence decay occurred at depths ranging from 5-8 mm depending on tissue type. As a simple rule of thumb, we propose that this technique be used at depths of 1 cm or greater. It should also be noted that in an experimental setting, the validity of the technique at depths in the 5-10 mm range could be detected in real time by evaluating the goodness of the exponential fit, such as by an R^2 value or some other measure, from an imaging target found at a depth in that range.

Several assumptions were made for this modeling study. First, we assumed that the bulk tissue was homogenous. In theory, you could deduce different attenuation coefficients in layers of tissue with different optical properties if there existed a chromophore that could be tracked during compression in each layer. In addition, the presence of these layers could be detected in the first place using ultrasound. However, this was not explicitly tested and will require experimental validation. Another

assumption was that skin compression was negligible, since it is much thinner than the bulk tissue. Finally, we ran simulations with only one optical fiber and ultrasound transducer geometry. The optical fiber was set at a 45-degree angle and the optical fiber was placed 7.5 mm from the imaging plane. We showed in the last section that when irradiation is conducted through skin, the optical fiber angle has little effect on fluence. In addition, optical fiber distances larger than 7.5 mm are not desirable because they would result in less light delivery to the imaging plane. It is difficult to decrease the optical fiber distance because of the size of linear ultrasound arrays. Because we expected deviations from the chosen parameters to be small, we did not investigate the effect of changing these extra parameters.

It was also assumed that tissue properties do not change when the tissue is pushed to induce compression. Our rationale is that tissue is generally assumed to be incompressible, due to high water content[180]. The necessary compression is also small, at only a few millimeters. Thus, it is likely that what appears as compression in the images is really a result of tissue being displaced sideways out of the imaging plane. Some literature has shown that optical properties of tissues do change with compression[181, 182]. However, there were several factors that make these not directly comparable to our approach. First, the experiments were conducted on tissue specimens less than 1 mm in thickness that were sandwiched between glass slides and/or mirrors. Thus, space for tissue to be displaced sideways was small. Second, the compression used was large, with the tissues compressed to thicknesses 1.5-4x smaller than the uncompressed thickness. This is much larger than the compression that would occur from the use of our technique. Third, there was strong evidence that the change in optical

properties was a result of irreversible dehydration (water loss) during the compression process. This would not occur during the use of our technique *in vivo*. Thus, we argue that this assumption is likely a valid one, although it would take further experimental work to prove it conclusively.

Another limitation of the technique is that it can provide relative concentrations of optical absorbers only. It is not capable, for example, of indicating the concentration of a marker in absolute terms (e.g. µg/mL). Nonetheless, relative quantitative comparisons of concentration within an image would still be highly useful. Given the large (51-97%) percent error in the photoacoustic intensity when the fluence is unadjusted, it would be easy to mischaracterize signal deep in tissue.

A second limitation is that this method is limited when using multi-wavelength techniques. The fluence compensation can only be completed for targets at different depths for each wavelength individually. It cannot compensate between wavelengths. The difference in relative fluence between the wavelengths would be limited to whatever ratio in fluence is present at the shallowest photoacoustic target since this is the target to which each wavelength is normalized. Fluence compensation between wavelengths could theoretically be conducted if a chromophore were identified in tissue in which the difference in absorption coefficient between the wavelengths was known. However, this could not be guaranteed in every imaging session.

The final limitation is that the study was conducted purely by simulation. Experiments will be needed first on phantoms consisting of high scattering liquids or gelatin. Point sources, such as graphite rods, can be tracked as the optical fiber and

transducer are pushed into the phantom. These studies should confirm that the exponential decrease in fluence as a function of depth is present by using compression. If successful, several other *ex vivo* studies would be of value. First, phantoms could be tested with multiple layers having different optical properties, to investigate the effect that heterogeneous tissue may have on the effectiveness of the technique. In addition, future work should focus on point absorbers in actual tissue. The purpose would be to determine if any change in optical properties of tissue due to compression is sufficient to make the technique ineffective. For each test, the minimum depth at which the technique becomes viable could also be evaluated. Finally, by using photoacoustic sources with known relative concentrations, the effectiveness of the compensation technique in reconstructing the true relative photoacoustic intensities could be evaluated.

4.6 Conclusion

In this chapter, we introduce a new technique that could be used to compensate fluence such that relative quantitative comparisons of photoacoustic signal intensity could be made in biological tissue. The technique involves slightly compressing tissue and recording the photoacoustic intensity of native absorbers as the tissue compresses. The change in photoacoustic intensity with depth can be used to determine the exponential attenuation coefficient of fluence in the tissue. Once determined, the attenuation coefficient can be used to compensate the acquired photoacoustic image in the uncompressed state. We investigate this technique using modeling methods. We establish that a constant exponential attenuation coefficient for fluence versus depth should be expected in most soft tissues at depths near or greater than 1 cm, illustrating the viability of the technique.

We estimate the expected improvement in comparisons of photoacoustic intensity between five high absorbing regions in a simulation using the optical properties of breast tissue at 789 nm. We find that errors are improved from 51-97% before using the technique to less than 5% afterwards. The studies illustrate the potential usefulness of the technique in clinical applications and justify further experimental study.

CHAPTER 5: SAFETY OF INTRAVASCULAR PHOTOACOUSTIC IMAGING – IN VITRO

5.1 Introduction

This chapter was adapted from: Sowers, T., et al. Laser threshold and cell damage mechanism for intravascular photoacoustic imaging. *Lasers Surg Med.*, 2018. **Oct 10**. doi: 10.1002/lsm.23026[183].

5.1.1 Abstract

Intravascular photoacoustic (IVPA) imaging is being developed to image atherosclerotic plaques, a leading cause of morbidity and mortality in the United States. However, the safety of this imaging modality, which requires repeated irradiation with short laser pulses, has not yet been investigated. This chapter has two objectives. First, determine *in vitro* the limit of cumulative fluence that can be applied to cells before death at IVPA relevant wavelengths. Second, evaluate if high single pulse fluences are a potential cause of cell death during IVPA imaging. Experiments were conducted using endothelial cells, macrophages, and smooth muscle cells. The cumulative fluence experiments were conducted at 1064 and 1197 nm, using a high pulse repetition frequency laser. Cells were irradiated with a wide range of cumulative fluences and evaluated for cell death. The thresholds for death were compared to the maximum expected clinical cumulative fluence. To evaluate the effect of single pulse fluences, cells were irradiated at 1064, 1210, and

1720 nm. Light was delivered at a range of pulse energies to emulate the fluences that cells would be exposed to during clinical IVPA imaging. At 1064 nm, all three cell types remained viable at cumulative fluences above the maximum expected clinical cumulative fluence, which is calculated based on common IVPA imaging protocols. At 1197 nm, cells were viable near or just below the maximum expected clinical cumulative fluence, with some cell type to cell type variation. All three cell types remained viable after irradiation with high single pulse fluences at all three wavelengths. The cumulative fluence experiments indicate that safety considerations are likely to put constraints on the amount of irradiation that can be used in IVPA imaging protocols. However, these experiments also indicates that it will be possible to use IVPA imaging safely, since cumulative fluences could be reduced by as much as two orders of magnitude below the maximum expected clinical cumulative fluence by varying the imaging protocol, albeit at the expense of image quality. The single pulse fluence experiments indicate that cell death from single pulse fluence is not likely during IVPA imaging. Thus, future studies should focus on heat accumulation as the likely mechanism of tissue damage.

5.1.2 Background

Cardiovascular disease is the leading cause of death worldwide, ahead of cancer and chronic lower respiratory disease[20]. Coronary artery disease, which is a subset of cardiovascular disease, resulted in an estimated 7.4 million deaths worldwide in 2015 alone[20]. Coronary artery disease results from lipid plaque formation, causing death either by extreme luminal narrowing or more often by coronary thrombus formation from

ruptured plaques[184, 185]. Based on histopathologic studies, these rupture prone plaques are characterized by large lipid rich necrotic cores, calcification, a thin fibrous cap, and erythrocyte infiltration[26, 37, 184, 186, 187]. The growth of these lipid plaques is asymptomatic[188], leaving clinicians unable to intervene prior to the development of symptoms, which commonly include unstable angina, acute myocardial infarction, or sudden coronary death[184]. Once symptoms occur, it is not always clear which plaques require intervention. Thus, a clinical tool capable of identifying and characterizing plaques would help clinicians determine the best treatments for culprit and non-culprit plaques, ultimately reducing morbidity and mortality. Patients with a history of heart disease or with risk factors associated with plaque progression (e.g. diabetes or hypertension) could be ideal candidates for more extensive imaging after an initial cardiac event. Multiple imaging modalities are being developed, and sometimes combined, to meet this need, with each modality having its own distinct advantages and disadvantages[189-192]. One such modality is intravascular photoacoustics.

In the last several years, there have been concerted efforts toward the translation of IVPA imaging to the clinic[13, 193]. These include, but are not limited to: continual improvements in catheter design[48], improvements in imaging resolution[194], the use of contrast agents to target biological markers, such as MMP2, of rupture prone plaques[195], combining IVPA with other modalities such as optical coherence tomography[196], real-time IVPA imaging[54], and *in vivo* real time imaging of non-native plaque in swine[55]. However, a review of the literature has shown no study to date that has investigated the safety of IVPA imaging. Since volumetric IVPA imaging requires the acquisition of many photoacoustic signals as the catheter is simultaneously rotated and retracted, vessel tissue

is subjected to many pulses of laser irradiation. Standards concerning human exposure to laser light (ANSI Z136.1 – Safe Use of Lasers) exist that give guidance for irradiation of the skin and eye but not for irradiation of vessel tissue. The advent of real-time imaging, which can require up to thousands of laser pulses in time periods on the order of seconds, makes safety studies a necessary prerequisite to clinical translation[54].

Studies that investigate cell death from laser irradiation have been conducted. For example, Denton *et al.*, studied the effect of heat accumulation from laser irradiation on cell death[197]. In this study, microthermography was used to relate cell death with temperature increases and found a correlation between cell death and an average peak temperature of 53°C. However, the authors were unable to find studies in which cells present in vessel tissue were irradiated at IVPA relevant wavelengths.

This chapter covers what is to my knowledge the first set of studies focused on the issue of IVPA safety. The response of the main three cell types present in the vessel (endothelial cells, macrophages, and smooth muscle cells) to laser irradiation at IVPA relevant wavelengths were investigated *in vitro*. Cell death by heat accumulation was studied with fast, high power lasers by irradiating cells with various levels of cumulative fluence based on common IVPA imaging parameters. These experiments were completed near the lipid absorption peak at 1197 nm and at 1064 nm. The latter was chosen since the Nd:YAG laser makes this wavelength easy to use for multiple wavelength imaging. Next, cell death from the mechanism of single pulse fluence was investigated. In these experiments, cells were irradiated at the higher range of single pulse fluences expected in clinical IVPA imaging using slow lasers at 1064, 1210, and 1720 nm and then evaluated for cell death.

5.2 Materials and Methods

5.2.1 Cell Culture

5.2.1.1 Cumulative Fluence Experiments

The cell studies were completed on the main cell types found in both healthy and diseased vessels. These included human coronary artery endothelial cells (HCAEC) (CC-2585, Lonza), mouse macrophages (TIB-67, ATCC), and human aortic smooth muscle cells (SMC) (C-007-5C, Cascade Biologics). Passage numbers for the HCAECs, macrophages, and SMCs were no higher than 7, 12, and 14, respectively. The HCAECs were cultured in vascular cell basal medium (CC-3156, Lonza) with an endothelial cell growth kit (CC-4176, Lonza) while the mouse macrophages were cultured in Dulbeco's Modified Eagle Media (10-013-CV, Corning) with 10% Fetal Bovine Serum and 1% Penicillin-Streptomycin. The SMCs were cultured in Medium 231 (M231500, Life Technologies) with 5% Smooth Muscle Growth Supplement (S00725, Life Technologies) and 1% Penicillin-Streptomycin-Glutamine (10378016, Thermo Fisher Scientific).

Cell death was used as a marker to determine if any side effects were likely from the irradiation dosages used for IVPA imaging. In addition, cell death *in vivo* could have negative effects. For example, death of endothelial cells could induce additional inflammation, which is a driver of atherosclerotic disease. At worst, it could also lead to the exposure of prothrombogenic factors inside the vessel wall, increasing the chance of blood clot formation. Meanwhile, macrophages and smooth muscle cells both have a role in the pathogenesis of atherosclerosis. Cell death, particularly by necrosis, of either cell type *in vivo* would result in the release of additional inflammatory cytokines. This could

exacerbate the severity of plaques already present or accelerate the development of plaque in regions of tissue not covered by plaque in patients suffering from atherosclerosis. For these reasons, cell death is used here as an indicator of potential side effects from IVPA imaging.

Prior to irradiation cells were plated on a polyethylene cell culture 96 well plate (353072, Corning) at 80-90% confluency but with a phenol red free base media (SMCs, macrophages: 21063029, Life Technologies; HCAECs: CC-3129, Lonza) since phenol red is highly absorbing. After irradiation, cells were returned to an incubator at 37°C with 5% CO_2. Cells were removed from the incubator either 6 or 24 hours after irradiation and evaluated for cell viability using an MTT assay (V131154, Life Technologies). Briefly, 10 µL 12 mM MTT stock solution was added to each well at the appropriate time point and incubated at 37°C for 4 hours. Then, 100 µL of a solution consisting of 1 gm SDS dissolved in 10 mL 0.01 M HCl was added to each well and incubated at 37°C for 4-18 hours. The absorbance at 570 nm was measured using a plate reader (Synergy HT, BioTek).

5.2.1.2 Single Pulse Fluence Experiments

The polyethylene well plates could not withstand the laser intensities used in the single pulse fluence tests without being damaged. To address this, single pulse fluence tests were performed using tissue chamber slides with a borosilicate glass bottom (macrophages, SMCs: 155411, Nunc, Inc.). It was necessary to plate the HCAECs on a tissue culture treated glass chamber (543079, Greiner Bio-One) for cell adhesion. Cells were plated at

80-90% confluency as previously described for cumulative fluence experiments. Passage numbers for the HCAECs, macrophages, and SMCs were no higher than 9, 15, and 17, respectively.

After irradiation, cells were returned to the cell incubator. Cell viability was evaluated using a fluorescence-based assay kit (30002-T, Biotium) instead of with the MTT assay because the plate reader used to evaluate the MTT assay was not compatible with the tissue chamber slides. A solution of 1 µM Calcein AM and 2 µM EthD, which respectively label live and dead cells, was prepared. Each well was washed with 100 µL of PBS to remove serum esterase activity. Then, the solution containing Calcein AM and EthD was added to each well and incubated at room temperature for 30-45 minutes. Photomicrographs were captured using a microscope (DMI3000 B, Leica) and camera (DFC290, Leica) at a magnification of 10x (10x/0.22, Leica). Cell counts of live and dead cells in one field of view for each well were performed by the same individual, from which the fractional cell viability was calculated for each experimental condition.

5.2.2 Irradiation Parameters

5.2.2.1 Cumulative Fluence Experiments

Cells were irradiated at 1064 nm with a Nd:YAG pump laser (SOL40W-1064, RPMC Lasers, Inc.) and at 1197 nm with a custom-made $Ba(NO_3)_2$–based Raman laser pumped with the 1064 Nd:YAG laser. These lasers had pulse durations of 5-15 ns. The 1197 nm wavelength was chosen because it is close to a peak in lipid absorption, relative

to water, while 1064 nm was chosen because it is a highly common wavelength that could easily be used for spectroscopic or ratiometric imaging of plaque in a clinical IVPA imaging system.

Constructing a three-dimensional IVPA dataset requires collecting A-lines while simultaneously rotating and retracting a side firing catheter. The spot size of the laser irradiation on the tissue is sufficiently large that a given section of tissue is irradiated many times. The number of times a segment of vessel is irradiated is related to the number of A-lines used to construct each image, the catheter pullback rate, and spot size of irradiation on the lumen surface of the vessel. In these experiments, cells were irradiated such that the cumulative fluence experienced by the cells would span a range both above and below the cumulative fluence experienced by the vessel wall during IVPA imaging, based on common imaging parameters from the literature. First, an expression was determined that can be used to calculate the cumulative fluence on the artery lumen in terms of common imaging parameters. Such an expression is briefly derived below.

First, it is assumed that the IVPA catheter is inside a cylindrical artery of constant diameter. It is also assumed that imaging is completed using a constant rate of catheter rotation and pullback. Finally, it is assumed that each location in the vessel will be irradiated by many catheter rotations during pullback, such that there is significant overlap in the area of vessel that is irradiated by the beam from one A-line to the next. Any area on the vessel wall will be successively irradiated by the entire laser beam but in subsections, including areas with hot spots or beam irregularities that may be present in the beam profile. As a result, irregularities in beam shape can be ignored, making it possible to use the sum of average fluences for the derivation. Note that this would not be valid in special instances

of IVPA imaging, such as imaging without pullback in which energy variation in the laser beam profile would cause variation in fluences at different locations on the vessel lumen. Given these assumptions, we can arrive at the following expression for the cumulative fluence (Eq. 3.1)

$$CF = \frac{E_p \, N_{A-lines}}{\pi \, D \, L_z} \times \frac{L_z \; PRF}{P_r \, N_{A-lines}} \quad , \qquad \text{(Eq. 3.1)}$$

where E_p is the energy per pulse, $N_{A\text{-lines}}$ is the number of A-lines per rotation, D is the inner diameter of the artery, L_z is the length of the laser spot size in the longitudinal direction, PRF is the pulse repetition frequency of the laser, and P_r is the pullback rate of the catheter.

In Equation (3.1), the cumulative fluence is a product of two terms. The first term represents the cumulative fluence irradiated on the tissue during one 360-degree rotation. The numerator is the total energy deposited while the denominator represents the cylindrical area irradiated on the lumen surface. In the second term, the length of the laser spot size in the longitudinal direction, L_z, divided by the pullback rate of the catheter, P_r, is equivalent to the amount of time over which a single location on the lumen will be irradiated. Multiplying this by the frame rate gives the total number of rotations during which the catheter will illuminate the same segment of tissue. Equation (3.1) could be further simplified by substituting the pulse repetition frequency, PRF, with the product of the number of A-lines, $N_{A\text{-lines}}$, and the imaging frame rate, F_r:

$$CF = \frac{E_p\ PRF}{\pi\ D\ P_r} = \frac{E_p\ N_{A-lines}\ F_r}{\pi\ D\ P_r}\ .$$ (Eq. 3.2)

The number of A-lines per image and the pullback rates cited in the literature[13, 193] generally vary from 64 to 256 and from 0.5 mm/s to 3 mm/s, respectively. The pulse energies used vary from 0.1 – 0.8 mJ per pulse. The maximum cumulative fluence would occur using 256 A-lines per image, a 0.5 mm/s pullback rate, and a pulse energy of 0.8 mJ. Assuming a maximum imaging frame rate of 30 Hz and a minimum inner (occluded) coronary artery diameter of 2 mm, this would result in a cumulative fluence of 195.6 ≈ 200 J/cm^2. This will be referred to as the maximum expected clinical cumulative fluence (MECCF) throughout this chapter and the next. It represents the highest amount of irradiation that would be reasonably expected in a clinical setting.

All three cell types were subjected to irradiation at each wavelength. Both lasers were operated at 7680 Hz, with the spot size equivalent to the well size in a 96 well plate (well diameter 6.4 mm). The pulse energy at 1064 nm was 0.8 mJ, while the pulse energy at 1197 nm was 0.08 mJ due to the Raman laser having a lower output. Seven irradiation conditions at various levels of cumulative fluence were used (**Error! Reference source not found.**). One control condition that was not irradiated was used so that the change in cell viability from irradiation could be determined. Higher cumulative fluences were attained by irradiating over longer time periods. The number of pulses each well was exposed to was tracked using software programmed with LabVIEW (National

Instruments). Once the desired cumulative fluence was achieved, a software-controlled 3D positioning system (Parker Hannifin) was used to move the well plate so that a new well was irradiated (Figure 5.1). The cumulative fluences for each condition were lowered by a factor of 10 at 1197 nm, due to the lower output of the Raman laser. However, the lower cumulative fluences were still sufficient to cause cell death using 1197 nm for some conditions. This is likely the result of the absorption coefficient of water, which is the primary component of cells, being about 10 times higher at this wavelength[198]. The cells were placed on a hotplate during irradiation so that they had a steady state temperature near the physiological norm (37°C +/- 3°C). The sample size for each condition was six, which was sufficient to attain statistically significant differences in cell viability.

Table 5.1 Cumulative fluence dosages at 1064 nm and 1197 nm for all 3 cell types. Data reproduced from Sowers et al.[183]

Cumulative Fluence Dosage (J/cm^2)	
1064 (nm)	**1197 (nm)**
0	0
14	1.4
69	6.9
276	27.6
689	68.9
1380	138
2070	207
4130	413

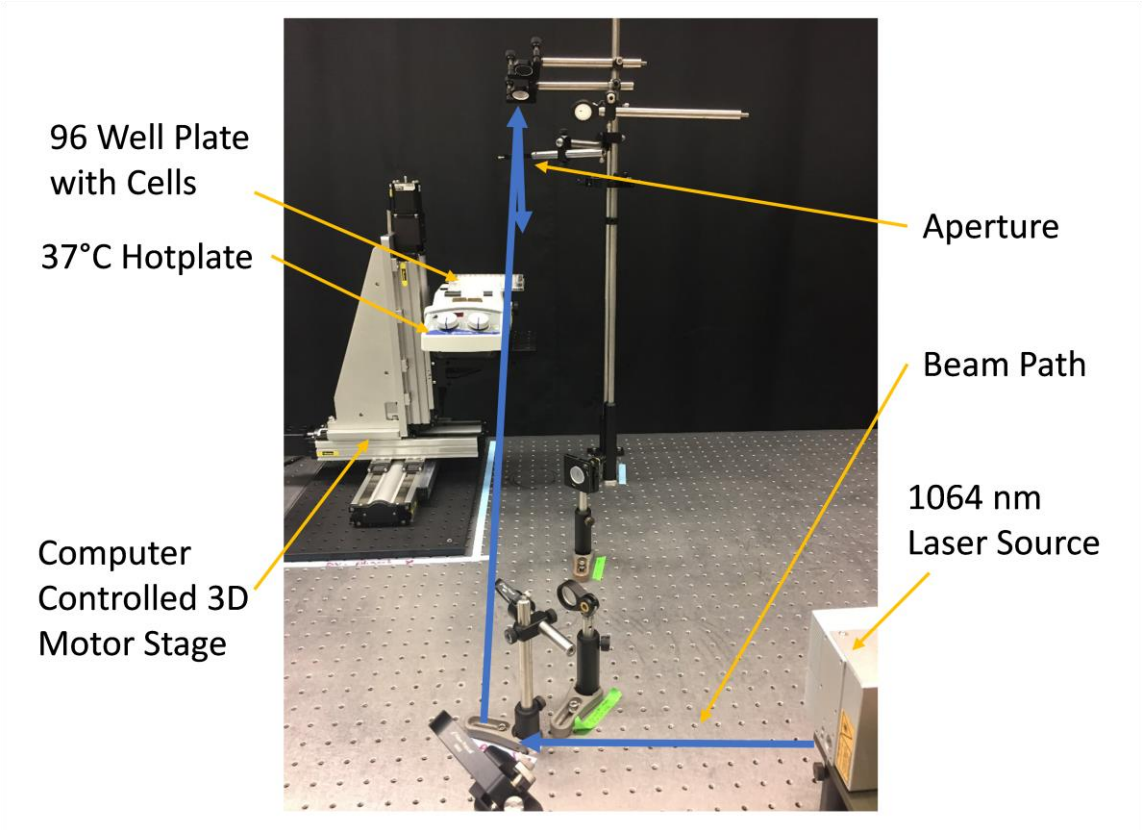

Figure 5.1 Photograph of the experimental setup used for the cumulative fluence experiments. The laser beam was elevated up and then down into the well plate, using an aperture to regulate the spot size. The well plate was placed on a hot plate that maintained the well temperature at 37°C. Only wells directly over the hotplate were irradiated. A computer software controlled 3D motor stage was used to control the location of the well plate during irradiation. For the single pulse fluence experiments, the laser beam was instead coupled into an optical fiber and delivered to the cells as described in the methods section. Figure reproduced from Sowers et al.[183].

5.2.2.2 Single Pulse Fluence Experiments

The single pulse fluence experiments were completed for all three cell types at 1064, 1210, and 1720 nm. The experiments at 1064 and 1210 were completed with a 10 Hz optical parametric oscillator (OPO) pumped at 532 nm (Vibrant, Opotek), while the 1720 nm experiments were completed using a 10 Hz OPO pumped at 355 nm (FRO-290 Quanta-Ray, Spectra-Physics) due to its higher output energy at that wavelength. These lasers had pulse durations of 7-10 ns.

The single pulse fluence experiments were designed to test for cell damage caused by high fluences in a single pulse. Cells were irradiated using the output of an optical fiber with an NA of 0.22 and a core diameter of 300 μm (1068000061, Polymicro Technologies), which is similar to those used in IVPA imaging. The maximum fluence in clinical IVPA imaging would occur when the catheter rests against the side of the artery, since the spot size will be smallest for a given pulse energy. The fiber was placed 1 mm above the cell adherent chamber slide surface to mimic this condition for a 2 mm diameter catheter and sheath. The optical fiber was then raster scanned across the chamber slide such that all the cells were irradiated. This was completed using a 3D positioning system (Parker Hannifin) controlled with software programmed in LabVIEW (National Instruments). Each location on the chamber slide was irradiated with 50 pulses instead of a single pulse during the raster scan, to ensure that any damage was detected. The pulse energies tested were 0.0 (control), 0.4, 0.8, and 1.2 mJ, which correspond to 0.0, 0.10, 0.21, and 0.31 J/cm^2 (300 μm diameter fiber core with 0.22 NA gives a spot size of 0.7 mm). The cells were placed on a hotplate during irradiation so that they had a steady state temperature near the physiological norm (37°C +/- 3°C).

5.2.3 Statistics

All statistical tests were performed in IBM SPSS Statistics. Levene's test ($p < 0.05$) was used to evaluate the homogeneity of variances for each cell type/wavelength combination, while the Shapiro-Wilkes test ($p < 0.05$) was used to test for normality, meaning the sample came from a normally distributed population. For data sets in which neither assumption was violated, a one way, two-tailed ANOVA with Tukey's honestly significant difference ($p < 0.05$) post hoc test was used for comparison groups. Five of the one hundred thirty-two conditions were found to violate the assumption of normality, but not the homogeneity of variances. However, ANOVA is known to be fairly robust against violations of the assumption of normality, and has in fact been shown to perform as well or better than the Kruskal-Wallis test for small samples sizes even on non-normal data[199]. Thus, an ANOVA with Tukey's honestly significant difference ($p < 0.05$) was still used to evaluate these data sets. Data sets that failed Levene's test for homogeneity of variance (sixteen out of one hundred thirty-two) were instead evaluated using the Brown-Forsythe test, since it has been shown to perform well for small sample sizes and when the number of populations is large[200]. Since Brown-Forsythe has been shown to be robust to violations of normality[201, 202], it was used on data sets that failed Levene's test whether or not they passed the Shapiro-Wilkes test for homogeneity of variances. When Brown-Forsythe indicated significance Games-Howell ($p < 0.05$) was used as the post hoc test.

5.3 Results

Cumulative fluence experiments were first completed at 1064 nm for all three cell types (Figure 5.2). Values of cumulative fluence were chosen that spanned approximately two orders of magnitude. The MECCF of 200 J/cm^2 is marked with the vertical red line in Figure 5.2. Significant between group differences were found for each combination of cell type and wavelength at some time points. Cell death was observed at 6 and 24 hours for all cell types at 1400 J/cm^2. At 690 J/cm^2, HCAECs showed a statistically significant level of cell death ($p = 0.026$) at the 24-hour time point only, while macrophages showed reduced viability at both time points. No cell death was observed for any cell type at the fourth condition of 280 J/cm^2, which is above the MECCF.

The results of the cumulative fluence experiments at 1197 nm are shown in Figure 5.3. However, since the output of the Raman laser was lower than the 1064 nm pump laser, the cumulative fluences used for each condition are correspondingly lower. Again, the ANOVA or Brown-Forsythe tests indicated significant between group differences for each combination of cell type and wavelength at some time points. Death of the macrophages irradiated at 1197 nm occurred below the MECCF. All cell types were still viable after irradiation at 70 J/cm^2, but macrophages showed reduced viability at 140 J/cm^2 as did the SMCs at the 6-hour time point. The endothelial cells proved more robust, with a decrease in fractional cell death only at 210 J/cm^2.

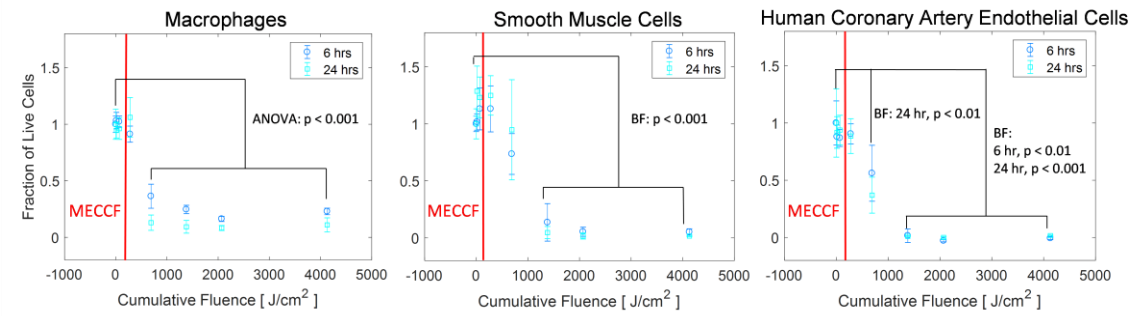

Figure 5.2 Cell viability for each cell type versus light dosage at 1064 nm. The y-axis shows the fraction of live cells, normalized to the cell viability in the nonirradiated control group. The x-axis shows the cumulative fluence dosage applied to cells at each condition. The red vertical line indicates the value of the maximum expected clinical cumulative fluence (MECCF) for clinical imaging. For each condition, n=6. BF: Brown–Forsythe. Reproduced from Sowers et al.[183]

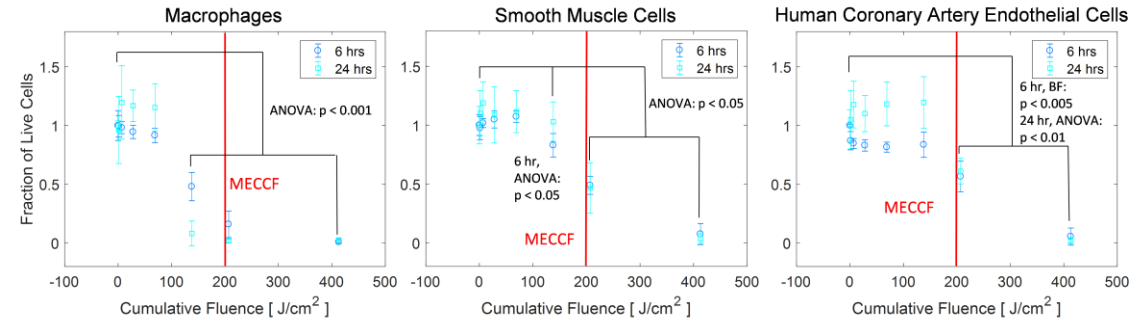

Figure 5.3 Cell viability for each cell types versus light dosage at 1197 nm. The y-axis shows the fraction of live cells, normalized to the cell viability in the nonirradiated control group. The x-axis shows the cumulative fluence dosage applied to cells at each condition. The red vertical line indicates the value of the maximum expected clinical cumulative fluence (MECCF) for clinical imaging. For each condition, n=6. BF: Brown–Forsythe. Reproduced from Sowers et al.[183]

Results for the single pulse fluence experiments for the macrophages, SMCs, and HCAECs are shown in Figure 5.4. The results are uniform across cell types and wavelengths. No cell death was observed for any of the conditions tested, with the fraction of live cells being near 1 in all cases. This is a positive result, and a strong indication that if cell death occurs from IVPA imaging, the likely mechanism will be heat accumulation over many laser pulses rather than optical breakdown from high single pulse fluences.

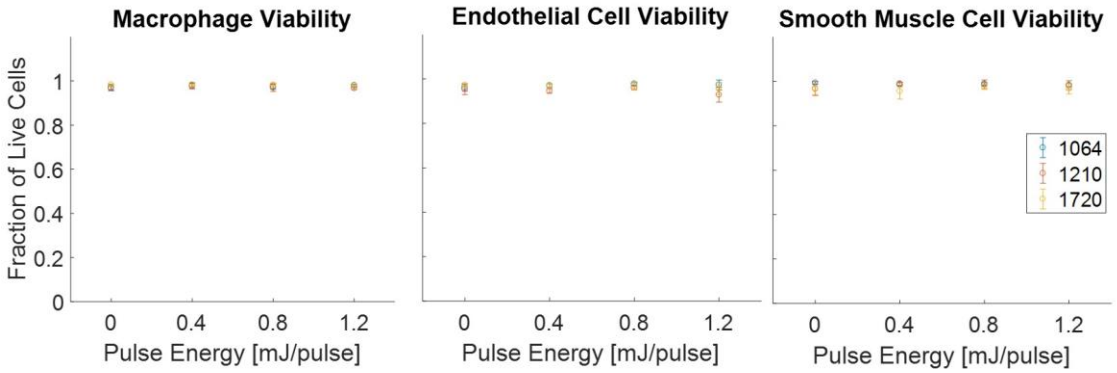

Figure 5.4 Single pulse experimental results for the macrophages, endothelial cells, and smooth muscle cells. The fraction of live cells is reported along the y-axis. The pulse energy out of the optical fiber for each condition in shown on the x-axis. The maximum dosage of 1.2 mJ is 0.4 mJ higher than the highest energy commonly used for *ex vivo* IVPA studies. For each condition, n=4. Figure produced using data from Sowers et al.[183]

5.4 Discussion

In the first part of this chapter, a maximum expected clinical cumulative fluence was determined that comprised the highest expected total fluence a region of tissue would be expected to experience in a clinical setting based on common IVPA imaging parameters in the literature. This value, the MECCF, was found to be 200 J/cm^2. Cells were irradiated with a range of cumulative fluences above and below this threshold. The conditions covered over 2 orders of magnitude, varying from 14 J/cm^2 through 4100 J/cm^2 at 1064 nm and from 1.4 J/cm^2 through 410 J/cm^2 at 1197 nm.

All three cell types showed cell death at 1400 J/cm^2 when irradiated at 1064 nm, with the macrophages and HCAECs showing signs of damage at 690 J/cm^2, although only after 24 hours for the HCAECs. At 1197 nm, all cell types showed loss of viability at a cumulative fluence of 210 J/cm^2, with macrophages also showing reduced viability at cumulative fluences of 140 J/cm^2 as did the SMCs after 6 hours. The most likely cause of the discrepancy at different wavelengths is the difference in the absorption coefficient of water [198]. The absorption coefficient of water is about 10 times larger at 1197 nm than at 1064 nm, leading to greater heat accumulation. It is not clear why the macrophages were more susceptible to damage by irradiation than the SMCs or HCAECs.

For both wavelengths and all three cells types, cell damage occurred near the MECCF. This implies that safety will place constraints on the types of imaging protocols that can be used clinically. However, the cumulative fluence during clinical imaging can easily be reduced by an order of magnitude below the MECCF by reducing the number of A-lines per image and increasing the pullback rate of the catheter, although there will be a

consequent reduction in image quality. In addition, recent *in vivo* studies have shown the ability to image lipid using only 0.08 mJ, which would lower the MECCF by a further order of magnitude[55]. However, this requires flushing the vessel with heavy water, which has a substantially lower absorption coefficient at wavelengths used for lipid imaging. The heavy water is not toxic, but its clinical usage will require FDA approval and would increase the cost of the imaging procedure. Catheter designs with narrower beam profiles and improved overlap with the ultrasound transducer footprint could also make it possible to reduce pulse energies without decreasing image quality[48]. Using lower frequency transducers may sufficiently increase the sensitivity of catheters such that lipid could be detected using much lower pulse energies through blood *in vivo*, although further studies will be needed to confirm this[203] and it will cause an accompanying decrease in spatial resolution. This study indicates that IVPA can be accomplished safely, but that safety will put constraints on the types of imaging protocols that can be used. This result warrants further study *ex vivo* and *in vivo*.

The result of the single pulse fluence experiments was that for all cell types at each wavelength, the fraction of live cells was near one. This was true regardless of wavelength, despite much higher absorption coefficients at the longer wavelengths (e.g. 10 times larger at 1197 nm and 40 times larger at 1720 nm for water, compared to 1064 nm)[198]. In addition, there was no statistical difference in the fraction of live cells between the control group and the irradiated cells. This is a strong indicator that the maximum single pulse fluences expected in IVPA imaging will not be a mechanism of cell death. Instead, future studies on the safety of IVPA imaging should focus on heat deposition as the mechanism of damage.

There were several limitations to the cumulative fluence studies. First, cell death was evaluated *in vitro* rather than in the tissue environment in which they would normally be found *in vivo*. There may be differences in cell behavior between the two environments. In particular, there was some indication of higher metabolism or cell growth following irradiation with lower cumulative fluences at the 24 hour time point, although the large standard deviation at these time points made statistical evidence inconsistent across all the experimental conditions tested. This effect has been found in a multitude of other *in vitro* studies in the literature [204]. Even if present, it is unclear if this effect would transfer to an *in vivo* environment, where cell growth would be regulated by biological factors.

In addition, since the mechanism of cell damage appears to be heat accumulation, differences in the heat transfer properties of surrounding materials between these experiments and the *in vivo* environment would affect the results. The thermal properties of the 96 well plate and media (similar to water) differ from that of tissue. The thermal diffusivity of blood vessel tissue is 1.3×10^{-7} m^2/s[205]. It is roughly 2.0×10^{-7} m^2/s for polyethylene[206, 207] and 1.49×10^{-7} m^2/s for water at 37°C[208]. The similar thermal diffusivities imply that the rate of cooling of the cells will be similar *in vivo*. However, the heat transfer from the cells and media in the experiment may be limited by the insulating effect of surrounding air, whereas heat *in vivo* would continue to be transported by conduction through surrounding tissue. This would make heat transfer more favorable *in vivo*. Less favorably, irradiation over 12 or 120 seconds was necessary to reach cumulative fluences near the MECCF at 1064 nm and 1197 nm, respectively. Clinical IVPA imaging protocols would happen over ~5 seconds, which would result in less time for heat transport away from the irradiation site. Conversely, clinical imaging *in vivo* will benefit from the

cooling effect of flowing blood or saline. This will cool the tissue both by carrying laser energy absorbed by the liquid away and by introducing a convective cooling effect on the interior surface of the vessel wall. Finally, since the smooth muscle cells and macrophages are located inside the vessel, the cumulative fluence they experience will be attenuated from absorption by any blood or saline that may be between the catheter and vessel wall or by any preceding vessel tissue. *Ex vivo* and *in vivo* studies which more accurately mimic the heat transfer environment during clinical IVPA imaging should be conducted to take these variables into account.

Despite these limitations, the experimental data agreed well with the ANSI Z136.1 standard for irradiation of skin. There are two sets of guidelines for repeated exposure of skin in this standard. One is that a maximum permissible exposure (MPE) for a single pulse must not be exceeded. The second is that a MPE for the pulse train must not be exceeded. For the single pulse guidelines, the MPE for skin is 0.1 J/cm^2 at 1064 and 1210 nm and 1 J/cm^2 at 1720 nm. Given a 300 μm fiber with an NA of 0.22, the spot size had a diameter of 0.7 mm. Thus, the maximum single pulse fluence tested was 0.31 J/cm^2. The MPE is equivalent to roughly 10% of the exposure at which damage should be expected 50% of the time (EC50). Since no cell death was detected in these experiments, all that can be concluded is that the "measured MPE" for this experiment would be 0.031 J/cm^2 or greater.

For the second ANSI guideline, the MPE for skin under these irradiation conditions is 1 W/cm^2 at 1064 and 1197 nm. Partial cell death, which we use as an approximation of the EC50, was detected in the cumulative fluence experiments at 690 J/cm^2 and 130 J/cm^2 for 1064 nm and 1197 nm, respectively. The irradiance at these conditions was 17.3 W/cm^2

and 1.73 W/cm^2. Given the relationship between EC50 and MPE, the "measured MPE" for these experiments would thus be 1.73 W/cm^2 and 0.173 W/cm^2. Damage from heat accumulation would be determined by the amount of heat generated from irradiation, which itself is dependent on the absorption coefficient of the tissue being irradiated. At 1064 nm the absorption coefficient of skin is about 2.6 times larger than water, while at 1197 nm it is smaller by a factor of 0.35[115, 198]. After adjusting the ANSI standards for skin based on this difference, an MPE for mostly water-based tissue would be nearer 2.6 W/cm^2 at 1064 nm and 0.35 W/cm^2 at 1197 nm. The "measured MPEs" for these experiments are lower than these values but by less than a factor of two. This shows strong agreement with the ANSI standards, despite the limitations of the *in vitro* setup. In vessel tissue, other endogenous chromophores, such as fibers and lipid, will be present. It will be necessary to conduct experiments *ex vivo* to determine if absorption from these components has a large effect on the damage threshold.

This study indicates that it will be possible for researchers to develop safe imaging protocols for clinical IVPA imaging, although safety considerations will play a constraint. Further, this work strongly indicates that heat accumulation is the damage mechanism of concern for IVPA imaging. However, future studies are needed *ex vivo* and *in vivo* to validate these results. Further experiments should also include the second lipid absorption peak at 1720 nm and use both diseased and healthy tissue.

5.5 Conclusion

This was the first study intended to investigate the safety of IVPA imaging. Cell viability in response to a variety of lasing conditions were tested on endothelial cells, macrophages, and smooth muscle cells, which are present in healthy and diseased vessels. Irradiation was conducted at 1210 nm and 1720 nm, which correspond to peaks in the absorption coefficient of lipid, and at 1064 nm, which could become a common wavelength for dual wavelength imaging due to its high accessibility from Nd:YAG lasers. Two sets of experiments were conducted. In the first, the effect of heat accumulation on cell viability was investigated by subjecting cells to various amounts of cumulative fluence. At 1064 nm, cell death was apparent only after irradiation above 280 J/cm^2. This is above the maximum expected clinical cumulative fluence (MECCF), which is an approximation of the highest cumulative fluence that could be expected in clinical imaging. At 1197 nm, cell death was apparent at 210 J/cm^2 for the endothelial and smooth muscle cells, but at 140 J/cm^2 for the macrophages at both time points and the SMCs after 6 hours. This result implies that damage from IVPA imaging is possible given current practices, although the cumulative fluence could be lowered two orders of magnitude below the MECCF at the cost of imaging quality. This is a positive result, and a strong indication that IVPA imaging can be translated safely. The second set of experiments were designed to determine if cell death during IVPA imaging will occur from single pulse fluences (peak optical intensity) or heat accumulation over multiple laser pulses. All three cell types were irradiated with 0.4, 0.8, and 1.2 mJ pulses using an optical fiber positioned 1 mm from the cells to replicate the maximum single pulse fluences expected during IVPA imaging. For all cell types and at each pulse energy no

cell death was observed, strongly indicating that heat accumulation is the mechanism of damage on which future studies should focus. The studies in this chapter justify further investigation of safety concerns around IVPA imaging *ex vivo* and *in vivo*.

CHAPTER 6: SAFETY OF INTRAVASCULAR PHOTOACOUSTIC IMAGING – IN VIVO

6.1 Introduction

6.1.1 Abstract

To the author's knowledge, this is the first study designed to evaluate the safety of intravascular photoacoustic imaging *in vivo*. The damage to blood vessel tissue from real-time *in vivo* delivery of light was investigated in the carotid arteries of swine. Damage was assessed at 1064 nm and the lipid imaging wavelength of 1720 nm in a dose dependent manner. Damage was assessed by Dr. Serge Rousselle, a trained pathologist and co-founder of Alizee Pathology. He determined that the only dose dependent type of damage in the tissue was media necrosis. This damage was detectable when tissue was subjected to a total dosage of 50 J/cm^2 or greater at 1720 nm. There was also damage at 700 J/cm^2 when 1064 nm light was used. Prior studies have already shown that lipid plaque can be imaged using similar or lesser dosages than those showing damage in this study. Moreover, in the opinion of the pathologist, the damage would be expected to heal, although additional studies would be needed to prove this conclusively. The results were consistent with the *in vitro* studies discussed in the prior chapter. The results are also compared to the ANSI Z136.1 standard for skin and it was found that it underestimates damage to the carotid arteries. Thus, the ANSI Z136.1 standard for skin may not be appropriate for vessel tissue. Future work should evaluate the progression of damage over longer time points and evaluate any potential increase in blood

thrombogenicity from irradiation. Nonetheless, these studies suggest that it will be possible to use IVPA imaging to identify lipid plaque in a clinical setting without damaging vessel tissue.

6.1.2 Background

In the prior chapter, the safety study had two main outcomes. First, it determined that any damage from IVPA imaging would be caused by heat accumulation rather than optical breakdown from high pulse energies. Second, it determined approximate thresholds for damage using 1064 nm and 1197 nm light. At 1064 nm, the damage threshold was between 280 and 690 J/cm2. At 1197 nm, the damage threshold was between 70 and 140 J/cm^2. The lower damage threshold at 1197 nm is due to the higher absorption coefficient in water, which is a primary component of soft tissues.

However, the threshold for tissue damage in IVPA imaging needs to be evaluated in a more realistic environment, namely in an *in vivo* experiment. Although *in vivo* real time IVPA imaging has been successfully conducted[55-57] with no apparent damage in the histological sections used for validation of the imaging results[56], no extensive (wavelength and dose dependent) study of tissue damage was found in the literature. It would be useful for researchers developing IVPA to know which energy dosages, and thus what imaging protocols, will be safe. In addition, a demonstration of safety is a necessary step to bring IVPA imaging to the clinic.

Thus, I describe here a set of experiments which aimed to evaluate the threshold for damage to vessel tissue from light irradiation in a wavelength and dose dependent manner. The experiments were conducted on the carotid arteries of swine *in vivo*. The carotid arteries were irradiated at 1064 nm and 1720 nm. At each wavelength, 3 dosages were applied to different regions of tissue. The dosages were chosen based on the damage thresholds found in the cell studies. The samples were sent to a pathologist who evaluated them for damage while blinded. The conclusions from that evaluation are shown here and the implications for clinical translation of IVPA imaging are discussed.

6.2 Materials and Methods

6.2.1 Laser System and Catheter

Light irradiation was produced by a high power, high pulse repetition rate (PRF) custom made laser (Ekspla, NT200). The laser consists of a Nd:YAG pumped optical parametric oscillator (OPO) capable of producing light in the wavelength range from 1690-1750 nm, which contains the lipid absorption peak at 1720 nm. The light from the Nd:YAG at 1064 nm could also be recovered from a side port in the laser. The laser had a maximum PRF of 3840 Hz. The power output of the laser varied from experiment to experiment. At the maximum PRF, it could roughly emit 8 mJ out of the laser at 1064 nm, although most of this was discarded before exiting the catheter. It could emit close to 0.6 mJ at the wavelengths near 1720 nm. All wavelengths were optically coupled into the same 300 μm optical fiber, although this coupling resulted in some energy loss. Upon exiting the

catheter, the maximum light emission was near 0.55 mJ per pulse at 1064 nm and 0.22 mJ per pulse at 1720 nm.

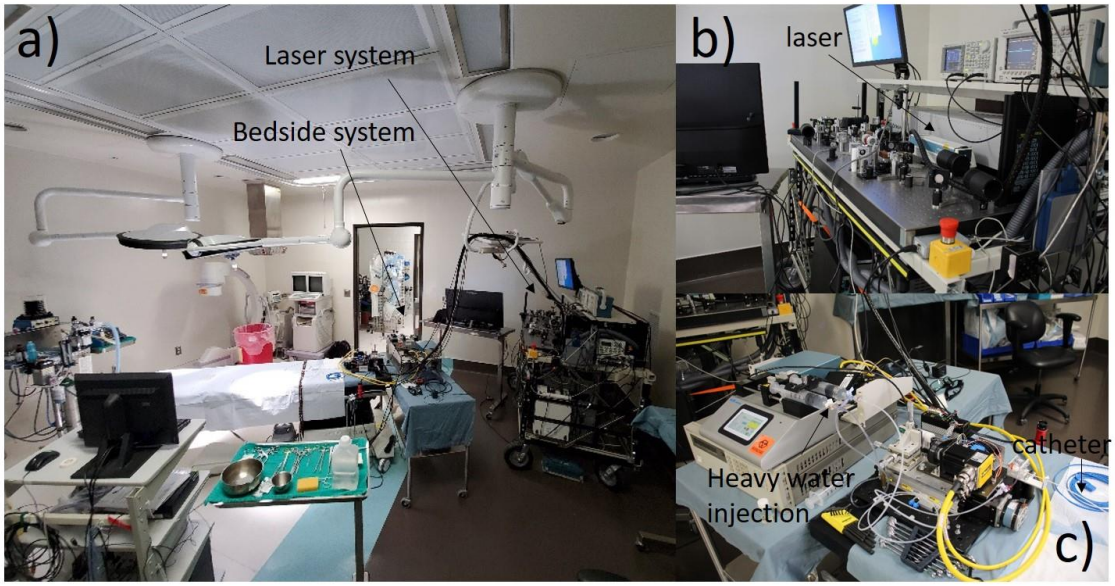

Figure 6.1 a) A picture of the operating room with the laser system. The laser system is present at the back-right corner of the room. The catheter, spindle, water injection, and other components are present on the bedside system. b) A picture of the laser system with the optical components to deliver the laser light into the optical fiber. c) A picture of the bedside system. The catheter extends off the front of the system toward the swine.

Because of the large size of the laser and optics, the system was split into two parts (Figure 6.1a). The first part (Figure 6.1b) consisted of the laser, the optical components to couple all wavelengths into the optical fiber, and the computational

hardware for running the laser and imaging system. The second part (Figure 6.1c) included a spindle which was used to rotate the catheter. The spindle electrically and optically connected the catheter to the computer system, electrical hardware, and laser on the non-bedside portion of the system. This second part was small enough that it could be placed next to the surgical table. The light from the laser was delivered to the bedside portion of the system through the 300 μm optical fiber.

The light was delivered to the vessel tissue through a catheter. The catheter consisted of a torque cable (Asahi Intecc USA, Inc.) containing a 300 μm optical fiber. The end of the optical fiber was polished to 37 degrees. This resulted in side-firing delivery of light from the catheter due to total internal reflection of the light on the inside angled surface of the optical fiber. The optical fiber was covered with a glass cap that was epoxied in place. This was done to prevent water from coming into contact with the surface of the optical fiber, which would have prevented total internal reflection of the laser light due to the higher index of refraction of water. A coaxial cable also ran through the torque cable, and was connected to an ultrasound transducer (20 MHz) at the end of the catheter for ultrasound imaging and acquisition of the photoacoustic signal.

The torque cable of the catheter was inserted into a polyethylene (BD Medical, 63018-781) sheath to prevent damage to vessel tissue from catheter rotation. The polyethylene sheath was connected to the torque cable with a 7 Fr introducer sheath (Terumo Pinnacle) normally used to deliver catheters into vessels during surgery. The presence of the introducer sheath also allowed liquid to be pushed through the catheter into the blood vessel. This liquid could displace blood in the lumen, pushing it into and through a port in the introducer and out of the blood vessel.

6.2.2 Animal Model and Procedure

Two Yorkshire swine were used for the safety study. The swine was put under anesthesia using 5% isoflurane in 100% oxygen and placed in the supine position on the operating table. Anesthesia was maintained at 1.5-2% isoflurane thereafter, supplemented with Propofol as needed. The laser irradiation was conducted on the inside of the carotid artery of each swine. Therefore, once the pig was anesthetized, a longitudinal neck incision was performed and tissue was dissected until about 10 cm of the carotid artery was exposed. A 7 Fr introducer was advanced into the superior (near the head) side of the vessel. The IVPA catheter was inserted into the vessel via the introducer.

Before irradiation, blood had to be removed from the lumen of the carotid artery. This is because blood has a high absorption coefficient near 1720 nm. As a result, much of the light dosage would be absorbed by blood instead of by tissue if blood were present. To prevent this, the inferior end of the carotid artery was ligated. With the artery segment isolated, heavy water (deuterium) was used to flush blood from the artery. Heavy water is a form of water with two neutrons in the hydrogen atoms. It is used instead of water because it has a low absorption coefficient at 1720 nm[209]. It is also non-toxic. The artery was first cleared with a 50 ml bolus flush of heavy water. Then, during the full length of the safety studies, heavy water was continuously flushed into the artery at a rate of 400 ml/hr. As explained previously, the water entered the catheter through the introducer used to mate the catheter torque cable and sheath. The blood/water mixture was able to exit the artery through the outlet port of the introducer used to deliver the catheter into the carotid artery. In the first swine, only the right carotid artery was irradiated. In the second pig,

both carotid arteries were irradiated. After irradiation, the pigs were euthanized using KCl or Euthasol while under deep anesthesia.

Table 6.1 Table of wavelength and light dosage conditions with sample sizes for each condition.

Condition Number	Wavelength [nm]	Fluence [J/cm^2]	Sample Number
C0	None	0	9
C1	1064	8.3	9
C2		100	7
C3		700	5
C4	1720	8.3	4
C5		50	10
C6		200	4

Tissues were irradiated with 6 wavelength and dosage combinations. The wavelengths used were 1064 and 1720 nm. Wavelength near 1720 nm are used for lipid imaging. Tissue has a higher absorption coefficient at this wavelength than at 1210 nm, so it represents the conservative case out of the two wavelengths generally used for lipid imaging using IVPA with regard to safety. The 1064 nm wavelength was chosen because it is commonly available with the Nd:YAG laser, thus making it desirable for dual

wavelength imaging. Three dosages were chosen for each wavelength (Table 6.1). Each condition also had a unique sample size, dependent on the pullback distance of the catheter for each condition. Due to the spring-like nature of the torque cable in the catheter, the sample size could not be controlled precisely, although it was possible to record the true pullback distance using fluoroscopy. The dosages were chosen using the damage thresholds found in the *in vitro* studies in the prior chapter as a guidance. The dosages were chosen such that the highest would be expected to cause damage, while the lowest would be well below the expected damage threshold. Each segment of tissue was irradiated with only one wavelength and at one dosage as the catheter was rotated and retracted during irradiation.

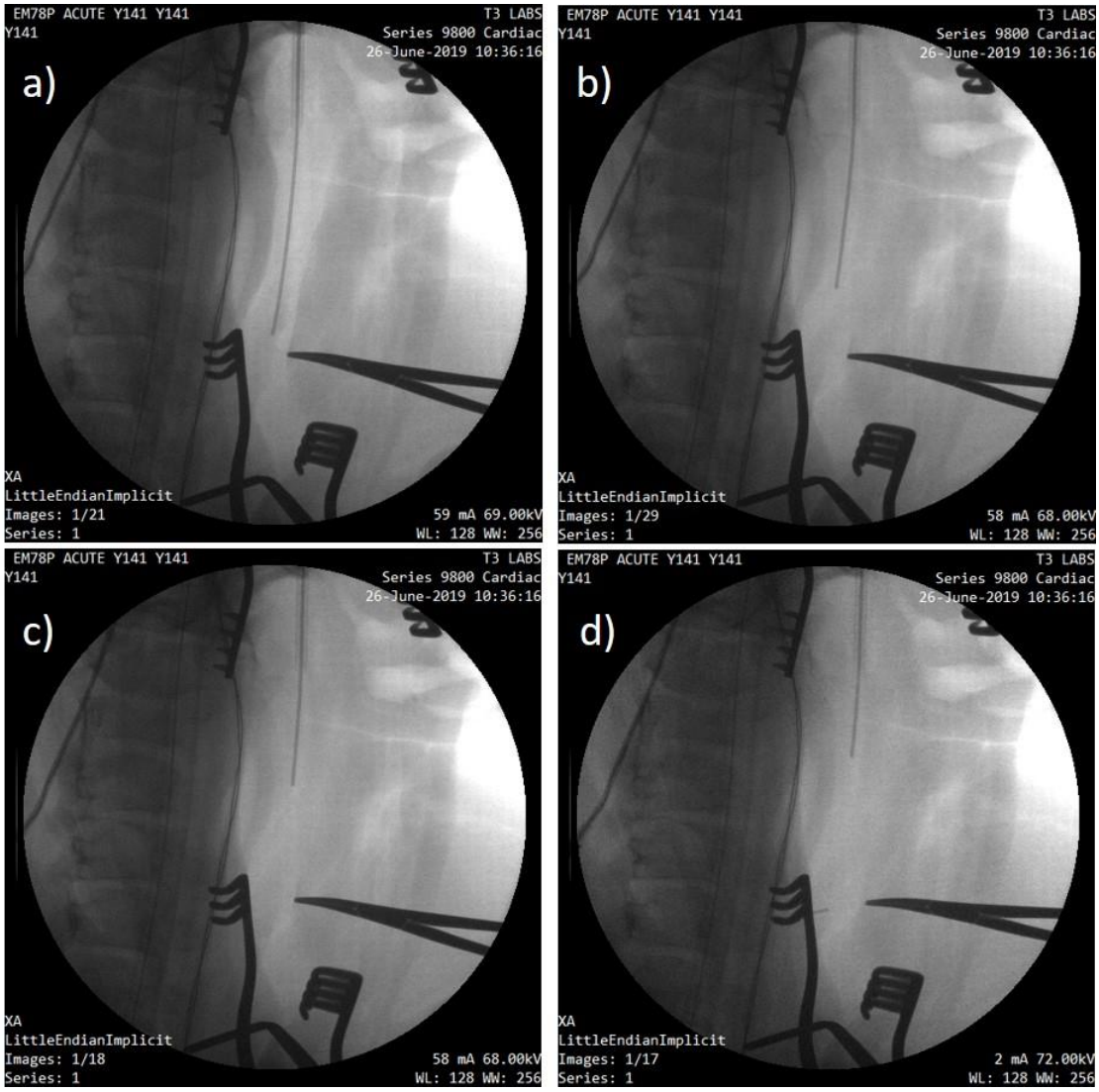

Figure 6.2 a-d) Sequential images showing the length the catheter was pulled backward for each of 3 light dosage conditions.

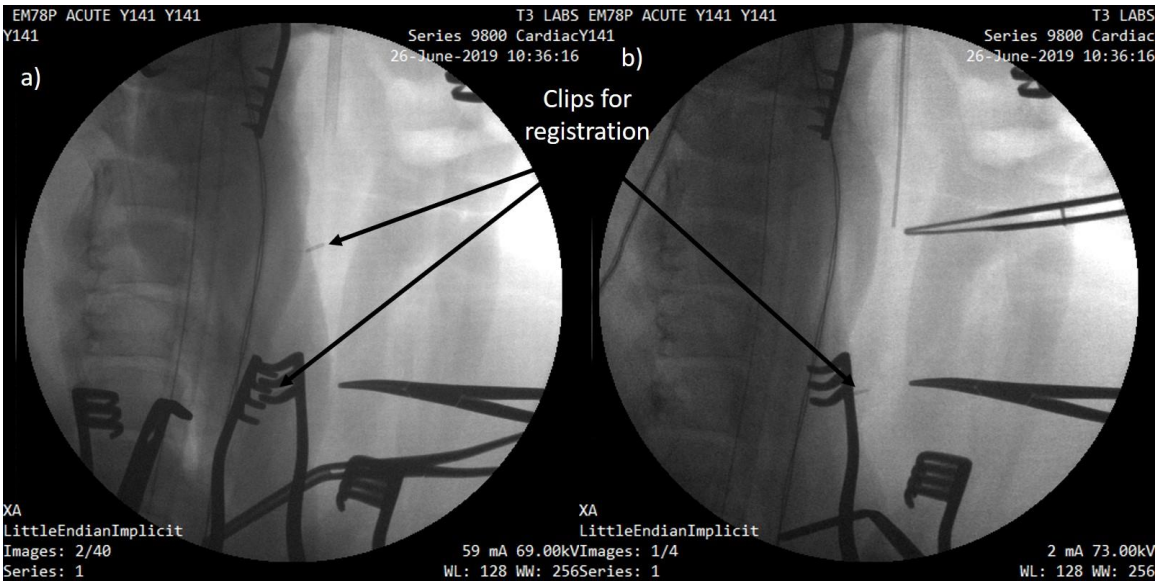

Figure 6.3 a) fluoroscopy image showing the two clips used to relate the pixel length in the fluoroscopy images to a physical distance. The bottom clip is partially obstructed by surgical equipment lying on the top of the swine. The bottom clip is more clearly visible in (b), although the top clip had not been added at that time.

Ultimately, the regions irradiated by each dosage needed to be identified after removal so they could be evaluated for damage. However, the torque cable in the catheter had a spring-like behavior. By this, it is meant that if the catheter was retracted by pulling it back a given distance using the bedside system, the tip of the catheter in the vessel wouldn't always move by the same distance. This made it necessary to track the catheter to determine the regions of the artery that were irradiated with each dosage. To achieve this, fluoroscopy images were taken before and after each dosage was applied to the vessel wall (Figure 6.2). Clips were placed in the image at a known distance (Figure 6.3). These points were used as a calibration length to convert the distance the catheter

moved between applied dosages (in pixels) to a physical unit of length (mm) in the fluoroscopy images. The clips were also placed at both ends of the carotid arteries. They acted as reference points to measure the length of the artery *in vivo* before the artery shrunk after being removed from the swine.

All surgeries were conducted in accordance with the IACUC protocol EM78P from T3 labs. Approval for off campus animal work was given by the IACUC at Georgia Institute of Technology.

6.2.3 Tissue Preparation and Pathology

The carotid arteries were removed after euthanasia and immediately placed in 10% neutral buffered formalin for fixation. The artery from the first pig was not stretched to its original size, so it shrank upon removal. To account for this, it was assumed that the artery shrank uniformly when registering locations on the vessel with a given dosage condition. The two carotid arteries irradiated in the second pig were stretched and pinned to a board of cork at their original length (determined using the known distance between the metal clips). The arteries were shipped in 10% neutral buffered formalin to Alizee Pathology in accordance with Georgia Tech's environmental health and safety policies. They were received in good condition, meaning the seals were intact and there was no damage to the containers.

The tissues were evaluated by Serge Rousselle at Alizee Pathology. Several steps had to be made to ensure meaningful results. First, the pathologist had to be blinded to

the wavelength and dosage applied to the tissue being evaluated. Second, we had to be sure that we could determine where a given tissue slice was located within the artery, since that would be necessary to correlate it with a given wavelength and dosage. To achieve both these objectives, each artery was cut into 16 segments of roughly equal length before shipment to the pathologist. Using the fluoroscopy images and metal clips, it was determined before shipment which wavelength and dosage was applied to each of the segments. The segments were labeled with an anonymous identifier (a number to designate the artery number and a letter to designate the segment), so the pathologist was blinded.

All samples were processed in a series of alcohol and xylene and embedded in paraffin wax for sectioning. Each segment was sectioned approximately at the center. Two sections were produced for each segment, each with a tissue thickness of 5 μm. One section was stained with Hemotoxylin & Eosin (H&E) and the other was stained with Gomori's Elastin Trichrome (GET). Hemotoxylin stains cell nuclei blue or purple while the eosin turns the extracellular matrix and cytoplasm pink. Thus, the H&E stain gives an overall picture of a tissue's layout. Gomori's Elastin Trichrome is meant to stain connective tissue and fibers. It stains connective and collagen tissue green or blue. Muscle, keratin, and cytoplasm will appear red. Nuclei will stain dark blue to black.

Multiple types of damage were evaluated using these stains. These damage types are recorded in the official pathology report (Appendix C). The pathologist produced raw data tables with evaluations of damage for each segment individually. After the raw data tables were generated, the pathologist was sent information that matched each segment with a wavelength and dosage. The results based on wavelength and dosage were

compiled and reported by the pathologist. Damage types were evaluated for trends with respect to wavelength and dosage. The level of background damage in negative controls (not irradiated) were also considered by the pathologist when evaluating the tissue. The results were compiled in a pathology report (Appendix C).

A written set of questions was also sent to the pathologist after receiving a written report. These were returned with written answers. The contents of the questions and answers (Appendix D) are used to contribute to the content of the results and discussion sections of this chapter.

6.2.4 Statistics

The initial evaluation by the pathologist was done on a categorical scale. Thus, the data was tested for significance using Brown-Forsythe with Games-Howell as the post hoc. Each wavelength (1064 nm and 1720 nm) is tested separately. To compensate for the increased likelihood of type I errors, the significance threshold is reduced by a factor of 2 ($p < 0.025$). All statistical tests were performed in IBM SPSS Statistics.

6.3 Results

Multiple damage types were evaluated by the pathologist. The different morphologies of damage were marked using a numeral categorization that ranged from 0 to 4 (Table 6.2) for each tissue segment (see Tabulated Microscopic Data in Appendix C). All the damage morphologies which received a non-zero damage score in at least some of the samples are

shown in Table 6.3. Examples of the types of damage that were indicative of these damage morphologies can be found in Table 6.4 with an accompanying definition and explanation of potential causes.

Table 6.2 Scoring method used by the pathologist.

Score	Description
0	Finding not present.
1	Present, but minimal feature.
2	Notable feature; mild.
3	Prominent feature; moderate.
4	Overwhelming feature; severe.

Table 6.3 Damage morphologies identified by the pathologist with non-zero damage scores in at least some of the histological images.

Damage Grouping	Damage Endpoint
Injury	Mural Acute Thermal Injury
	Media Necrosis
	Hyalinized Collagen without Other Thermal Injury
Inflammation	Inflammation Mean
	Inflammation Median
	Neutrophils
	Inflammation, Adventitia
Healing	Endothelialization
	Endothelium Erosion (terminal or artifact)
	Hemosiderin/Hemorrhage, Vessel Wall
	Adventitia Edema

Table 6.4 Damage types found in the tissue specimens with a description taken from the pathologist report (Appendix C).

Damage Type	Description
Endothelial Cell loss	Most sensitive endpoint. Endothelial cells are highly susceptible to any mechanical shear stress or thermal effect and are typically the first cell type to be lost.
Hypereosinophilic Smooth Muscle Cells	Acute cell injury in the media. The staining alteration indicates generally a change in cytoplasmic homeostasis. This can be an artifact of tissue handling or fixation if fixation conditions are not optimal or can be a very early sign of peracute mural damage. Interpretation is based on comparison between control and treated vessels as well as pattern and distribution of the change and associated changes (context).
Compressive/Pressure Necrosis/Cell Effacement (loss)	Concentric change characterized by sheets of smooth muscle cells showing hypereosinophilia and pyknotic to karyorrhectic nuclei to cytolysis (loss of cellular features) leaving the vessel wall matrix intact. This change can be radial to circumferential and is always concentric (inside out).
Contraction bands	Alternating bands of hypereosinophilic and contracted smooth muscle cells alternating with pale hypocellular or acellular areas. This change indicates excessive vasoconstrictive stress and may lead to necrosis or regeneration.
Necrotic/Apoptotic Cells	Individual cell necrosis; may present as hypereosinophilia, pyknosis, karyorrhexis, cell debris and/or apoptotic body
Collagen denaturation	Loss of fine fibrillar texture with collagenous areas showing hyalinization (homogenous thick bundles typically hypereosinophilic and sometimes picking up hematoxylin stain (purple) to varying degrees). This change indicates heat exposure (thermal denaturation).

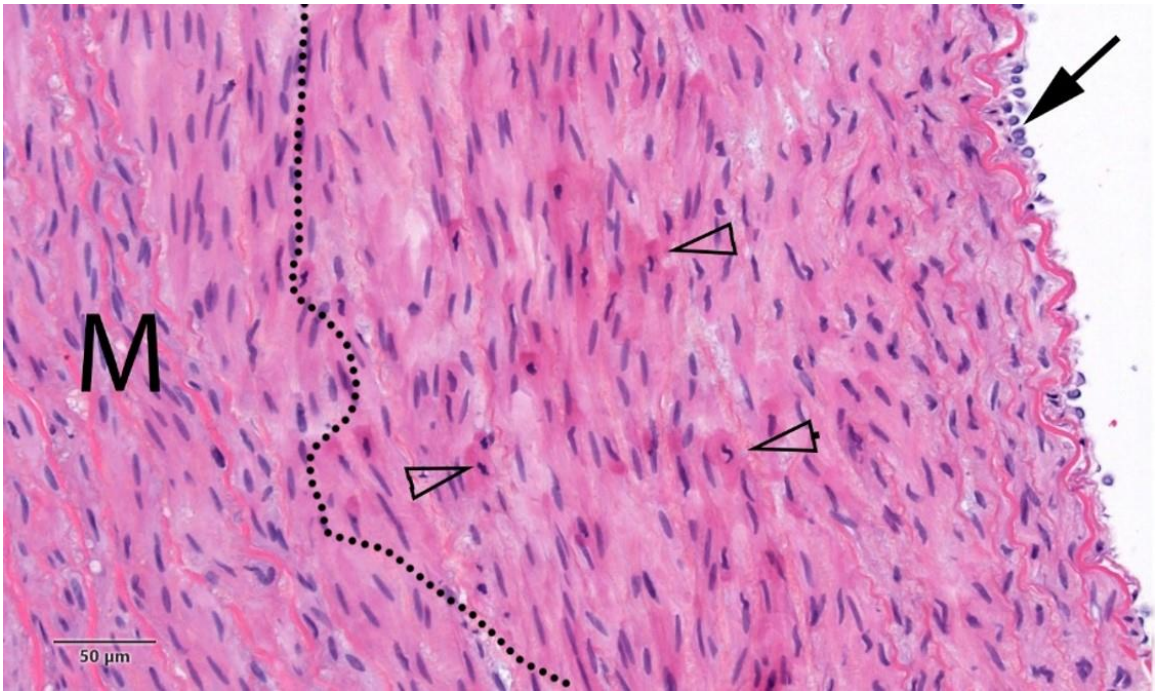

Figure 6.4 Segment 1C (H&E). C0 (No activation). The region M contains intact outer media with the black dotted line separating the region from an inner media area showing necrotic smooth muscle cells (clear arrowheads; hypereosinophilic and contracted smooth muscle cells). Some of the endothelium is intact (solid arrow).

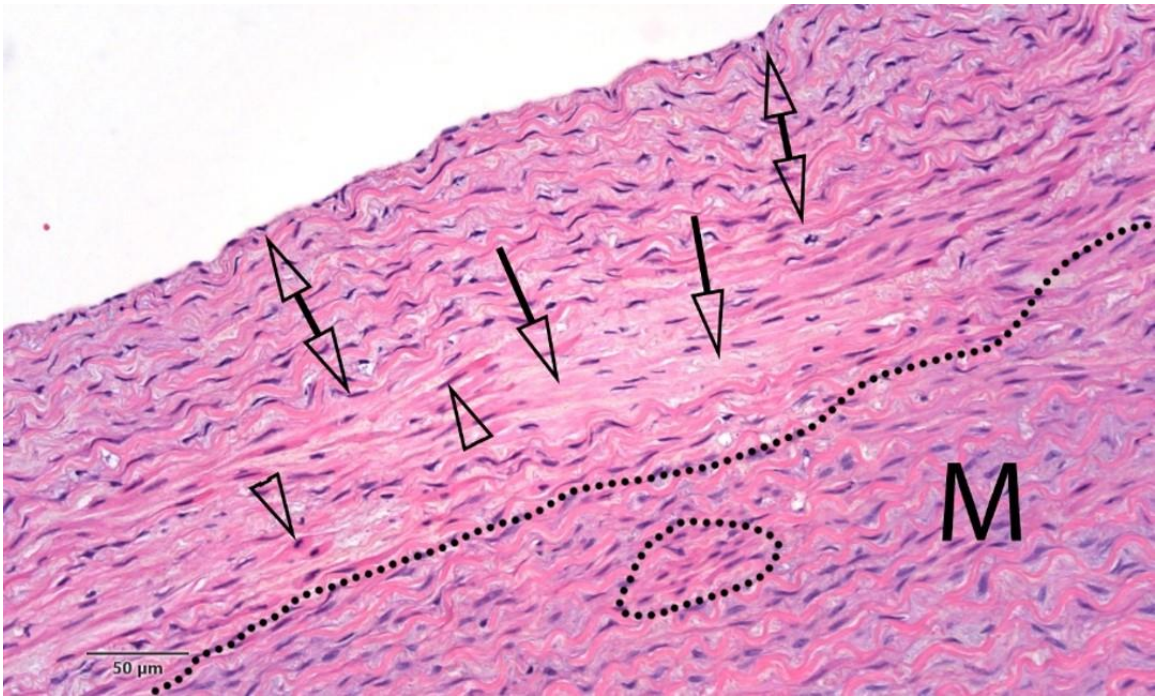

Figure 6.5 Segment 2D (H&E). C1 (1064 nm - 8.3 J/cm2). The black dotted line defines a boundary between the intact outer media (M) and the inner affected media showing hypereosinophilic smooth muscle cells (arrowheads) and clear spaces of smooth muscle cell effacement and loss (clear arrows). Clear double arrows indicate areas in the innermost media showing pyknosis in smooth muscle cell nuclei (generally consistent with compressive necrosis).

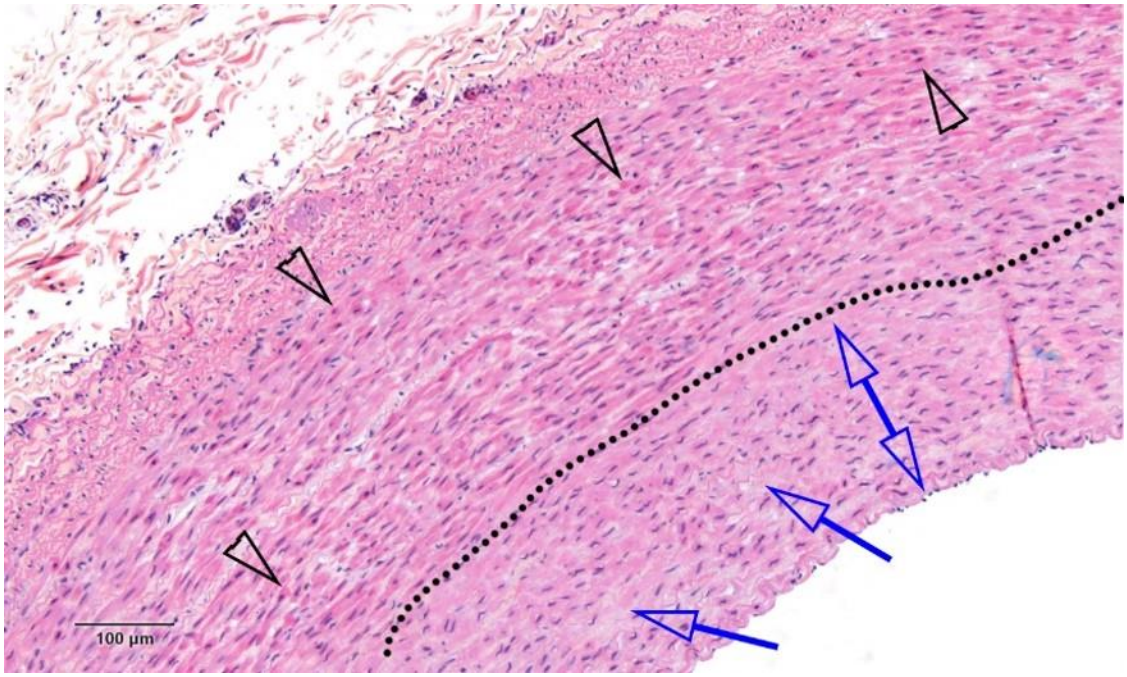

Figure 6.6 Segment 1I (H&E). C2 (1064 nm - 100 J/cm2). The black dotted line defines the boundary between the intact outer media and the inner affected media showing hypereosinophilic smooth muscle cells (clear arrowheads) and increased interstitial clear spaces. The blue double arrow indicate region in the innermost media showing pyknosis in smooth muscle cell nuclei (generally consistent with compressive necrosis). The blue arrows point to clear spaces in the inner media (smooth muscle cell loss) denoting possible energy injury.

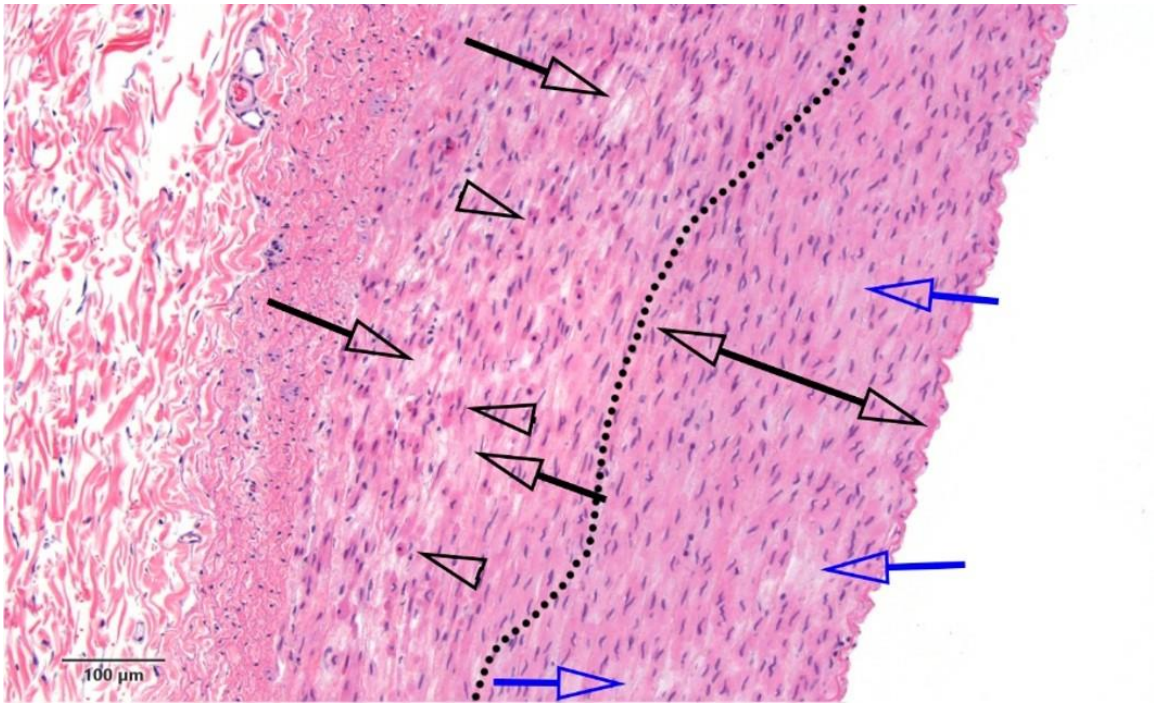

Figure 6.7 Segment 1L (H&E). C3 (1064 nm - 700 J/cm2). The black dotted line marks the boundary between the intact inner media (clear double arrow) and the outer affected media showing hypereosinophilic smooth muscle cells (clear arrowheads) and increased interstitial clear spaces (clear arrows). The blue arrows point to clear spaces in the inner media (smooth muscle cell loss).

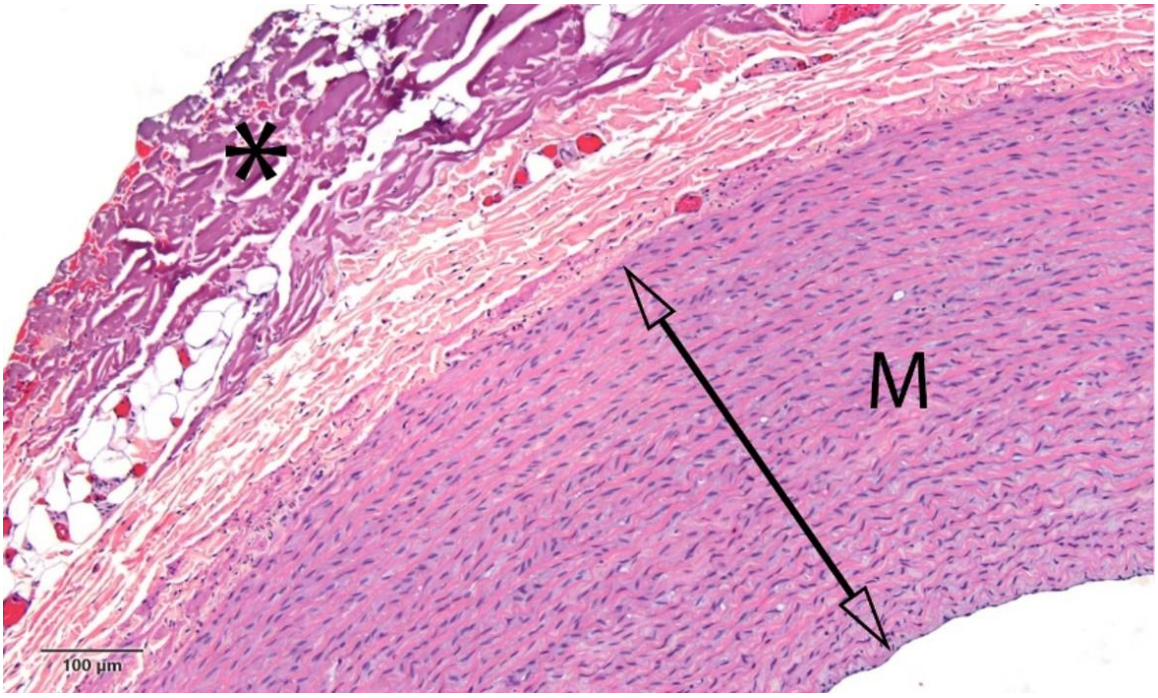

Figure 6.8 Segment 3C (H&E). C4 (1720 nm – 8.3 J/cm2). The black asterisk marks collagen denaturation in the adventitia, likely caused by electrocauterization during the surgical procedure. The clear double arrow crosses the length of intact media (M).

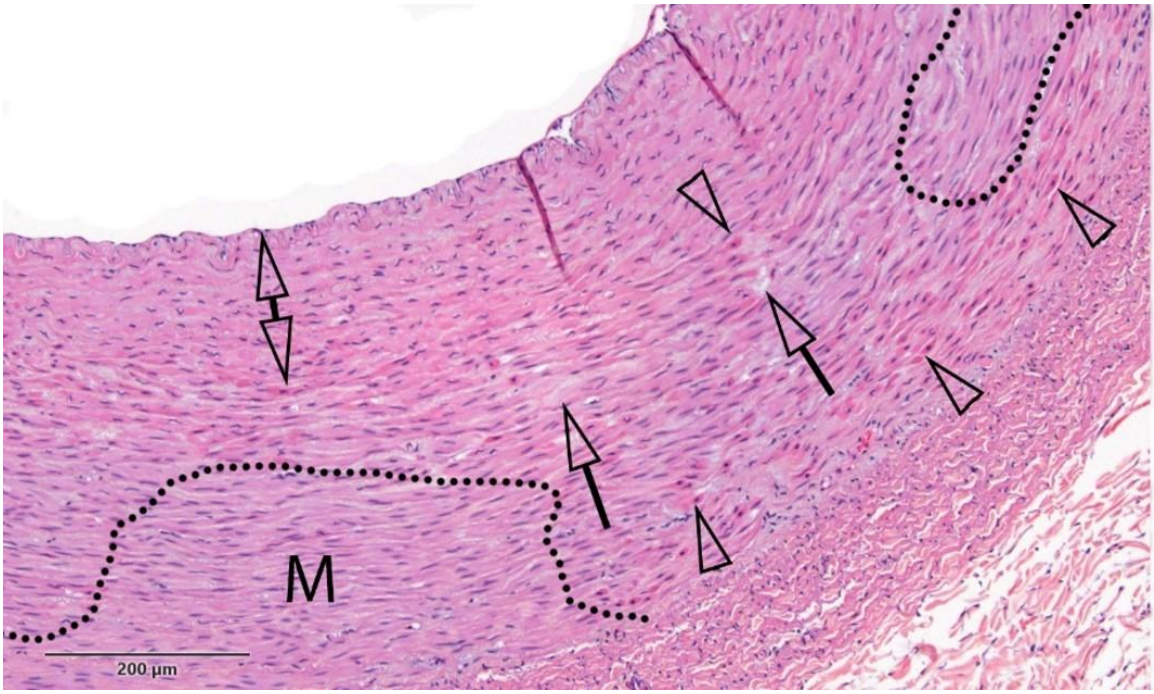

Figure 6.9 Segment 3L (H&E). C5 (1720 nm – 50 J/cm2). The black dotted lines mark the boundary between the intact outer and mid media (M) and the affected media showing hypereosinophilic and contracted smooth muscle cells (clear arrowheads) and increased interstitial clear spaces (clear arrows). The innermost media (clear double arrow) shows pyknotic nuclei and hypereosinophilic smooth muscle cells (typically suggestive of compressive injury).

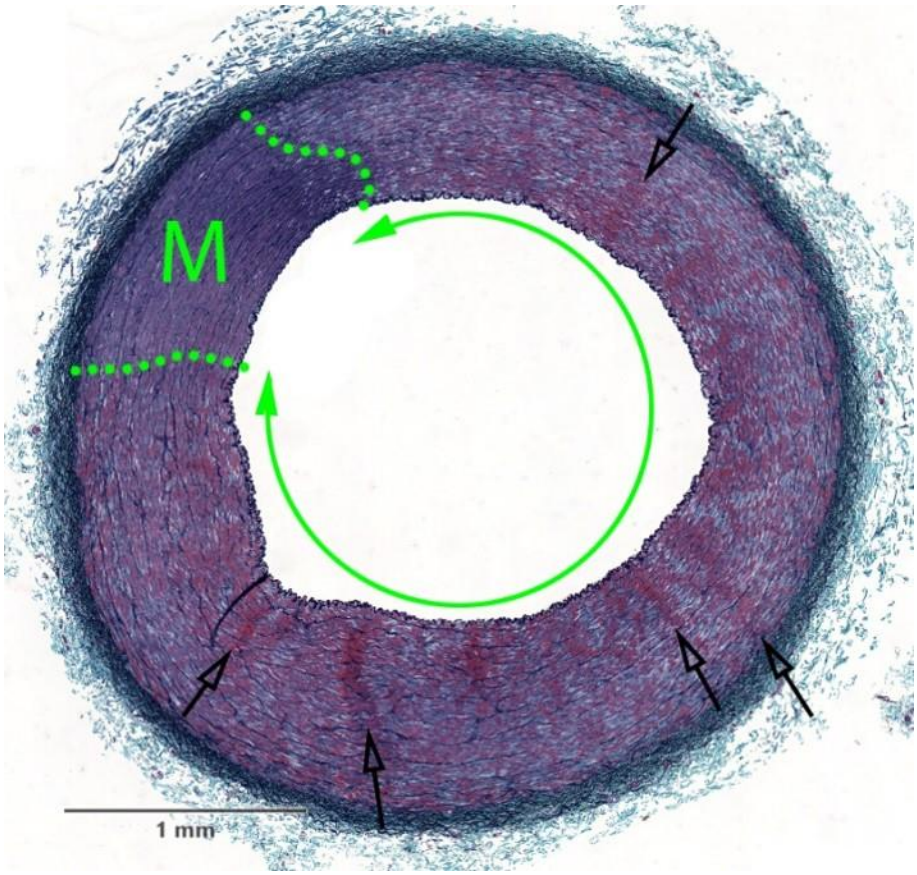

Figure 6.10 Segment 1P (GET). C6 (1720 nm – 200 J/cm2). Section showing widespread media necrosis (circular green double arrow) and a short segment of intact media (M, delineated by green dotted line). The clear arrows point to radial clusters of hyperchromatic and shrunken smooth muscle cells evoking contraction bands.

Twenty-six images of the 48 tissue segments are shown in the report with annotations and a description of any damage written by the pathologist (Appendix C). One of these images is shown for each light dosage condition as an example (Figure 6.4 - Figure 6.10), with the annotation from the pathologist edited for formatting consistency only. In other words, the substance of the annotations was not changed. Damage is present at the lowest conditions, including the control. Compressive necrosis, collagen

denaturization in the adventitia, and endothelial cell loss were present at all conditions. With increasing severity, hypereosinophilic smooth muscle cells, cell effacement, and necrotic/apoptotic cells were present in the tissue as the irradiation dosage increased. At the highest dosage at 1720 nm, compression bands were also present.

Table 6.5 Damage morphologies for endothelialization and media necrosis. The damage for endothelialization was significant for all conditions, which is common for all catheterization procedures. The media necrosis score showed increased severity as the light dosage was increased.

Condition Number	Wavelength [nm]	Fluence [J/cm^2]	Endothelialization	Media Necrosis
C0	None	0	4.0	0.7
C1	1064	8.3	4.0	1.1
C2		100	4.0	0.7
C3		700	4.0	1.4
C4	1720	8.3	4.0	0.5
C5		50	4.0	2.2
C6		200	4.0	3.3

The pathologist determined that damage was present in the tissue at clearly detectable levels for only two of the damage morphologies listed in Table 6.3: endothelialization and media necrosis. The average pathologist scores for each of these

damage morphologies are shown in Table 6.5. Endothelialization was scored at the highest possible severity (4.0) for every tissue condition. The scores for media necrosis ranged from 0.5 to 3.3.

Although some media necrosis was present at all conditions, the severity and extent of the damage increased at higher dosages. Media necrosis was determined by the pathologist to clearly exceed the baseline damage found in the controls for C5 and C6. Damage was also found to exceed the baseline damage threshold in the controls for C3, although it was noted that the damage was more equivocal (a trend) when compared with the negative controls.

The statistical analysis yielded similar results. For the 1720 nm wavelength, the Brown-Forsythe test indicated significant between group differences ($p < 0.001$). The post hoc test between the control and treatment groups indicated a significant difference between the control and C5 ($p = 0.0017$) and C6 ($p = 0.00027$), but not C4 ($p = 0.989$). At 1064 nm, the Brown-Forsythe test did not indicate significance between group differences ($p = 0.240$). The Games-Howell post hoc showed a p value of 0.198 between C0 and C3, indicating no significant difference.

6.4 Discussion

The pathologist identified endothelialization and media necrosis as the only two damage morphologies with a large enough severity to be caused by the treatment. Endothelialization was scored at the highest severity of 4.0 for each sample. This was expected. Catheterization regularly causes endothelialization due to the shear stress of

moving the catheter along the vessel wall. This is an effect of all surgical catheterization procedures and would heal after surgery. Thus, it does not present a safety concern that would inhibit the use of IVPA imaging in the clinic. The second damage morphology that was deemed significant was media necrosis. The necrosis was found in smooth muscle cells in the vessel media. The severity of necrosis increased as the irradiation dosage increased (Table 6.5). The pathologist observed a clear treatment effect at conditions C5 and C6 (1720 nm: 50 and 200 J/cm^2). A more equivocal treatment effect (trend) was also observed for condition C3 (1064 nm: 700 J/cm^2). The pathologist determined that all damage observed would be expected to heal, although it would take long time point (1-2 months) studies to prove this conclusively.

The results of the statistical tests were mostly consistent with this result. Significant differences in media necrosis compared to the control condition was clear for C5 ($p = 0.0017$) and C6 ($p = 0.00027$). However, a significant difference was not identified ($p = 0.240$) between the control and tissue irradiated at 1064 nm. At C3, the pathologist reported some damage, although he wrote in the report that the observation was somewhat equivocal (indicative of a trend) because of the level of background damage in the control tissue. The p value between C0 and C3 was 0.198. Given the low sample size (n for C3 = 5), a non-significant result could be a result of low power. Since this is a safety study meant to determine damage, type I errors are preferable to type II errors. Thus, for the remainder of the discussion it is assumed that increased media necrosis was identified for condition C3. However, future studies with higher power would be necessary to determine with higher certainty.

There were several limitations and assumptions that affect the interpretation of this study. First, the control groups had multiple sources of damage. These sources include catheterization (endothelialization and compressive trauma due to catheter bulk and rigidity), electrocauterization to clear tissue during surgery, the effects of tissue removal and handling, and cutting the tissues into segments after removal. In addition, the time length from tissue irradiation to tissue removal and fixation was only a few hours, meaning there was relatively little time for damage to manifest. All these factors made it more difficult for the pathologist to identify damage as having been caused by irradiation rather than from the procedure. Nonetheless, the pathologist was still able to draw conclusions. Second, the amount of time it took to deliver the dosage varied for each condition. The amount of time one location in the tissue was irradiated is equivalent to the total time it took to apply the dose multiplied by the quotient of the spot size of the laser on the tissue in the axial direction and the total length over which the dosage was applied. Both the total time length and the physical length over which the dosage was applied were recorded during the experiment. The spot size can be calculated using geometry. Assume that the length of the optical fiber in the axial direction or the artery is 0.6 mm. Also, the half angle of light exiting the optical fiber would be ~12 degrees, based on the NA of the optical fiber. Given a maximum artery radius of 2.5 mm measured during the experiment, the spot size was approximately 1.66 mm in the axial direction along the artery. Using these parameters, the amount of time it took to apply each dosage to a region of tissue for C1-C6 were approximately 1, 13, 89, 3, 19, and 76 seconds, respectively. Time periods of 20 seconds or less (C1, C2, C4, C5) would be unlikely to affect damage since it is not a significant time length for heat transfer.

However, it is possible that the level of damage at conditions C3 and C6 were underestimated due to the length of time it took to apply these dosages in tissue. Future work could address this, although it would require higher power lasers than any that have been currently reported for real-time IVPA imaging[55-57]. Third, although the vessel was isolated and flushed, it is likely that at least some residual blood was present in the blood vessel. This would have lowered the actual light dosage that reached the tissue. It should be noted that despite this our experiment would still overestimate damage, since vessel isolation and flushing would not be conducted during clinical IVPA imaging. The vessel would instead be filled with pure blood. Finally, during clinical IVPA imaging the blood would be flowing. This would exert a convective cooling effect on the blood vessel, potentially decreasing damage from heat.

These damage thresholds for media necrosis compare favorably with our previously published work on cells[183] that is described in the prior chapter. In those studies, some cell types first showed statistically significant loss of viability at 690 J/cm^2 when irradiated with light at 1064 nm. This is consistent with the results of this *in vivo* safety study, in which damage was detected at 1064 nm for dosages of 700 J/cm^2. The IVPA lipid imaging wavelength used in that study was 1197 nm. At this condition, cell death was first apparent for some cell types at 140 J/cm^2. In this study, damage was clear at 50 J/cm^2, but not at 8.3 J/cm^2. If you assume that the midpoint between these values is the true transition point for the damage, then you get a damage threshold near 30 J/cm^2. This is 4.7x smaller than the *in vitro* threshold of 140 J/cm^2. However, the absorption coefficient of water and vessel tissue is anywhere from 2-5x larger at 1720 nm than at 1197 nm[115, 198, 210], so a lower damage threshold at 1720 nm would be expected since

more heat would be absorbed given the same light dosage. These results are in good agreement considering the large differences between the *in vitro* and *in vivo* heat transfer environments.

It is also worth comparing these results to the ANSI Z136.1 guideline for the safe use of lasers. Although this standard applies to the skin and eyes, we can compare our results to the requirements for skin to determine if the results seem reasonable. The maximum permissible exposure (MPE) as defined by the standard varies for each wavelength depending on the time length of irradiation. For time lengths below 10 seconds, it is defined in terms of the fluence applied to the tissue. For time lengths above 10 seconds, it is defined in terms of the irradiance applied over that time. The actual fluence dosage applied in our experiments is already given for each condition in Table 6.1. The irradiance can be calculated by dividing the fluence at each dosage by the length of time it took to apply that dosage to a given region of tissue.

Table 6.6 A comparison of the MPE predicted by ANSI Z136.1 for skin to our experimental results on blood vessel tissue. Note that the ANSI Z136.1 standard defines the MPE as 10x smaller than the dosage that will cause damage 50% of the time (EC50). Thus, the MPE must be multiplied by 10 before comparing it to the applied dosage.

Condition	Wavelength [nm]	Experimentally Applied Fluence [J/cm^2]	Experimentally Applied Irradiance [W/cm^2]	MPE fluence [J/cm^2]	MPE irradiance [W/cm^2]	Expected Damage from MPE (Y/N)	Damage Found Experimentally (Y/N)
C1	1064	8.3	N/A	5.5	N/A	N	N
C2	1064	N/A	7.8	N/A	1	N	N
C3	1064	N/A	7.8	N/A	1	N	Y
C4	1720	8.3	N/A	1	N/A	N	N
C5	1720	N/A	2.6	N/A	0.1	Y	Y
C6	1720	N/A	2.6	N/A	0.1	Y	Y

A comparison of the experimentally applied fluence, experimentally applied irradiance, and the MPE for each condition are shown in Table 6.6. Table 6.6 also shows if the ANSI standard would predict damage for each condition. Remember from the prior chapter that the MPE has a safety factor of 10, so the MPE must be multiplied by 10 to determine where damage would first be detectable. The prediction of damage using the ANSI standard is compared to our experimental results, in which damage was identified by the pathologist. These results are all in agreement, except that our experiments identified damage at condition C3 that was not predicted based on the MPE. This underestimate of damage based on the MPE is not unexpected, since the standard applies to skin. The absorption coefficient of vessel tissue is higher than skin at both

wavelengths[115, 198, 210], so damage at lower dosages should be expected. Also, damage at condition C3 was considered by the pathologist to be more equivocal. The statistical test yielded no significance, albeit with low sample size. Nonetheless, these results substantiate that the ANSI standards for skin may not be adequate for determining if damage can be expected to vessel tissue.

Our experimental results indicate a damage threshold between 8.3 and 50 J/cm2 at 1720 nm. Assuming that the true threshold for damage is the average of these conditions, the transition point would be at 30 J/cm^2. Reducing by the safety factor of 10 gives an MPE near 3 J/cm^2 at 1720 nm. An IVPA imaging protocol that used 128 A-lines per frame, 0.1 mJ per pulse, and a 2 mm/s pullback in a 2 mm diameter (occluded) artery would be near this MPE, at 3.13 J/cm^2. Recent real-time *in vivo* studies have successfully imaged plaque lipid using imaging protocols that used equivalent or lower exposures[55-57]. This indicates that it will be possible to use IVPA imaging for lipid identification safely. It should also be noted that the true limits for safe IVPA imaging may be higher than the thresholds identified in this study if future work shows that the damage from irradiation found in this study would heal over time.

To the author's knowledge, this is the first experimental study to investigate the safety of IVPA imaging in depth *in vivo*. We found that damage to vessels from heat accumulation is unlikely to inhibit the use of IVPA imaging clinically due to safety concerns. However, the study could be improved in several ways. First, repeating the study but with termination of the swine at 3-7 days after irradiation would make it easier to differentiate between damage caused by catheterization and light irradiation. Second, conducting a study in which damage was evaluated 1-2 months after irradiation would

make it possible to determine if the vessels would heal from the type of damage found in our histological specimens. It should be noted, however, that such a study would involve some practical difficulties. We found during the course of the imaging studies that it is difficult to completely flush blood from the artery in a survival surgery, because methods of isolating the vessel will still allow some blood to flow in over time. During a terminal surgery, this can be dealt with by flushing large volumes of water. However, the amount of liquid that can be injected into the swine during survival is limited. Besides attenuating the light, static blood in the vessel could coagulate which would absorb almost all the light emitted from the catheter and potentially prove fatal to the pig after the surgery. Finally, this study did not examine the effect of irradiation on blood. Future studies would be needed to assess the effect of these irradiation dosages on blood cells and any consequent increase in thrombogenicity.

6.5 Conclusions

To the author's knowledge, this is the first study designed to evaluate the safety of IVPA *in vivo*. The damage to blood vessel tissue from real-time *in vivo* delivery of light was investigated in the carotid arteries of swine. Damage was assessed at 1064 nm and the lipid imaging wavelength of 1720 nm in a dose dependent manner. Damage was assessed by a trained pathologist. The pathologist determined that the only dose dependent type of damage in the tissue was media necrosis. There was clear damage to the tissue when subjected to 50 J/cm^2 at 1720 nm. There was also damage at 700 J/cm^2 when 1064 nm light was used, although the pathologist stated the damage was more equivocal when compared to the controls. An MPE defined by the damage results at

1720 nm could be met with an imaging protocol using 128 A-lines, 0.1 mJ per pulse, and a pullback rate of 2 mm/s in a 2 mm diameter occluded artery. Prior studies have already shown that lipid plaque can be imaged using similar or lesser dosages. Moreover, in the opinion of the pathologist, the damage that was detected at the higher dosages would be expected to heal, although additional studies will be needed to prove this conclusively. The results were consistent with the *in vitro* studies discussed in the prior chapter. We found that the ANSI Z136.1 standard for skin underestimates the damage compared to our experimental results. We conclude that this standard may not be appropriate for vessel tissue. Future work should evaluate the progression of damage over longer time points (1-2 months) and evaluate any potential increase in blood thrombogenicity. Regardless, these studies suggest that it will be possible to use IVPA imaging to identify lipid in plaque in a clinical setting without damaging the vessel tissue.

APPENDIX A: Fluence versus Depth for all Monte Carlo Simulations

Summary: This appendix contains the fluence as a function of depth along the center of the imaging plane (raw data) for all simulations conducted in Chapter 2.

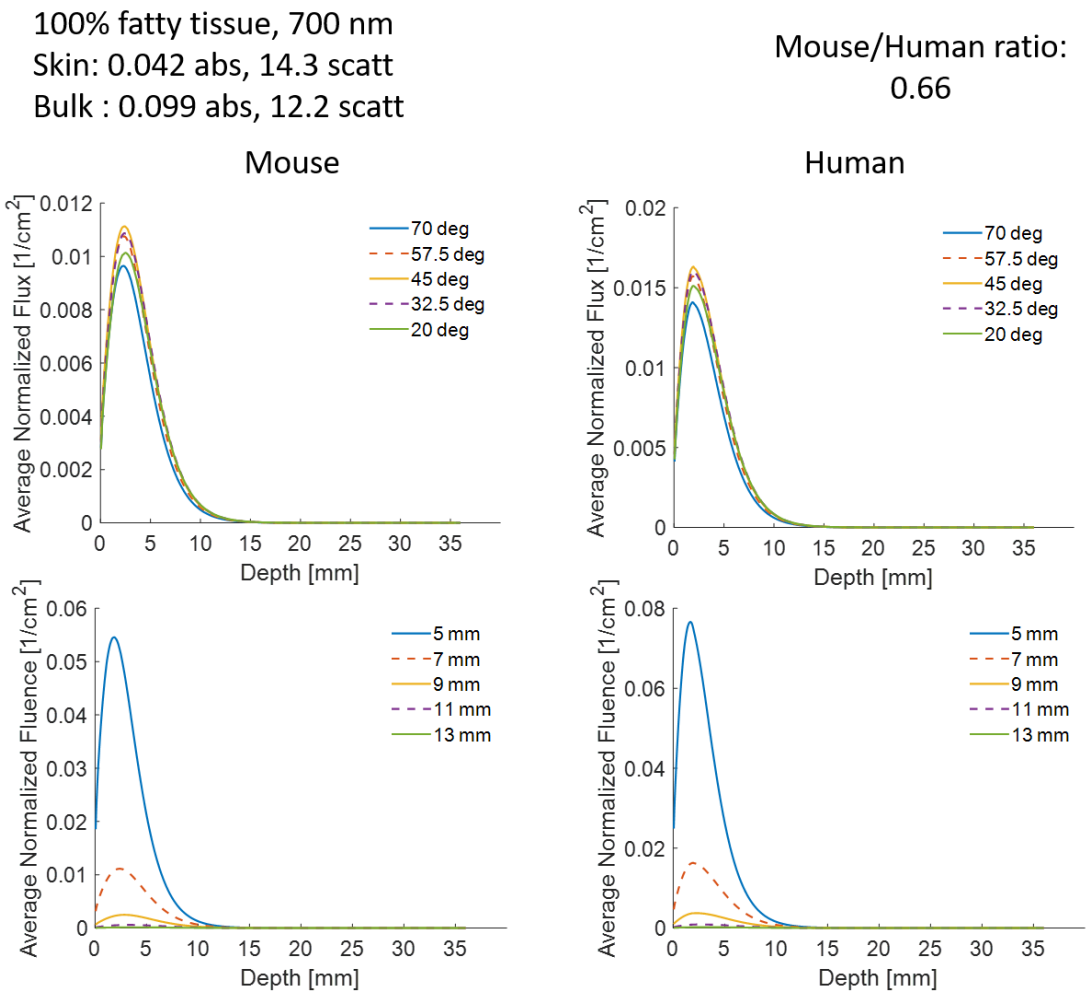

Figure_Apx A-1 Simulation results using 100% fatty tissue with light at 700 nm. The plots show the fluence versus depth at the center of the imaging plane for mice (left) and humas (right). The two plots on top show simulations at multiple optical fiber angles and the distance held constant at 7.5 mm, while the bottom two plots show simulations conducted at multiple fiber bundle to imaging plane distances and angle held constant at 45 degrees. The optical properties of the skin and bulk tissue as well as the ratio of maximum fluence between simulations conducted with mice skin thickness and human skin thickness are shown at the top.

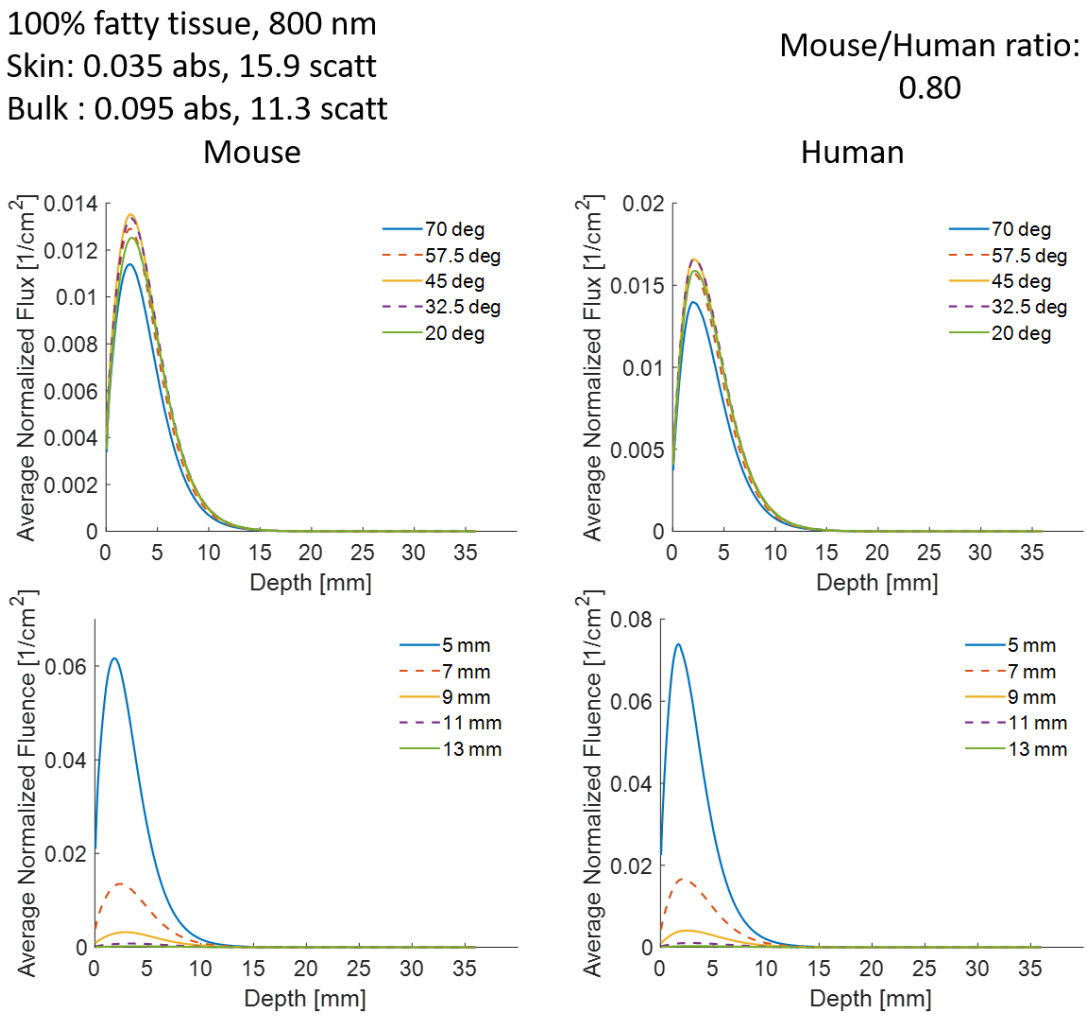

Figure_Apx A-2 Simulation results using 100% fatty tissue with light at 800 nm. The plots show the fluence versus depth at the center of the imaging plane for mice (left) and humas (right). The two plots on top show simulations at multiple optical fiber angles and the distance held constant at 7.5 mm, while the bottom two plots show simulations conducted at multiple fiber bundle to imaging plane distances and angle held constant at 45 degrees. The optical properties of the skin and bulk tissue as well as the ratio of maximum fluence between simulations conducted with mice skin thickness and human skin thickness are shown at the top.

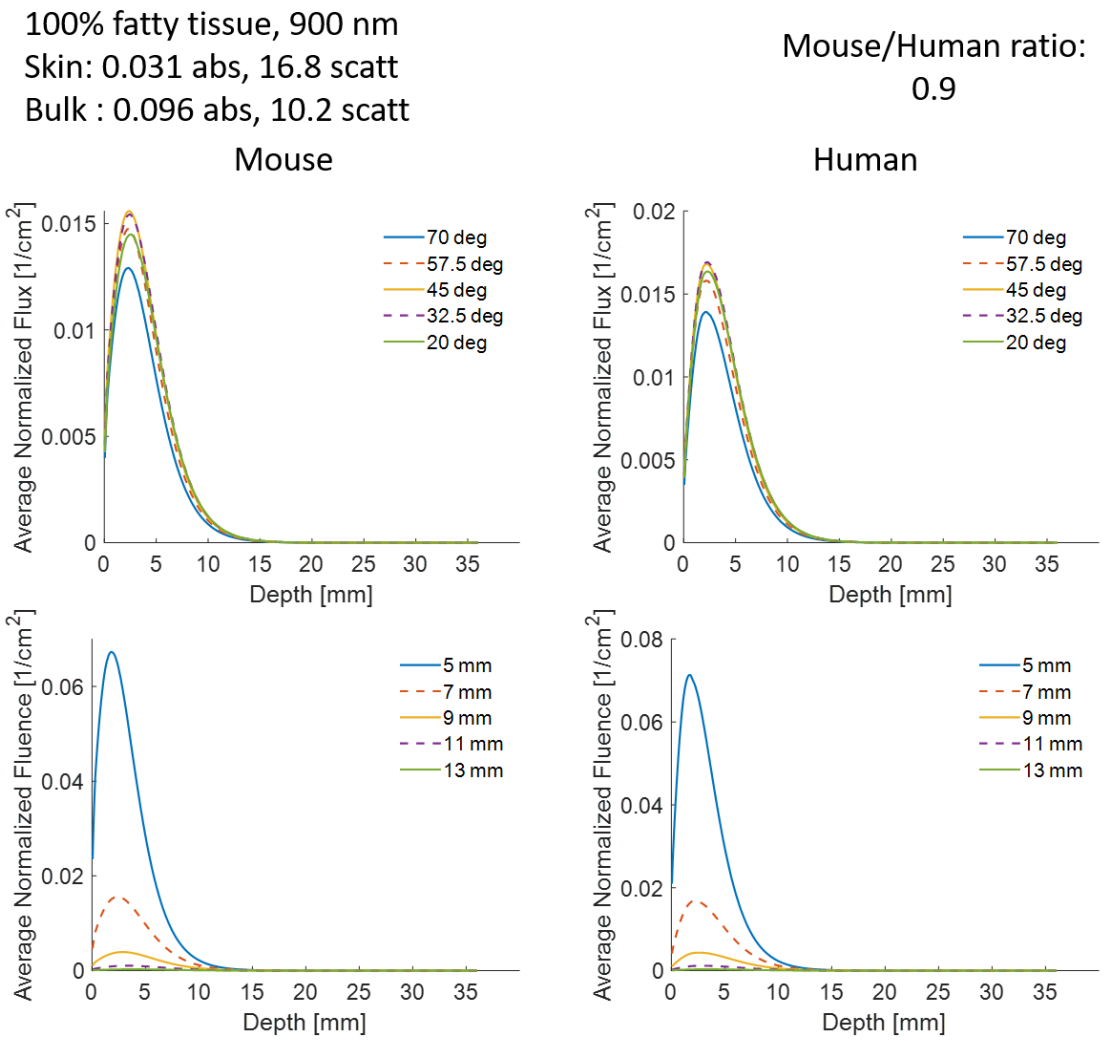

Figure_Apx A-3 Simulation results using 100% fatty tissue with light at 900 nm. The plots show the fluence versus depth at the center of the imaging plane for mice (left) and humas (right). The two plots on top show simulations at multiple optical fiber angles and the distance held constant at 7.5 mm, while the bottom two plots show simulations conducted at multiple fiber bundle to imaging plane distances and angle held constant at 45 degrees. The optical properties of the skin and bulk tissue as well as the ratio of maximum fluence between simulations conducted with mice skin thickness and human skin thickness are shown at the top.

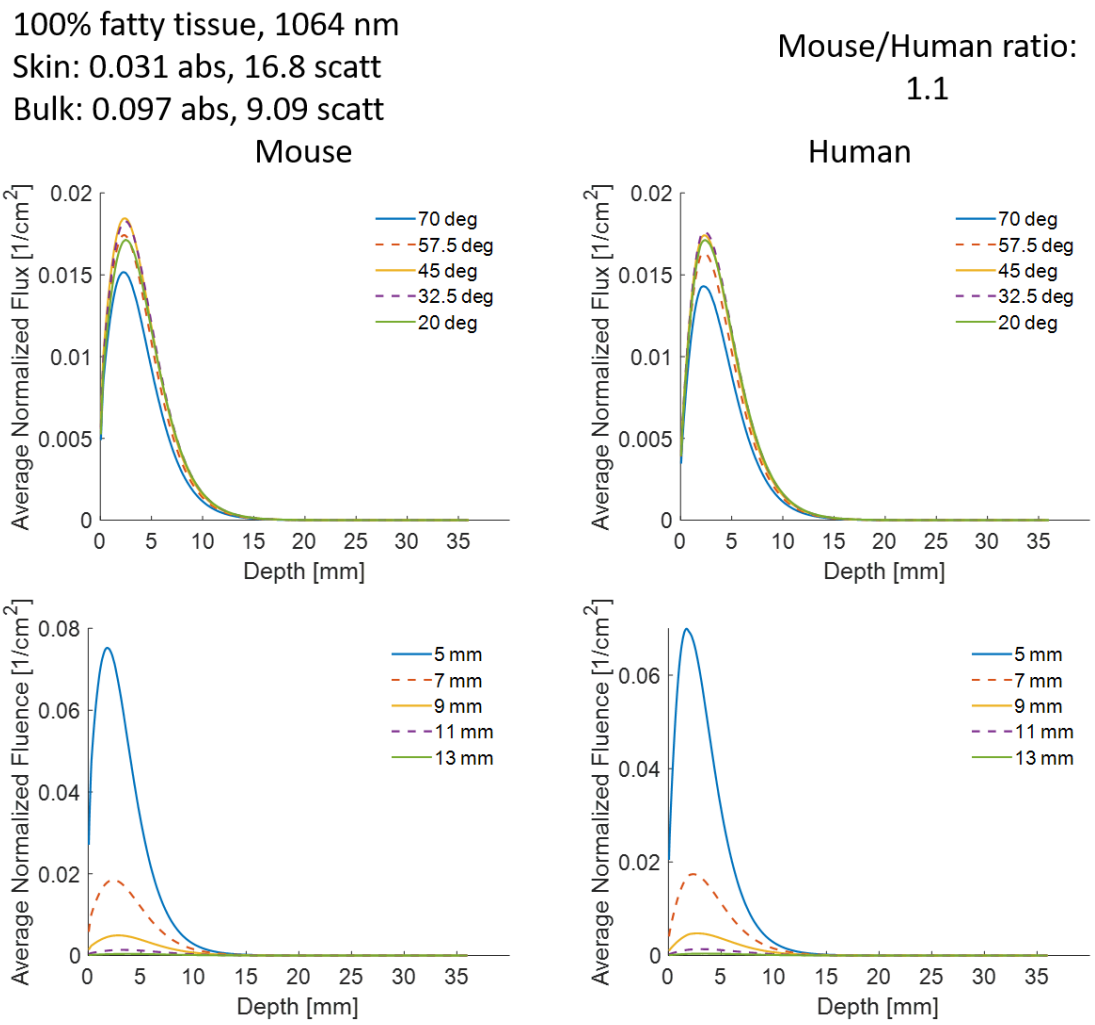

Figure_Apx A-4 Simulation results using 100% fatty tissue with light at1064 nm. The plots show the fluence versus depth at the center of the imaging plane for mice (left) and humas (right). The two plots on top show simulations at multiple optical fiber angles and the distance held constant at 7.5 mm, while the bottom two plots show simulations conducted at multiple fiber bundle to imaging plane distances and angle held constant at 45 degrees. The optical properties of the skin and bulk tissue as well as the ratio of maximum fluence between simulations conducted with mice skin thickness and human skin thickness are shown at the top.

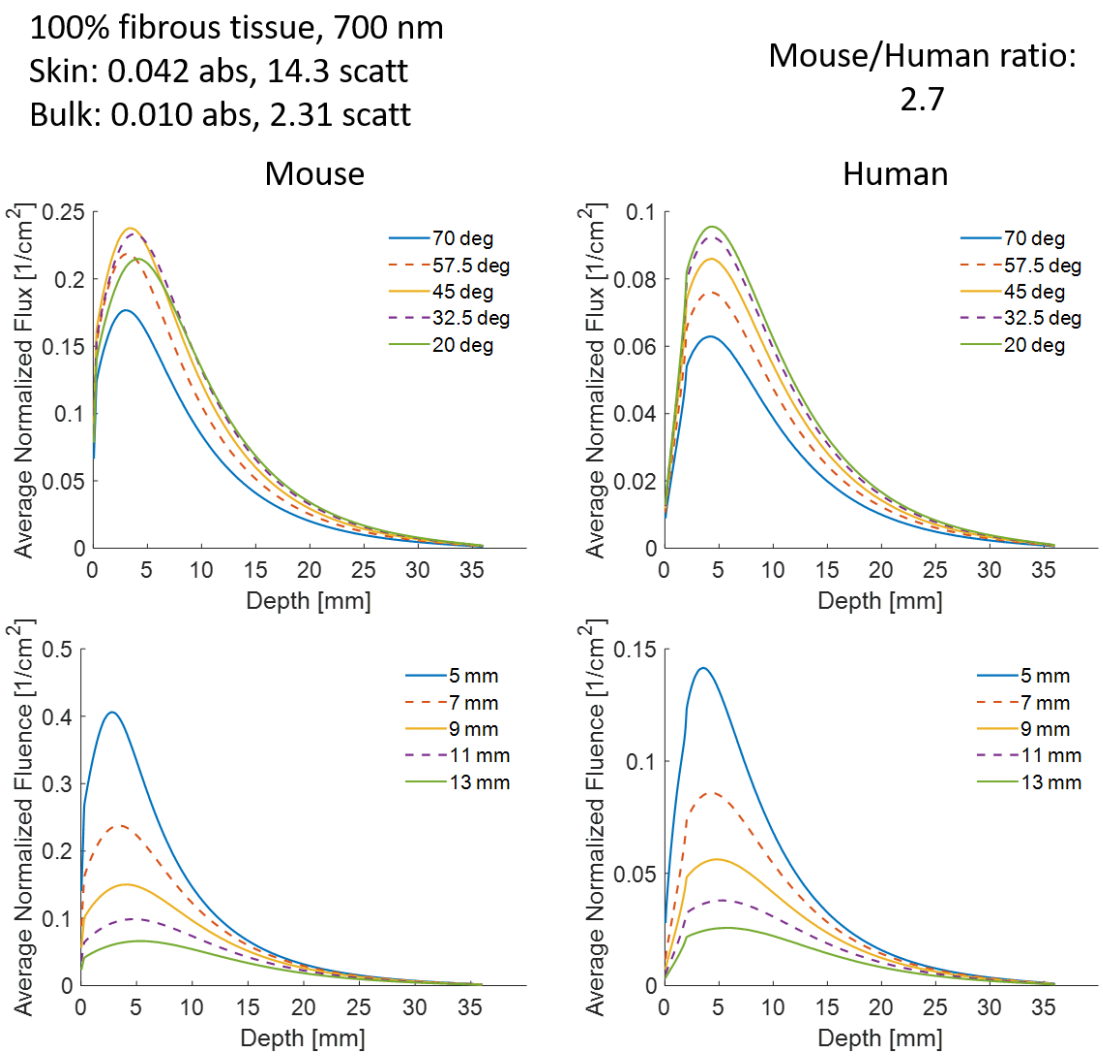

Figure_Apx A-5 Simulation results using 100% fibrous tissue with light at 700 nm. The plots show the fluence versus depth at the center of the imaging plane for mice (left) and humas (right). The two plots on top show simulations at multiple optical fiber angles and the distance held constant at 7.5 mm, while the bottom two plots show simulations conducted at multiple fiber bundle to imaging plane distances and angle held constant at 45 degrees. The optical properties of the skin and bulk tissue as well as the ratio of maximum fluence between simulations conducted with mice skin thickness and human skin thickness are shown at the top.

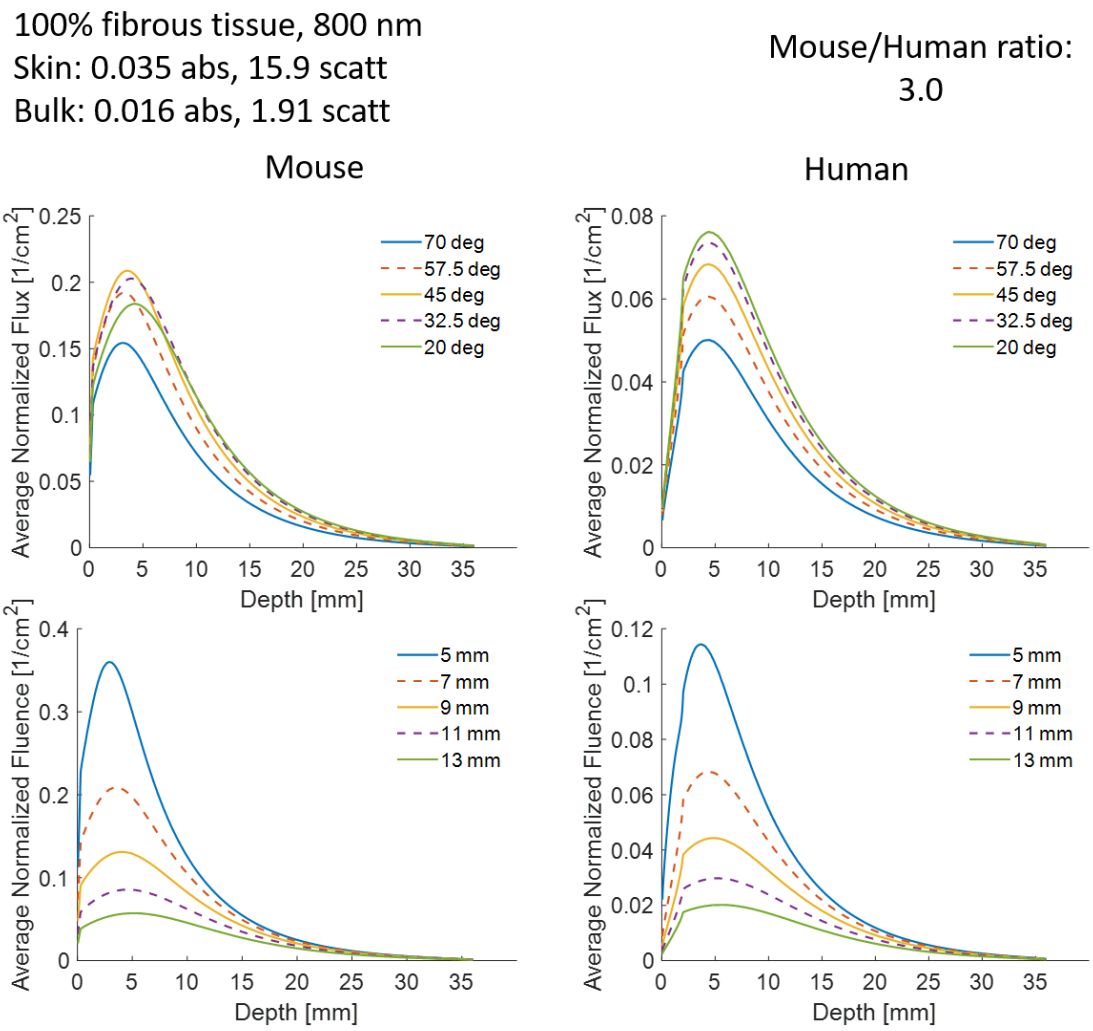

Figure_Apx A-6 Simulation results using 100% fibrous tissue with light at 800 nm. The plots show the fluence versus depth at the center of the imaging plane for mice (left) and humas (right). The two plots on top show simulations at multiple optical fiber angles and the distance held constant at 7.5 mm, while the bottom two plots show simulations conducted at multiple fiber bundle to imaging plane distances and angle held constant at 45 degrees. The optical properties of the skin and bulk tissue as well as the ratio of maximum fluence between simulations conducted with mice skin thickness and human skin thickness are shown at the top.

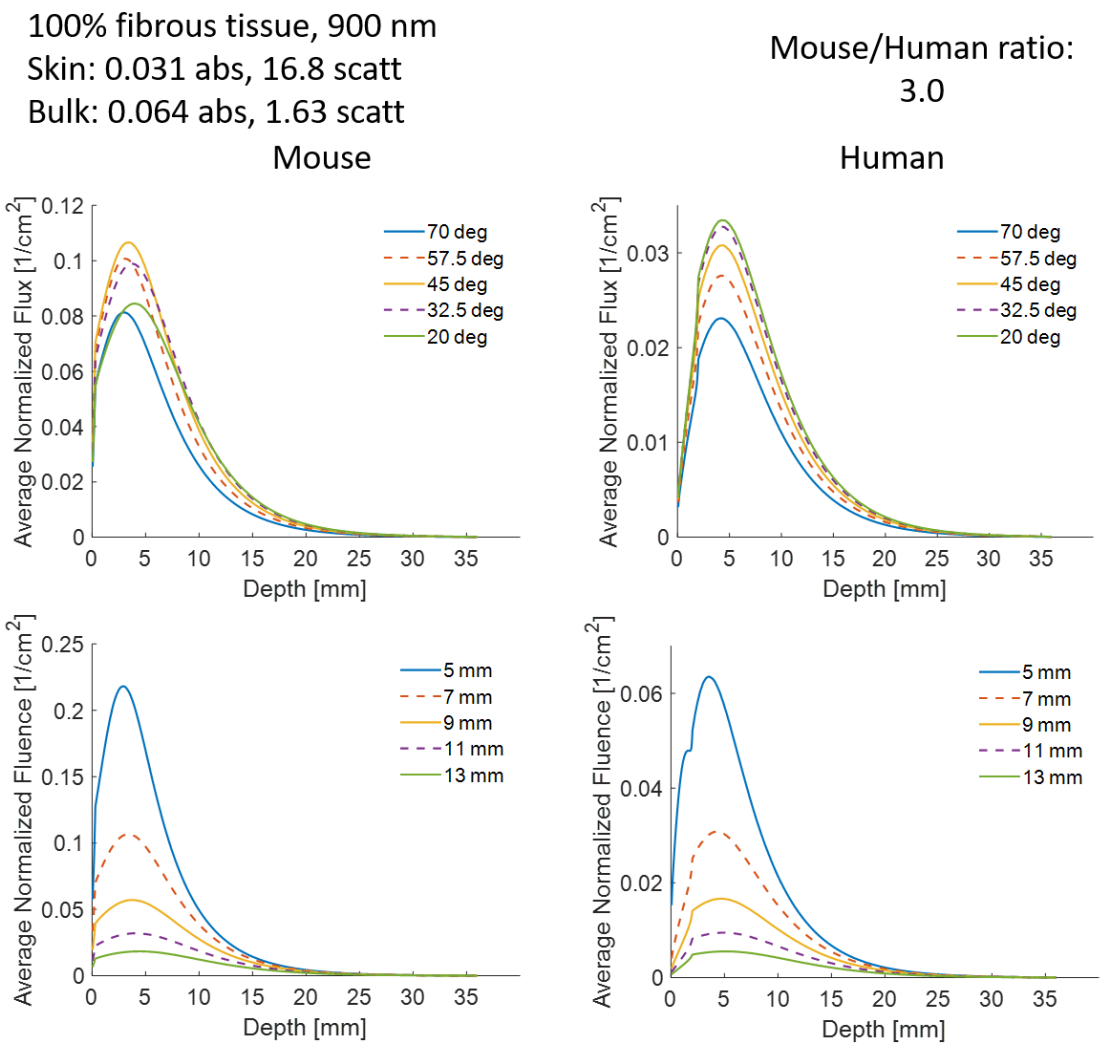

Figure_Apx A-7 Simulation results using 100% fibrous tissue with light at 900 nm. The plots show the fluence versus depth at the center of the imaging plane for mice (left) and humas (right). The two plots on top show simulations at multiple optical fiber angles and the distance held constant at 7.5 mm, while the bottom two plots show simulations conducted at multiple fiber bundle to imaging plane distances and angle held constant at 45 degrees. The optical properties of the skin and bulk tissue as well as the ratio of maximum fluence between simulations conducted with mice skin thickness and human skin thickness are shown at the top.

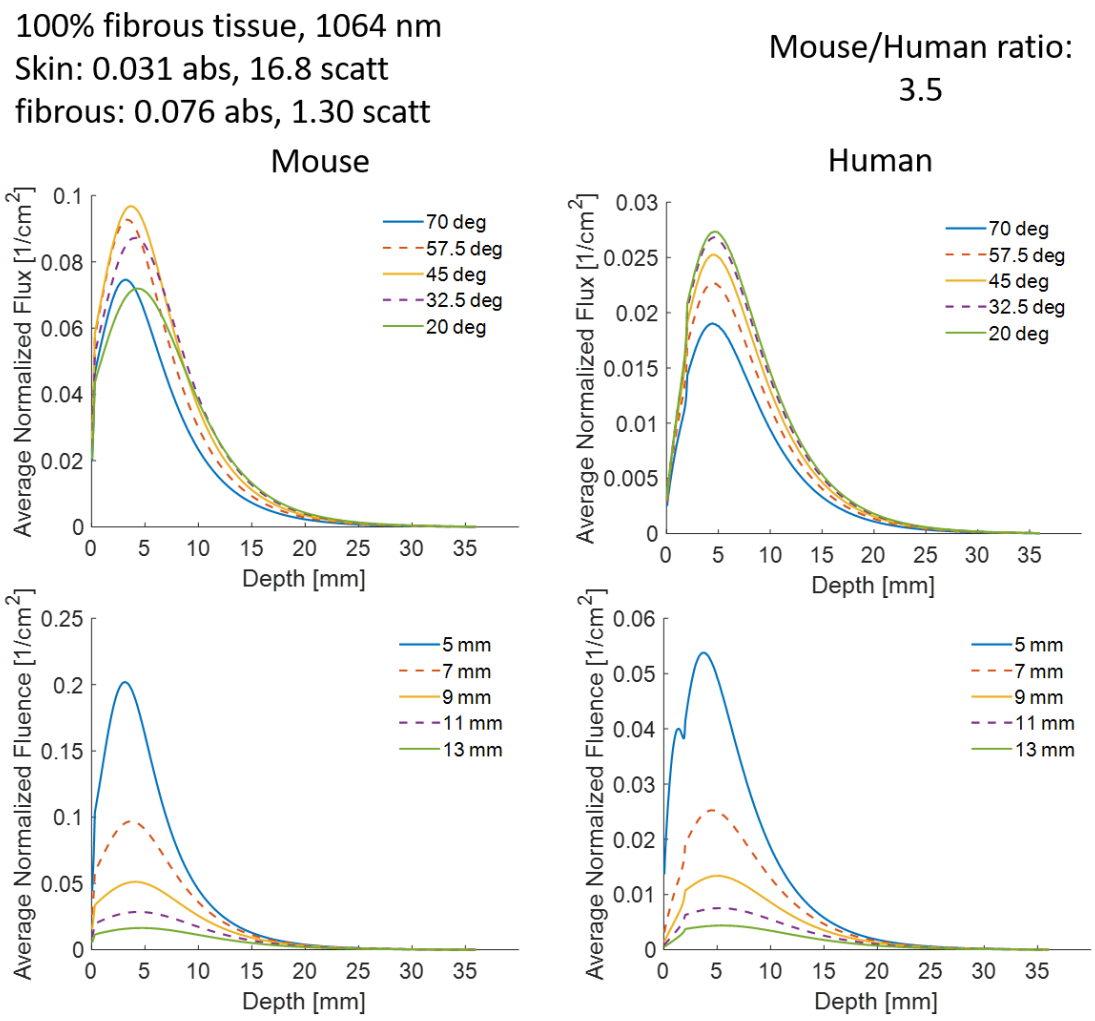

Figure_Apx A-8 Simulation results using 100% fibrous tissue with light at 1064 nm. The plots show the fluence versus depth at the center of the imaging plane for mice (left) and humas (right). The two plots on top show simulations at multiple optical fiber angles and the distance held constant at 7.5 mm, while the bottom two plots show simulations conducted at multiple fiber bundle to imaging plane distances and angle held constant at 45 degrees. The optical properties of the skin and bulk tissue as well as the ratio of maximum fluence between simulations conducted with mice skin thickness and human skin thickness are shown at the top.

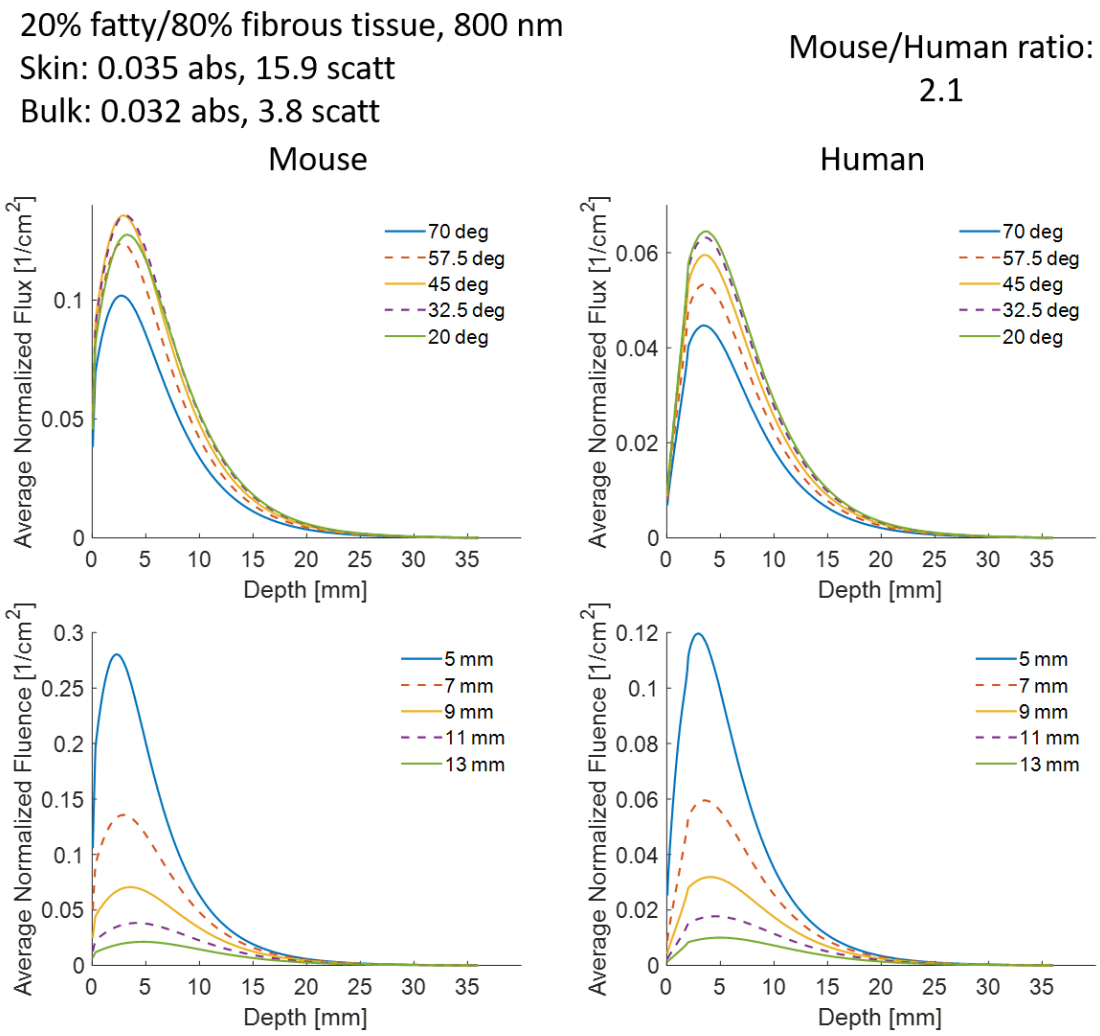

Figure_Apx A-9 Simulation results using 20% fatty and 80% fibrous tissue with light at 800 nm. The plots show the fluence versus depth at the center of the imaging plane for mice (left) and humas (right). The two plots on top show simulations at multiple optical fiber angles and the distance held constant at 7.5 mm, while the bottom two plots show simulations conducted at multiple fiber bundle to imaging plane distances and angle held constant at 45 degrees. The optical properties of the skin and bulk tissue as well as the ratio of maximum fluence between simulations conducted with mice skin thickness and human skin thickness are shown at the top.

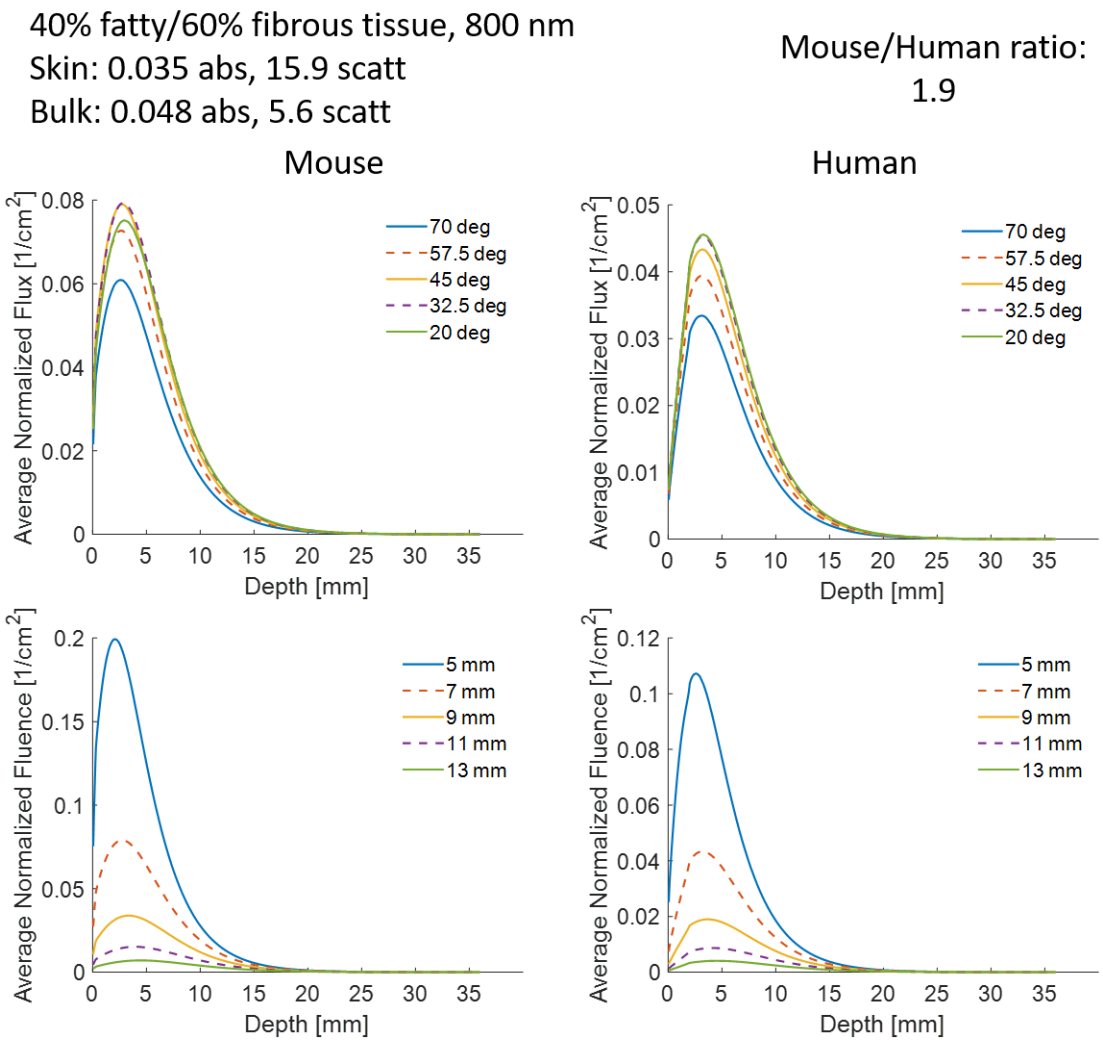

Figure_Apx A-10 Simulation results using 40% fatty and 60% fibrous tissue with light at 800 nm. The plots show the fluence versus depth at the center of the imaging plane for mice (left) and humas (right). The two plots on top show simulations at multiple optical fiber angles and the distance held constant at 7.5 mm, while the bottom two plots show simulations conducted at multiple fiber bundle to imaging plane distances and angle held constant at 45 degrees. The optical properties of the skin and bulk tissue as well as the ratio of maximum fluence between simulations conducted with mice skin thickness and human skin thickness are shown at the top.

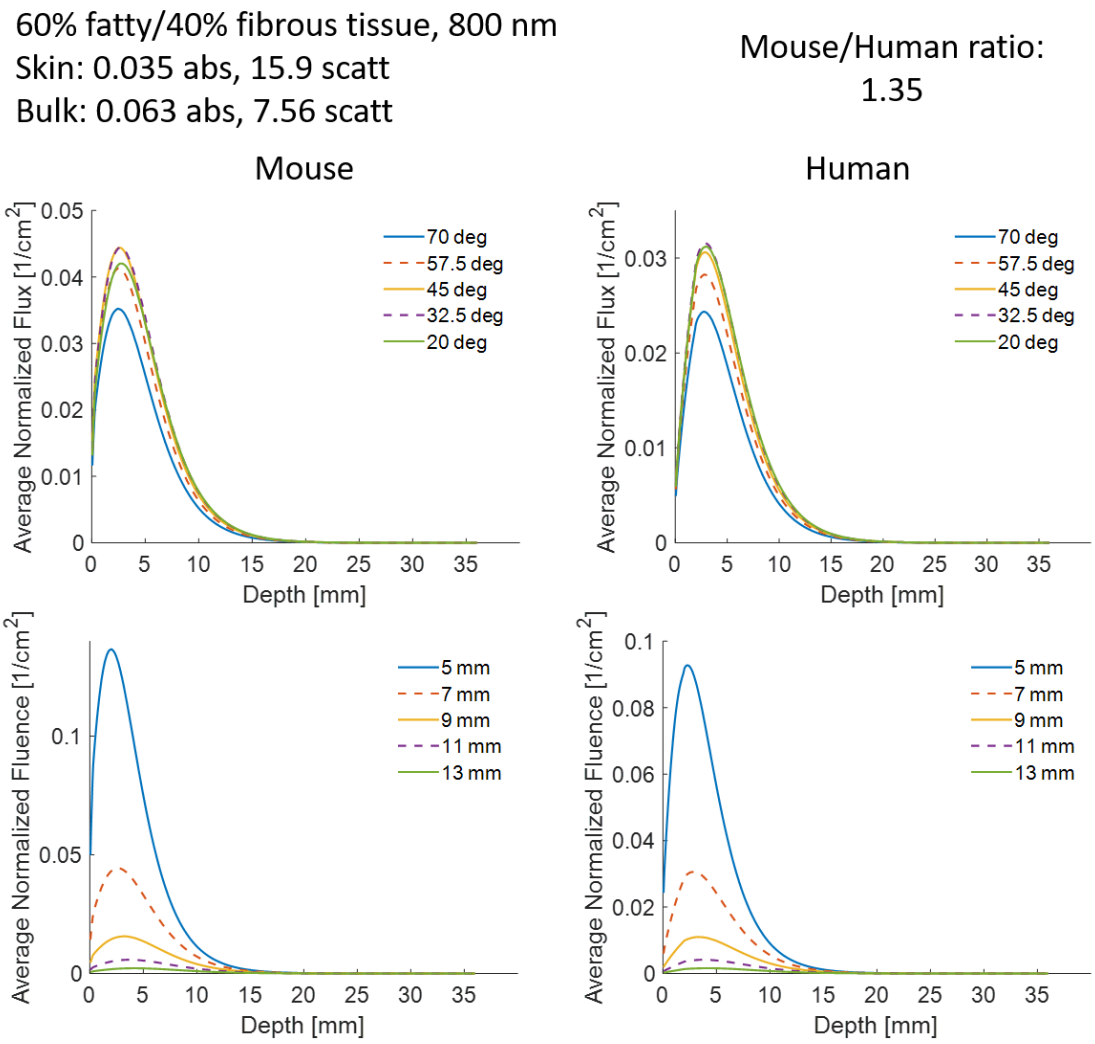

Figure_Apx A-11 Simulation results using 60% fatty and 40% fibrous tissue with light at 800 nm. The plots show the fluence versus depth at the center of the imaging plane for mice (left) and humas (right). The two plots on top show simulations at multiple optical fiber angles and the distance held constant at 7.5 mm, while the bottom two plots show simulations conducted at multiple fiber bundle to imaging plane distances and angle held constant at 45 degrees. The optical properties of the skin and bulk tissue as well as the ratio of maximum fluence between simulations conducted with mice skin thickness and human skin thickness are shown at the top.

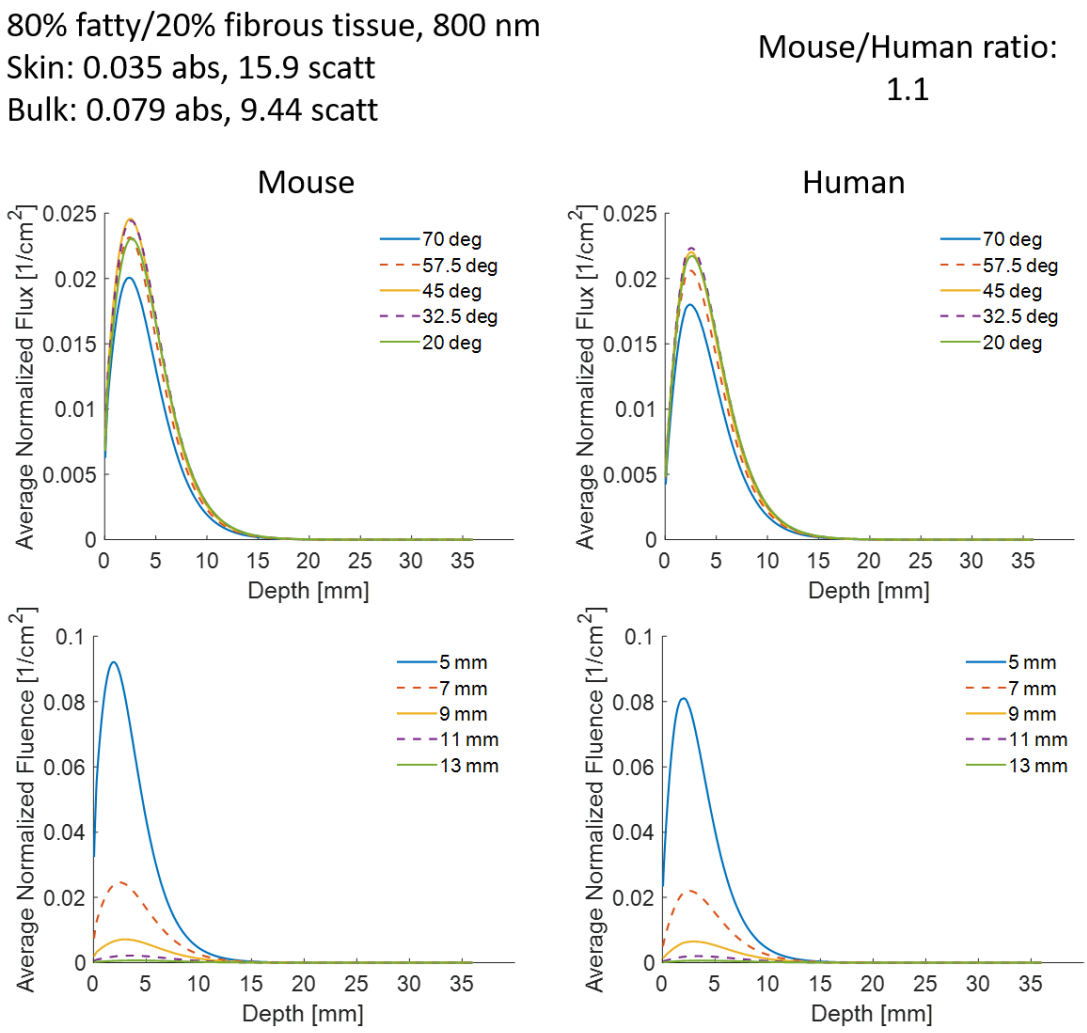

Figure_Apx A-12 Simulation results using 80% fatty and 20% fibrous tissue with light at 800 nm. The plots show the fluence versus depth at the center of the imaging plane for mice (left) and humas (right). The two plots on top show simulations at multiple optical fiber angles and the distance held constant at 7.5 mm, while the bottom two plots show simulations conducted at multiple fiber bundle to imaging plane distances and angle held constant at 45 degrees. The optical properties of the skin and bulk tissue as well as the ratio of maximum fluence between simulations conducted with mice skin thickness and human skin thickness are shown at the top.

APPENDIX B: Effective Attenuation coefficient versus position for multiple tissue combinations for all 4 wavelengths (700, 800, 900, 1064 nm) simulated.

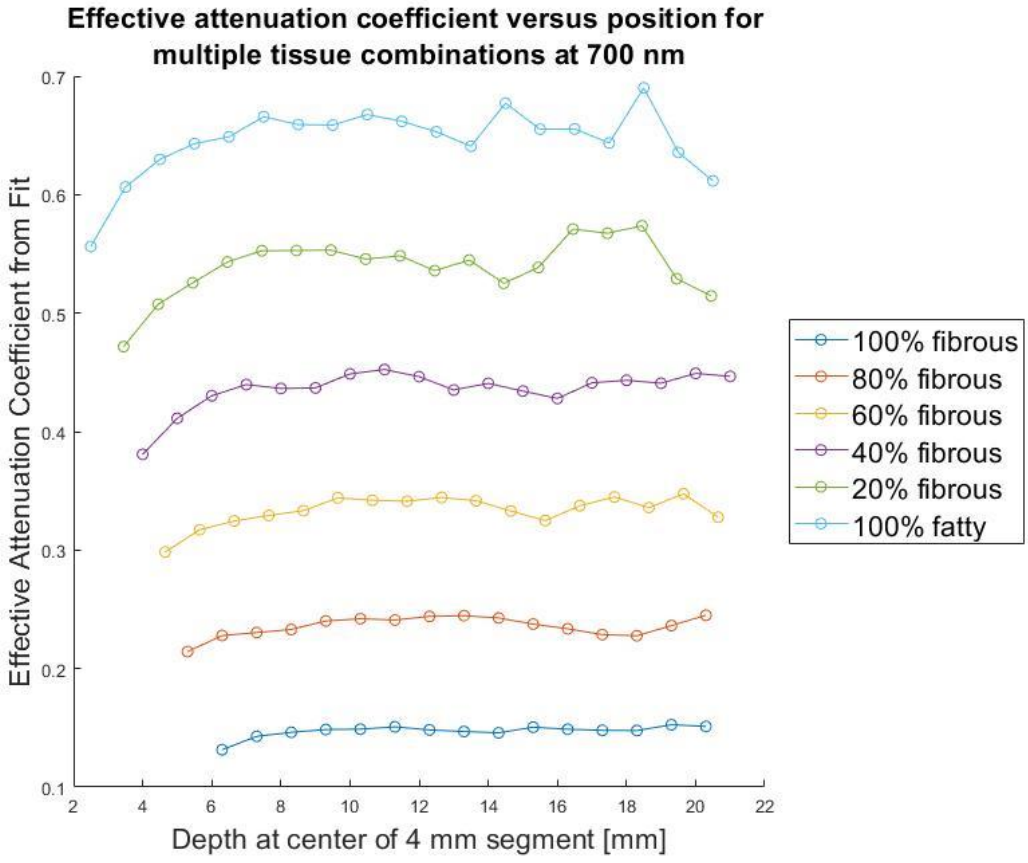

Figure_Apx B-1 Plot of the effective attenuation coefficient as a function of the depth at which the exponential fit was applied for fluence versus depth in simulations conducted at 700 nm for various tissue compositions. The fit was applied over 4 mm segments in increments of 1 mm. The depth at which the fit is the true rate of decay occurs once the effective attenuation coefficient becomes roughly constant, usually 4-5 data points from the left. The variation in the effective attenuation seen at the right is due to probabilistic variation in the simulation results, which arises from the small number of photons reaching deep into the tissue.

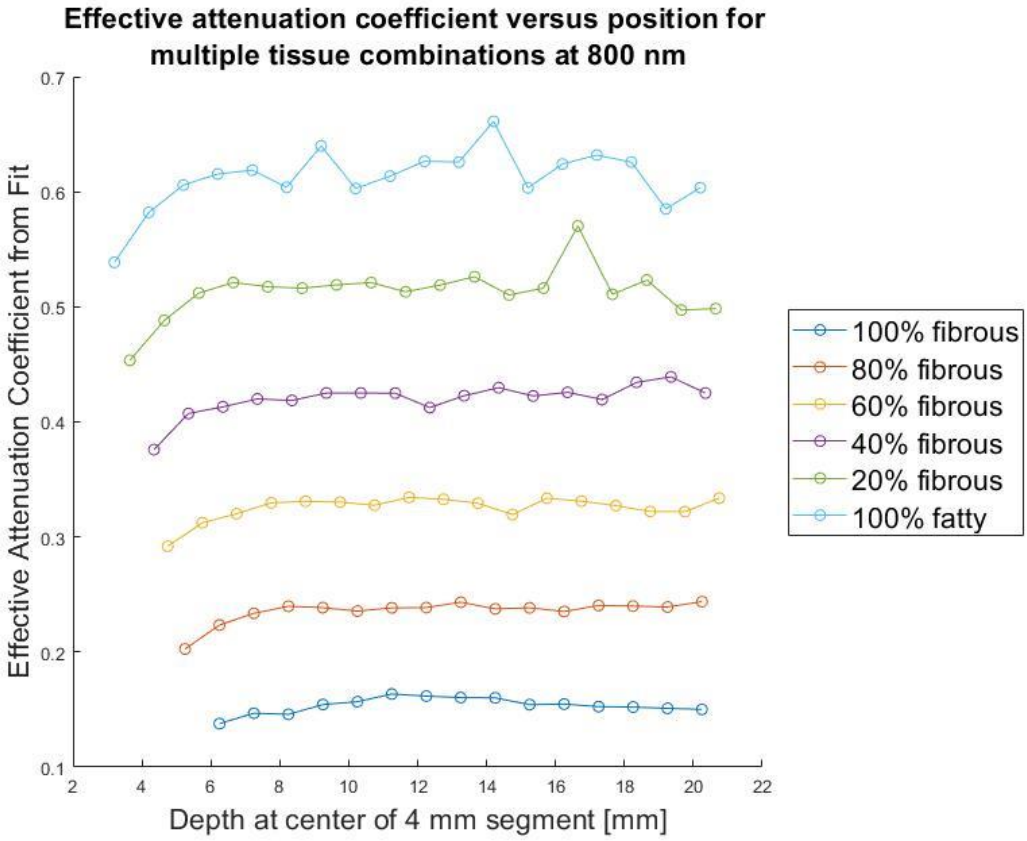

Figure_Apx B-2 Plot of the effective attenuation coefficient as a function of the depth at which the exponential fit was applied for fluence versus depth in simulations conducted at 800 nm for various tissue compositions. The fit was applied over 4 mm segments in increments of 1 mm. The depth at which the fit is the true rate of decay occurs once the effective attenuation coefficient becomes roughly constant, usually 4-5 data points from the left. The variation in the effective attenuation seen at the right is due to probabilistic variation in the simulation results, which arises from the small number of photons reaching deep into the tissue.

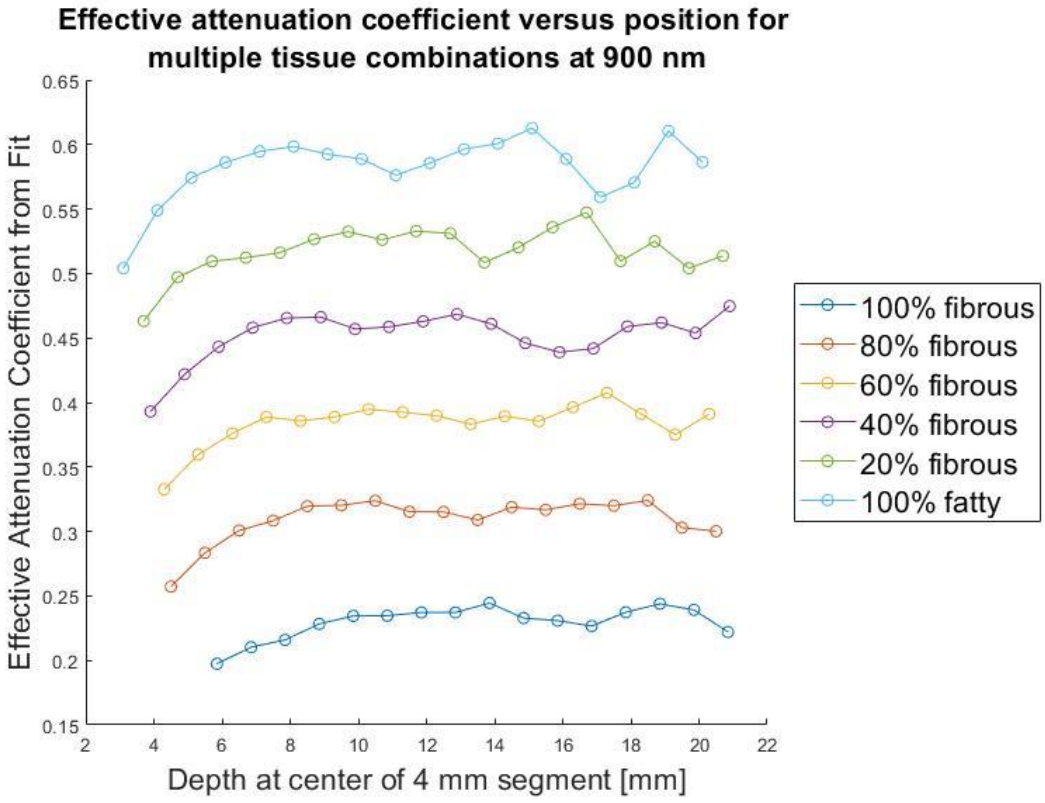

Figure_Apx B-3 Plot of the effective attenuation coefficient as a function of the depth at which the exponential fit was applied for fluence versus depth in simulations conducted at 900 nm for various tissue compositions. The fit was applied over 4 mm segments in increments of 1 mm. The depth at which the fit is the true rate of decay occurs once the effective attenuation coefficient becomes roughly constant, usually 4-5 data points from the left. The variation in the effective attenuation seen at the right is due to probabilistic variation in the simulation results, which arises from the small number of photons reaching deep into the tissue.

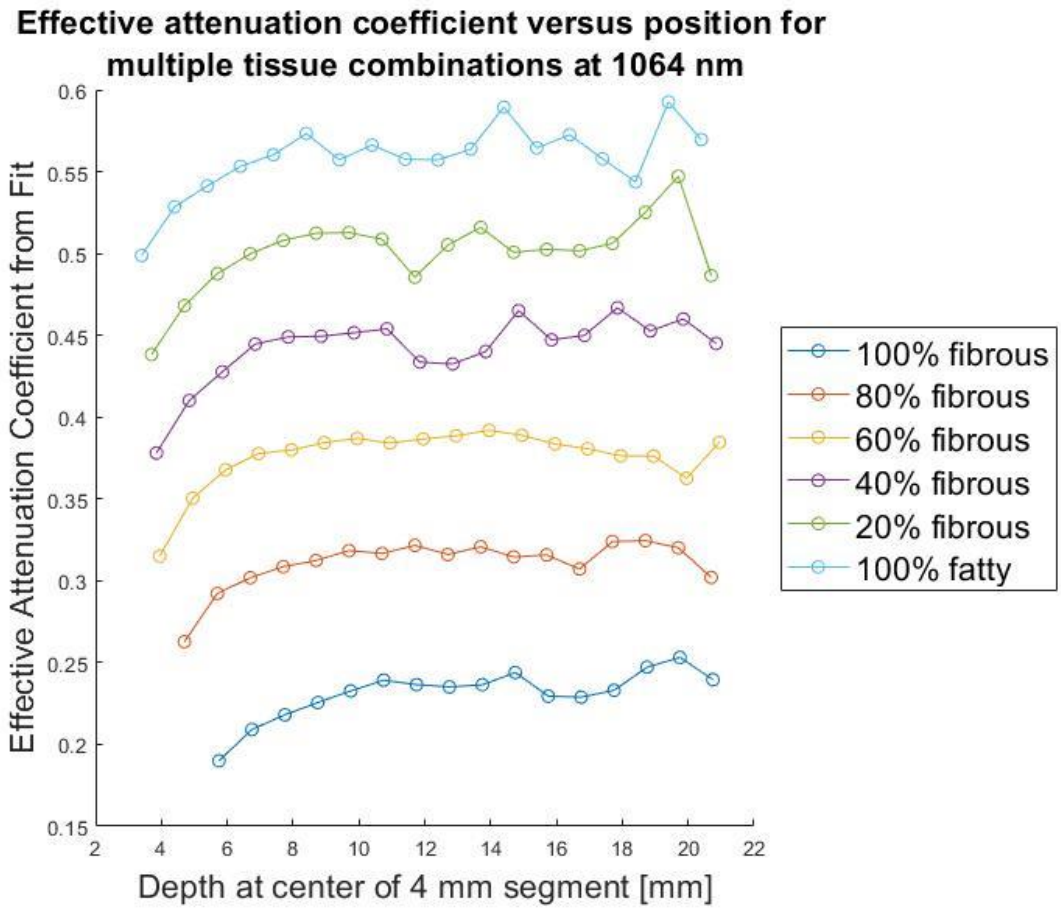

Figure_Apx B-4 Plot of the effective attenuation coefficient as a function of the depth at which the exponential fit was applied for fluence versus depth in simulations conducted at 1064 nm for various tissue compositions. The fit was applied over 4 mm segments in increments of 1 mm. The depth at which the fit is the true rate of decay occurs once the effective attenuation coefficient becomes roughly constant, usually 4-5 data points from the left. The variation in the effective attenuation seen at the right is due to probabilistic variation in the simulation results, which arises from the small number of photons reaching deep into the tissue.

APPENDIX C: Pathology Report

The following is a copy of the pathology report, emailed to us by Alizee Pathology on August 7th, 2020. The formatting has been changed to fit the requirements of this dissertation, but no content was altered.

Alizée Pathology, LLC	Executive Summary Pathology Report
Alizée Project Number	HJC19-339
Study Title	Safety Evaluation of Swine Carotid Arteries Subjected to Intravascular Photoacoustic Imaging (IVPA) at Varying Power
Histopathology Site	Alizée Pathology, LLC (Alizée) [a StageBio Company] 20 Frederick Road Thurmont, MD 21788
Prepared for	Georgia Institute of Technology 793 Marietta Street Atlanta, GA 30318
Date	8/7/2020

Objective

The objective of this study was to histologically evaluate the local response of Intravascular Photoacoustic Imaging (IVPA) on swine carotid arteries.

Methods

The histology and pathology portions of Alizée Project Number HJC13-339 conducted at Alizée Pathology were neither intended nor required to be in compliance with United States Food and Drug Administration GLP regulations set forth in Title 21 Code of Federal Regulations (CFR) Part 58. As such, quality assurance inspections and oversight were not performed. However, all study conduct performed at Alizée was completed in accordance with the technical memo, study protocol, Alizée Standard Operating Procedures (SOP) and sound scientific judgment. The results from analysis provided in this report have undergone a thorough quality control review. In addition to the hard copy, an electronic copy of this report in portable document format (PDF) will be provided to Georgia Institute of Technology. The PDF is a representation of the pathology report hard copy; however, only the signed hard copy of the pathology report is considered raw data. Digital images appearing in this report are for illustrative purposes only. All pathologic diagnoses were derived from the original histological preparations.

This pathology executive summary report by Alizée presents the results of microscopic assessment of a total of forty eight (48) carotid artery segments (16 segments per artery)

from swine when treated with laser irradiation at several dosages for Georgia Institute of Technology, Atlanta, GA. This study, including all surgical procedures and tissue harvests, was conducted at the Georgia Institute of Technology, under the direction of Tim Sowers. Histological processing was performed at Alizée Pathology, Thurmont, MD. Resulting slides were evaluated, in a manner blinded to treatment, via light microscopy at Alizée by Serge D. Rousselle, DVM, DACVP, Study Pathologist.

According to the protocol and client communication, a total of 3 carotid arteries from swine were assigned to this study, in which there were seven total conditions (treatments). These consisted of two wavelengths of laser light (1064 nm and 1720 nm) with 3 different dosages of light at each wavelength, as well a negative control which was not irradiated with any light. The wavelength number and light dosage (fluence) are given for each condition, as shown in **Table A**. After laser irradiation at several dosages, each artery was dissected into sixteen segments and placed in containers filled with 10% neutral buffered formalin. All collected samples were sent to Alizée for histology and microscopic evaluation.

A total of sixteen (16) segments each from 3 carotid arteries (Artery 1, Artery 2 and Artery 3, respectively) were received at Alizée, fixed in 10% neutral buffered formalin. Samples were received in good condition, defined as all seals intact with no damage to containers or shipment. Histology sample totals and treatment assignment are presented in **Table A**.

Table_Apx C-1 Condition and Sample Correlation

Condition Number	Wavelength [nm]	Fluence [J/cm^2]	Sample Numbers
C0 (negative control)	None	0	1A, 1B, 1C, 1D, 2A, 2B, 2P, 3A, 3B
C1	1064	8.3	1E*, 1F*, 1G, 1H, 2C, 2D, 2E, 2F, 2G
C2	1064	100	1I, 1J, 2H, 2I, 2J, 2K, 2L
C3	1064	700	1K, 1L, 2M, 2N, 2O
C4	1720	8.3	1M, 3C, 3D, 3E
C5	1720	50	1N, 1O, 3F, 3G, 3H, 3I, 3J, 3K, 3L, 3M
C6	1720	200	1P, 3N, 3O, 3P

* = Treatment applied to ~¼ of vessel circumference.

The pre-trimmed carotid artery segments were processed in a series of graded alcohols and xylene and paraffin wax embedded. The resulting paraffin blocks were sectioned twice serially, with an effort to capture the center of each segment, at an approximate 5 µm thickness and mounted to slide. One slide was stained with hematoxylin and eosin (H&E) and the other with Gomori's Elastin Trichrome (GET). Microscopic evaluation of the resulting slides was conducted by Serge Rousselle, DVM, DACVP. Tabulated microscopic data are presented in **Appendix A**.

Morphology parameters were generally scored using the following semi-quantitative scale (0-4):

Table_Apx C-2 Scoring table for damage morphology parameters

Score	Description
0	Finding not present.
1	Present, but minimal feature.
2	Notable feature; mild.
3	Prominent feature; moderate.
4	Overwhelming feature; severe.

Definitions and causes of damage types:

Endothelial Cell Loss: Most sensitive endpoint. Endothelial cells are highly susceptible to any mechanical shear stress or thermal effect and are typically the first cell type to be lost.

Hypereosinophilic Smooth Muscle Cells: Acute cell injury in the media. The staining alteration indicates generally a change in cytoplasmic homeostasis. This can be an artifact of tissue handling or fixation if fixation conditions are not optimal or can be a very early sign of peracute mural damage. Interpretation is based on comparison between control and treated vessels as well as pattern and distribution of the change and associated changes (context).

Compressive/Pressure Necrosis/Cell Effacement (loss): Concentric change characterized by sheets of smooth muscle cells showing hypereosinophilia and pyknotic to karyorrhectic

nuclei to cytolysis (loss of cellular features) leaving the vessel wall matrix intact. This change can be radial to circumferential and is always concentric (inside out).

Contraction bands: Alternating bands of hypereosinophilic and contracted smooth muscle cells alternating with pale hypocellular or acellular areas. This change indicates excessive vasoconstrictive stress and may lead to necrosis or regeneration.

Necrotic/Apoptotic Cells: Individual cell necrosis; may present as hypereosinophilia, pyknosis, karyorrhexis, cell debris and/or apoptotic body.

Collagen denaturation: Loss of fine fibrillar texture with collagenous areas showing hyalinization (homogenous thick bundles typically hypereosinophilic and sometimes picking up hematoxylin stain (purple) to varying degrees). This change indicates heat exposure (thermal denaturation).

Results & Discussion

Microscopic scoring of the local response of a total of forty-eight (48) segments from 3 swine carotid arteries when treated with laser irradiation at several dosages showed the following:

Table_Apx C-3 Histopathology Group Summary

HJC19-339		INJURY			INFLAMMATION				HEALING			
		Mural Acute Thermal Injury	Media Necrosis	Hyalinized Collagen without Other Thermal Injury	Inflammation Mean	Inflammation Median	Neutrophils	Inflammation, Adventitia	Endothelialization	Endothelium Erosion (terminal or artifact)	Hemosiderin/Hemorrhage, Vessel Wall	Adventitia Edema
C0	n	9	9	9	9	9	9	9	9	9	9	9
	Mean	0.0	**0.7**	**0.3**	**0.1**	0.0	**0.4**	**0.4**	**4.0**	**1.8**	**0.8**	**0.1**
	StDev	0.0	**0.7**	**0.7**	**0.2**	**0.2**	**0.5**	**0.5**	0.0	**1.1**	**0.7**	**0.3**
C1	n	9	9	9	9	9	9	9	9	9	9	9
	Mean	0.0	**1.1**	**0.1**	**0.2**	0.0	**0.7**	**0.7**	**4.0**	**1.3**	**0.9**	**0.6**
	StDev	0.0	**0.6**	**0.3**	**0.2**	**0.2**	**0.5**	**0.5**	0.0	**0.5**	**0.3**	**0.7**
C2	n	7	7	7	7	7	7	7	7	7	7	7
	Mean	0.0	**0.7**	0.0	**0.1**	0.0	**0.1**	**0.1**	**4.0**	**0.4**	**0.7**	0.0
	StDev	0.0	**1.0**	0.0	**0.2**	**0.2**	**0.4**	**0.4**	0.0	**0.5**	**0.5**	0.0
C3	n	5	5	5	5	5	5	5	5	5	5	5
	Mean	0.0	**1.4**	0.0	**0.2**	0.0	**0.6**	**0.6**	**4.0**	**1.2**	**1.0**	0.0
	StDev	0.0	**0.5**	0.0	**0.2**	**0.2**	**0.5**	**0.5**	0.0	**0.4**	0.0	0.0
C4	n	4	4	4	4	4	4	4	4	4	4	4
	Mean	0.0	**0.5**	**0.5**	**0.4**	**0.5**	**0.8**	**0.8**	**4.0**	**0.8**	**0.3**	0.0
	StDev	0.0	**1.0**	**1.0**	**0.3**	**0.3**	**0.5**	**0.5**	0.0	**0.5**	**0.5**	0.0
C5	n	10	10	10	10	10	10	10	10	10	10	10
	Mean	**0.2**	**2.2**	0.0	**0.2**	**0.2**	**0.6**	**0.6**	**4.0**	**1.9**	**0.6**	0.0
	StDev	**0.4**	**0.8**	0.0	**0.2**	**0.2**	**0.5**	**0.5**	0.0	**0.9**	**0.5**	0.0
C6	n	4	4	4	4	4	4	4	4	4	4	4
	Mean	0.0	**3.3**	0.0	0.0	0.0	0.0	0.0	**4.0**	**3.5**	**1.0**	0.0
	StDev	0.0	**0.5**	0.0	0.0	0.0	0.0	0.0	0.0	**0.6**	**0.8**	0.0

General Perspective on Acute Vascular Changes Associated with Energy Delivery:

Energy delivery produce non-specific microscopic changes in tissues essentially characterized by degeneration and necrosis sometimes accompanied by evidence of extracellular protein matrix denaturation. In vessels, these changes target endothelial cells and media smooth muscle cells primarily. Extracellular matrix (ECM) can be affected by mechanical or energy delivery and cause laceration or tears (mechanical stress) or coagulation (radiative energy). Spurious factors can and frequently do complicate interpretation of vascular histology. Vascular histology can be significantly influenced by experimental conditions in-vivo and at tissue harvest (tissue handling and fixation). Catheterization of a target vessel alone can and typically erodes the endothelial surface through mechanical shear stress. Catheter bulk and relative rigidity can also impart localized compressive trauma sufficient to bruise the vessel wall and cause cell death in the media. This can be aggravated by vasospasm at the time of treatment.

Tissue collection can also produce changes that mimic necrosis unless the tissue is fixed in-situ prior to dissection and excision/trimming. Tissue handling and pulling during dissection as well as trimming of target segments can also cause tissue damage that mimics compressive injury (crushing). Use of cauterizing scalpel can cause coagulation necrosis and denaturation of ECM.

Morphologically, the resulting effect on vascular cells include vacuolization, shrinkage and hypereosinophilia of the cytoplasm, pyknosis, localized cellular effacement or stretch tears in cellular sheets. Effect on ECM includes lacerations and coagulation/hyalinization (heat-induced denaturation). Interpreting the significance and cause of acute vascular changes must take into account the level of background noise as observed in concurrent untreated controls.

Microscopic Finding Ascribable to Treatment:

Table_Apx C-4 Average Severity of Media Necrosis

	Media Necrosis (Average Score)
C0	0.7
C1	1.1
C2	0.7
C3	1.4
C4	0.5
C5	2.2
C6	3.3

In this study, the only change that was clearly dose-related consisted of media necrosis. This change is characterized by areas of media hypereosinophilia with pyknosis and/or karyorrhexis. It was observed at low severity in control segments (C0) and showed a clear increase in severity, incidence and circumferential extension at highest doses (C5 and C6). In group C3, there was a slight increase in incidence and circumferential extent that was of equivocal significance biologically (possible trend) considering the level of background noise in the controls. The changes observed at lower doses (C1, C4) were consistent with background noise.

C0 (NO ACTIVATION)

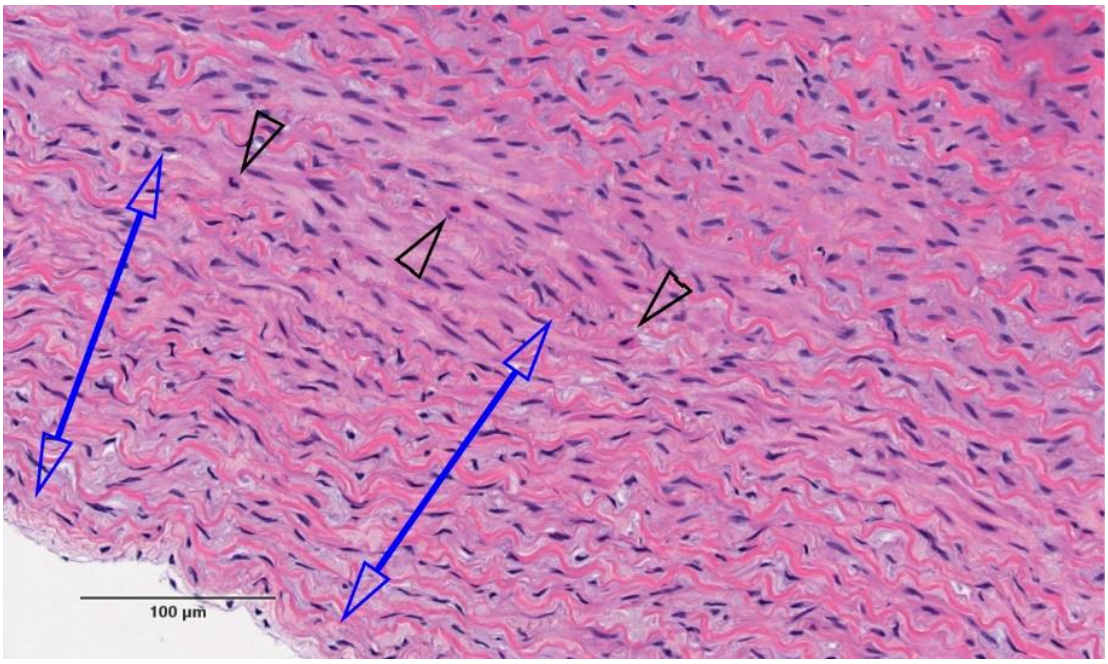

Figure_Apx C-1 Segment 2A (H&E). C0 (No activation). Clear arrowheads = rare contracted and hyper eosinophilic smooth muscle cells in the media (media necrosis score '1'); blue double arrows = inner media showing compressed smooth muscle cells with pyknotic nuclei (compression injury).

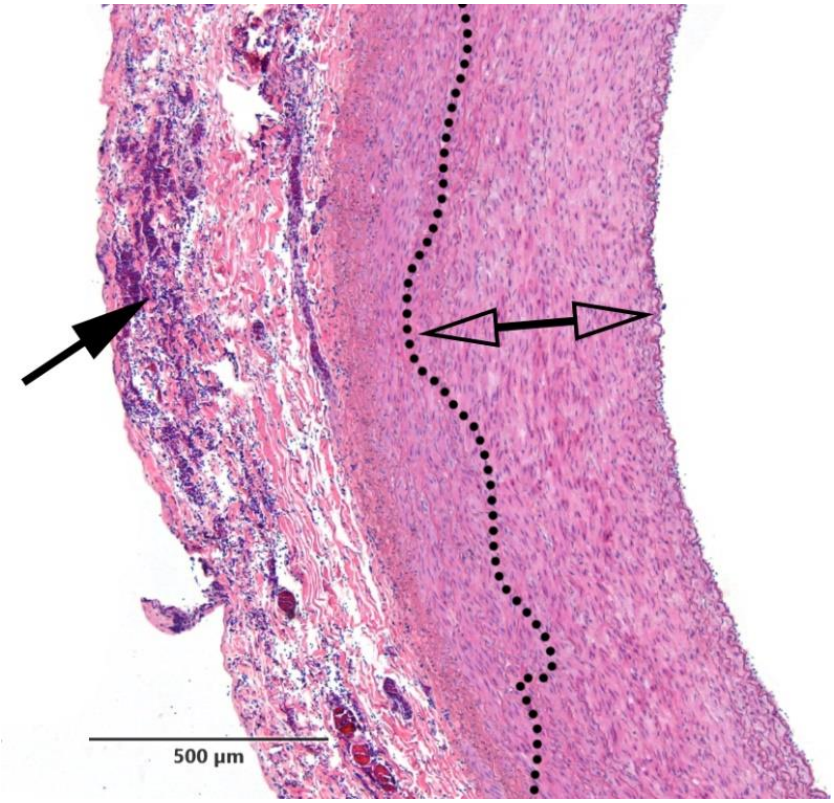

Figure_Apx C-2 Segment 1C (H&E). C0 (No activation). Clear double arrow inside dotted line = inner media showing smooth muscle cells with pyknotic nuclei and variably hypereosinophilic and contracted cytoplasm; solid arrow = slight adventitial hermorrhage (possible collection artifact).

C0 (NO ACTIVATION) (CONTINUED)

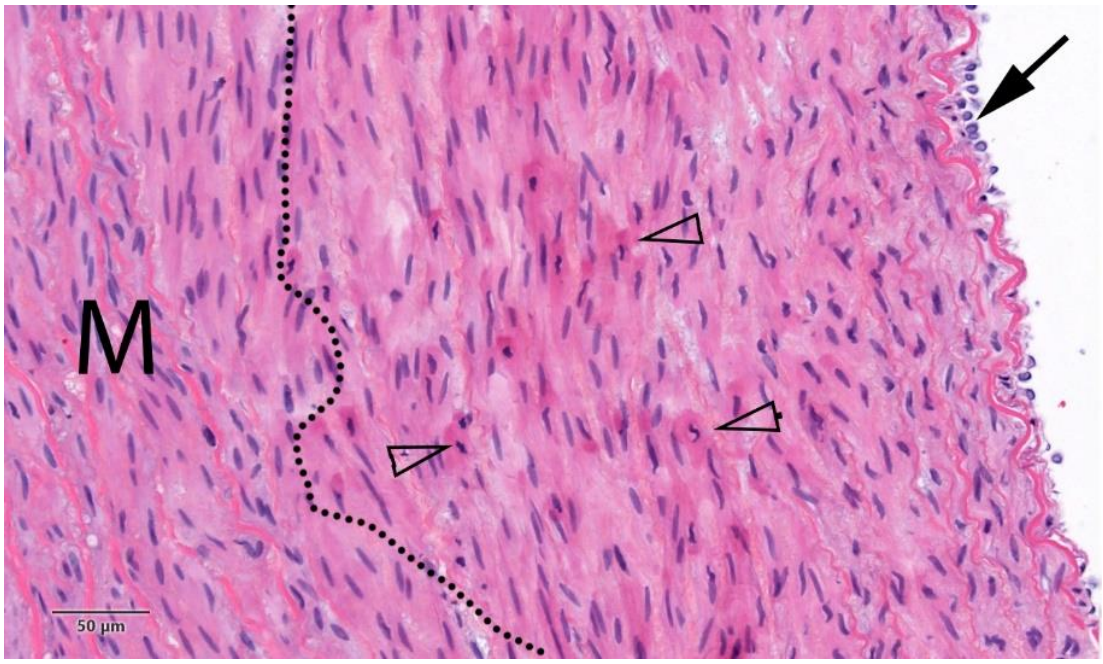

Figure_Apx C-3 Segment 1C (H&E). C0 (No activation). M = intact outer media; black dotted line = outline of inner media area showing necrotic smooth muscle cells (clear arrowheads = hypereosinophilic and contracted smooth muscle cells); solid arrow = intact endothelium.

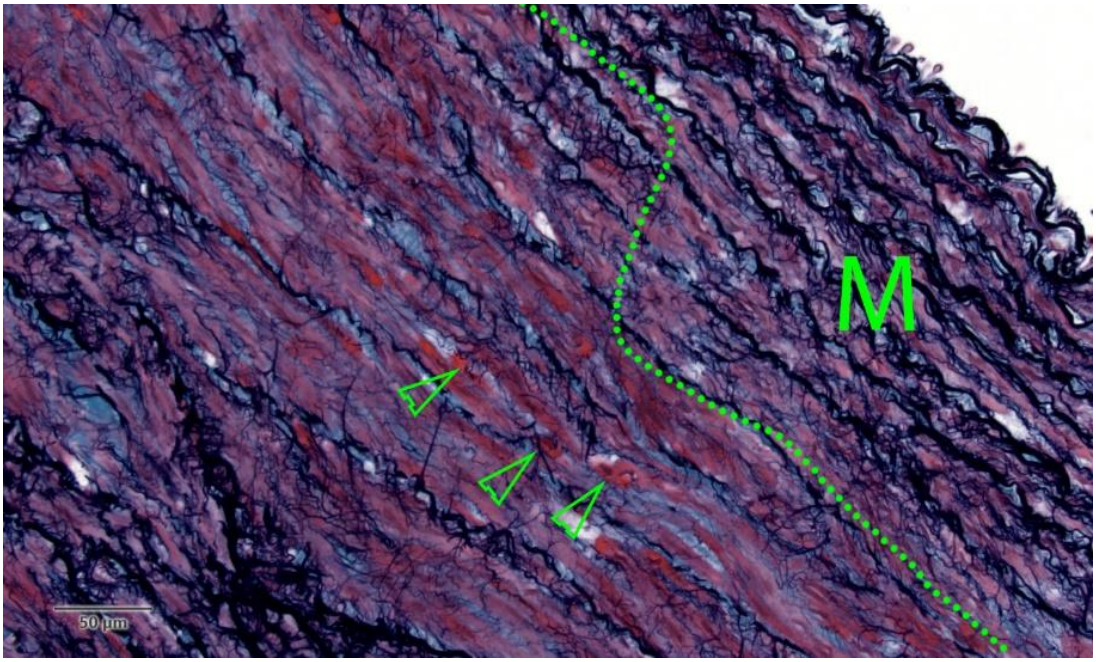

Figure_Apx C-4 Segment 1C (GET). C0 (No activation). M = intact inner media; green dotted line = outline of deep media area showing necrotic smooth muscle cells; green arrowheads = hyperchromatic and contracted smooth muscle cells (necrosis).

C0 (NO ACTIVATION) (CONTINUED)

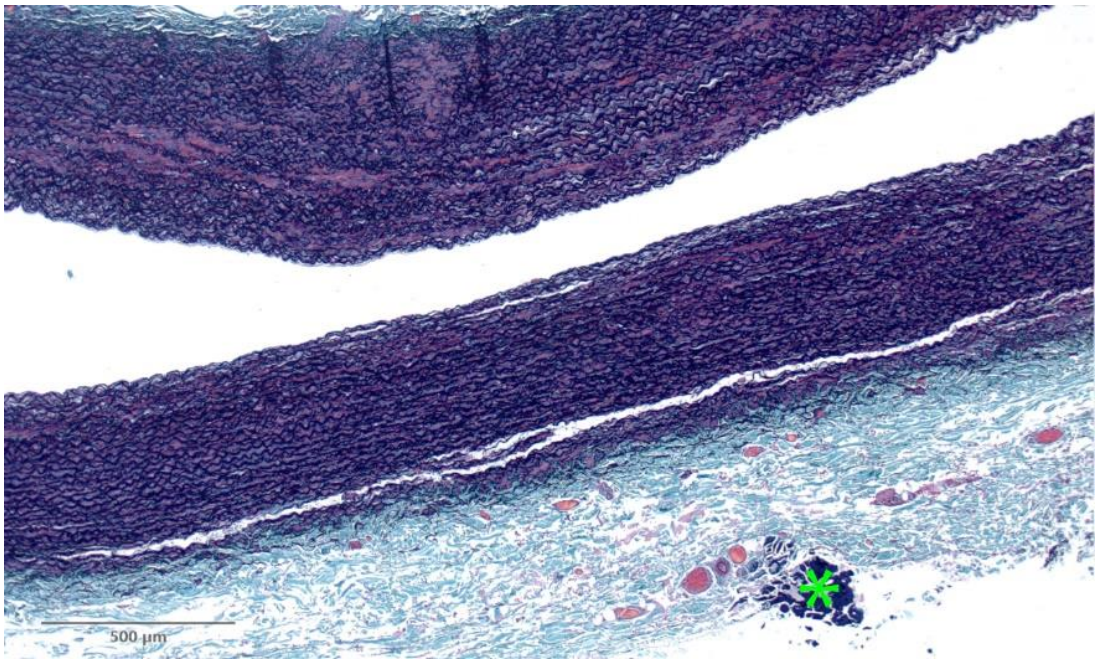

Figure_Apx C-5 Segment 2A (GET). C0 (No activation). Green asterisk = focal collagen denaturation of the adventitial collagen (consistent with focal cauterization).

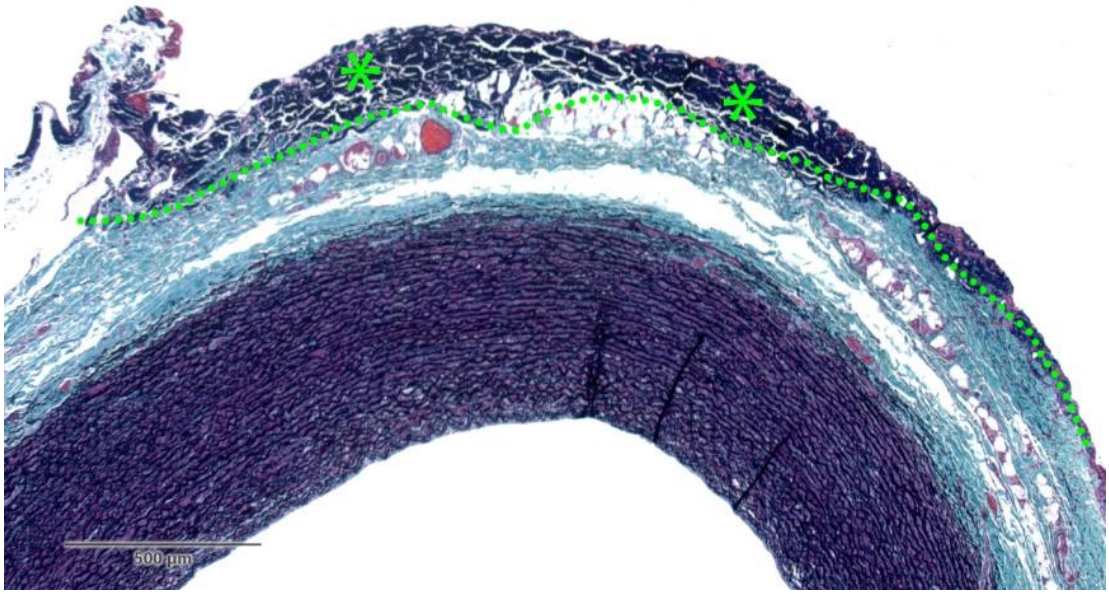

Figure_Apx C-6 Segment 3B (GET). C0 (No activation). Green asterisks = locally extensive collagen denaturation of the adventitia (consistent with focal cauterization), delineated by green dotted line.

C1 (1064 nm - 8.3 J/cm^2)

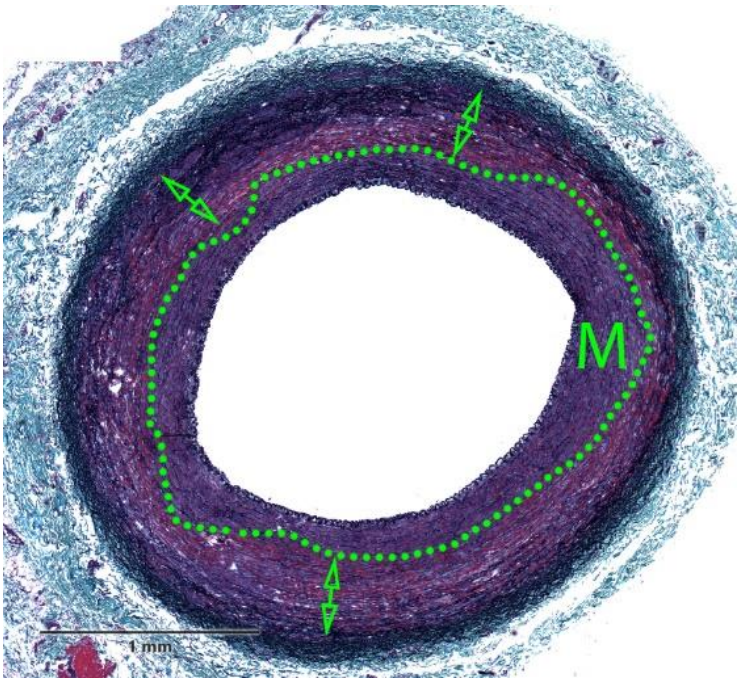

Figure_Apx C-7 Segment 1H (GET). C1 (1064 nm - 8.3 J/cm^2). Green dotted line = boundary between the intact inner media (M) and the outer affected media (green double-arrows) showing hyperchromatic smooth muscle cells.

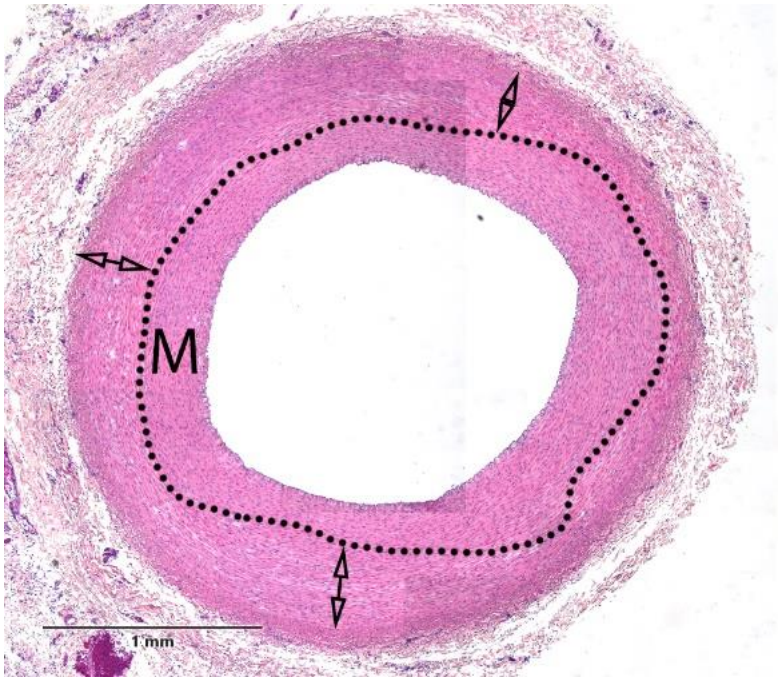

Figure_Apx C-8 Segment 1H (H&E). C1 (1064 nm - 8.3 J/cm^2). Black dotted line = boundary between the intact inner media (M) and the outer affected media (clear double-arrows) showing hypereosinophilic smooth muscle cells.

C1 (1064 nm - 8.3 J/cm^2) (CONTINUED)

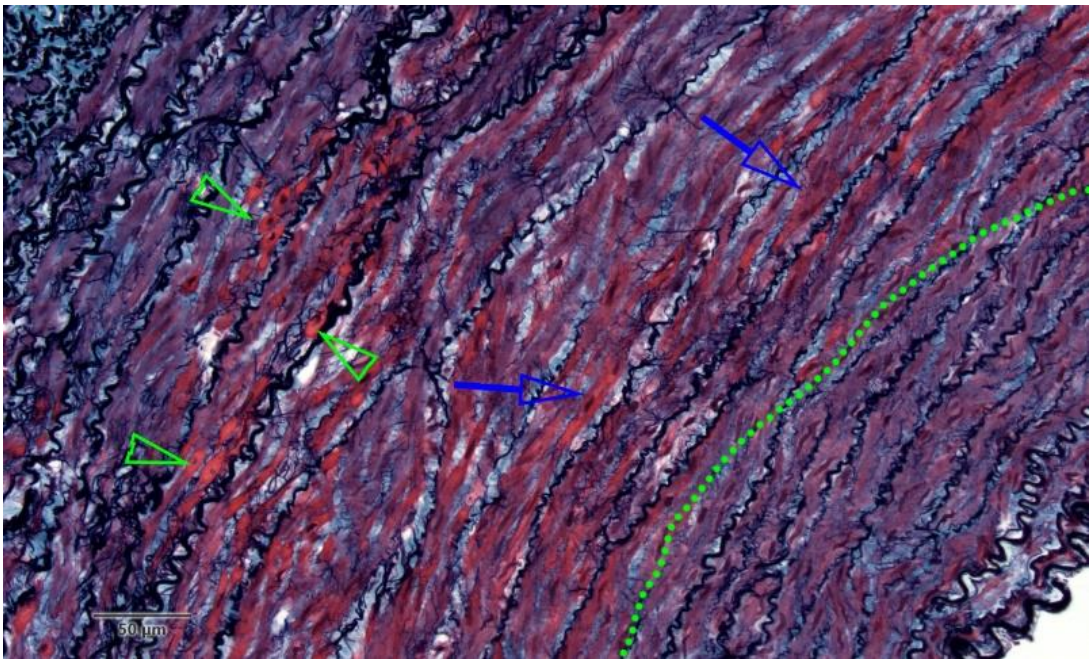

Figure_Apx C-9 Segment 1H (GET). C1 (1064 nm - 8.3 J/cm^2). Green dotted line = outline of deep media area showing necrotic smooth muscle cells; green arrowheads = hyperchromatic and contracted smooth muscle cells (necrosis); blue arrows = hyperchromatic elongated smooth muscle cells (equivocal injury).

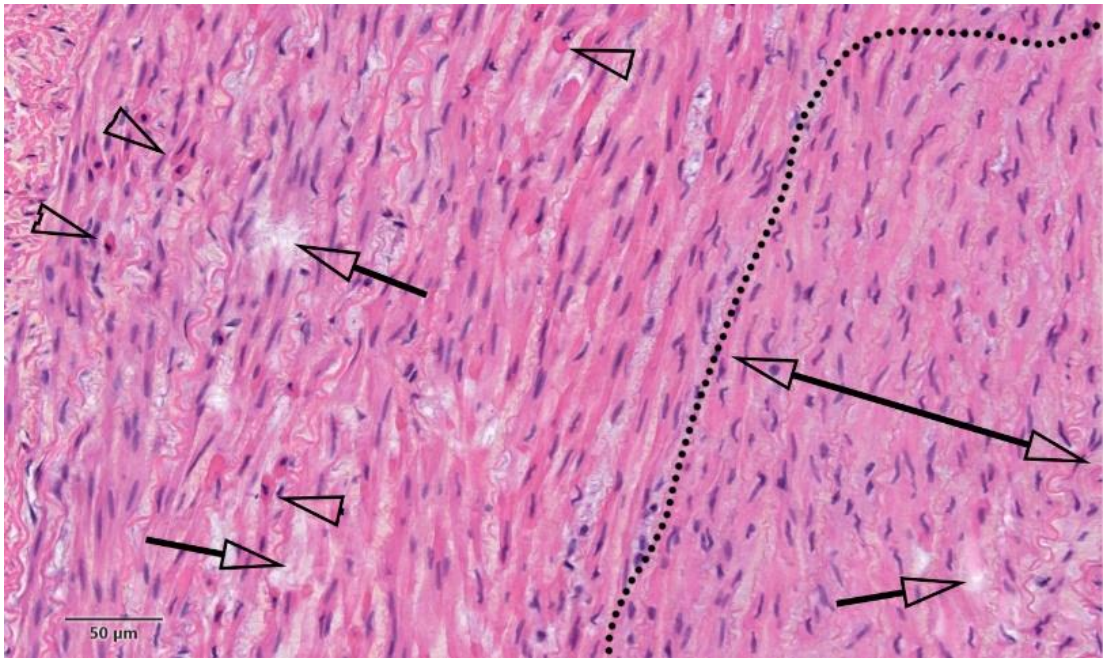

Figure_Apx C-10 Segment 1H (H&E). C1 (1064 nm - 8.3 J/cm2). Black dotted line = outline of deep media area showing necrotic smooth muscle cells; clear arrowheads = hyperchromatic and contracted smooth muscle cells (necrosis); clear arrows = clear spaces between smooth muscle cells (edema and/or smooth muscle cell dissociation and loss); clear double arrow = inner media appearing intact, although a few clear interstitial spaces are evident (possible early damage).

C1 (1064 nm - 8.3 J/cm^2) (CONTINUED)

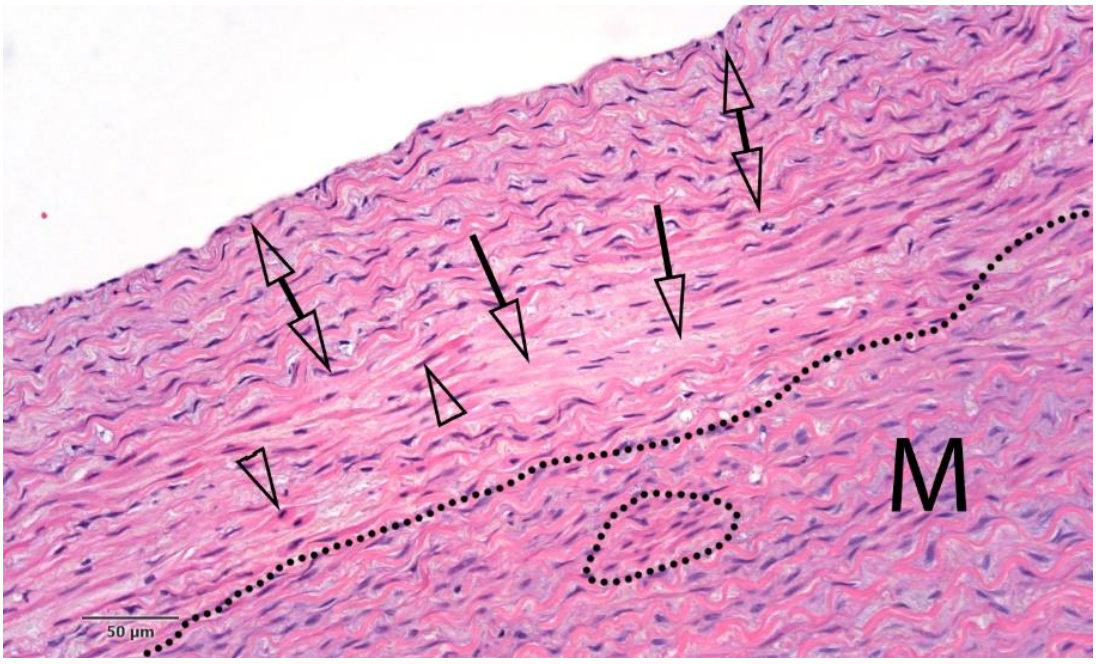

Figure_Apx C-11 Segment 2D (H&E). C1 (1064 nm - 8.3 J/cm^2). Black dotted line = boundary between the intact outer media (M) and the inner affected media showing hypereosinophilic smooth muscle cells (arrowheads) and clear spaces of smooth muscle cell effacement and loss (clear arrows); clear double arrows = innermost media showing pyknosis in smooth muscle cell nuclei (generally consistent with compressive necrosis).

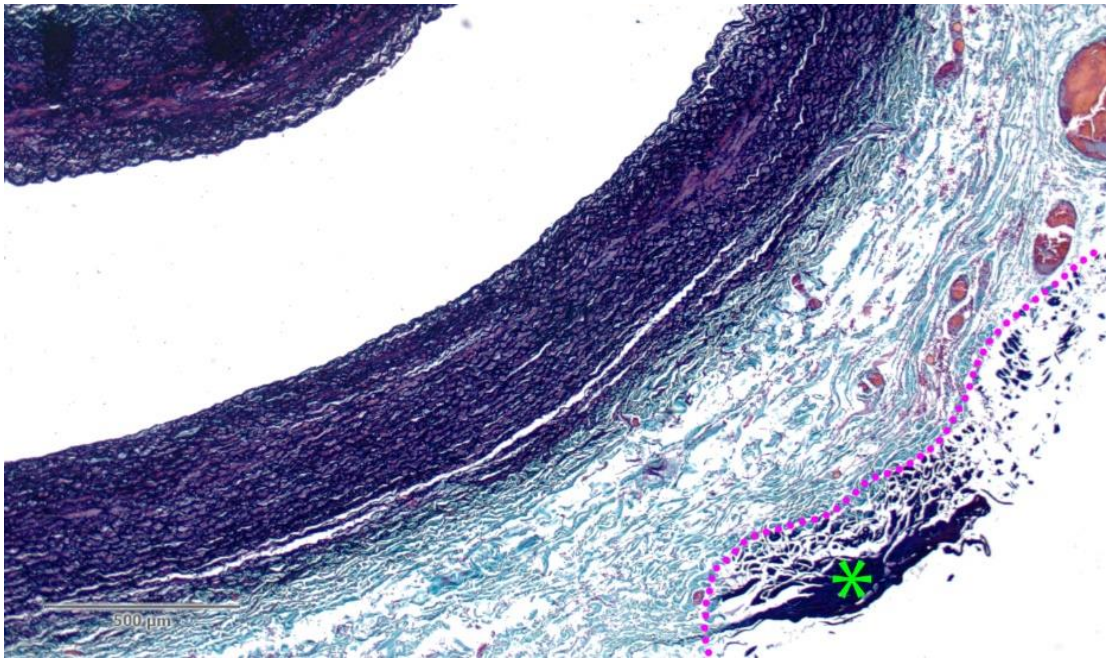

Figure_Apx C-12 Segment 2D (GET). C1 (1064 nm - 8.3 J/cm2). Green asterisk bounded by dotted line = focal collagen denaturation of the adventitial collagen (consistent with focal cauterization).

C2 (1064 nm – 100 J/cm^2)

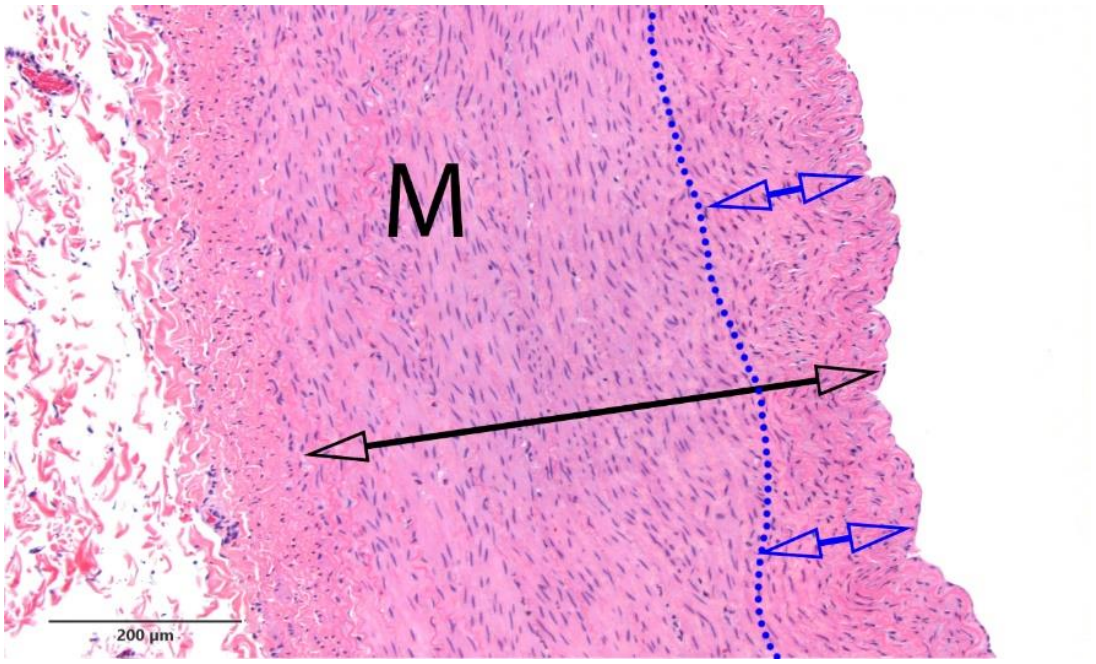

Figure_Apx C-13 Segment 2J (H&E). C2 (1064 nm - 100 J/cm2). Clear double arrow = media (M) showing no evident necrosis; blue dotted line and blue double arrows = inner media showing pyknosis on SMC nuclei, generally consistent with pressure necrosis.

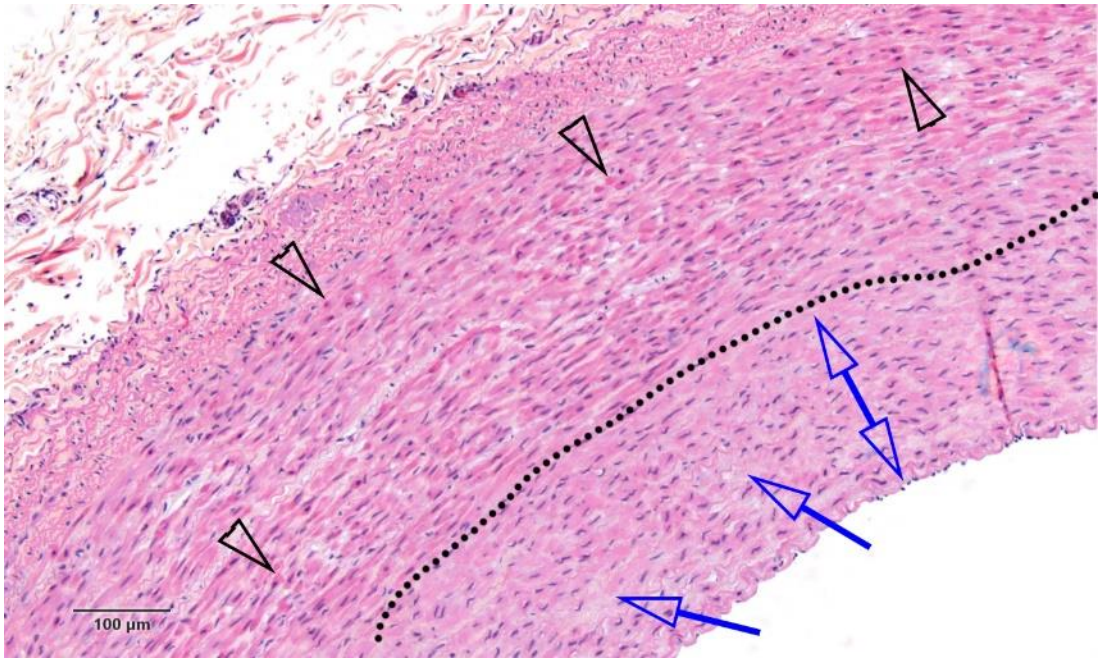

Figure_Apx C-14 Segment 1I (H&E). C2 (1064 nm - 100 J/cm2). Black dotted line = boundary between the intact outer media and the inner affected media showing hypereosinophilic smooth muscle cells (clear arrowheads) and increased interstitial clear spaces; blue double arrow = innermost media showing pyknosis in smooth muscle cell nuclei (generally consistent with compressive necrosis); blue arrows = clear spaces in the inner media (smooth muscle cell loss) denoting possible energy injury.

C2 (1064 nm – 100 J/cm^2) (CONTINUED)

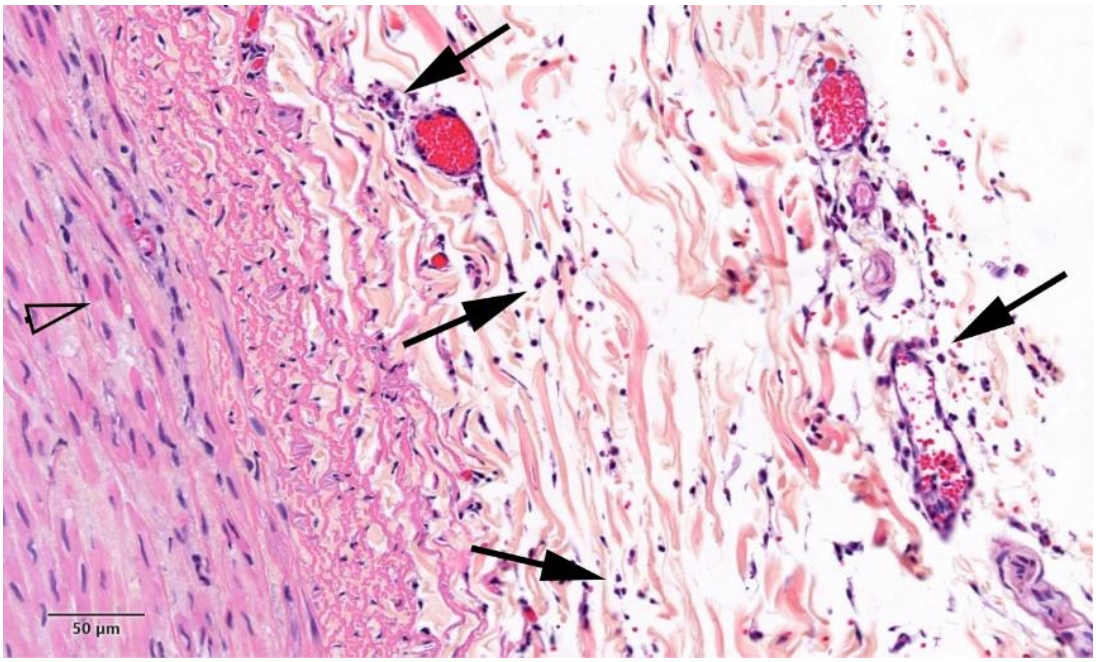

Figure_Apx C-15 Segment 1I (H&E). C2 (1064 nm - 100 J/cm2). Solid arrows = minimal inflammation in the adventitia (neutrophils); clear arrowhead = necrotic smooth muscle cells in the outer media.

C3 (1064 nm – 700 J/cm^2)

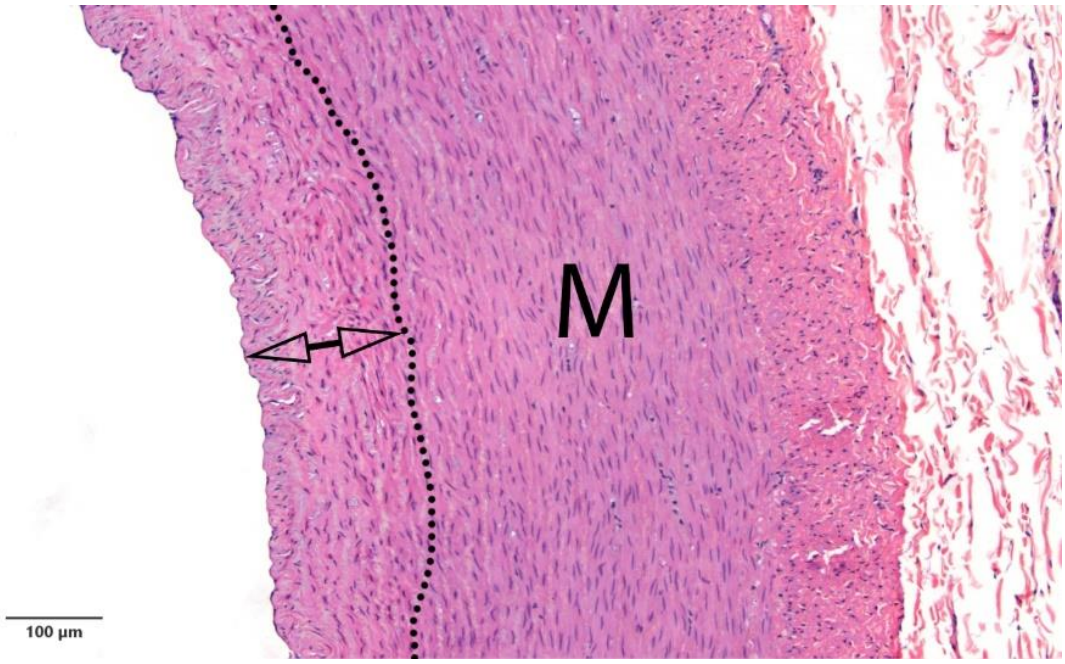

Figure_Apx C-16 Segment 2N (H&E). C3 (1064 nm - 700 J/cm^2). Clear double arrow inside dotted line = media showing no evident treatment-induced necrosis. There is concentric hypereosinophilia and pyknosis typically consistent with endovascular compression; M = intact media.

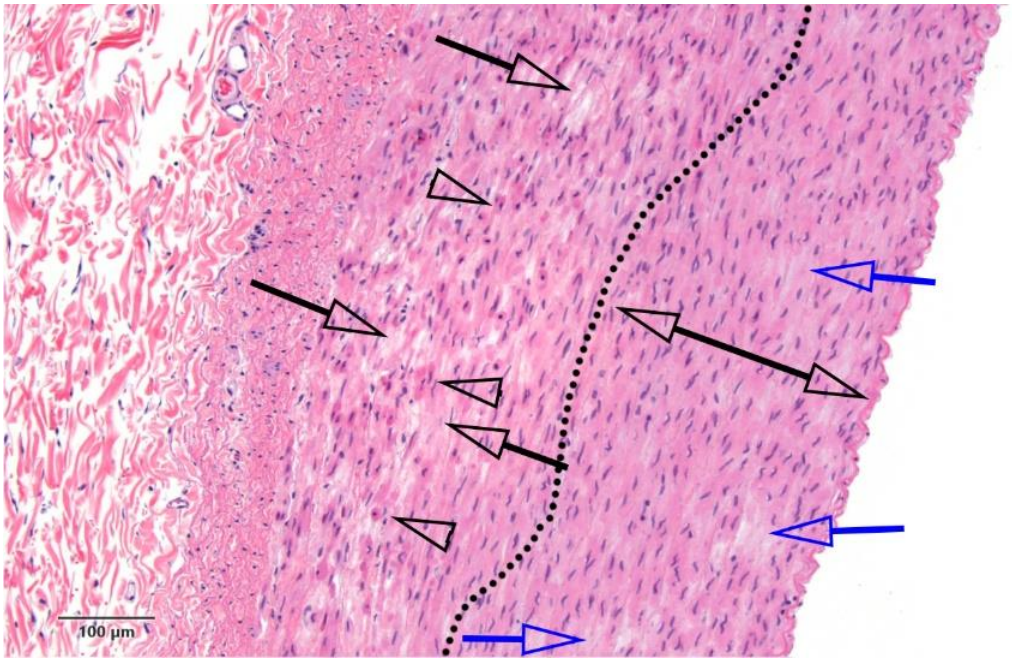

Figure_Apx C-17 Segment 1L (H&E). C3 (1064 nm - 700 J/cm^2). Black dotted line = boundary between the intact inner media (clear double arrow) and the outer affected media showing hypereosinophilic smooth muscle cells (clear arrowheads) and increased interstitial clear spaces (clear arrows); blue arrows = clear spaces in the inner media (smooth muscle cell loss).

C4 (1720 nm - 8.3 J/cm^2)

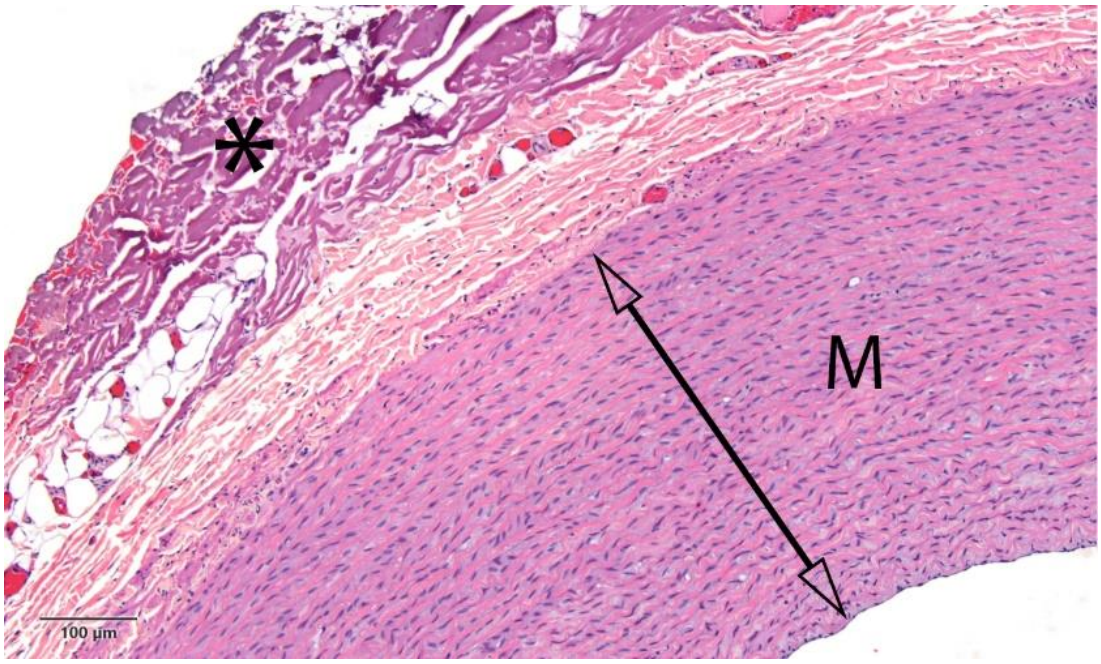

Figure_Apx C-18 Segment 3C (H&E). C4 (1720 nm – 8.3 J/cm^2). Black asterisk = collagen denaturation in the adventitia; clear double arrow = intact media (M).

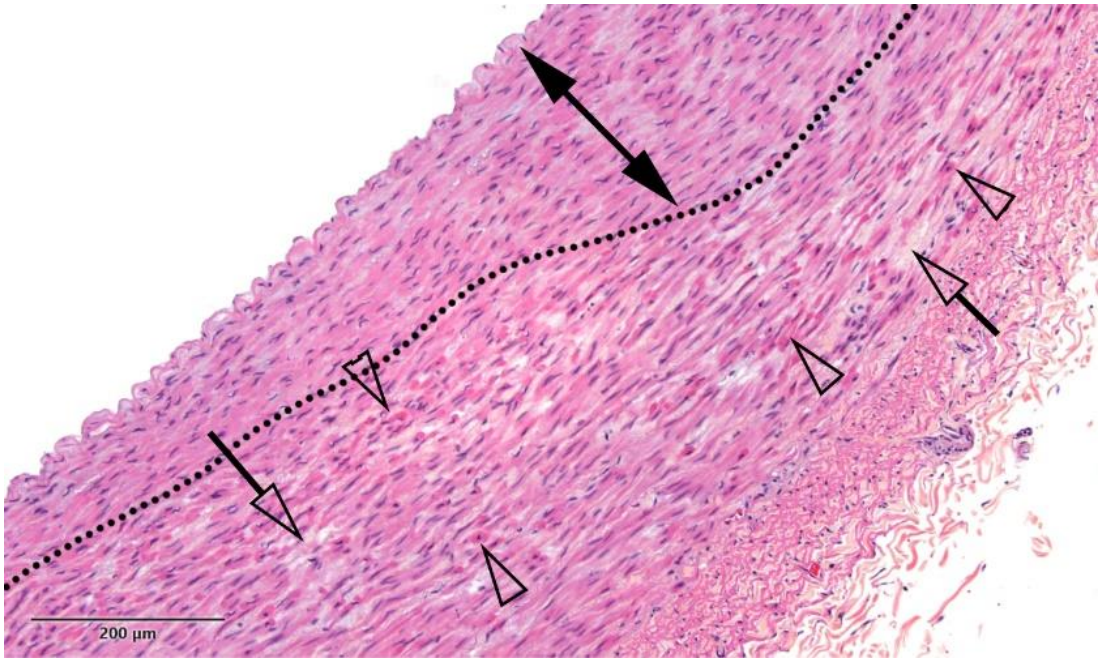

Figure_Apx C-19 Segment 1M (H&E). C4 (1720 nm – 8.3 J/cm^2). Black dotted line = boundary between the intact (albeit possibly compressed) inner media (solid double arrow) and the outer affected media showing hypereosinophilic and contracted smooth muscle cells (clear arrowheads) and increased interstitial clear spaces (clear arrows).

C4 (1720 nm - 8.3 J/cm^2) (CONTINUED)

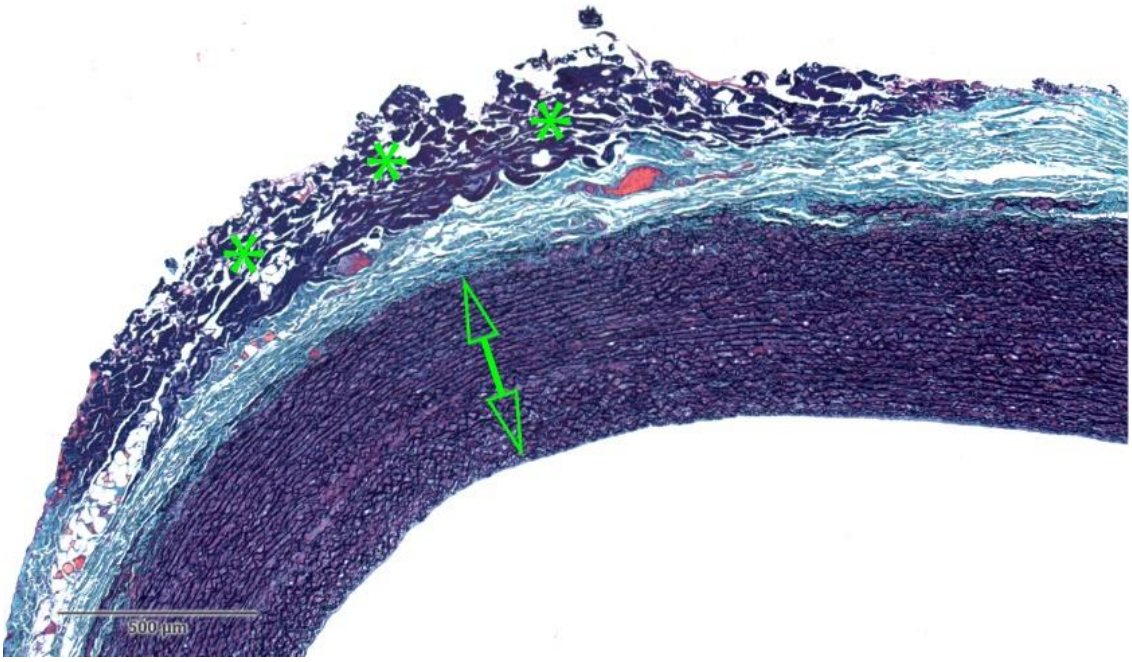

Figure_Apx C-20 Segment 3C (GET). C4 (1720 nm – 8.3 J/cm^2). Green asterisks = locally extensive collagen denaturation of the adventitia (consistent with focal cauterization); green double arrow = intact media.

C5 (1720 nm - 50 J/cm^2)

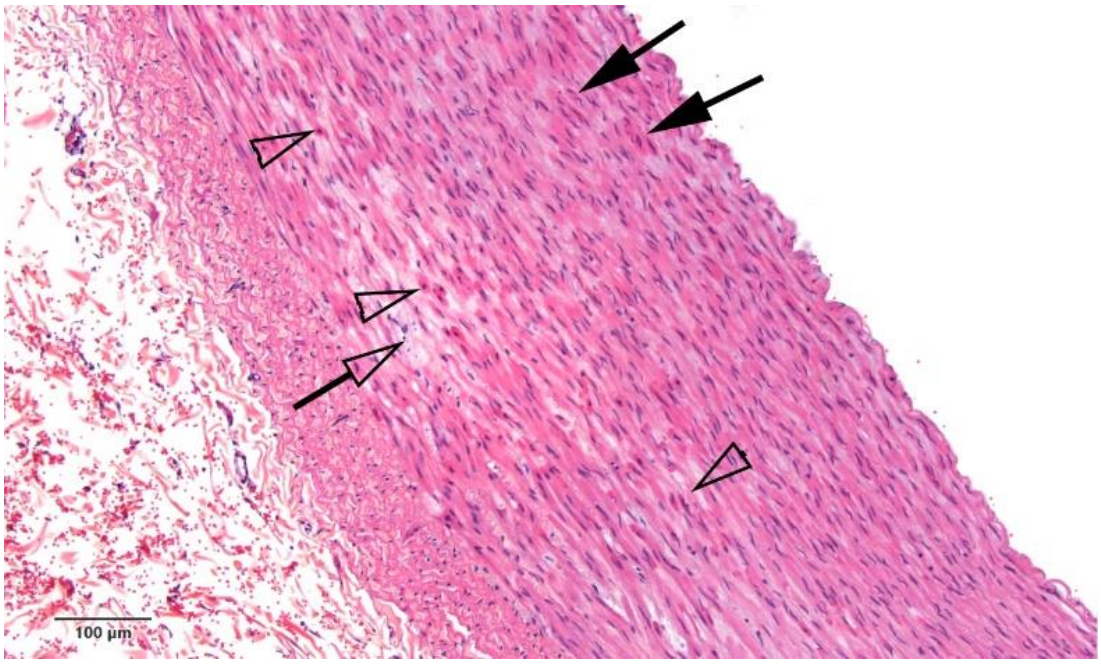

Figure_Apx C-21 Segment 1N (H&E). C5 (1720 nm – 50 J/cm^2). Affected media showing hypereosinophilic and contracted smooth muscle cells (clear arrowheads) and increased interstitial clear spaces (clear arrow); solid arrows = hypereosinophilic smooth muscle cells with pyknotic nuclei in the inner media (typically consistent with compressive necrosis).

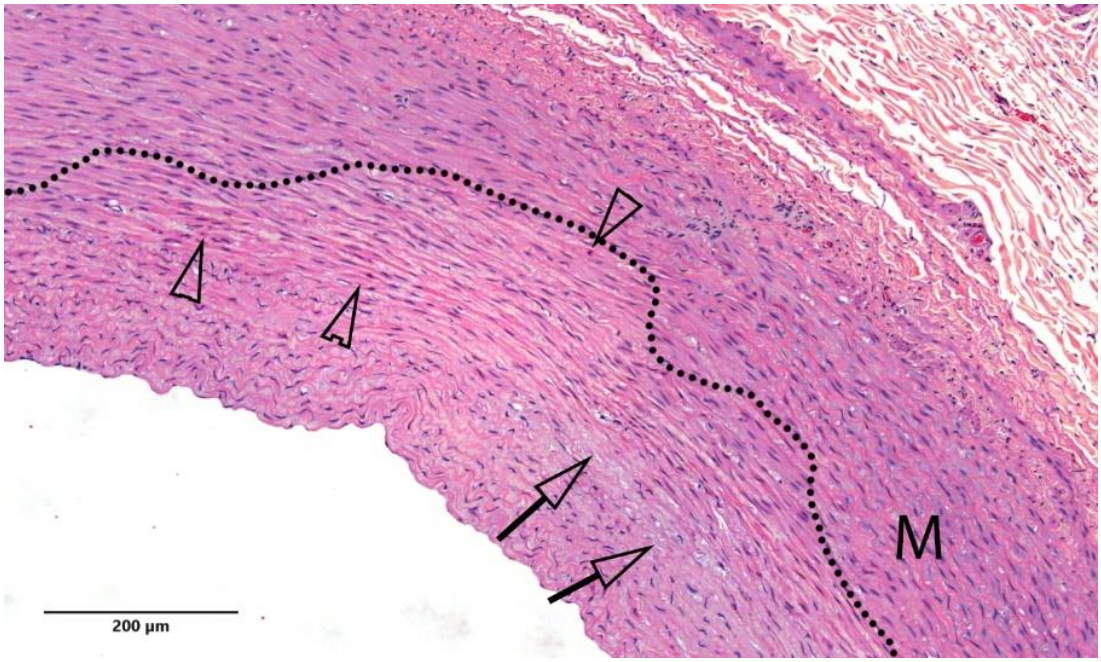

Figure_Apx C-22 Segment 3H (H&E). C5 (1720 nm – 50 J/cm^2). Media inside dotted line = affected media showing hypereosinophilic and contracted smooth muscle cells (clear arrowheads) and increased interstitial clear spaces (clear arrows); M = intact media.

C5 (1720 nm - 50 J/cm^2) (CONTINUED)

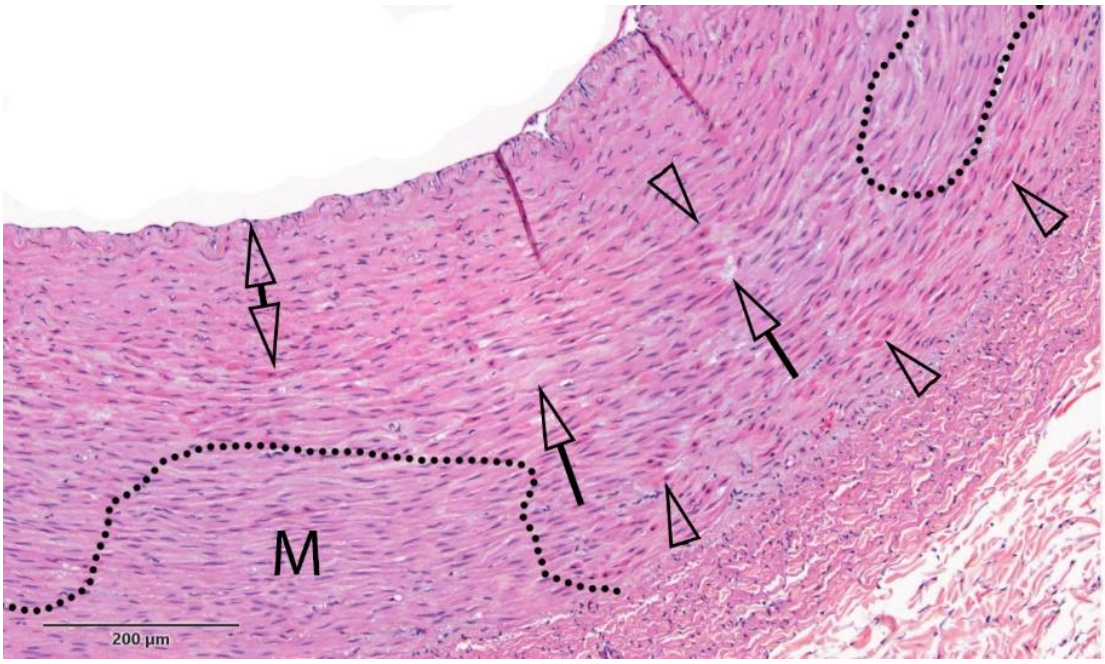

Figure_Apx C-23 Segment 3L (H&E). C5 (1720 nm – 50 J/cm^2). Black dotted lines = boundary between the intact outer and mid media (M) and the affected media showing hypereosinophilic and contracted smooth muscle cells (clear arrowheads) and increased interstitial clear spaces (clear arrows), the innermost media (clear double arrow) shows pyknotic nuclei and hypereosinophilic smooth muscle cells (typically suggestive of compressive injury).

C6 (1720 nm - 200 J/cm^2)

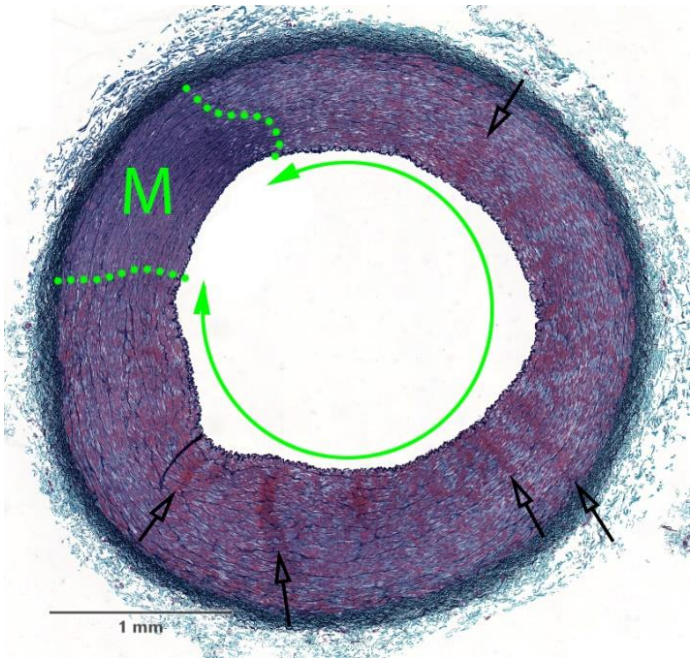

Figure_Apx C-24 Segment 1P (GET). C6 (1720 nm – 200 J/cm^2). Section showing widespread media necrosis (circular green double arrow) and a short segment of intact media (M, delineated by green dotted line); clear arrows = radial clusters of hyperchromatic and shrunken smooth muscle cells evoking contraction bands.

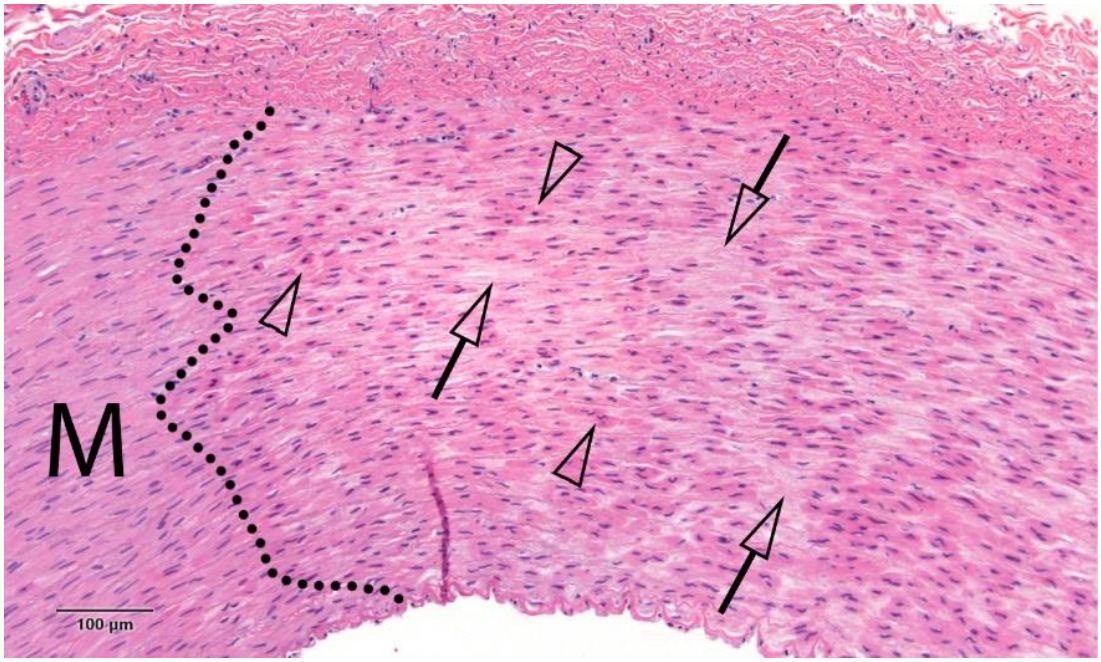

Figure_Apx C-25 Segment 1P (H&E). C6 (1720 nm – 200 J/cm^2). Black dotted line = radial boundary between the intact media (M) and the affected media showing widespread hypereosinophilic and contracted smooth muscle cells (clear arrowheads) and increased interstitial clear spaces (clear arrows).

C6 (1720 nm - 200 J/cm^2) (CONTINUED)

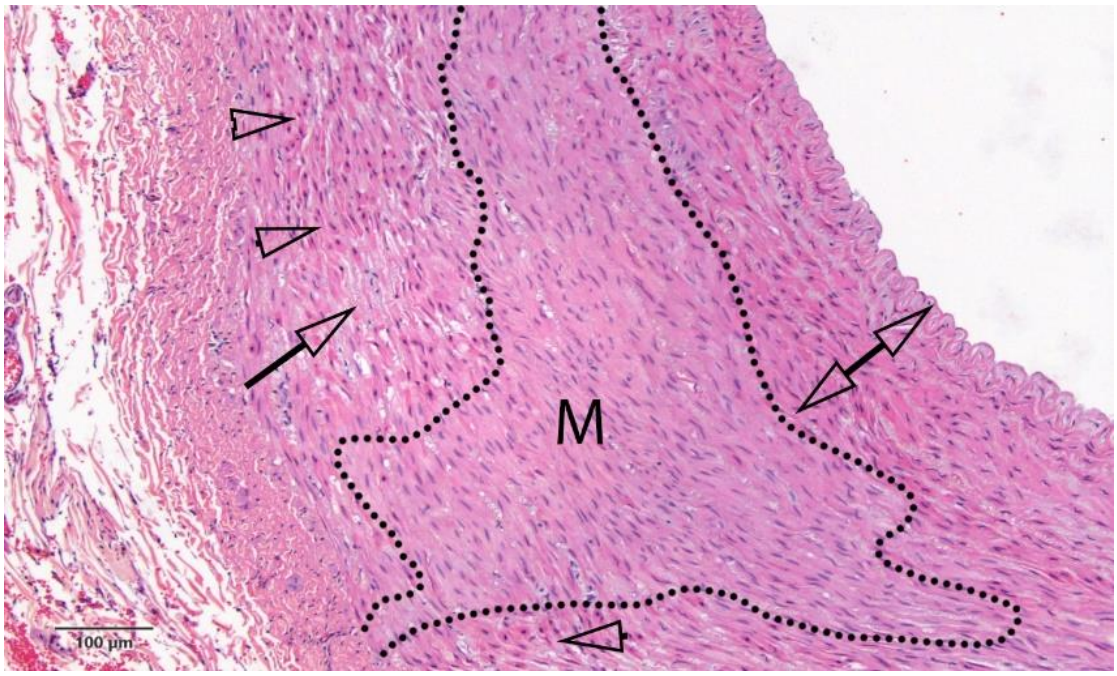

Figure_Apx C-26 Segment 3O (H&E). C6 (1720 nm – 200 J/cm^2). Black dotted line = boundary between the intact outer and mid media (M) and the affected media showing widespread hypereosinophilic and contracted smooth muscle cells (clear arrowheads) and increased interstitial clear spaces (clear arrows); the innermost media (clear double arrow) shows pyknotic nuclei and hypereosinophilic smooth muscle cells (typically suggestive of compressive injury).

Conclusion

Changes induced by treatment overlap with changes induced by catheterization +/- vasospasm (*i.e.*, compressive necrosis and stretch necrosis). Outer media necrosis characterized by smooth muscle cell hypereosinophilia and contraction is most characteristic. Treatment effect was clear in C3 (1064 nm; 700 J/cm^2) and C5 < C6 (1720 nm; 50, 200 J/cm^2, respectively). Possible treatment effects sporadically at lower doses (C1, C2 and C4). The tissue damage at these levels are not considered life threatening and are expected to heal. While nothing in this study represents a safety concern, a chronic time period (approximately 4 weeks) would be required to confirm that healing is uneventful.

_____

_____

Serge D. Rousselle, DVM, DACVP Date

Study Pathologist

Table_Apx C-5 Tabulated Microscopic Data (Part 1)

HJC19-339		INJURY									INFLAMMATION									
				Vessel Wall Injury		Severe Injury (Disruptions)			Thermal Injury				See pathology narrative for scoring definitions.							
											Mural Inflammation		Inflammatory Cell Types					Inflammation Distribution		
		Injury Mean	Injury Median	Mural Erosion	Mural Dissection	Mural Avulsion	Mural Acute Thermal Injury	Media Necrosis	Media Hyalinization	Hyalinized Collagen without Other Thermal Injury	Inflammation Mean	Inflammation Median	Neutrophils	Eosinophils	Lymphocytes	Histiocytes	Foreign Body Giant cells	Inflammation, Neointima	Inflammation, Media	Inflammation, Adventitia
C0	n	9	9	9	9	9	9	9	9	9	9	9	9	9	9	9	9	9	9	9
	Mean	0.0	0.0	0.0	0.0	0.0	0.0	0.7	0.0	0.3	0.1	0.0	0.4	0.0	0.0	0.0	0.0	0.0	0.0	0.4
	StDev	0.0	0.0	0.0	0.0	0.0	0.0	0.7	0.0	0.7	0.2	0.2	0.5	0.0	0.0	0.0	0.0	0.0	0.0	0.5
C1	n	9	9	9	9	9	9	9	9	9	9	9	9	9	9	9	9	9	9	9
	Mean	0.0	0.0	0.0	0.0	0.0	0.0	1.1	0.0	0.1	0.2	0.0	0.7	0.0	0.0	0.0	0.0	0.0	0.0	0.7
	StDev	0.0	0.0	0.0	0.0	0.0	0.0	0.8	0.0	0.3	0.2	0.2	0.5	0.0	0.0	0.0	0.0	0.0	0.0	0.5
C2	n	7	7	7	7	7	7	7	7	7	7	7	7	7	7	7	7	7	7	7
	Mean	0.0	0.0	0.0	0.0	0.0	0.0	0.7	0.0	0.0	0.1	0.0	0.1	0.0	0.0	0.0	0.0	0.0	0.0	0.1
	StDev	0.0	0.0	0.0	0.0	0.0	0.0	1.0	0.0	0.0	0.2	0.2	0.4	0.0	0.0	0.0	0.0	0.0	0.0	0.4
C3	n	6	6	6	6	6	6	6	6	6	6	6	6	6	6	6	6	6	6	6
	Mean	0.0	0.0	0.0	0.0	0.0	0.0	1.4	0.0	0.0	0.2	0.0	0.6	0.0	0.0	0.0	0.0	0.0	0.0	0.6
	StDev	0.0	0.0	0.0	0.0	0.0	0.0	0.6	0.0	0.0	0.2	0.2	0.5	0.0	0.0	0.0	0.0	0.0	0.0	0.5
C4	n	4	4	4	4	4	4	4	4	4	4	4	4	4	4	4	4	4	4	4
	Mean	0.0	0.0	0.0	0.0	0.0	0.0	0.5	0.0	0.5	0.4	0.5	0.8	0.0	0.0	0.0	0.0	0.0	0.0	0.8
	StDev	0.0	0.0	0.0	0.0	0.0	0.0	1.0	0.0	1.0	0.3	0.3	0.5	0.0	0.0	0.0	0.0	0.0	0.0	0.5
C5	n	10	10	10	10	10	10	10	10	10	10	10	10	10	10	10	10	10	10	10
	Mean	0.0	0.0	0.0	0.0	0.0	0.2	2.2	0.0	0.0	0.2	0.2	0.6	0.0	0.0	0.0	0.0	0.0	0.0	0.6
	StDev	0.0	0.0	0.0	0.0	0.0	0.4	0.8	0.0	0.0	0.2	0.2	0.5	0.0	0.0	0.0	0.0	0.0	0.0	0.5
C6	n	4	4	4	4	4	4	4	4	4	4	4	4	4	4	4	4	4	4	4
	Mean	0.0	0.0	0.0	0.0	0.0	0.0	3.3	0.0	0.0	0.0	0.0	0.0	0.0	0.0	0.0	0.0	0.0	0.0	0.0
	StDev	0.0	0.0	0.0	0.0	0.0	0.0	0.6	0.0	0.0	0.0	0.0	0.0	0.0	0.0	0.0	0.0	0.0	0.0	0.0

n = Number of segments used in calculations;
StDev = Standard Deviation

Table_Apx C-5 Continued 1: Tabulated Microscopic Data Continued (Part 2)

HJC19-339		HEALING																		
		See pathology narrative for scoring definitions.																		
		Endovascular								Vessel Wall								Other		
		Endothelialization	Endothelium Erosion (terminal or artifact)	Leukocyte Margination	Thrombosis	Occlusion	Neointima Fibrin	Neointima Maturity	Neointima - Hyalinization	Hemosiderin/Hemorrhage, Vessel Wall	Mural - Necrosis/Hyalinization	Mural Calcification	Mural Neovascularization	Media Fibrosis	Adventitia Edema	Adventitial Fibrosis	Adventitia Granulation Tissue	Vasculitis/Perivasculitis- Branch	Branch - Thrombus	Aneurysmal Dilation
C0	n	8	8	8	8	8	8	8	8	8	8	8	8	8	8	8	8	8	8	8
	Mean	4.0	1.8	0.0	0.0	0.0	0.0	0.0	0.0	0.8	0.0	0.0	0.0	0.0	0.1	0.0	0.0	0.0	0.0	0.0
	StDev	0.0	1.1	0.0	0.0	0.0	0.0	0.0	0.0	0.7	0.0	0.0	0.0	0.0	0.3	0.0	0.0	0.0	0.0	0.0
C1	n	9	9	9	9	9	9	9	9	9	9	9	9	9	9	9	9	9	9	9
	Mean	4.0	1.3	0.0	0.0	0.0	0.0	0.0	0.0	0.9	0.0	0.0	0.0	0.0	0.6	0.0	0.0	0.0	0.0	0.0
	StDev	0.0	0.5	0.0	0.0	0.0	0.0	0.0	0.0	0.3	0.0	0.0	0.0	0.0	0.7	0.0	0.0	0.0	0.0	0.0
C2	n	7	7	7	7	7	7	7	7	7	7	7	7	7	7	7	7	7	7	7
	Mean	4.0	0.4	0.0	0.0	0.0	0.0	0.0	0.0	0.7	0.0	0.0	0.0	0.0	0.0	0.0	0.0	0.0	0.0	0.0
	StDev	0.0	0.5	0.0	0.0	0.0	0.0	0.0	0.0	0.5	0.0	0.0	0.0	0.0	0.0	0.0	0.0	0.0	0.0	0.0
C3	n	6	6	6	6	6	6	6	6	6	6	6	6	6	6	6	6	6	6	6
	Mean	4.0	1.2	0.0	0.0	0.0	0.0	0.0	0.0	1.0	0.0	0.0	0.0	0.0	0.0	0.0	0.0	0.0	0.0	0.0
	StDev	0.0	0.4	0.0	0.0	0.0	0.0	0.0	0.0	0.0	0.0	0.0	0.0	0.0	0.0	0.0	0.0	0.0	0.0	0.0
C4	n	4	4	4	4	4	4	4	4	4	4	4	4	4	4	4	4	4	4	4
	Mean	4.0	0.8	0.0	0.0	0.0	0.0	0.0	0.0	0.3	0.0	0.0	0.0	0.0	0.0	0.0	0.0	0.0	0.0	0.0
	StDev	0.0	0.5	0.0	0.0	0.0	0.0	0.0	0.0	0.5	0.0	0.0	0.0	0.0	0.0	0.0	0.0	0.0	0.0	0.0
C5	n	10	10	10	10	10	10	10	10	10	10	10	10	10	10	10	10	10	10	10
	Mean	4.0	1.9	0.0	0.0	0.0	0.0	0.0	0.0	0.6	0.0	0.0	0.0	0.0	0.0	0.0	0.0	0.0	0.0	0.0
	StDev	0.0	0.9	0.0	0.0	0.0	0.0	0.0	0.0	0.5	0.0	0.0	0.0	0.0	0.0	0.0	0.0	0.0	0.0	0.0
C6	n	4	4	4	4	4	4	4	4	4	4	4	4	4	4	4	4	4	4	4
	Mean	4.0	3.5	0.0	0.0	0.0	0.0	0.0	0.0	1.0	0.0	0.0	0.0	0.0	0.0	0.0	0.0	0.0	0.0	0.0
	StDev	0.0	0.6	0.0	0.0	0.0	0.0	0.0	0.0	0.8	0.0	0.0	0.0	0.0	0.0	0.0	0.0	0.0	0.0	0.0

n = Number of segments used in calculations;
StDev = Standard Deviation

Table_Apx C-5 Continued 2: Tabulated Microscopic Data Continued (Part 3)

HJC19-339						INJURY																INFLAMMATION											
						Vessel Wall Injury (scored per quadrant)						Severe Injury (Disruptions)			Thermal Injury				See pathology narrative for scoring definitions.															
																			Mural Inflammation (scored per quadrant)						Inflammatory Cell Types					Inflammation Distribution		
Wavelength (nm)	Condition Number	Fluence (J/cm²)	Specimen (Artery)	Segment	I	II	III	IV	Injury Mean	Injury Median	Mural Erosion	Mural Dissection	Mural Avulsion	Mural Acute Thermal Injury	Media Necrosis	Media Hyalinization	Hyalinized Collagen without Other Thermal Injury	I	II	III	IV	Inflammation Mean	Inflammation Median	*Neutrophils*	*Eosinophils*	*Lymphocytes*	*Histiocytes*	*Foreign Body Giant cells*	Inflammation, Neointima	Inflammation, Media	Inflammation, Adventitia
None	C0	0	1	1-A	0	0	0	0	0.0	0.0	0	0	0	0	**1**	0	0	0	**1**	0	0	**0.3**	0.0	**1**	0	0	0	0	0	0	**1**
				1-B	0	0	0	0	0.0	0.0	0	0	0	0	**1**	0	0	0	0	0	0	0.0	0.0	0	0	0	0	0	0	0	0
				1-C	0	0	0	0	0.0	0.0	0	0	0	0	**2**	0	0	0	**1**	0	0	**0.3**	0.0	**1**	0	0	0	0	0	0	**1**
				1-D**	0	0	0	0	0.0	0.0	0	0	0	0	**1**	0	0	0	0	0	**1**	**0.3**	0.0	**1**	0	0	0	0	0	0	**1**
			2	2-A	0	0	0	0	0.0	0.0	0	0	0	0	**1**	0	**1**	0	0	0	0	0.0	0.0	0	0	0	0	0	0	0	0
				2-B	0	0	0	0	0.0	0.0	0	0	0	0	0	0	0	0	0	0	0	0.0	0.0	0	0	0	0	0	0	0	0
				2-P***	0	0	0	0	0.0	0.0	0	0	0	0	0	0	0	0	0	0	0	0.0	0.0	0	0	0	0	0	0	0	0
			3	3-A	0	0	0	0	0.0	0.0	0	0	0	0	0	0	0	0	0	0	0	0.0	0.0	0	0	0	0	0	0	0	0
				3-B	0	0	0	0	0.0	0.0	0	0	0	0	0	0	**2**	**1**	**1**	0	0	**0.5**	**0.5**	**1**	0	0	0	0	0	0	**1**

* = Treatment applied to ~1/4 of circumference;
** = Section is incomplete;
*** = Marker suture hole present

Table_Apx C-5 Continued 3: Tabulated Microscopic Data Continued (Part 4)

HJC19-339					INJURY														INFLAMMATION													
					Vessel Wall Injury (scored per quadrant)						Severe Injury (Disruptions)				Thermal Injury				See pathology narrative for scoring definitions.													
																			Mural Inflammation (scored per quadrant)						Inflammatory Cell Types					Inflammation Distribution		
Wavelength (nm)	Condition Number	Fluence (J/cm²)	Specimen (Artery)	Segment	I	II	III	IV	Injury Mean	Injury Median	Mural Erosion	Mural Dissection	Mural Avulsion	Mural Acute Thermal Injury	Media Necrosis	Media Hyalinization	Hyalinized Collagen without Other Thermal Injury	I	II	III	IV	Inflammation Mean	Inflammation Median	*Neutrophils*	*Eosinophils*	*Lymphocytes*	*Histiocytes*	*Foreign Body Giant cells*	Inflammation, Neointima	Inflammation, Media	Inflammation, Adventitia
1064	C1	8.3	1	1-E*	0	0	0	0	0.0	0.0	0	0	0	0	1	0	0	1	0	0	0	0.3	0.0	1	0	0	0	0	0	0	1
				1-F*	0	0	0	0	0.0	0.0	0	0	0	0	2	0	0	0	0	0	0	0.0	0.0	0	0	0	0	0	0	0	0
				1-G	0	0	0	0	0.0	0.0	0	0	0	0	1	0	0	0	0	0	1	0.3	0.0	1	0	0	0	0	0	0	1
				1-H	0	0	0	0	0.0	0.0	0	0	0	0	2	0	0	0	0	1	1	0.5	0.5	1	0	0	0	0	0	0	1
			2	2-C	0	0	0	0	0.0	0.0	0	0	0	0	1	0	0	0	1	0	0	0.3	0.0	1	0	0	0	0	0	0	1
				2-D	0	0	0	0	0.0	0.0	0	0	0	0	1	0	1	0	0	0	0	0.0	0.0	0	0	0	0	0	0	0	0
				2-E	0	0	0	0	0.0	0.0	0	0	0	0	1	0	0	0	0	0	1	0.3	0.0	1	0	0	0	0	0	0	1
				2-F	0	0	0	0	0.0	0.0	0	0	0	0	1	0	0	0	0	0	0	0.0	0.0	0	0	0	0	0	0	0	0
				2-G	0	0	0	0	0.0	0.0	0	0	0	0	0	0	0	0	0	1	1	0.5	0.5	1	0	0	0	0	0	0	1
	C2	100	1	1-I	0	0	0	0	0.0	0.0	0	0	0	0	2	0	0	1	1	0	0	0.5	0.5	1	0	0	0	0	0	0	1
				1-J	0	0	0	0	0.0	0.0	0	0	0	0	2	0	0	0	0	0	0	0.0	0.0	0	0	0	0	0	0	0	0
			2	2-H	0	0	0	0	0.0	0.0	0	0	0	0	0	0	0	0	0	0	0	0.0	0.0	0	0	0	0	0	0	0	0
				2-I	0	0	0	0	0.0	0.0	0	0	0	0	0	0	0	0	0	0	0	0.0	0.0	0	0	0	0	0	0	0	0
				2-J	0	0	0	0	0.0	0.0	0	0	0	0	0	0	0	0	0	0	0	0.0	0.0	0	0	0	0	0	0	0	0
				2-K	0	0	0	0	0.0	0.0	0	0	0	0	0	0	0	0	0	0	0	0.0	0.0	0	0	0	0	0	0	0	0
				2-L	0	0	0	0	0.0	0.0	0	0	0	0	1	0	0	0	0	0	0	0.0	0.0	0	0	0	0	0	0	0	0
	C3	700	1	1-K	0	0	0	0	0.0	0.0	0	0	0	0	2	0	0	1	0	0	1	0.5	0.5	1	0	0	0	0	0	0	1
				1-L	0	0	0	0	0.0	0.0	0	0	0	0	2	0	0	0	1	0	0	0.3	0.0	1	0	0	0	0	0	0	1
			2	2-M	0	0	0	0	0.0	0.0	0	0	0	0	1	0	0	0	0	0	1	0.3	0.0	1	0	0	0	0	0	0	1
				2-N	0	0	0	0	0.0	0.0	0	0	0	0	1	0	0	0	0	0	0	0.0	0.0	0	0	0	0	0	0	0	0
				2-O	0	0	0	0	0.0	0.0	0	0	0	0	1	0	0	0	0	0	0	0.0	0.0	0	0	0	0	0	0	0	0

* = Treatment applied to ~1/4 of circumference;
** = Section is incomplete;
*** = Marker suture hole present

Table_Apx C-5 Continued 4: Tabulated Microscopic Data Continued (Part 5)

HJC19-339					INJURY													INFLAMMATION												
					Vessel Wall Injury (scored per quadrant)						Severe Injury (Disruptions)			Thermal Injury				See pathology narrative for scoring definitions.												
																		Mural Inflammation (scored per quadrant)					Inflammatory Cell Types					Inflammation Distribution		
Wavelength (nm)	Condition Number	Fluence (J/cm²)	Specimen (Artery)	Segment	I	II	III	IV	Injury Mean	Injury Median	Mural Erosion	Mural Dissection	Mural Avulsion	Mural Acute Thermal Injury	Media Necrosis	Media Hyalinization	Hyalinized Collagen without Other Thermal Injury	I	II	III	IV	Inflammation Mean	Inflammation Median	Neutrophils	Eosinophils	Lymphocytes	Histiocytes	Foreign Body Giant cells	Inflammation, Neointima	Inflammation, Media	Inflammation, Adventitia
1720	C4	8.3	1	1-M	0	0	0	0	0.0	0.0	0	0	0	0	**2**	0	0	1	0	0	**1**	**0.5**	**0.5**	1	0	0	0	0	0	0	**1**
			3	3-C	0	0	0	0	0.0	0.0	0	0	0	0	0	0	**2**	1	0	0	1	**0.5**	**0.5**	1	0	0	0	0	0	0	**1**
				3-D	0	0	0	0	0.0	0.0	0	0	0	0	0	0	0	0	0	0	0	0.0	0.0	0	0	0	0	0	0	0	0
				3-E	0	0	0	0	0.0	0.0	0	0	0	0	0	0	0	1	0	0	1	**0.5**	**0.5**	1	0	0	0	0	0	0	**1**
	C5	50	1	1-N	0	0	0	0	0.0	0.0	0	0	0	**1**	**2**	0	0	0	1	0	0	**0.3**	0.0	1	0	0	0	0	0	0	**1**
				1-O	0	0	0	0	0.0	0.0	0	0	0	**1**	**3**	0	0	0	1	1	0	**0.5**	**0.5**	1	0	0	0	0	0	0	**1**
			3	3-F	0	0	0	0	0.0	0.0	0	0	0	0	**1**	0	0	1	0	0	1	**0.5**	**0.5**	1	0	0	0	0	0	0	**1**
				3-G	0	0	0	0	0.0	0.0	0	0	0	0	**1**	0	0	0	0	1	0	**0.3**	0.0	1	0	0	0	0	0	0	**1**
				3-H	0	0	0	0	0.0	0.0	0	0	0	0	**2**	0	0	0	1	1	0	**0.5**	**0.5**	1	0	0	0	0	0	0	**1**
				3-I	0	0	0	0	0.0	0.0	0	0	0	0	**2**	0	0	0	1	0	0	**0.3**	0.0	1	0	0	0	0	0	0	**1**
				3-J	0	0	0	0	0.0	0.0	0	0	0	0	**2**	0	0	0	0	0	0	0.0	0.0	0	0	0	0	0	0	0	0
				3-K	0	0	0	0	0.0	0.0	0	0	0	0	**3**	0	0	0	0	0	0	0.0	0.0	0	0	0	0	0	0	0	0
				3-L	0	0	0	0	0.0	0.0	0	0	0	0	**3**	0	0	0	0	0	0	0.0	0.0	0	0	0	0	0	0	0	0
				3-M	0	0	0	0	0.0	0.0	0	0	0	0	**3**	0	0	0	0	0	0	0.0	0.0	0	0	0	0	0	0	0	0
	C6	200	1	1-P	0	0	0	0	0.0	0.0	0	0	0	0	**3**	0	0	0	0	0	0	0.0	0.0	0	0	0	0	0	0	0	0
			3	3-N	0	0	0	0	0.0	0.0	0	0	0	0	**4**	0	0	0	0	0	0	0.0	0.0	0	0	0	0	0	0	0	0
				3-O	0	0	0	0	0.0	0.0	0	0	0	0	**3**	0	0	0	0	0	0	0.0	0.0	0	0	0	0	0	0	0	0
				3-P	0	0	0	0	0.0	0.0	0	0	0	0	**3**	0	0	0	0	0	0	0.0	0.0	0	0	0	0	0	0	0	0

* = Treatment applied to ~1/4 of circumference;
** = Section is incomplete;
*** = Marker suture hole present

Table_Apx C-5 Continued 5: Tabulated Microscopic Data Continued (Part 6)

HJC19-339					HEALING																			
					See pathology narrative for scoring definitions.																			
					Endovascular									Vessel Wall								Other		
Wavelength (nm)	Condition Number	Fluence (J/cm²)	Specimen (Artery)	Segment	Endothelialization	Endothelium Erosion (luminal or artifact)	Leukocyte Margination	Thrombosis	Occlusion	Neointima Fibrin	Neointima Maturity	Neointima - Hyalinization	Hemosiderin/Hemorrhage, Vessel Wall	Mural - Necrosis/Hyalinization	Mural Calcification	Mural Neovascularization	Media Fibrosis	Adventitia Edema	Adventitial Fibrosis	Adventitia Granulation Tissue	Vasculitis/Perivasculitis- Branch	Branch - Thrombus	Aneurysmal Dilation
None	C0	0	1	1-A	4	1	0	0	0	0	0	0	1	0	0	0	0	0	0	0	0	0	0
				1-B	4	1	0	0	0	0	0	0	1	0	0	0	0	0	0	0	0	0	0
				1-C	4	1	0	0	0	0	0	0	1	0	0	0	0	0	0	0	0	0	0
				1-D**	4	2	0	0	0	0	0	0	1	0	0	0	0	0	0	0	0	0	0
			2	2-A	4	4	0	0	0	0	0	0	0	0	0	0	0	0	0	0	0	0	0
				2-B	4	3	0	0	0	0	0	0	1	0	0	0	0	1	0	0	0	0	0
				2-P***	4	2	0	0	0	0	0	0	2	0	0	0	0	0	0	0	0	0	0
			3	3-A	4	1	0	0	0	0	0	0	0	0	0	0	0	0	0	0	0	0	0
				3-B	4	1	0	0	0	0	0	0	0	0	0	0	0	0	0	0	0	0	0

* = Treatment applied to ~1/4 of circumference;
** = Section is incomplete;
*** = Marker suture hole present

Table_Apx C-5 Continued 6: Tabulated Microscopic Data Continued (Part 7)

HJC19-339					HEALING																				
					See pathology narrative for scoring definitions.																				
					Endovascular									Vessel Wall									Other		
Wavelength (nm)	Condition Number	Fluence (J/cm²)	Specimen (Artery)	Segment	Endothelialization	Endothelium Erosion (teminal or artifact)	Leukocyte Margination	Thrombosis	Occlusion	Neointima Fibrin	Neointima Maturity	Neointima - Hyalinization	Hemosiderin/Hemorrhage, Vessel Wall	Mural - Necrosis/Hyalinization	Mural Calcification	Mural Neovascularization	Media Fibrosis	Adventitia Edema	Adventitial Fibrosis	Adventitia Granulation Tissue	Vasculitis/Perivasculitis- Branch	Branch - Thrombus	Aneurysmal Dilation
1064	C1	8.3	1	1-E*	4	1	0	0	0	0	0	0	1	0	0	0	0	0	0	0	0	0	0	0	0
				1-F*	4	2	0	0	0	0	0	0	0	0	0	0	0	0	0	0	0	0	0	0	0
				1-G	4	1	0	0	0	0	0	0	1	0	0	0	0	0	0	0	0	0	0	0	0
				1-H	4	1	0	0	0	0	0	0	1	0	0	0	0	0	0	0	0	0	0	0	0
			2	2-C	4	2	0	0	0	0	0	0	1	0	0	0	0	1	0	0	0	0	0	0	0
				2-D	4	2	0	0	0	0	0	0	1	0	0	0	0	0	0	0	0	0	0	0	0
				2-E	4	1	0	0	0	0	0	0	1	0	0	0	0	1	0	0	0	0	0	0	0
				2-F	4	1	0	0	0	0	0	0	1	0	0	0	0	2	0	0	0	0	0	0	0
				2-G	4	1	0	0	0	0	0	0	1	0	0	0	0	1	0	0	0	0	0	0	0
	C2	100	1	1-I	4	1	0	0	0	0	0	0	0	0	0	0	0	0	0	0	0	0	0	0	0
				1-J	4	1	0	0	0	0	0	0	0	0	0	0	0	0	0	0	0	0	0	0	0
			2	2-H	4	0	0	0	0	0	0	0	1	0	0	0	0	0	0	0	0	0	0	0	0
				2-I	4	0	0	0	0	0	0	0	1	0	0	0	0	0	0	0	0	0	0	0	0
				2-J	4	0	0	0	0	0	0	0	1	0	0	0	0	0	0	0	0	0	0	0	0
				2-K	4	0	0	0	0	0	0	0	1	0	0	0	0	0	0	0	0	0	0	0	0
				2-L	4	1	0	0	0	0	0	0	1	0	0	0	0	0	0	0	0	0	0	0	0
	C3	700	1	1-K	4	1	0	0	0	0	0	0	1	0	0	0	0	0	0	0	0	0	0	0	0
				1-L	4	1	0	0	0	0	0	0	1	0	0	0	0	0	0	0	0	0	0	0	0
			2	2-M	4	1	0	0	0	0	0	0	1	0	0	0	0	0	0	0	0	0	0	0	0
				2-N	4	1	0	0	0	0	0	0	1	0	0	0	0	0	0	0	0	0	0	0	0
				2-O	4	2	0	0	0	0	0	0	1	0	0	0	0	0	0	0	0	0	0	0	0

* = Treatment applied to ~1/4 of circumference;
** = Section is incomplete;
*** = Marker suture hole present

Table_Apx C-5 Continued 7: Tabulated Microscopic Data Continued (Part 8)

HJC19-339					HEALING																			
					See pathology narrative for scoring definitions.																			
					Endovascular									Vessel Wall								Other		
Wavelength (nm)	Condition Number	Fluence (J/cm²)	Specimen (Artery)	Segment	Endothelialization	Endothelium Erosion (terminal or artifact)	Leukocyte Margination	Thrombosis	Occlusion	Neointima Fibrin	Neointima Maturity	Neointima - Hyalinization	Hemosiderin/Hemorrhage, Vessel Wall	Mural - Necrosis/Hyalinization	Mural Calcification	Mural Neovascularization	Media Fibrosis	Adventitia Edema	Adventitial Fibrosis	Adventitia Granulation Tissue	Vasculitis/Perivasculitis- Branch	Branch - Thrombus	Aneurysmal Dilation
1720	C4	8.3	1	1-M	4	1	0	0	0	0	0	0	1	0	0	0	0	0	0	0	0	0	0	0
			3	3-C	4	0	0	0	0	0	0	0	0	0	0	0	0	0	0	0	0	0	0	0
				3-D	4	1	0	0	0	0	0	0	0	0	0	0	0	0	0	0	0	0	0	0
				3-E	4	1	0	0	0	0	0	0	0	0	0	0	0	0	0	0	0	0	0	0
	C5	50	1	1-N	4	1	0	0	0	0	0	0	1	0	0	0	0	0	0	0	0	0	0	0
				1-O	4	1	0	0	0	0	0	0	1	0	0	0	0	0	0	0	0	0	0	0
			3	3-F	4	1	0	0	0	0	0	0	0	0	0	0	0	0	0	0	0	0	0	0
				3-G	4	1	0	0	0	0	0	0	0	0	0	0	0	0	0	0	0	0	0	0
				3-H	4	2	0	0	0	0	0	0	0	0	0	0	0	0	0	0	0	0	0	0
				3-I	4	3	0	0	0	0	0	0	0	0	0	0	0	0	0	0	0	0	0	0
				3-J	4	3	0	0	0	0	0	0	1	0	0	0	0	0	0	0	0	0	0	0
				3-K	4	2	0	0	0	0	0	0	1	0	0	0	0	0	0	0	0	0	0	0
				3-L	4	2	0	0	0	0	0	0	1	0	0	0	0	0	0	0	0	0	0	0
				3-M	4	3	0	0	0	0	0	0	1	0	0	0	0	0	0	0	0	0	0	0
	C6	200	1	1-P	4	3	0	0	0	0	0	0	0	0	0	0	0	0	0	0	0	0	0	0
			3	3-N	4	3	0	0	0	0	0	0	1	0	0	0	0	0	0	0	0	0	0	0
				3-O	4	4	0	0	0	0	0	0	1	0	0	0	0	0	0	0	0	0	0	0
				3-P	4	4	0	0	0	0	0	0	2	0	0	0	0	0	0	0	0	0	0	0

* = Treatment applied to ~1/4 of circumference;
** = Section is incomplete;
*** = Marker suture hole present

APPENDIX D: Pathologist Q&A

The following gives a series of questions for the pathologist with answers. The questions were originally answered in a phone call and answered verbally. However, the pathologist also returned the questions with written answers while sending us the final report. Our questions are in black, while the pathologist's responses are in red.

Definitions and Causes of Damage Types:

Please clarify the meaning of the following types of damage:

Hypereosinophilic (smooth muscle cells)

Compressive/pressure necrosis

Contraction bands

Is there a hierarchy of damage severity for the damage types you describe (shown below)? Can you categorize these in terms of their potential causes (mechanical catheter damage, heat accumulation, heavy water flushing)

Hypereosinophilic (SMCs)

Collagen denaturation

Necrotic/apoptotic cells

Cell effacement

Contraction bands

Endothelialization

Pathologist Response: *Added clarification for the above in the Executive Summary Pathology Report.*

Is there a primary damage mechanism we should be looking at?

Can you categorize these types of damage in terms of their potential causes? In terms of our experiments, possibilities include:

(a) mechanical damage from catheter

(b) heat accumulation from laser

(c) heavy water injection (possible higher pressure for extended periods)

(d) cutdown via electrocauterization (the cardiologist knew the purpose of the experiment, and thus should have avoided direct contact with the artery, but I don't think we should rule out some local damage remaining)

(e) lack of nutrients/oxygen delivery from blood flushing (1-2 hours from blood flushing to tissue fixation)

Pathologist Response: There is not a morphological change that is specific or pathognomonic for the type of energy that you are delivering. What makes your modality different is the mode of delivery and hence to distribution of these changes. Recognizing it requires experience with your treatment and experimental settings and comparison between control and test. Reducing background noise and artifacts will help sharpen up the acute signal.

Conditions/Image Specific Questions:

Slide 11, Figure 16 – "area has no evident necrosis but also hypereosinophilia and pyknosis consistent with compression necrosis". Seems to contradict. Can you explain?

Is collagen denaturization tabulated anywhere?

Pathologist Response: Clarified caption for Figure 16 – please see Executive Summary Pathology Report. For collagen denaturation, please see collagen injury subheading in data table, namely hyalinized collagen.

Analysis/Interpretation Questions:

Certain types of damage (compression necrosis, focal cauterization of collagen in adventitia) are present at all conditions. Why is it that damage at higher dosages was rated as more severe?

Pathologist Response: Reading was done blind, so severity scores reflect extent seen at time of evaluation.

Was there an increase in intensity in collagen denaturization between conditions types (this feature was present in controls)?

Pathologist Response: I can't account for presence in controls except for cauterization during dissection.

At lower dosages, the outer media seems affected while the internal media is intact. At higher dosages, damage is present in the internal layer and sometime the outer layers. What is your interpretation of this?

Pathologist Response: Variations in energy delivery with dose. Some amount is background noise so I would refrain from trying to over analyze this until you produce cleaner results (less handling and fixation artifacts).

Big Picture Questions:

Are there specific conditions where more samples would be informative, or would it be better to test other intermediate conditions between the energy levels already chosen? If so, please specify which.

Pathologist Response: Highest order of priority is to decrease background noise as stated above.

Will the tissue at these damage levels heal? Do expect any of these types of damage to be life threatening?

Pathologist Response: Yes, they will heal and no, they are not life threatening.

Would a chronic study (injury then sacrifice two month later) be useful?

Pathologist Response: Yes and will be required to demonstrate healing and lack of adverse changes.

What does the FDA usually require to ensure the safety of a device like this? Is there anything you can suggest to make our experiments meet their expected requirements more closely?

Pathologist Response: See above: reach a steady state of recovery and healing and no permanent damage that impact function (i.e. stenosis).

In more laymen's terms, how do the histological types of damage found in this analysis relate to the safety/well-being of an animal or patient undergoing imaging?

Pathologist Response: Nothing seen here represents a safety concern but a chronic time period (4 weeks) would be required to confirm that healing is uneventful.

What conditions or changes to protocol should be made to the next set of experiments?

Pathologist Response: Optimize tissue harvest conditions: no cauterization, perfusion fixation prior to tissue extraction, contention of tissue on a rigid support to avoid longitudinal recoil and shrinkage. Add recovery/healing timepoint.

REFERENCES

1. Wang, L.V. and J. Yao, A practical guide to photoacoustic tomography in the life sciences. *Nat Methods*, 2016. **13**(8): p. 627-38.
2. Xu, M.H. and L.H.V. Wang, Photoacoustic imaging in biomedicine. *Review of Scientific Instruments*, 2006. **77**(4).
3. Bell, A.G., *Upon the production of sound by radiant energy*. 1881, Washington,: Gibson brothers, printers. 45 p. incl. plates.
4. Gusev, V.E. and A.A. Karabutov, *Laser optoacoustics*. 1993, New York: American Institute of Physics. xvii, 271 p.
5. Oraevsky, A.A., S.L. Jacques, and F.K. Tittel, Measurement of tissue optical properties by time-resolved detection of laser-induced transient stress. *Appl Opt*, 1997. **36**(1): p. 402-15.
6. Emelianov, S.Y., et al., Synergy and Applications of Combined Ultrasound, Elasticity, and Photoacoustic Imaging. *2006 Ieee Ultrasonics Symposium, Vols 1-5, Proceedings*, 2006: p. 405-+.
7. Diot, G., A. Dima, and V. Ntziachristos, Multispectral opto-acoustic tomography of exercised muscle oxygenation. *Opt Lett*, 2015. **40**(7): p. 1496-9.
8. Erpelding, T.N., et al., Sentinel lymph nodes in the rat: noninvasive photoacoustic and US imaging with a clinical US system. *Radiology*, 2010. **256**(1): p. 102-10.
9. Li, R., et al., Assessing breast tumor margin by multispectral photoacoustic tomography. *Biomedical Optics Express*, 2015. **6**(4): p. 1273-1281.
10. Luke, G.P., D. Yeager, and S.Y. Emelianov, Biomedical Applications of Photoacoustic Imaging with Exogenous Contrast Agents. *Annals of Biomedical Engineering*, 2012. **40**(2): p. 422-437.
11. Pramanik, M. and L.V. Wang, Thermoacoustic and photoacoustic sensing of temperature. *J Biomed Opt*, 2009. **14**(5): p. 054024.
12. Sowers, T. and S. Emelianov, Exogenous imaging contrast and therapeutic agents for intravascular photoacoustic imaging and image-guided therapy. *Physics in Medicine and Biology*, 2018. **63**(22).
13. Wang, B., et al., Intravascular Photoacoustic Imaging. *Ieee Journal of Selected Topics in Quantum Electronics*, 2010. **16**(3): p. 588-599.
14. Zackrisson, S., S.M.W.Y. van de Ven, and S.S. Gambhir, Light In and Sound Out: Emerging Translational Strategies for Photoacoustic Imaging. *Cancer Research*, 2014. **74**(4): p. 979-1004.
15. Oraevsky, A.A., et al., Clinical optoacoustic imaging combined with ultrasound for coregistered functional and anatomical mapping of breast tumors. *Photoacoustics*, 2018. **12**: p. 30-45.
16. Haisch, C., et al., Combined optoacoustic/ultrasound system for tomographic absorption measurements: possibilities and limitations. *Anal Bioanal Chem*, 2010. **397**(4): p. 1503-10.
17. Niederhauser, J.J., et al., Combined ultrasound and optoacoustic system for real-time high-contrast vascular imaging in vivo. *IEEE Trans Med Imaging*, 2005. **24**(4): p. 436-40.

18. Kim, C., et al., Deeply penetrating in vivo photoacoustic imaging using a clinical ultrasound array system. *Biomedical Optics Express*, 2010. **1**(1): p. 278-284.
19. Sivasubramanian, K., V. Periyasamy, and M. Pramanik, Non-invasive sentinel lymph node mapping and needle guidance using clinical handheld photoacoustic imaging system in small animal. *Journal of Biophotonics*, 2018. **11**(1).
20. Organization, W.H. *Cardiovascular diseases (CVDs)*. 2017 [cited 2017 Feb 2018]; Available from: http://www.who.int/mediacentre/factsheets/fs317/en/.
21. Libby, P., Inflammation in atherosclerosis. *Nature*, 2002. **420**(6917): p. 868-74.
22. Fischman, D.L., et al., A randomized comparison of coronary-stent placement and balloon angioplasty in the treatment of coronary artery disease. Stent Restenosis Study Investigators. *N Engl J Med*, 1994. **331**(8): p. 496-501.
23. Kolodgie, F.D., et al., Pathologic assessment of the vulnerable human coronary plaque. *Heart*, 2004. **90**(12): p. 1385-1391.
24. van der Wal, A.C. and A.E. Becker, Atherosclerotic plaque rupture--pathologic basis of plaque stability and instability. *Cardiovasc Res*, 1999. **41**(2): p. 334-44.
25. Virmani, R., et al., Lessons from sudden coronary death - A comprehensive morphological classification scheme for atherosclerotic lesions. *Arteriosclerosis Thrombosis and Vascular Biology*, 2000. **20**(5): p. 1262-1275.
26. Farb, A., et al., Coronary plaque erosion without rupture into a lipid core - A frequent cause of coronary thrombosis in sudden coronary death. *Circulation*, 1996. **93**(7): p. 1354-1363.
27. Quillard, T., et al., Mechanisms of erosion of atherosclerotic plaques. *Current Opinion in Lipidology*, 2017. **28**(5): p. 434-441.
28. Skeoch, S. and I.N. Bruce, Atherosclerosis in rheumatoid arthritis: is it all about inflammation? *Nature Reviews Rheumatology*, 2015. **11**(7): p. 390-400.
29. Glass, C.K. and J.L. Witztum, Atherosclerosis. the road ahead. *Cell*, 2001. **104**(4): p. 503-16.
30. Libby, P., et al., Atherosclerosis. *Nat Rev Dis Primers*, 2019. **5**(1): p. 56.
31. Rafieian-Kopaei, M., et al., Atherosclerosis: process, indicators, risk factors and new hopes. *Int J Prev Med*, 2014. **5**(8): p. 927-46.
32. Doradla, P., et al., Biomechanical Stress Profiling of Coronary Atherosclerosis: Identifying a Multifactorial Metric to Evaluate Plaque Rupture Risk. *JACC Cardiovasc Imaging*, 2020. **13**(3): p. 804-816.
33. Li, S., et al., Circulating microRNAs as potential biomarkers for coronary plaque rupture. *Oncotarget*, 2017. **8**(29): p. 48145-48156.
34. Libby, P., et al., Reassessing the Mechanisms of Acute Coronary Syndromes. *Circ Res*, 2019. **124**(1): p. 150-160.
35. Otsuka, F., et al., Pathology of coronary atherosclerosis and thrombosis. *Cardiovasc Diagn Ther*, 2016. **6**(4): p. 396-408.
36. Davies, M.J., Stability and instability: two faces of coronary atherosclerosis. The Paul Dudley White Lecture 1995. *Circulation*, 1996. **94**(8): p. 2013-20.
37. Narula, J., et al., Histopathologic characteristics of atherosclerotic coronary disease and implications of the findings for the invasive and noninvasive detection of vulnerable plaques. *J Am Coll Cardiol*, 2013. **61**(10): p. 1041-51.
38. Van der Wal, A.C., et al., Site of Intimal Rupture or Erosion of Thrombosed Coronary Atherosclerotic Plaques Is Characterized by an Inflammatory Process

Irrespective of the Dominant Plaque Morphology. *Circulation*, 1994. **89**(1): p. 36-44.
39. Libby, P. and G. Pasterkamp, Requiem for the 'vulnerable plaque'. *Eur Heart J*, 2015. **36**(43): p. 2984-7.
40. Naghavi, M., et al., From vulnerable plaque to vulnerable patient: a call for new definitions and risk assessment strategies: Part II. *Circulation*, 2003. **108**(15): p. 1772-8.
41. Stone, G.W., et al., A prospective natural-history study of coronary atherosclerosis. *N Engl J Med*, 2011. **364**(3): p. 226-35.
42. Waksman, R., et al., Identification of patients and plaques vulnerable to future coronary events with near-infrared spectroscopy intravascular ultrasound imaging: a prospective, cohort study. *Lancet*, 2019. **394**(10209): p. 1629-1637.
43. Libby, P. and P. Theroux, Pathophysiology of coronary artery disease. *Circulation*, 2005. **111**(25): p. 3481-8.
44. Jansen, K., et al., Photoacoustic imaging of human coronary atherosclerosis in two spectral bands. *Photoacoustics*, 2014. **2**(1): p. 12-20.
45. Sowers, T. and S. Emelianov, Exogenous imaging contrast and therapeutic agents for intravascular photoacoustic imaging and image-guided therapy. *Phys Med Biol*, 2018. **63**(22): p. 22TR01.
46. Karpiouk, A.B., B. Wang, and S.Y. Emelianov, Development of a catheter for combined intravascular ultrasound and photoacoustic imaging. *Review of Scientific Instruments*, 2010. **81**(1).
47. Sethuraman, S., et al., Intravascular photoacoustic imaging using an IVUS imaging catheter. *Ieee Transactions on Ultrasonics Ferroelectrics and Frequency Control*, 2007. **54**(5): p. 978-986.
48. Cao, Y.C., et al., High-sensitivity intravascular photoacoustic imaging of lipid-laden plaque with a collinear catheter design. *Scientific Reports*, 2016. **6**.
49. Wang, B. and S. Emelianov, Thermal intravascular photoacoustic imaging. *Biomed Opt Express*, 2011. **2**(11): p. 3072-8.
50. Jansen, K., et al., Intravascular photoacoustic imaging of human coronary atherosclerosis. *Opt Lett*, 2011. **36**(5): p. 597-9.
51. Jansen, K., et al., Spectroscopic intravascular photoacoustic imaging of lipids in atherosclerosis. *J Biomed Opt*, 2014. **19**(2): p. 026006.
52. Sethuraman, S., et al., Spectroscopic intravascular photoacoustic imaging to differentiate atherosclerotic plaques. *Opt Express*, 2008. **16**(5): p. 3362-7.
53. Yeager, D., et al., Intravascular photoacoustic imaging of exogenously labeled atherosclerotic plaque through luminal blood. *Journal of Biomedical Optics*, 2012. **17**(10).
54. VanderLaan, D., et al., Real-Time Intravascular Ultrasound and Photoacoustic Imaging. *IEEE Trans Ultrason Ferroelectr Freq Control*, 2017. **64**(1): p. 141-149.
55. Wu, M., et al., Real-time volumetric lipid imaging in vivo by intravascular photoacoustics at 20 frames per second. *Biomedical Optics Express*, 2017. **8**(2): p. 943-953.

56. Kole, A., et al., Comparative Quantification of Arterial Lipid by Intravascular Photoacoustic-Ultrasound Imaging and Near-Infrared Spectroscopy-Intravascular Ultrasound. *J Cardiovasc Transl Res*, 2019. **12**(3): p. 211-220.
57. Iskander-Rizk, S., et al., In vivo intravascular photoacoustic imaging of plaque lipid in coronary atherosclerosis. *EuroIntervention*, 2019. **15**(5): p. 452-456.
58. Vancraeynest, D., et al., Imaging the vulnerable plaque. *J Am Coll Cardiol*, 2011. **57**(20): p. 1961-79.
59. Falk, E., Plaque rupture with severe pre-existing stenosis precipitating coronary thrombosis. Characteristics of coronary atherosclerotic plaques underlying fatal occlusive thrombi. *Br Heart J*, 1983. **50**(2): p. 127-34.
60. Takano, M., et al., Mechanical and structural characteristics of vulnerable plaques: analysis by coronary angioscopy and intravascular ultrasound. *J Am Coll Cardiol*, 2001. **38**(1): p. 99-104.
61. Thieme, T., et al., Angioscopic evaluation of atherosclerotic plaques: validation by histomorphologic analysis and association with stable and unstable coronary syndromes. *J Am Coll Cardiol*, 1996. **28**(1): p. 1-6.
62. Ueda, Y., et al., Assessment of plaque vulnerability by angioscopic classification of plaque color. *Am Heart J*, 2004. **148**(2): p. 333-5.
63. DeMaria, A.N., et al., Imaging vulnerable plaque by ultrasound. *J Am Coll Cardiol*, 2006. **47**(8 Suppl): p. C32-9.
64. Di Mario, C., et al., Detection and characterization of vascular lesions by intravascular ultrasound: an in vitro study correlated with histology. *J Am Soc Echocardiogr*, 1992. **5**(2): p. 135-46.
65. Choudhury, R.P., V. Fuster, and Z.A. Fayad, Molecular, cellular and functional imaging of atherothrombosis. *Nat Rev Drug Discov*, 2004. **3**(11): p. 913-25.
66. Huang, D., et al., Optical coherence tomography. *Science*, 1991. **254**(5035): p. 1178-81.
67. Jang, I.K., et al., Visualization of coronary atherosclerotic plaques in patients using optical coherence tomography: comparison with intravascular ultrasound. *J Am Coll Cardiol*, 2002. **39**(4): p. 604-9.
68. Myerburg, R.J., et al., Frequency of sudden cardiac death and profiles of risk. *Am J Cardiol*, 1997. **80**(5B): p. 10F-19F.
69. Packard, R.R. and P. Libby, Inflammation in atherosclerosis: from vascular biology to biomarker discovery and risk prediction. *Clin Chem*, 2008. **54**(1): p. 24-38.
70. Regar, E., et al., Optical coherence tomography. *Cardiovasc Radiat Med*, 2003. **4**(4): p. 198-204.
71. Sawada, T., et al., Feasibility of combined use of intravascular ultrasound radiofrequency data analysis and optical coherence tomography for detecting thin-cap fibroatheroma. *Eur Heart J*, 2008. **29**(9): p. 1136-46.
72. Stamper, D., N.J. Weissman, and M. Brezinski, Plaque characterization with optical coherence tomography. *J Am Coll Cardiol*, 2006. **47**(8 Suppl): p. C69-79.
73. Schneiderman, J., et al., Diagnosis of thin-cap fibroatheromas by a self-contained intravascular magnetic resonance imaging probe in ex vivo human aortas and in situ coronary arteries. *J Am Coll Cardiol*, 2005. **45**(12): p. 1961-9.

74. Toussaint, J.F., et al., Water diffusion properties of human atherosclerosis and thrombosis measured by pulse field gradient nuclear magnetic resonance. *Arterioscler Thromb Vasc Biol*, 1997. **17**(3): p. 542-6.
75. Caplan, J.D., et al., Near-infrared spectroscopy for the detection of vulnerable coronary artery plaques. *J Am Coll Cardiol*, 2006. **47**(8 Suppl): p. C92-6.
76. Chapman, I., Relationships of recent coronary artery occlusion and acute myocardial infarction. *J Mt Sinai Hosp N Y*, 1968. **35**(2): p. 149-54.
77. Constantinides, P., Pathogenesis of cerebral artery thrombosis in man. *Arch Pathol*, 1967. **83**(5): p. 422-8.
78. Friedman, M. and G.J. Van den Bovenkamp, Role of thrombus in plaque formation in the human diseased coronary artery. *Br J Exp Pathol*, 1966. **47**(6): p. 550-7.
79. Wang, J., et al., Near-infrared spectroscopic characterization of human advanced atherosclerotic plaques. *J Am Coll Cardiol*, 2002. **39**(8): p. 1305-13.
80. Yeager, D., et al., Intravascular photoacoustic imaging of gold-nanorod labeled atherosclerotic plaques. *Photons Plus Ultrasound: Imaging and Sensing 2012*, 2012. **8223**.
81. Lee, H.Y., J.P. Despres, and K.K. Koh, Perivascular adipose tissue in the pathogenesis of cardiovascular disease. *Atherosclerosis*, 2013. **230**(2): p. 177-84.
82. McKenney-Drake, M.L., et al., Epicardial Adipose Tissue Removal Potentiates Outward Remodeling and Arrests Coronary Atherogenesis. *Ann Thorac Surg*, 2017. **103**(5): p. 1622-1630.
83. Verhagen, S. and F. FVisseren, Perivascular adipose tissue as a cause of atherosclerosis. *Atherosclerosis*, 2010. **214**(1): p. 3-10.
84. Abran, M., et al., Development of a photoacoustic, ultrasound and fluorescence imaging catheter for the study of atherosclerotic plaque. *IEEE Trans Biomed Circuits Syst*, 2014. **8**(5): p. 696-703.
85. Dai, X.J., et al., Miniature Endoscope for Multimodal Imaging. *Acs Photonics*, 2017. **4**(1): p. 174-180.
86. Mathews, S.J., et al. *All-optical intravascular probe for dual-mode photoacoustic imaging and optical coherence tomography (Conference Presentation)*. in *Proc. SPIE 10494, Photons Plus Ultrasound: Imaging and Sensing 2018*. 2018. San Francisco, CA.
87. Castano, A.P., T.N. Demidova, and M.R. Hamblin, Mechanisms in photodynamic therapy: part one-photosensitizers, photochemistry and cellular localization. *Photodiagnosis and Photodynamic Therapy*, 2004. **1**(4): p. 279-293.
88. Lucky, S.S., K.C. Soo, and Y. Zhang, Nanoparticles in Photodynamic Therapy. *Chemical Reviews*, 2015. **115**(4): p. 1990-2042.
89. Huang, Z., A review of progress in clinical photodynamic therapy. *Technol Cancer Res Treat*, 2005. **4**(3): p. 283-93.
90. Woodburn, K.W., et al., Phototherapy of cancer and atheromatous plaque with texaphyrins. *J Clin Laser Med Surg*, 1996. **14**(5): p. 343-8.
91. Hayase, M., et al., Photoangioplasty with local motexafin lutetium delivery reduces macrophages in a rabbit post-balloon injury model. *Cardiovasc Res*, 2001. **49**(2): p. 449-55.

92. Waksman, R., et al., PhotoPoint photodynamic therapy promotes stabilization of atherosclerotic plaques and inhibits plaque progression. *J Am Coll Cardiol*, 2008. **52**(12): p. 1024-32.
93. Cheung, J., et al., Longer term assessment of photodynamic therapy for intimal hyperplasia: a pilot study. *Journal of Photochemistry and Photobiology B-Biology*, 2004. **73**(3): p. 141-147.
94. Kereiakes, D.J., et al., Phase I drug and light dose-escalation trial of motexafin lutetium and far red light activation (phototherapy) in subjects with coronary artery disease undergoing percutaneous coronary intervention and stent deployment - Procedural and long-term results. *Circulation*, 2003. **108**(11): p. 1310-1315.
95. Letourneur, D. and P.N. Trohopoulos, Atherosclerotic disease and management challenges with nanomedicine: EU FP7 NMP funded "NanoAthero" and "CosmoPHOS-nano" large-scale projects. *European Journal of Nanomedicine*, 2014. **6**(2): p. 115-119.
96. Kosuge, H., et al., Near infrared imaging and photothermal ablation of vascular inflammation using single-walled carbon nanotubes. *J Am Heart Assoc*, 2012. **1**(6): p. e002568.
97. Gao, W., et al., Copper sulfide nanoparticles as a photothermal switch for TRPV1 signaling to attenuate atherosclerosis. *Nature Communications*, 2018. **9**.
98. Yeager, D., et al., Intravascular photoacoustics for image-guidance and temperature monitoring during plasmonic photothermal therapy of atherosclerotic plaques: a feasibility study. *Theranostics*, 2013. **4**(1): p. 36-46.
99. Kharlamov, A.N., et al., Silica-gold nanoparticles for atheroprotective management of plaques: results of the NANOM-FIM trial. *Nanoscale*, 2015. **7**(17): p. 8003-8015.
100. Sowers, T., H. Yoon, and S. Emelianov, Investigation of light delivery geometries for photoacoustic applications using Monte Carlo simulations with multiple wavelengths, tissue types, and species characteristics. *J Biomed Opt*, 2020. **25**(1): p. 1-16.
101. Beard, P., Biomedical photoacoustic imaging. *Interface Focus*, 2011. **1**(4): p. 602-31.
102. Oraevsky, A.A., et al., Laser-Based Optoacoustic Imaging in Biological Tissues. *Laser-Tissue Interaction V, Proceedings Of*, 1994. **2134**: p. 122-128.
103. Sun, T. and G.J. Diebold, Generation of Ultrasonic-Waves from a Layered Photoacoustic Source. *Nature*, 1992. **355**(6363): p. 806-808.
104. Xia, W., et al., Handheld Real-Time LED-Based Photoacoustic and Ultrasound Imaging System for Accurate Visualization of Clinical Metal Needles and Superficial Vasculature to Guide Minimally Invasive Procedures. *Sensors (Basel)*, 2018. **18**(5).
105. Li, D.S., et al., Polypyrrole-Coated Perfluorocarbon Nanoemulsions as a Sono-Photoacoustic Contrast Agent. *Nano Letters*, 2017. **17**(10): p. 6184-6194.
106. Yoon, H., et al., Super-Resolution Imaging With Ultrafast Ultrasound Imaging of Optically Triggered Perfluorohexane Nanodroplets. *IEEE Trans Ultrason Ferroelectr Freq Control*, 2018. **65**(12): p. 2277-2285.

107. Wang, G.H., et al., Simulation of light delivery for photoacoustic breast imaging using the handheld probe. *Chinese Optics Letters*, 2014. **12**(5).
108. Sivasubramanian, K., et al., Optimizing light delivery through fiber bundle in photoacoustic imaging with clinical ultrasound system: Monte Carlo simulation and experimental validation. *Journal of Biomedical Optics*, 2017. **22**(4).
109. Sangha, G.S., N.J. Hale, and C.J. Goergen, Adjustable photoacoustic tomography probe improves light delivery and image quality. *Photoacoustics*, 2018. **12**: p. 6-13.
110. Fang, Q. and D.A. Boas, Monte Carlo simulation of photon migration in 3D turbid media accelerated by graphics processing units. *Opt Express*, 2009. **17**(22): p. 20178-90.
111. Fang, Q.Q., Mesh-based Monte Carlo method using fast ray-tracing in Plucker coordinates. *Biomedical Optics Express*, 2010. **1**(1): p. 165-175.
112. Yu, L.M., et al., Scalable and massively parallel Monte Carlo photon transport simulations for heterogeneous computing platforms. *Journal of Biomedical Optics*, 2018. **23**(1).
113. Filatova, S.A., I.A. Shcherbakov, and V.B. Tsvetkov, Optical properties of animal tissues in the wavelength range from 350 to 2600 nm. *J Biomed Opt*, 2017. **22**(3): p. 35009.
114. Marquez, G., et al., Anisotropy in the absorption and scattering spectra of chicken breast tissue. *Appl Opt*, 1998. **37**(4): p. 798-804.
115. Bashkatov, A.N., et al., Optical properties of human skin, subcutaneous and mucous tissues in the wavelength range from 400 to 2000 nm. *Journal of Physics D-Applied Physics*, 2005. **38**(15): p. 2543-2555.
116. Tuchin, V.V., *Tissue Optics: Light Scattering Methods and Instruments for Medical Diagnosis*. TT38 ed. Vol. TT38. 2000, Washington: SPIE Press.
117. Jacques, S.L., Optical properties of biological tissues: a review (vol 58, pg R37, 2013). *Physics in Medicine and Biology*, 2013. **58**(14): p. 5007-5008.
118. Schmitt, J.M. and G. Kumar, Optical scattering properties of soft tissue: a discrete particle model. *Applied Optics*, 1998. **37**(13): p. 2788-2797.
119. Wang, R.K.K., Modelling optical properties of soft tissue by fractal distribution of scatterers. *Journal of Modern Optics*, 2000. **47**(1): p. 103-120.
120. Sabino, C.P., et al., The optical properties of mouse skin in the visible and near infrared spectral regions. *J Photochem Photobiol B*, 2016. **160**: p. 72-8.
121. Calabro, K., et al., Gender variations in the optical properties of skin in murine animal models. *Journal of Biomedical Optics*, 2011. **16**(1).
122. Joshi, N., C. Donner, and H.W. Jensen, Noninvasive measurement of scattering anisotropy in turbid materials by nonnormal incident illumination. *Opt Lett*, 2006. **31**(7): p. 936-8.
123. Ramakrishna, S.A. and K.D. Rao, Estimation of light transport parameters in biological media using coherent backscattering. *Pramana-Journal of Physics*, 2000. **54**(2): p. 255-267.
124. Stocker, S., et al., Broadband Optical Properties of Milk. *Applied Spectroscopy*, 2017. **71**(5): p. 951-962.
125. Walstra, P., et al., *Dairy Technology: Principles of Milk Properties and Processes*, ed. I. Marcel Dekker. 1999, New York.

126. Cook, J.R., R.R. Bouchard, and S.Y. Emelianov, Tissue-mimicking phantoms for photoacoustic and ultrasonic imaging. *Biomedical Optics Express*, 2011. **2**(11): p. 3193-3206.
127. Hale, G.M. and M.R. Querry, Optical Constants of Water in the 200-nm to 200-microm Wavelength Region. *Appl Opt*, 1973. **12**(3): p. 555-63.
128. Yoon, H. and S. Emelianov, Combined multi-wavelength photoacoustic and plane-wave ultrasound imaging for probing dynamic phase-change contrast agents. *IEEE Trans Biomed Eng*, 2018. **66**(2): p. 595-598.
129. Yoon, H., et al., Design and Demonstration of a Configurable Imaging Platform for Combined Laser, Ultrasound, and Elasticity Imaging. *IEEE Trans Med Imaging*, 2018. **38**(7): p. 1622-1632.
130. Ranasinghesagara, J.C., Y. Jiang, and R.J. Zemp, Reflection-mode multiple-illumination photoacoustic sensing to estimate optical properties. *Photoacoustics*, 2014. **2**(1): p. 33-8.
131. Ranasinghesagara, J.C. and R.J. Zemp, Combined photoacoustic and oblique-incidence diffuse reflectance system for quantitative photoacoustic imaging in turbid media. *J Biomed Opt*, 2010. **15**(4): p. 046016.
132. Kruizinga, P., et al., Photoacoustic imaging of carotid artery atherosclerosis. *Journal of Biomedical Optics*, 2014. **19**(11).
133. Held, G., et al., Effect of irradiation distance on image contrast in epi-optoacoustic imaging of human volunteers. *Biomed Opt Express*, 2014. **5**(11): p. 3765-80.
134. Xie, Z.X., L.H.V. Wang, and H.F. Zhang, Optical fluence distribution study in tissue in dark-field confocal photoacoustic microscopy using a modified Monte Carlo convolution method. *Applied Optics*, 2009. **48**(17): p. 3204-3211.
135. Periyasamy, V. and M. Pramanik, Monte Carlo simulation of light transport in tissue for optimizing light delivery in photoacoustic imaging of the sentinel lymph node. *J Biomed Opt*, 2013. **18**(10): p. 106008.
136. Frenz, M. and M. Jaeger, Optimization of tissue irradiation in optoacoustic imaging using a linear transducer: theory and experiments - art. no. 68561Y. *Photons Plus Ultrasound: Imaging and Sensing 2008: The Ninth Conference on Biomedical Thermoacoustics, Optoacoustics, and Acoustic-Optics*, 2008. **6856**: p. Y8561-Y8561.
137. Li, M.C., et al., Linear array-based real-time photoacoustic imaging system with a compact coaxial excitation handheld probe for noninvasive sentinel lymph node mapping. *Biomedical Optics Express*, 2018. **9**(4): p. 1408-1422.
138. Montilla, L.G., et al., Real-time photoacoustic and ultrasound imaging: a simple solution for clinical ultrasound systems with linear arrays. *Physics in Medicine and Biology*, 2013. **58**(1): p. N1-N12.
139. Wang, Y., et al., Optimizing the light delivery of linear-array-based photoacoustic systems by double acoustic reflectors. *Sci Rep*, 2018. **8**(1): p. 13004.
140. Wang, L.D., et al., Video-rate functional photoacoustic microscopy at depths. *Journal of Biomedical Optics*, 2012. **17**(10).
141. Jaeger, M., J.C. Bamber, and M. Frenz, Clutter elimination for deep clinical optoacoustic imaging using localised vibration tagging (LOVIT). *Photoacoustics*, 2013. **1**(2): p. 19-29.

142. Jaeger, M., M. Frenz, and D. Schweizer, Iterative reconstruction algorithm for reduction of echo background in optoacoustic images. *Photons Plus Ultrasound: Imaging and Sensing 2008: The Ninth Conference on Biomedical Thermoacoustics, Optoacoustics, and Acoustic-Optics*, 2008. **6856**.
143. Jaeger, M., et al., Deformation-compensated averaging for clutter reduction in epiphotoacoustic imaging in vivo. *Journal of Biomedical Optics*, 2012. **17**(6).
144. Jaeger, M., et al., Improved contrast deep optoacoustic imaging using displacement-compensated averaging: breast tumour phantom studies. *Physics in Medicine and Biology*, 2011. **56**(18): p. 5889-5901.
145. Jaeger, M., et al., Improved contrast optoacoustic imaging of deep breast tumors using displacement-compensated averaging: Phantom studies. *Photons Plus Ultrasound: Imaging and Sensing 2010*, 2010. **7564**.
146. Jaeger, M., et al., Reduction of background in optoacoustic image sequences obtained under tissue deformation. *Journal of Biomedical Optics*, 2009. **14**(5).
147. Zhao, L.Y., et al., Optical fluence compensation for handheld photoacoustic probe: An in vivo human study case. *Journal of Innovative Optical Health Sciences*, 2017. **10**(4).
148. Nie, L.M., et al., Photoacoustic tomography through a whole adult human skull with a photon recycler. *Journal of Biomedical Optics*, 2012. **17**(11).
149. Wang, Z., S. Ha, and K. Kim, A new design of light illumination scheme for deep tissue photoacoustic imaging. *Opt Express*, 2012. **20**(20): p. 22649-59.
150. Yu, J., et al., A Light Illumination Enhancement Device for Photoacoustic Imaging: In Vivo Animal Study. *IEEE Trans Ultrason Ferroelectr Freq Control*, 2017. **64**(8): p. 1205-1211.
151. Sangha, G.S., E.H. Phillips, and C.J. Goergen, In vivo photoacoustic lipid imaging in mice using the second near-infrared window. *Biomedical Optics Express*, 2017. **8**(2): p. 736-742.
152. Ash, C., et al., Effect of wavelength and beam width on penetration in light-tissue interaction using computational methods. *Lasers Med Sci*, 2017. **32**(8): p. 1909-1918.
153. Cox, B., et al., Quantitative spectroscopic photoacoustic imaging: a review. *J Biomed Opt*, 2012. **17**(6): p. 061202.
154. Lutzweiler, C. and D. Razansky, Optoacoustic imaging and tomography: reconstruction approaches and outstanding challenges in image performance and quantification. *Sensors (Basel)*, 2013. **13**(6): p. 7345-84.
155. Zhou, X., et al., Evaluation of Fluence Correction Algorithms in Multispectral Photoacoustic Imaging. *Photoacoustics*, 2020. **19**: p. 100181.
156. Hochuli, R., et al., Quantitative photoacoustic tomography using forward and adjoint Monte Carlo models of radiance. *J Biomed Opt*, 2016. **21**(12): p. 126004.
157. Jacques, S.L., Coupling 3D Monte Carlo light transport in optically heterogeneous tissues to photoacoustic signal generation. *Photoacoustics*, 2014. **2**(4): p. 137-42.
158. Liu, Y., H. Jiang, and Z. Yuan, Two schemes for quantitative photoacoustic tomography based on Monte Carlo simulation. *Med Phys*, 2016. **43**(7): p. 3987.
159. Zhu, C. and Q. Liu, Review of Monte Carlo modeling of light transport in tissues. *J Biomed Opt*, 2013. **18**(5): p. 50902.

160. Bhatt, M., K.R. Ayyalasomayajula, and P.K. Yalavarthy, Generalized Beer-Lambert model for near-infrared light propagation in thick biological tissues. *J Biomed Opt*, 2016. **21**(7): p. 76012.
161. Duncan, A., et al., Measurement of cranial optical path length as a function of age using phase resolved near infrared spectroscopy. *Pediatr Res*, 1996. **39**(5): p. 889-94.
162. Duncan, A., et al., Optical pathlength measurements on adult head, calf and forearm and the head of the newborn infant using phase resolved optical spectroscopy. *Phys Med Biol*, 1995. **40**(2): p. 295-304.
163. Hiraoka, M., et al., A Monte Carlo investigation of optical pathlength in inhomogeneous tissue and its application to near-infrared spectroscopy. *Phys Med Biol*, 1993. **38**(12): p. 1859-76.
164. Kocsis, L., P. Herman, and A. Eke, The modified Beer-Lambert law revisited. *Phys Med Biol*, 2006. **51**(5): p. N91-8.
165. Kohl, M., et al., Determination of the wavelength dependence of the differential pathlength factor from near-infrared pulse signals. *Phys Med Biol*, 1998. **43**(6): p. 1771-82.
166. Sassaroli, A. and S. Fantini, Comment on the modified Beer-Lambert law for scattering media. *Phys Med Biol*, 2004. **49**(14): p. N255-7.
167. Bauer, A.Q., et al., Quantitative photoacoustic imaging: correcting for heterogeneous light fluence distributions using diffuse optical tomography. *J Biomed Opt*, 2011. **16**(9): p. 096016.
168. Daoudi, K., et al., Correcting photoacoustic signals for fluence variations using acousto-optic modulation. *Opt Express*, 2012. **20**(13): p. 14117-29.
169. Hussain, A., et al., Quantitative blood oxygen saturation imaging using combined photoacoustics and acousto-optics. *Opt Lett*, 2016. **41**(8): p. 1720-3.
170. Kumavor, P.D., et al., Target detection and quantification using a hybrid hand-held diffuse optical tomography and photoacoustic tomography system. *J Biomed Opt*, 2011. **16**(4): p. 046010.
171. Rajian, J.R., P.L. Carson, and X. Wang, Quantitative photoacoustic measurement of tissue optical absorption spectrum aided by an optical contrast agent. *Opt Express*, 2009. **17**(6): p. 4879-89.
172. Harrison, T., P. Shao, and R.J. Zemp, A least-squares fixed-point iterative algorithm for multiple illumination photoacoustic tomography. *Biomed Opt Express*, 2013. **4**(10): p. 2224-30.
173. Held, K.G., et al., Multiple irradiation sensing of the optical effective attenuation coefficient for spectral correction in handheld OA imaging. *Photoacoustics*, 2016. **4**(2): p. 70-80.
174. Ranasinghesagara, J.C., et al., Photoacoustic technique for assessing optical scattering properties of turbid media. *J Biomed Opt*, 2009. **14**(4): p. 040504.
175. Shao, P., B. Cox, and R.J. Zemp, Estimating optical absorption, scattering, and Grueneisen distributions with multiple-illumination photoacoustic tomography. *Appl Opt*, 2011. **50**(19): p. 3145-54.
176. Shao, P., T. Harrison, and R.J. Zemp, Iterative algorithm for multiple illumination photoacoustic tomography (MIPAT) using ultrasound channel data. *Biomed Opt Express*, 2012. **3**(12): p. 3240-9.

177. Shao, P., T.J. Harrison, and R.J. Zemp, Consecutively reconstructing absorption and scattering distributions in turbid media with multiple-illumination photoacoustic tomography. *J Biomed Opt*, 2014. **19**(12): p. 126009.
178. Zemp, R.J., Quantitative photoacoustic tomography with multiple optical sources. *Appl Opt*, 2010. **49**(18): p. 3566-72.
179. Troy, T.L., D.L. Page, and E.M. Sevick-Muraca, Optical properties of normal and diseased breast tissues: prognosis for optical mammography. *J Biomed Opt*, 1996. **1**(3): p. 342-55.
180. Fung, Y.C., *Biomechanics : mechanical properties of living tissues*. 2nd ed. 1993, New York: Springer-Verlag. xviii, 568 p.
181. Chan, E.K., et al., Effects of Compression on Soft Tissue Optical Properties. *IEEE Journal of Selected Topics in Quantum Electronics*, 1996. **2**: p. 943-950.
182. Liu, Y., *Measurement of tissue optical properties during mechanical compression using swept source optical coherence tomography*, in *Biomedical Engineering*. 2009, Virginia Polytechnic Institute and State University: Blacksburg, VA. p. 55.
183. Sowers, T., et al., Laser threshold and cell damage mechanism for intravascular photoacoustic imaging. *Lasers Surg Med*, 2018.
184. Kolodgie, F.D., et al., Pathologic assessment of the vulnerable human coronary plaque. *Heart*, 2004. **90**(12): p. 1385-91.
185. Virmani, R., et al., Lessons from sudden coronary death: a comprehensive morphological classification scheme for atherosclerotic lesions. *Arterioscler Thromb Vasc Biol*, 2000. **20**(5): p. 1262-75.
186. Kolodgie, F.D., et al., Intraplaque hemorrhage and progression of coronary atheroma. *N Engl J Med*, 2003. **349**(24): p. 2316-25.
187. Kolodgie, F.D., et al., Intraplaque hemorrhage and progression of coronary atheroma. *New England Journal of Medicine*, 2003. **349**(24): p. 2316-2325.
188. Falk, E., P.K. Shah, and V. Fuster, Coronary Plaque Disruption. *Circulation*, 1995. **92**(3): p. 657-671.
189. Ma, T., et al., A Review of Intravascular Ultrasound-based Multimodal Intravascular Imaging: The Synergistic Approach to Characterizing Vulnerable Plaques. *Ultrasonic Imaging*, 2016. **38**(5): p. 314-331.
190. Ochijewicz, D., et al., Intravascular imaging of coronary artery disease: recent progress and future directions. *Journal of Cardiovascular Medicine*, 2017. **18**(10): p. 733-741.
191. Bourantas, C.V., et al., Hybrid Intravascular Imaging. *Journal of the American College of Cardiology*, 2013. **61**(13): p. 1369-1378.
192. Bourantas, C.V., et al., Hybrid intravascular imaging: recent advances, technical considerations, and current applications in the study of plaque pathophysiology. *European Heart Journal*, 2017. **38**(6): p. 400-U32.
193. Jansen, K., G. van Soest, and A.F.W. van der Steen, Intravascular Photoacoustic Imaging: A New Tool for Vulnerable Plaque Identification. *Ultrasound in Medicine and Biology*, 2014. **40**(6): p. 1037-1048.
194. Bai, X., et al., Intravascular optical-resolution photoacoustic tomography with a 1.1 mm diameter catheter. *PLoS One*, 2014. **9**(3): p. e92463.

195. Qin, H., et al., Inflammation-targeted gold nanorods for intravascular photoacoustic imaging detection of matrix metalloproteinase-2 (MMP2) in atherosclerotic plaques. *Nanomedicine*, 2016. **12**(7): p. 1765-1774.
196. Shang, S., et al., Simultaneous imaging of atherosclerotic plaque composition and structure with dual-mode photoacoustic and optical coherence tomography. *Opt Express*, 2017. **25**(2): p. 530-539.
197. Denton, M.L., et al., Spatially correlated microthermography maps threshold temperature in laser-induced damage. *Journal of Biomedical Optics*, 2011. **16**(3).
198. Hale, G.M. and M.R. Querry, Optical Constants of Water in the 200-nm to 200-micron Wavelength Region. *Appl Opt*, 1973. **12**(3): p. 555-63.
199. Khan, A. and G.D. Tayner, Robustness to Non-Normality of Common Tests for the Many-Sample Location Problem. *Journal of Applied Mathematics and Decision Sciences*, 2003. **7**(4): p. 187-206.
200. Hartung, J., D. Argac, and K.H. Makambi, Small sample properties of tests on homogeneity in one-way Anova and Meta-analysis. *Statistical Papers*, 2002. **43**(2): p. 197-235.
201. Olejnik, S.F. and J. Algina, Type I Error Rates and Power Estimates of Selected Parametric and Nonparametric Tests of Scale. *Journal of Educational and Behavioral Statistics*, 1987. **12**(1): p. 45-61.
202. Ramsey, P.H., Testing Variances in Psychological and Educational Research. *Journal of Educational and Behavioral Statistics*, 1994. **19**(1): p. 23-42.
203. Daeichin, V., et al., Frequency Analysis of the Photoacoustic Signal Generated by Coronary Atherosclerotic Plaque. *Ultrasound Med Biol*, 2016. **42**(8): p. 2017-25.
204. Bayat, M., et al., Comparison of the in vitro effects of low-level laser therapy and low-intensity pulsed ultrasound therapy on bony cells and stem cells. *Prog Biophys Mol Biol*, 2017.
205. Hasgall, P.A., et al., *IT'IS Database for thermal and electromagnetic parameters of biological tissues*. 2015: Online.
206. Kalaprasad, G., et al., Thermal conductivity and thermal diffusivity analyses of low-density polyethylene composites reinforced with sisal, glass and intimately mixed sisal/glass fibres. *Composites Science and Technology*, 2000. **60**(16): p. 2967-2977.
207. Kamal, M.R., V. Tan, and F. Kashani, The thermal conducitvity and diffusivity of polyethylene solids and melts. *Advances in Polymer Technology*, 1983. **3**(2): p. 89-98.
208. Incropera, F.P., et al., *Introduction to Heat Transfer*. 5th ed. 2006, United States of America.
209. Waggener, W.C., Absorbance of Liquid Water and Deuterium Oxide between 0.6 and 1.8 Microns. *Analytical Chemistry*, 1958. **30**: p. 1569-1570.
210. Keijzer, M., et al., Fluorescence spectroscopy of turbid media: Autofluorescence of the human aorta. *Appl Opt*, 1989. **28**(20): p. 4286-92.